Investigating the Manufacturability of Flexible Thin-Film Device (TEG) Using Roll-to-Roll

Xudong Tao, Linacre College

Department of Materials

University of Oxford



A thesis

submitted for the degree of Doctor of Philosophy at University of Oxford, 2021

Abstract

Investigating the Manufacturability of Flexible Thin-Film Device (TEG) Using Roll-to-Roll

Doctor of Philosophy Xudong Tao

Hilary Term 2021 Linacre College

This thesis investigates how to large-scale manufacture flexible thin-film electronics using high-throughput/cost-effective roll-to-roll processing. In this case, a flexible/wearable thermoelectric generator is explored which can locally provide a continuous low-power source for a variety of wearable technologies, to be a competitive alternative to the portable (Li-ion) battery-based system (with typical issues of recharging, short lifetime, energy storage limit and replacement cost, etc.). One of the best conventional thermoelectric materials for wearable thermoelectric generators, bismuth telluride, is studied for scale-up in an industrial-scale roll-to-roll web coater. Magnetron sputtering is employed as a promising technique for scale-up because it is stable, controllable, continuous, already widely used in industrial manufacturing, scalable for fabricating high-quality films at moderate throughput speed, easily incorporated into the roll-to-roll process, compatible with fabrication lines (patternable).

Four key challenges are explored to achieve the goal of advanced roll-to-roll manufacture of flexible thermoelectric generators: (1) exploration of using very thin films to balance the fast roll-to-roll web speed and low vacuum-deposition rate; (2) post-deposition radiation treatments to improve thermoelectric performance and use of interlayers to improve mechanical resilience; (3) replacing a solid shadow mask by other approaches (compatible with roll-to-roll), to make in-line patterns; (4) exploring the preferred

architecture of flexible thermoelectric generators suitable for both wearable applications and roll-to-roll.

Correspondingly, (1) a thinner bismuth telluride film is found to possess a greater thermoelectric performance which also satisfies a high deposition throughput; (2) two feasible post-deposition annealing means to be compatible with high-throughput roll-to-roll processes are studied, besides, two types of substrate-to-coating interlayers are proposed to improve the mechanical resilience of flexible thermoelectric films; (3) a selective metallisation technique is explored to pattern flexible thermoelectric generators; (4) the dimension of the thermoelectric strip and cheap/high-performance contact materials are studied, most interestingly a novel stacked design is invented for flexible thermoelectric generators.

These studies give a significant boost to the commercialisation of flexible thin-film electronics, to fulfil the increasing demand for flexible electronics in the upcoming era of the Internet of Things and Artificial Intelligence.

Preface

The project is conducted by the author at the Department of Materials, University of Oxford, from 2017 to 2021, supervised by Professor Hazel Assender. No part of this thesis has been submitted/accepted for a degree at this or any other universities.

Some parts of this thesis have been published and some are under the progress of patent and publications. Xudong is the 1st author for all listed below.

Publication list:

1. Thermoelectric behaviour of Bi-Te films on polymer substrates DC-sputtered at room-temperature in moving web deposition (*Surf. Coat. Technol.*, 385, 2020)
   --- Chapter 3 in the thesis.
2. Bi_xTe_y thermoelectric thin films sputtered at room temperature onto moving polymer web: Effect of gas pressure on materials properties (*Thin Solid Film*, 712, 2020)
   --- This is not present in the thesis due to lack of space.
3. Static and dynamic post-annealing strategies for roll-to-roll fabrication of DC magnetron sputtered bismuth telluride thin films onto polymer webs (*ACS Appl. Mater. Interfaces*, 13, 2021) --- Chapter 4.
4. Device optimisation and large-scale roll-to-roll manufacturability of flexible thermoelectric generator (*Energy Technol*., 9, 2001008, 2021) --- Chapter 6.
5. Novel stacking design of flexible thin-film thermoelectric generator in a metal-insulator-semiconductor architecture (*Adv. Electron. Mater*., 2100201, 2021) --- Chapter 7.

To be published:

1. Elastic (acrylate/polydimethylsiloxane) substrate-to-coating interlayers for improving the mechanical resilience of Bi-Te thermoelectric films on poly(ethylene terephalate) during roll-to-roll manufacture and in-service operation --- Chapter 4.
2. Roll-to-roll manufacture of flexible thermoelectric generator using flexography with vacuum deposition --- Chapter 5.

Patent application filed: Thermoelectric Generator Device.

Acknowledgments

Firstly I would like to express my heartfelt gratitude to my supervisor Professor Hazel Assender for her guidance, help, and patience throughout the whole project. There is more than the mere supervision of this project. I gain much from her profound knowledge/experience and serious attitude to science. Besides, I sincerely appreciate her significant inputs (time, patience, idea, and suggestions) on my academic writings for journal papers. All in all, THANK YOU VERY MUCH.

Many thanks to all the help from my group: Dr. Kai Zhang, Dr. Bryan Stuart, Mr. Richard Turner, Mr. Botao Hao, and Dr. Vincent Tobin.

I would like to thank the equipment access in Oxford University: Solar Energy Materials Group, Superconducting Materials Group, Semiconductor and Silicon Photovoltaics group, Oxford Materials Characterisation Services, David Cockayne Centre for Electron Microscopy, Furnace Laboratory Oxford Materials; Queen Mary University of London: Materials Engineering Division; University of Nottingham: Advanced Component Engineering Laboratory. Especially I would like to acknowledge: Professor Andrew Watt, Mr. Daniel Gregory, Dr. Wing Chung, Dr. Nanlin Zhang, Mr. Zheng Zhang, Professor Susie Speller, Dr. Clara Barker, Professor Peter Wilshaw, Dr. Ruy Sebastian Bonilla, Mr. Joshua Deru, Mr. John O'Sullivan, Dr. Colin Johnston, Mrs. Nicola Flanagan, Dr. Philip Holdway, Dr. Radka Chakalova, Mrs. Jennifer Holter, Mr. Greg Cook, Mr. Chris Salter, Mr. Anthony Wheeler, Dr. Emiliano Bilotti, Ms. Kening Wan, Dr. James Murray.

Lastly, special thanks to my family for the encouragement, support, and love.

Thank you very much to all for helping me realise my dream.

Table of contents

Chapter 1 Literature review 1

1.1 Introduction 1

1.2 Thermoelectric generators 2

1.2.1 Basic principle 3

1.2.2 Development of wearable TEGs: rigid to flexible 4

1.2.2.1 Wearable rigid TEGs 5

1.2.2.2 Wearable flexible TEGs 6

1.2.3 Classification of flexible TEGs 7

1.2.3.1 Materials: Organic *vs* Inorganic 7

1.2.3.2 Configuration: In-plane TEG *vs* Cross-plane TEG 9

1.2.3.3 Architecture: Single (n- or p-) type TEG *vs* Double type TEG 10

1.2.4 Materials discovery in flexible thin-film TEG 10

1.2.4.1 Thermoelectric semiconductor 10

1.2.4.2 Metal contact 11

1.2.5 Current trend to nanomaterial TEGs 13

1.2.6 Thin-film fabrication of nanomaterial TEGs 14

1.2.6.1 Sputtering technique 17

1.2.6.2 Sputtering parameters 19

1.2.6.2.1 Chamber pressure 19

1.2.6.2.2 Sputter power 19

1.2.6.2.3 Target and substrate temperature 19

1.2.7 Thermoelectric parameters 21

1.3 Roll-to-roll manufacturability of flexible thin-film TEGs 24

1.4 Summary 27

1.5 Reference 27

Chapter 2 Coating fabrication and characterisation 42

2.1 Thin-film fabrication in roll-to-roll 42

2.2 Acrylate-layer fabrication 44

2.3 Characterisation techniques 44

2.3.1 Thermoelectric characterisation 45

2.3.2 Film thickness measurement 48

2.3.3 Electrical resistivity measurement 48

2.3.4 Mechanical test 49

2.3.5 Contact resistance measurement 50

2.3.6 X-ray diffraction 51

2.3.7 Atomic force microscopes 53

2.3.8 Scanning electron microscope/Energy dispersive x-ray 54

2.3.9 UV-Vis spectroscopy 55

2.3.10 Fourier-transform infrared spectroscopy 57

2.3.11 X-ray photoelectron spectrometer 57

2.3.12 Hall effect measurement system/van der Pauw 58

2.3.13 Optical profilometer MicroXAM 61

2.3.14 Scanning Kelvin probe 62

2.6 Summary 64

2.7 Reference 64

Chapter 3 Exploration of using very thin films to balance the fast roll-to-roll webspeed and low vacuum-deposition rate ... 67

3.1 Introduction 67

3.2 Results and discussion 68

3.2.1 Film thickness 68

3.2.2 Surface topography 68

3.2.3 Elemental composition 72

3.2.4 Thermoelectric parameters 75

3.2.4.1 Electrical resistivity 75

3.2.4.2 Seebeck coefficient 77

3.2.4.3 Carrier concentration and mobility 81

3.2.5 Thermoelectric behaviour: Power factor 82

3.3 Summary 82

3.2 Reference 83

Chapter 4 Post-deposition radiation treatments to improve TE performance and use of interlayers to improve mechanical resilience 88

4.1 Post-deposition anneal 88

4.2 Annealing strategies in roll-to-roll 89

4.3 Results and discussion 92

4.3.1 Structural properties of as-deposited/annealed Bi-Te films 92

4.3.1.1 As-deposited film 92

4.3.1.2 Static vacuum-oven annealed film 96

4.3.1.3 Static electron beam annealed film 97

4.3.1.4 Dynamic infrared and electron beam annealed films 97

4.3.2 Thermoelectric behaviour of as-deposited/annealed films 97

4.3.2.1 Electrical resistivity and Seebeck coefficient 99

4.3.2.2 Power factor 101

4.3.3 Decreasing the treatment time for roll-to-roll anneals 102

4.4 Mechanical deformation 104

4.5 Buffer-layer fabrication 105

4.6 Results and discussion 106

4.6.1 Film thickness and surface morphology 106

4.6.2 Buckling test 108

4.6.2.1 Changes in morphology during buckling strain 109

4.6.2.2 Changes in thermoelectric behaviours during buckling strain 111

4.6.2.3 Power measurements during cyclical buckling test 112

4.7 Summary 115

4.8 Reference 116

Chapter 5 Replacing a solid shadow mask by selective metallisation technique to make in-line patterns 122

5.1 Introduction 122

5.2 Roll-to-roll manufacture of flexible TEGs using SMT 124

5.3 Results and discussion 125

5.3.1 Non-SMT fabricated samples 125

5.3.1.1 Phase identification 125

5.3.1.2 Electrical performance 127

5.3.1.3 Mechanical performance 129

5.3.2 SMT fabricated TEGs 129

5.3.2.1 Images of Cu/Bi-Te patterns 129

5.3.2.2 Seebeck performance of SMT-fabricate TEGs 132

5.3.2.3 Why does R_{TEG} increases using SMT? 134

5.4 Summary 138

5.5 Reference 139

Chapter 6 Device optimisation and large-scale roll-to-roll manufacturability of flexible TEGs 141

6.1 Introduction 141

6.2 Device fabrication 146

6.2.1 Patterning by solid mask 146

6.2.2 Patterning by laser cutter and printing technique 147

6.3 Results and discussion 148

6.3.1 Surface morphology, electrical performance and uniformity ... 148

6.3.2 Band-diagram predication 150

6.3.3 Analysis of reactions at interface..... 152

6.3.4 Seebeck characterisation of Al/, Cu/, Au/Bi-Te based TEGs ... 156

6.3.5 Cu/Bi-Te based TEGs..... 158

6.3.5.1 In-line patterning connection 158

6.3.5.2 Dimensions of the thermoelectric strip 159

6.3.6 Large-scale manufacturability of in-line patterned TEGs 162

6.4 Summary 164

6.5 Reference..... 166

Chapter 7 A novel stacking design of flexible TEGs 170

7.1 Introduction 170

7.2 A novel stacking design..... 173

7.3 COMSOL simulation 175

7.4 Results and discussion 176

7.4.1 Surface topography and cross-section of stackings..... 176

7.4.2 Phase identification..... 178

7.4.3 Thermoelectric performance..... 180

7.4.3.1 Seebeck behaviour of stacked TEGs 180

7.4.3.2 Thermoelectric strips connected in plane *vs* in stacking 187

7.4.3.3 In-plane connection of stacked TEGs 191

7.4.3.4 Mechanical test 194

7.5 Summary 197

7.6 Reference 198

Chapter 8 Conclusions and future work 204

8.1 Conclusions 204

8.2 Suggestions for future work 205

List of abbreviations

R2R	Roll-to-roll	**XRD**	X-ray diffraction
TEGs	Thermoelectric generators	d	Spacing between crystal planes
TE	Thermoelectric	θ	Incident angle
V	Voltage	λ	Wavelength of x-ray beam
ΔT	Temperature difference	$FWHM$	Full width half maximum
PET	Polyethylene terephthalate	**AFM**	Atomic force microscope
PEN	Polyethylene naphthalate	**SEM**	Scanning electron microscope
PI	Polyimide	**EDX**	Energy dispersive x-ray
CP-TEG	Cross-plane TEG	**UV-Vis**	UV-Vis spectroscopy
IP-TEG	In-plane TEG	R_H	Hall coefficient
ZT	Figure of merit	$E_{kinetic}$	Kinetic energy
E_g	Bandgap	hv	Energy of an x-ray
RT	Room temperature	$E_{binding}$	Binding energy
M-S	Metal-semiconductor	Φ	Work function
E_{VBM}	The maximum valance band energy	**FTIR**	Fourier-transform infrared spectroscopy
E_F	Fermi level	V_H	Hall voltage
E_{CBM}	The minimum conduction band energy	**XPS**	X-ray photoelectron spectrometer
E_0	Vacuum level	B	Magnetic field
SB	Schottky barrier	n	Carrier concentration
WF_M	Work function of metal	μ	Carrier mobility
W_D	Depletion region	Bi_2Te_3	Bismuth telluride
W_A	Accumulation region	**RMSR**	Root mean square roughness

$\chi_{p\text{-}s}$	Electron affinity	**S-VO**	Static vacuum oven
Ar	Argon	**S-Eb**	Static pulsed electron beam
DC	Direct current	**D-Eb**	Dynamic electron beam
T_S	Substrate temperature	**S-IR**	Static infrared
T_M	Melting point	**D-IR**	Dynamic infrared
S	Seebeck coefficient	E	Young's modulus
T	Absolute temperature	**SMT**	Selective metallization Tech.
ρ	Electrical resistivity	R_{TEG}	Internal resistance of TEG
σ	Electrical conductivity	R_L	load resistance
λ	Thermal conductivity	S_{TEG}	Seebeck coefficient of TEG
PF	Power factor	P	Power output
Rs	Sheet resistance	V_{OC}	Open-circuit voltage
t	Film thickness	I_{SC}	Short-circuit current
I	Current	**F**	Fluorine
e-beam	Electron beam	**FIB**	Focused ion beam
IR	Infrared	FF	Fill factor
TPGDA	Tripropyleneglycol diacrylate	**n-i-p**	n-type – insulator – p-type semiconductor
S'	An induced TE current in response to ΔT	**m-i-s**	Metal – insulator – semiconductor
PDMS	Polydimethylsiloxane	R_C	Contact resistance
A	Contact area	ε	Surface emissivity
V_{jump}	Voltage jump	P_{max}	The maximum power output
T_g	Glass transition temperature		

List of Figures

Chapter 1 1

Figure 1.1. Schematic of a basic thermoelectric theory 3

Figure 1.2. (a) A TEG element composed of an n-type and p-type materials; (b) A typical TEG system 4

Figure 1.3. (a) Schematic configuration of in-plane TEG and cross-plane TEG; (b) The traditional n-m-p TEG design and single n-type TEG design 9

Figure 1.4. *ZT* of the currently used or prospective TE materials 11

Figure 1.5. (a) (c) Schottky and (b) (d) Ohmic junctions at m-s interface 12

Figure 1.6. Sputtering deposition 17

Figure 1.7. The principle of magnetron sputtering 18

Figure 1.8. Schematics of coating structure as a function of Ar pressure and substrate temperature 20

Figure 1.9. Dependence of ρ, S and λ on different materials 23

Figure 1.10. Schematic diagram of the effect of energy barrier on the potential difference generated 24

Figure 1.11. (a) Sputtering source; (b) Roll-to-roll handing; (c) Flexography 26

Chapter 2 42

Figure 2.1. Aerre Machines web coater (a) left side (b) right side; Edwards 306 system (c) side view (d) face view 42

Figure 2.2. Vacuum jet deposition of acrylate 44

Figure 2.3. (a) An MMR Tech. Seebeck effect system; (b) A home-built Seebeck setup with a schematic diagram 46

Figure 2.4. Comparison of results between Oxford home-build Seebeck setup and a commercial Seebeck system.....47

Figure 2.5. Comparison between two point probe and four point probe.....49

Figure 2.6. Buckling test 50

Figure 2.7. Schematic diagram of contact resistance measurement.....51

Figure 2.8. Constructive interference and diffraction of x-rays from crystal planes .52

Figure 2.9. The principle of AFM 53

Figure 2.10. Signals and their regions generated by beam-sample interaction in SEM and x-ray generation process.....55

Figure 2.11. UV-Vis transitions 56

Figure 2.12. (a) Hall effect measurement and (b) van der Pauw method 59

Figure 2.13. Calculation of resistivity using van der Pauw method 60

Figure 2.14. The optical setup of MicroXAM and a simple white light interferometer, and the theory of interference effect: constructive/destructive interference 62

Figure 2.15. The electronic energy level of the sample and tip for three cases (a) separated with no electrical contact, (b) electrically contacted, (c) external bias applied 63

Chapter 3 67

Figure 3.1. (a-f) AFM topography images and (g) example line profiles 70

Figure 3.2. Part A: (a) RMSR of Bi-Te films, (b) Schematic of the variation of RMSR with thickness of films grown by RT sputtering; Part B: AFM images of substrates and coatings.....71

Figure 3.3. SEM images and AFM phase images 72

Figure 3.4. Elemental ratio of Te and Bi as a function of deposition time 74

Figure 3.5. Plots of ρ, S (a) and PF (b) for Bi-Te films with various deposition time, and schematic representations of the relationship 76

Figure 3.6. (a) Tauc plot of Bi-Te films and (b) The variation of E_g 77

Figure 3.7. XRD pattern of ~80-nm film grown Si wafer and ~1-μm Bi-Te film grown on polymer substrate 79

Figure 3.8. (a) TEM image of Bi-Te film; (b) TEM diffraction pattern of a Bi-Te film; (c-d) HRTEM images of a Bi-Te film 80

Figure 3.9. Variation of (a) carrier concentration and (b) carrier mobility 81

Chapter 4 88

Figure 4.1. Schematics of four different post-annealing strategies 90

Figure 4.2. (a) XRD patterns of as-deposited and post-annealed Bi-Te films, (b) Te/Bi ratio determined from EDX before and after various treatments; (c) Example Williamson-Hall analysis 93

Figure 4.3. Part A: SEM images of the as-deposited and post-treated Bi-Te films; Part B: The elemental mapping 95

Figure 4.4. Part A: (a) ρ, (b) S, (c) PF, (d) n, (e) μ and (f) E_g of as-deposited and post-annealed films; Part B: (a-c) the expected relations of S and ρ with n and μ; Plots of (d) ρ *vs* crystallite size, (e) μ *vs* crystallite size, (f) μ *vs* ratio of Te:Bi, (g) n *vs* ratio of Te:Bi and (h) n *vs* E_g; and (i) ratio of Te:Bi *vs* E_g 98

Figure 4.5. (a) The variation of temperature on the drum in static and dynamic situations under half/full powers of an IR source, and (b) The temperature on a rotating drum under full power to the IR heater 102

Figure 4.6. Plots of (a) ρ, (b) S and (c) PF for Bi-Te films with various annealing times of dynamic IR/e-beam irradiations in webcoater. 103

Figure 4.7. (a) Stress-strain relations of polymer substrate and post static IR annealed polymer substrate, (b) FTIR spectra of polymer substrate and a 1-hour post static IR annealed polymer substrate, (c) Stress-strain relations of the as-deposited and post dynamic IR annealed films on polymer substrates..... 104

Figure 4.8. (a) The thickness of buffer coatings; (b) the calculated relation between the strain applied to the Bi-Te film and the displacement during buckling tests..... 107

Figure 4.9. AFM images and RMSR..... 108

Figure 4.10. Two mechanisms of buffer layers to maintain Bi-Te coating 109

Figure 4.11. MicroXAM images of during-buckling-strained Bi-Te films on PET sheets with/without buffer layers 110

Figure 4.12. (a) Changes in ρ, S and PF of Bi-Te film on PET under various strains during buckling test; (b-d) Changes in ρ, S and PF of Bi-Te film on PET with/without buffer layers under various strains; (e-g) Changes in ρ, S and PF of Bi-Te film on PET with various-thickness buffer layers during a buckling strain of 2%..... 112

Figure 4.13. (a) Resistance measurement for Bi-Te film grown on PET sheets under various buckling strains in cycling fatigue testing; (c) Current, (e) Voltage and (g) Power measurements of Bi-Te film on PET substrates (strip: 5-mm width × 37-mm length) with/without buffer layers in cycles of 1%-strain buckling tests..... 114

Chapter 5 122

Figure 5.1. (a) Plot of vapour pressure and temperature of Krytox® 1506 vacuum oil; (b) Temperature recording of IR source in web coater 124

Figure 5.2. (a) Schematics of continuous R2R setups and stepwise processes; (b) A real image of flexography setup 125

Figure 5.3. (a) XRD and XPS results of evaporated Cu films; (b) XRD, XPS and TEM results of Bi-Te films; (c) Variations of the (1 1 1) peak in XRD of Cu films under 10 and 50 mins under e-beam or IR treatments 127

Figure 5.4. ρ of as deposited and post-treated (a) Cu films and (b) Bi-Te films..... 128

Figure 5.5. Tensile stress-strain or force-displacement plot of PET with/without post-deposition treatments for ~50 mins 129

Figure 5.6. Images of patterns using SMT 131

Figure 5.7. (a) Plot of V_{OC} vs ΔT, (b) Plot of I_{SC} vs ΔT, (c) P output of TEGs, (d) Plot to calculate R_{TEG} through the linear fit 133

Figure 5.8. (a & b) Resistances of SMT-fabricated Cu and Bi-Te strips, (c) R_C of Cu/Bi-Te interface of a standard TEG and SMT-fabricated TEGs..... 136

Figure 5.9. XPS results of for SMT-fabricated patterns after IR/e-beam treatment 137

Chapter 6 141

Figure 6.1. (a) Solid shadow masks for patterning of TEGs with different dimensions; (b) Schematic diagram of making in-series (or in-parallel) connected TEGs..... 146

Figure 6.2. (a) Schematics of continuous R2R setups and stepwise processes; (b) Setup to measure a change in resistance of a segmented sample during bending; (c) Seebeck measurement of a segmented sample 148

Figure 6.3. (a-f) MicroXAM and SEM images of PET substrate and films grown on PET sheets, (g) XRD results of evaporated metal films, sputtered Bi-Te film, and Si wafer substrate, (h) Roughness, film thickness and electrical resistivity of film grown on PET sheets, (i) EDX spectrum of Bi-Te film, Elements (k) Bi and (l) Te distribution in (j) Bi-Te film 149

Figure 6.4. (a) Tauc plot of ~80-nm thick Bi-Te film, (b) XPS valence scan to determine WF by an intersection of the linear extrapolations to the cutoff regions of E_F

and E_{VBM}; (c) i: Positions of *WF*, E_g, and valance/conduction bands of Bi-Te and metal films, ii-v: Vacuum aligned band diagram, without consideration of any new phase formed at M-S interface 151

Figure 6.5. (a) Resistance measurements from metal to semiconductor or from semiconductor to metal, (b) Contact resistance measurement of interface between Bi-Te and metal films; (c-f) XPS spectrum of Ag, Al, Cu and Au films..... 154

Figure 6.6. (a-d) Elemental profiles of line scale at cross sections of Bi-Te film/metal films on Si wafers; (e-h) Elemental mappings of Bi-Te film/Ag film on PET substrate; (i) Elemental ratio of Ag, Bi and Te at positions 1, 2, 3, 4 and 5 in (e)..... 155

Figure 6.7. (a-b) V_{OC} and I_{SC} of five-strip TEGs using three different electrodes: Al, Cu, Au, (c-e) Output *V*, *I* and calculated *P* of five-strip TEGs in an Ohm's circuit, (c) A plot to deduce S_{TEG} and R_{TEG} 157

Figure 6.8. Part A: (a) V_{OC} and I_{SC} of in-series and in-parallel connected Cu-TEGs as a function of number of strips, with fit lines in parentheses, (b & c) *P* output of in-series and in-parallel connected Cu-TEGs for 1 – 5 strips at a ΔT of 11.4 ± 0.2°C; Part B: (a-c) *V*, *I* and *P* output of in-series connected Cu-TEGs with 5 strips of fixed width (2 mm) but varying length (13 – 50 mm) under 11.4 ± 0.2°C, (d-f) *V*, *I* and *P* output of Cu-TEGs with 5 strips of fixed length (20 mm) but varying width (0.5 – 4 mm) under 11.4 ± 0.2°C. Part C: The calculated S_{TEG} and R_{TEG} for (a) in-series and in-parallel modes, (b & c) strip dimension 161

Figure 6.9. (a-d) Optical microscopy images of laser-cut samples using different laser powers: 8%, 8.3%, 8.6% and 9% of 40 W; (e) resistance crossing laser-cut line of samples with different powers in laser cutting; (f) Change in resistance at a middle area of pristine sample and segmented sample by laser cutting, in buckling testing; (g-i) Output *I*, *V* and *P* of pristine and segmented samples..... 163

Chapter 7 170

Figure 7.1. Mask designs for making (a) in-series stacked strips, (b) in-parallel stacked strips, and (c) in-plane connects between individual stacks in series or parallel; (d) The fabrication process of in-series stacked strips, and then in-series connect these stacked strips in plane. 173

Figure 7.2. (a) A cross-section view of an in-series and an in-parallel stacked strip; (b) displays a top view of final devices; In-series/parallel connection in plane of (c) in-series stacked strips and (d) in-parallel stacked strips..... 174

Figure 8.3 (a-c) AFM images of (a) PET substrate, (b) Bi-Te, (c) Cu and (d) acrylate polymer coatings on PET sheets, (e) 9^{th} stacked Cu film, (f) 13^{th} stacked Cu film, (g) RMSR of PET, Bi-Te, Cu, acrylate coatings and roughness changes in stacked layers 178

Figure 7.4. Part A: (a-c) SEM surface image of Bi-Te, Cu and acrylate coatings, (d) TEM image of Bi-Te film, (e-f) SEM cross-section view of stacked layers and elemental analysis in a line scan mode of EDX; Part B: (a-b) XRD patterns of Bi-Te and Cu films on Si wafers, (c-d) XPS analysis of Bi-Te and Cu films on polymer sheets; (e) TEM diffraction pattern of a Bi-Te film, (f-g) HRTEM images 179

Figure 7.5. XRD of in-parallel stacked coatings 180

Figure 7.6. (a) Plot of open-circuit voltage vs ΔT as increasing number of stacked strips in series, (b) Plot of short-circuit current vs ΔT as increasing number of stacked strips in parallel, (c) Plot of temperature on the sample surface vs time for samples with different stacked layers..... 182

Figure 7.7. COMSOL simulation of heat transfer in TEGs under an ambient condition of 293 K and a heat of 305 K to simulate a real wearable application..... 186

Figure 7.8. Part A: comparisons of the measured current, voltage and calculated power output between TEGs structured in plane and in stacking, Part B: plots of *V*, *I* and *P* as the number of strips in the device 189

Figure 7.9. Part A: in-plane connection of in-series stacked TE strips; Part B: in-plane connection of in-parallel stacked TE strips. 193

Figure 7.10. Cyclical strain testing under buckling of a series-connected stack 195

Figure 7.11. Cyclical strain testing under buckling of a Bi-Te film directly grown on a PET sheet..... 196

List of Table

Chapter 1 ..... **1**

Table 1.I. A summary of wearable TEGs types and their target electronics devices... 2

Table 1.II. A summary of wearable rigid TEGs studies 5

Table 1.III. A summary of flexible TEGs studies since 2001 6

Table 1.IV. A comparison of PET, PEN and PI..... 8

Table 1.V. The work function and electrical resistivity of selected materials 12

Table 1.VI. Summaries of TEGs fabrication techniques..... 15

Table 1.VII. Comparison of vacuum deposition techniques for TE films 16

Chapter 2 ..... **42**

Table 2.I. Materials characterizations used in this project 44

Table 2.II. Undesirable voltages in Hall effect measurement..... 59

Table 2.III. Hall effect measurements..... 59

Chapter 3 ..... **67**

Table 3.I. Bi-Te samples obtained by varying deposition time..... 68

Table 3.II. XRD details of a ~1-μm thick Bi-Te film 79

Chapter 4 ..... **88**

Table 4.I. Conditions of various annealing approaches 91

Table 4.II. The average crystallite size, micro-strain and lattice parameters of as-deposited and post-annealed films 94

Table 4.III. The relation between strain and displacement during buckling tests for all samples, using a calculation method considering the thickness of Bi-Te film, buffer layer and PET substrate 107

Chapter 5 122

Table 5.I. Elemental compositions for SMT-fabricated patterns after IR and e-beam treatments 138

Chapter 7 170

Table 7.I. Material properties used in COMSOL simulation 175

Chapter 1 Literature Review

1.1 Introduction

The demand for wearable smart electronic devices is growing tremendously (e.g. $34 billion of wearable fitness market in 2020 [1]), so an exploration of high-throughput/cheap roll-to-roll (R2R) processing is of interest to commercially scale up the manufacture of wearable/flexible thin-film electronics. One example device attracting my interest here is wearable/flexible thermoelectric generators (TEGs) which is a clean, green, and renewable energy source [2] that can locally provide a small constant power for wearable/portable electronics (to minimise issues in portable (Li-ion) battery-based power systems like multiple-time charging, energy storage limit, short lifetime and replacement cost [3]).

TEGs utilise thermoelectric (TE) materials that can directly convert a temperature gradient (ΔT) into electric energy and *vice versa* [4, 5]. A commercial product of TE materials is Peltier/TE coolers used as refrigerators. In wearable TEGs, the human body is regarded as a thermal-energy source. In recent years, wearable TEGs have received considerable attention as an environmentally friendly and continuous source of power generation [6], for converting the human body's waste heat to electricity e.g. to power wearable electronics and biomedical devices [7]. Research related to wearable TEGs has investigated them on a laboratory scale while there are few studies on large-scale manufacture, and this appears to be one of the major challenges in commercialisation for all wearable/flexible electronics. High throughput/cheap R2R process is worth considering since it has been well established in the modern industrial system, and most importantly, the fabrication technique of flexible electronics could be easily integrated into R2R lines. Hence, this project investigates the impacts of moving laboratory-scale

outcomes to high-throughput manufacture on wearable/flexible TEGs using an R2R process.

1.2 Thermoelectric generators

A TEG is a type of solid-state energy harvester which is regarded as a renewable and reliable means to generate power by converting thermal energy to electricity [2]. Wearable TEGs utilise the human body temperature as a constant heat source, which have been extensively developed to fulfil specific power needs from mW to μW, as summarised in Table 1.I with their corresponding target electronics. (Note: this table does not contain the large bulk TEG type (>W) which is applied in the recovery of industrial waste heat [8]).

TEG researches on the commercialisation process of target electronic devices are ongoing. In this study, I mainly investigate the thin-film TEG. The thin-film TE materials can be studied in different ways [9, 10] to research on a thickness from a few nm to μm.

Table 1.I. *A summary of wearable TEG types and their target electronics [11-15].*

TEG type (the generated power range)	Target electric device (power demand)
Small TEGs (≈mW)	Biosensors (150 - 0.14 mW)
	Remote controller (100 mW)
	Music player (50 mW)
	FM radio (30 mW)
	Wrist GPS (10 - 1.5 mW)
Micro TEGs (mW-μW)	RFID tracker (<1.5 mW)
	Hearing aid (1 mW)
	Wireless sensors nodes (100 μW)
	Pacemaker (50 μW)
	Neurological stimulator (mW - 30 μW)
Thin-film TEGs (≈μW)	Wristwatch (5 μW)

1.2.1 Basic principle

The TE effect was first discovered by Thomas Johann Seebeck (1821) from a study of the magnetic polarisation of metals and ores produced by ΔT [16]. As a consequence, the direct conversion of ΔT to electric voltage and *vice versa via* a thermocouple is called the 'Seebeck effect'. Remarkably, he investigated PbS and ZnSb two centuries ago, which were proved by Telkes (1938) as two of the best materials for TE energy conversion [17]. The voltage generated by the Seebeck effect refers to the thermal electromotive force (*e.m.f.*) generated under an open-circuit condition (see Figure 1.1) [18-20]. Under applied different temperatures at junctions 'C' and 'D', an open circuit *e.m.f.* voltage is generated between 'A' and 'B'. The voltage generated is found to be directly proportional to ΔT (see equation (1.1) [23].

$$V = S \cdot \Delta T \tag{1.1}$$

where V is the voltage (V) generated between 'A' and 'B'; the S is the Seebeck coefficient (V/K), and ΔT is the temperature gradient (Kelvin).

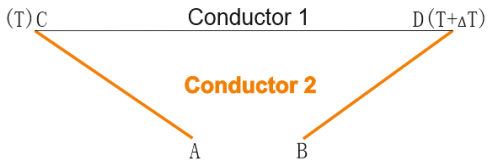


Figure 1.1. *Schematic of a basic thermoelectric theory.*

The TEG system is based on the Seebeck effect as illustrated above. A typical TEG element is displayed in Figure 1.2 (a) [2, 21, 22]. As a ΔT is applied to semiconductors, charge carriers at the hot side (thermally induced carrier excitation to cross the bandgap) have more kinetic energy than those at the cold end, thus they diffuse towards the cold side to be equilibrium until a sufficient potential gradient is established to prevent further net migration [21]. During this process, the majority of carriers move from the hot end towards the cold end, consequently, the hot end of an n-type material becomes positively

charged because of electron transport towards the cold end, while the hot end of a p-type material becomes negatively charged because of hole transport towards the cold end. Here a conductive material is linked between the n-type and p-type materials, acting as a metal-semiconductor (M-S) junction. As a result, an electric current can be generated in an external circuit because of the flow of surplus holes and electrons in n-type and p-type materials, respectively, generated by a continuous supply of heat to the TE materials. Therefore, thermal energy is converted into electricity.

TEGs are semiconductor devices [23] typically composed of a large number of TEG elements [24, 25]. As seen in Figure 1.2 (b) [12], these TEG elements are electrically connected in series and thermally in parallel to increase the power output [2, 12].

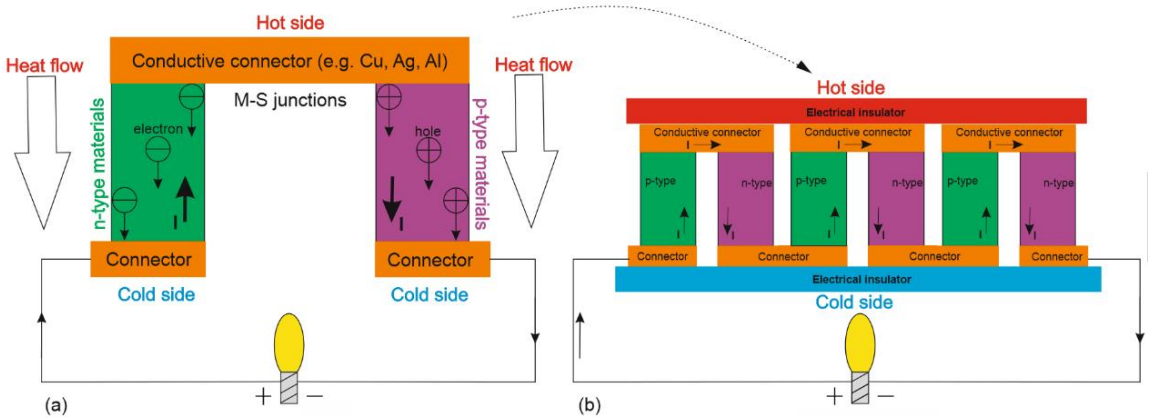


Figure 1.2. *(a) A TEG element composed of n-type and p-type materials; (b) A typical TEG system. (where I is the current flow; M-S junction is the metal-semiconductor junction). Heat flows from the hot side to the cold side, and electric current flows from n-type to p-type materials.*

1.2.2 Development of wearable TEGs: rigid to flexible

A wearable TEG is one of the most recent technological advancements in the field of portable electronics [2]. A large number of studies have been carried out for wearable TEGs, classified into TEGs with rigid or flexible substrates.

1.2.2.1 Wearable rigid TEGs

Wearable rigid-substrate TEGs, the primary subject of the earlier research (Table 1.II), are limited in size for wearable applications as they cannot match the body shape well, and thus affecting the comfort and conversion efficiency, therefore, flexible TEGs were introduced in 2001 [26].

Table 1.II. *A summary of wearable rigid TEGs studies.*

Ref.	Samples	Output	Applications
[27]	p-SiGe and n-SiGe pairs on Si substrates	1 - 2 μW (watch size)	Wearable wrist electronics
[28]	Thermopile blocks on Al plates	20 $\mu W/cm^2$	Wireless sensor nodes
[29]	TEGs + PV cell on Si substrates	7 - 30 $\mu W/cm^2$	Wearable sensors & medical devices
[30]	BiTe thermopile pairs on Al plates	10 $\mu W/cm^2$	Wearable wireless sensors
[31]	Thermopile blocks on Al plates	1 - 10 mW/cm^2	Batteries in low-power wearable electronics
[32]	Implanted TEGs on rigid substrates	20 $\mu W/cm^3$	Biosensors
[33]	NiMo and $LaSrTiO_3$ on ceramic plates	2.4 $\mu W/mm^2$	Sensor network systems
[34]	BiTe elements on Cu plates	28.5 $\mu W/cm^2$	Wearable wristband
[35]	Commercial rigid TEGs from Tellurex®	2.2 $\mu W/cm^2$	Wearable &implantable devices
[36]	BiTeSb-BiSbTe on glass substrates	0.8 mW/mm^2	Microelectronics
[37]	ZnSb on a $Si0_2$/Si wafer substrates	0.22 mW/cm^2	Flexible thermoelectric devices
[38]	BiTe-SbTe on glass substrates	3.8 mW/cm^2	Wearable self-powered mobile electronics
[39]	Carbon nanotube on glass substrates	413 $\mu W/(K^2 \cdot m)$	-

1.2.2.2 Wearable flexible TEGs

The output power of TEGs is theoretically and experimentally proven to be proportional to the contact area between the TEG and the skin surface [40], hence wearable flexible TEGs are introduced that can be bent and conformably attached to the curved skin surface as much as possible to increase the TEGs-skin thermal contact, thereby improving the output power.

A first attempt to fabricate flexible TEGs was conducted by Qu *et al.* in 2001 [26]. A flexible TEG of 100 Sb-Bi strips deposited onto a Cu foil substrate was fabricated with overall dimensions 16 × 20 × 0.05 mm^3 through a few steps including photoresist coating and lithography on Cu foils, electrodeposition of semiconductors, embedding, and wet chemical etching. This device was reported to have a TE output of 8.4 mV/K (i.e. approx. 250 mV corresponding to a ΔT of 30 K). A summary of the important research on wearable flexible TEGs is presented in Table 1.III. In addition to a desired heat-electricity conversion efficiency (i.e. figure of merit, *ZT*), an ideal flexible TEG should possess similar properties to a textile fabric (e.g. flexible, non-toxic, lightweight, breathable, and washable [41]).

Table 1.III. *A summary of flexible TEGs studies since 2001.*

Reference	Samples	Performance
[42], 2003	Cu-Ni on polyimide (PI) sheets	1.54 μV/K per couple
[43], 2005	Cu-Ni on PI sheets	16 μV/K per couple
[44], 2006	Bi-Sb on PI foils	0.8 mV at ΔT = 5°C
[45], 2008	Ni-Ag inside a textile	19.6 μV/K per couple
[46], 2008	Bi-Te on SU-8 moulds	218 μW/cm^2 at ΔT =40K
[47], 2009	BiTe on polymer moulds	0.29 μW/($cm^2 \cdot k^2$)
[48], 2010	BiSbTe on PEN sheets	0.06 μW/($cm \cdot k^2$)

[49], 2011	Bi-Te-Se on PI sheets	6 mV at ΔT = 20K
[50], 2011	BiTe-SbTe on Kapton© foils	108 μV/K per couple
[51], 2012	BiTe on PMMA moulds	0.11 μW/K
[52], 2012	P_3HT-C_6H_5Cl on flexible substrates	285 μV/K per couple
[53], 2012	Bi-Te-Se-Sb on Kapton© PI	210 μV/K per couple
[54], 2013	Bi-Sb-Te on polymer matrix	152 μW/cm^2
[55], 2013	BiTe-SbTe on Kapton© substrates	2.4 nW/K per couple
[56], 2013	BiTe on PET sheets	49 μV/K per couple
[57], 2013	BiTe-SbTe on Kapton© substrates	1.2 V
[58], 2013	CNT-polystyrene on PET sheets	55 mW/m^2 at ΔT = 70°C
[59], 2013	BiTe-SbTe on flexible substrates	139 μV/cm^2
[60], 32014	BiTe-SbTe on Kapton© substrates	227 μV/K per couple
[61], 2014	n-/p-type Si on PET sheets	9.3 mV at ΔT = 54°C
[62], 2014	BiSbTe-BiSeTe in polymer-based fabrics	60 μV/K per couple
[63], 2014	BiTe-SbTe on PI substrates	1.2 mW/cm^2 at ΔT =50K
[64], 2014	CNT/carbon/ACT on PET substrates	0.46 mW/m^2 at ΔT=36°C
[65], 2014	BiTe-SbTe on fabrics	3.8 mW/cm^2 at ΔT =50K
[66], 2015	Al-doped ZnO/Zn-Sb on Kapton© PI film	246.3 μW at ΔT =180K

1.2.3 Classification of flexible TEGs

1.2.3.1 Materials: Organic *vs* Inorganic

Flexible/wearable TEGs can be either fully organic [67-70] or inorganic/organic hybrids [71-74]. Organic TEGs have been the subject of extensive scientific interest during recent decades due to their merits e.g. weak toxicity, low cost, low density, ease of processing, and mechanical flexibility [75, 76]. However, organic semiconductors are still not widely employed mainly because of their low TE efficiency [77] which still needs to be greatly improved and studies are currently ongoing for organic TEGs.

Conversely, traditional inorganic TE materials have much better TE efficiency. Inorganic TE materials coated onto a flexible substrate (which could be either a polymer sheet [78] or a textile [38]) is one typical kind of inorganic/organic hybrid. This project investigates a flexible polymer-bonded TEG in which inorganic TE thin films are deposited onto flexible polymer sheets *via* vacuum thin-film deposition techniques. A comparison of three typical/commonly studied polymer sheets is given in Table 1.IV.

Table 1.IV. *A comparison of Polyethylene terephthalate (PET), Polyethylene naphthalate (PEN), and Polyimide (PI), where T_M is melting point, T_g is glass transition temperature, TS is tensile strength.*

Polymers	T_M **(°C)**	T_g **(°C)**	***TS*** **(MPa)**	**Cost**
PET	250	67-81	55-75	Cheap
PEN	270	120	270	Moderately high
PI	It is stable from -269°C to 400°C		231	Expensive

Cost is worth considering in real commercial manufacture, and polymer strength is vital in R2R processing and during a real wearable condition. Temperature resistance is another consideration during thin-film deposition. Functional materials normally require a high-temperature substrate during deposition to obtain high-quality films. However, heating a polymer substrate in a high-throughput R2R process is an engineering challenge in itself. To achieve a hot substrate, two main strategies are currently used for polymer-substrate processes: (i) a high-T_g polymer (e.g. PI) is selected for the high-temperature deposition [79, 80] (this is still a problem for R2R processing); (ii) materials are deposited at room temperature, then annealed [81, 82].

1.2.3.2 Configuration: In-plan TEG *vs* Cross-plan TEG

Flexible TEGs can be assembled in either cross-plane (CP-TEG) or in-plane (IP-TEG) structural designs (see Figure 1.3 a), which allow heat flows/TE legs perpendicular and parallel, respectively, to the substrate [83].

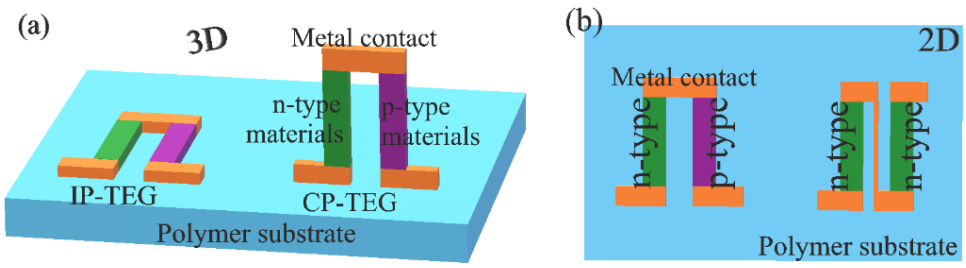


Figure 1.3. *(a) Schematic configuration of in-plane TEG and cross-plane TEG; (b) The traditional n-m-p TEG design and single n-type TEG design (where n, m, and p are n-type semiconductor, metal and p-type semiconductor, respectively)*

CP-TEGs have already been commercialised in bulk TEGs and some μ-thick TEGs, however, to further decrease the size (e.g. to nano range: nanostructures can improve TE efficiency [84-87]), the CP-configuration is not practical because maintaining a large ΔT across a nano-thick TE leg is impossible [88, 89] and thus there is poor power output (e.g. [90-97]). Although the development of nano-size CP-TEG is restricted, nanomaterials still significantly attract scientists' interest and research on IP-TEG is moving towards the use of nanomaterials (e.g. thin film [98], quantum well [99], and nanowire [100]), due to an extraordinary improvement in TE performance [84].

This project studies the IP-TEG. Due to a long and thin TE leg in the in-plane direction for charge carrier movement, the internal electrical resistance (R_{TEG}) of IP-TEG is usually large leading to a relatively high voltage output but a small working current output [40, 83, 101]. Besides, IP-TEGs cannot be directly used simply lying flat on the human body (because the ΔT must be maintained between one end on the other [102]). To make it wearable in practice, scientists have proposed a variety of smart/feasible means/designs,

e.g. coiled-up coin-shape [44], Y-type [103], corrugated-structure [104] / folded-mode [88] and slope-type [105].

1.2.3.3 Architecture: Single (n- or p-) type TEG *vs* Double type TEG

A traditional TEG, as shown in Figure 1.2, is designed to have metal contacts, and n- and p-type semiconductors, in what is called an 'n-m-p structure'. This design is commonly studied since it uses both n-type and p-type semiconductors. However for fabrication, this structure is more complicated: the ease of synthesis/deposition, material stability, and reliability of two different-type semiconductors must be considered.

This project is a fast prototype/demonstration of the scale-up manufacture of flexible TEGs, so an easy architecture is desired. As can be seen in Figure 1.3 b, TEGs can also be designed by a single (n- or p-) type semiconductor coupled with a metal shunt [106], which is named as 's-m structure'. This structure is not commonly used because it has an inherent/parasitic drawback that the metal strip has good thermal conductivity and can conduct heat from the hot side to the cold side (consequently a decrease in ΔT leads to less power output). However, many studies [88, 107] have investigated s-m structures and it has been confirmed that the difference of power output between n-m-p TEGs and s-m TEGs is very small for the thin-film geometry [88].

1.2.4 Materials discovery in flexible thin-film TEG

Materials exploration is always of primary importance in the development of flexible TEGs. In addition to a polymer substrate, a flexible TEG typically consists of two main parts: TE semiconductor and metal contacts.

1.2.4.1 Thermoelectric semiconductor

TE materials can be categorised according to their groups in the periodic table [21], materials types [108], and their working temperature range [109]. Take the working temperature range for an example, TE materials are classified as low (<200°C), middle,

and high temperature (>900°C). Figure 1.4 shows two examples of typical thermoelectric performance values in various temperature ranges for most already used or potentially used TE materials. Wearable TEGs correspond to the low-temperature range, typically bismuth telluride (Bi_2Te_3) and its alloys. As a traditional inorganic TE material, Bi_2Te_3 is a type of V_2-VI_3 binary chalcogenide compound semiconductor with a narrow bandgap (E_g) of around 0.2 eV [110-112]. Since the early boom of TE research in the 1950s - 1960s [113], Bi_2Te_3 has become one of the most promising TE materials for operation at room temperature (RT), exhibiting relatively high Seebeck coefficient, low electrical resistivity and low thermal conductivity [114]. To carry out a study of large-scale manufacturing, Bi_2Te_3 is a good choice. Later, this manufacturing technique could also be applied to alternative materials.

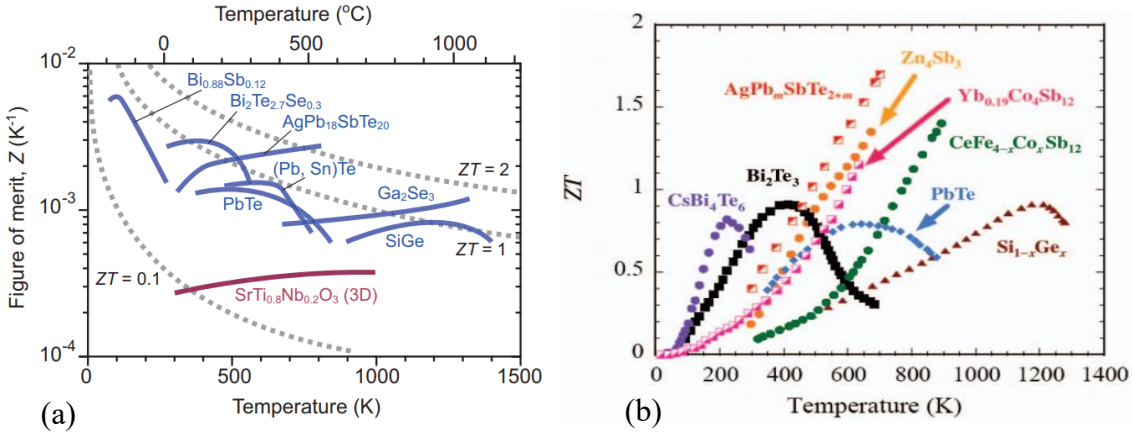


Figure 1.4. *Figure of merit (ZT) of the currently used or prospective TE materials. (a from* [115] *and b from* [116]*). ZT is defined in section 1.2.7.*

1.2.4.2 Metal contact

The metal contact used to contact the n-type and p-type semiconductors makes metal-semiconductor (M-S) junctions, the nature of which (Schottky, Ohmic, Figure 1.5) affects the electrical property (carrier transport) of the device [117].

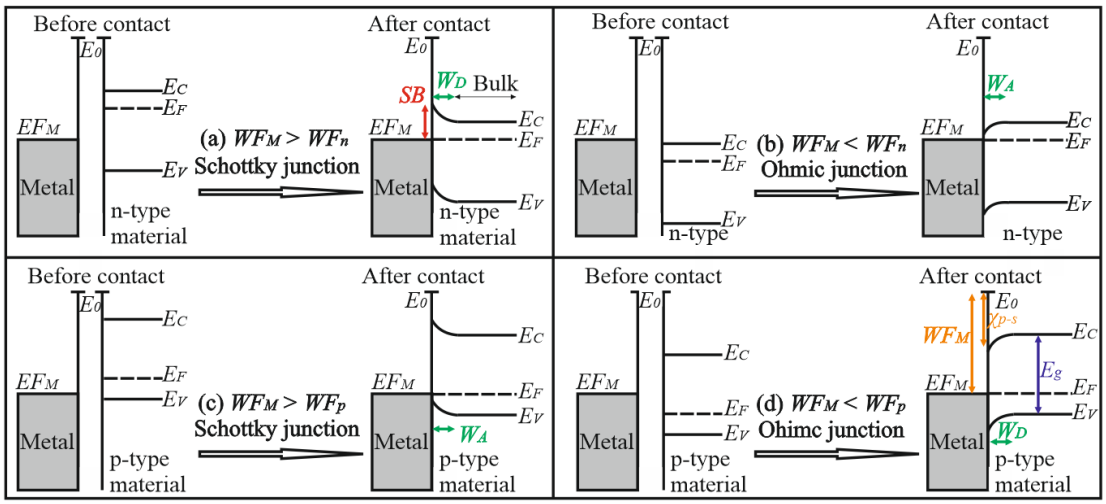


Figure 1.5. *(a) (c) Schottky and (b) (d) Ohmic junctions of a metal and semiconductors (where E_V is the maximum valance band energy, E_F is Fermi level, E_C is the minimum conduction band energy, E_0 is vacuum level, SB is Schottky barrier, WF_M is work function of metal, W_D is depletion region or space charge layer, W_A is accumulation region, E_g is bandgap energy of semiconductors, and χ_{p-s} is electron affinity of semiconductors). Adapted from* [118, 119].

The energy barrier could play an important role in the charge/carrier movement in TEGs, however there are few reports about this. This will be considered as part of this project to maximise charge transport in the device. The energy barrier depends on the relative work function between semiconductor and metal. A list of the commonly acceptable metals in the fabrication of devices is shown below, in addition to some alloys are used in TEGs fabrication such as W/Al and W/Ag. Cost should also be a factor. Further studies are required to find the best suitable materials for the contact material in TEGs.

Table 1.V. *The work function (WF) and electrical resistivity (ρ) of selected materials. (The data were acquired from* https://en.wikipedia.org/wiki/Work_function *and* https://en.wikipedia.org/wiki/Electrical_resistivity_and_conductivity *)*

Materials	**Ag**	**Cu**	**Au**	**Al**	**W**	**Zn**	**Pt**	**Sn**
***WF* (eV)**	4.26	4.65	5.1	4.28	4.32	3.63	5.12	4.42
ρ (nΩ·m)	15.87	16.78	22.14	28.2	52.8	59	105	115

1.2.5 Current trend to nanomaterial TEGs

In recent years, nanostructured materials have increasingly attracted the attention of researchers for improving the *ZT* of TEG materials [120]. Compared with bulk materials with the same chemical composition, nanostructured TE materials show a much more promising performance, as summarised from [2, 121, 122].

- Improvements in mechanical properties (reduce brittleness and improve machining);
- Improvements in TE behaviours;
- Providing more novel designs and applications;
- Being cost-effective, thin, and flexible (for thin-film configuration).

It has been reported that the rapid solidification processes (e.g. gas atomisation and melt spinning) can modify the intrinsic brittleness and TE anisotropy of Bi-Te-based TE materials due to the formation of a fine-grained and homogeneous microstructure [123]. Zhao *et al.* [124] also revealed the 'ultra-strength' phenomenon for nanostructured TEGs materials, which achieved a 10% increase in strength compared with its ideal strength (i.e. the highest achievable stress of a defect-free crystal at zero temperature), but the shear strength they reported was comparatively low. Mechanical resilience is a key factor during R2R processing, hence it is also of interest in this project.

Over the past few decades, TEG researches have been moving towards the use of nanomaterials (e.g. thin films, superlattices [125], quantum wells by molecular beam epitaxy [99], and nanowires by a silver-induced or electroless-etching method [100, 126]), because nanostructures (through adjusting the density of states, quantum confinement, interface/boundary effect, and defect engineering) can provide a chance to break the linkage among TE parameters (i.e. the intrinsic ability of nanomaterials to tailor electron and phonon transport [127-129]), and thus potentially enhance the TE performance. At

this stage, these studies are carried out based on laboratory growth/fabrication techniques that are not ready to scale-up for industrial manufacturing. Hence, it is timely to find a suitable fabrication technique for the device scale-up manufacture. This is the main purpose of the present project.

1.2.6 Thin-film fabrication of nanomaterial TEGs

Wearable TEGs are often applied as thin films. Unlike bulk TE materials, a thin-film configuration is lightweight, cheap and mechanically flexible [130], and, most importantly, has potential to improve *ZT* because of the influences of carrier scattering and quantum confinement [125]. In recent publications [131-135], sputtered bismuth telluride films (Bi-Te) were reported to have a TE performance (power factor) ranging from 3×10^{-4} to 9.5×10^{-4} W/mK^2.

Various techniques have been reported in the literature for the fabrication of flexible TEGs, including printing, lithography, lift-off process, vacuum deposition, etc. Two summaries [2, 136] of flexible TEG fabrication methods have been reported. By far, printing is the most commonly used method because of its straightforward process (i.e. convenient and fast to create complex patterns), its capability to be incorporated into an R2R process for large-scale manufacturing, minimal human labour requirements, high precision dispensing, and little material waste [136]. However, using printing techniques to make a nano-thick film is difficult.

Vacuum deposition techniques offer much more promising TE performance (Table 1.VI). Many thin-film vacuum deposition techniques, including chemical and physical deposition methods such as metal-organic chemical vapour deposition [137], thermal co-evaporation [138], flash evaporation [139], molecular beam epitaxy [140], pulsed laser deposition [141], ion beam sputtering [142], and (co-)sputtering deposition [133, 134,

143], are applied for flexible TEG studies. The lack of scale-up and low-cost manufacturing processes remains a major challenge for commercialisation.

Compared with others (Table 1.VII), the sputtering technique appears most promising for the scale-up of TEGs, because it possesses the inherent dominance on industrial manufacturing, such as continuous throughput, good speed, cost advantage, stable process, and mass production of a high-quality film. Most importantly, sputtering can be easily incorporated into R2R manufacturing [144], as well as being compatible with fabrication lines to deposit a huge array of materials [145]. Hence, the sputtering technique is employed in this study.

Table 1.VI. *Summaries of TEG fabrication techniques (where the reference numbers are from their original articles (a)* [136] *and (b)* [2]*).*

(a)

Methods	Materials: p-type	Materials: n-type	D_{film} (μm)	R_{in} (Ω)	ΔT (K)	N	V_{oc} (mV)	P_{max} (μW)	Ref.
Screen printing	Sb_2Te_3/epoxy	Bi_2Te_3/epoxy	500	<1	50	8	90	10.5	21*
	PEDOT:PSS	—	1.3	138	65	576	0.18	5.5×10^{-5}	83*
	—	CNT composite	0.1	26	100	5	20	4	84
	Sb_2Te_3/PEDOT:PSS	Bi_2Te_3/PEDOT:PSS	40	145	50	7	85	12	85
	PEDOT:PSS	—	20	10	100	300	40	50	86
	Sb_2Te_3/epoxy	Bi_2Te_3/epoxy	65	800	20	4	25	0.19	87
	CNT/polystyrene	—	150	352	70	1985	305	66	88*
	Sb_2Te_3/epoxy	Bi_2Te_3/epoxy	60	7200	20	8	36	0.04	89
Inkjet printing	Sb_2Te_3/epoxy	Bi_2Te_3/epoxy	500	300	30	20	25	2	20*
	poly[Cu_x(Cu-ett)]/PVDF	poly[K_x(Ni-ett)]/PVDF	3	54	25	6	15	1	90
	—	$Bi_2Te_{3-x}Se_x$/epoxy	120	480	20	62	220	25	93
	$Bi_{0.5}Sb_{1.5}Te_3$/epoxy	—	120	800	20	60	270	21	94
	$Bi_{0.5}Sb_{1.5}Te_3$/epoxy	Bi/epoxy	120	100	70	10	210	130	95
Molding	$Bi_{0.5}Sb_{1.5}Te_3$/epoxy	$Bi_2Te_{3-x}Se_x$/epoxy	4000	170	25	15	35	5	96*
	Cu(i)-ett	poly[K_x(Ni-ett)]	5000	557	60	220	1510	1000	97*
Lithography	PEDOT:Tos	TTF-TCNQ	30	—	10	54	—	0.13	14*
	Sb_2Te_3	Bi_2Te_3	0.7	2400	20	63	37	0.14	98
CNT composites	CNT	CNT/PEI	—	16 000	50	45	21	0.66	100
	CNT/SDBS	CNT/PEI	8	12 000	50	72	460	4.4	68
	CNT/tpp	CNT/TCNQ	80	82	20	3	6	0.11	101
Vacuum deposition	$(Bi_{0.15}Sb_{0.85})_2Te_3$	—	200	77	34	24	130	55	102
	$Bi_{0.4}Sb_{1.6}Te_3$	$Bi_2Te_{2.7}Se_{0.3}$	1	1200	130	18	600	100	103
	Sb_2Te_3	Bi_2Te_3	16	8300	20	10	42	5.3×10^{-2}	104

D_{film}, R_{in}, ΔT, n, V_{oc} and P_{max} stand for, respectively, the thickness of each element, total internal resistance of the TEG, temperature difference (the highest achieved), number of TE element pairs, open circuit voltage, and maximum power output with matching load resistance. In the references marked with *, the temperature gradient is in the cross-plane direction; otherwise, it is in the in-plane direction. In the materials columns, PVDF is poly(vinylidene fluoride), TTF-TCNQ is tetrathiafulvalene-tetracyanoquinodimethane, SDBS is sodium dodecylbenzenesulfonate, and tpp is triphenylphosphine.

(b) Reference	Materials	No. of pairs	Tem. (K)	Fabrication Technology	Voltage	Power
Qu et al. [77]	Sb-Bi	100	30	Foil lithography	0.25 V	
Hasebe et al. [78]	Ni-Cu	78		Lift-off process	15.4 μV K^{-1} per couple	
Itoigawa et al. [79]	Ni-Cu	38		Lift-off process	16 μV K^{-1} per couple	4.1 pW K^{-2} per couple
Takashiria et al. [80]	$Bi_{0.4}Te_{3.0}Sb_{1.6}$ and $Bi_{2.0}Te_{2.7}Se_{0.3}$	7	30	Flash evaporation	83.3 mV	0.21 μW
Yadav et al. [81]	Ni-Ag	7	6.6	Evaporation thin film	19.6 μV K per couple	2 nW
Schwyter et al. [82]	$Bi_{2+x}Te_{3-x}$		40	photolithography and etching		278 μW cm^{-2}
Glatz et al. [83]	Ni-Cu Bi_2Te_3					2.6×10^{-3} μW $cm^{-2}K^{-2}$ 0.29 μW $cm^{-2}K^{-2}$
Navone et al. [85]	$Bi_{0.5}Sb_{1.5}Te_3$ and $Bi_2Se_{0.3}Te_{2.7}$		50	Screen-printing	30 mV	0.06 μW $cm^{-2}K^{-2}$
Lee et al. [86]	ZnSb		70	Screen-printing		0.22 mW cm^{-2}
Francioso et al. [14]	Bi_2Te_3 and Sb_2Te_3	100	15	Sputtering	160 mV	4.18 nW
Jo et al. [92]	Bi_2Te_3	8	19	Dispenser printing	7 mV	2.1 μW
Yang et al. [100]			55		38 mV	
Delaizira et al. [99]	$Bi_2(Te_{0.9},Se_{0.1})_3$ and $(Bi_{0.245},Sb_{0.755})_2Te_3$	17	14	Spark plasma sintering technique	51 mV	
Madan et al. [91]	$Bi_{0.5}Sb_{1.5}Te_3$		20	Dispenser printing	130 mV	20.5 μW
Cao et al. [87]	Bi_2Te_3 and Sb_2Te_3	4	20	Screen-printing	6 mV per couple	48 nW
Kim et al. [89]	Bi_2Te_3	20	7	Dispenser printing	2.1 mV	15 nW
			27		7.3 mV	178 nW
Suemori et al. [102]	Carbon nanotubes and polystyrene		70	Printing process		55 mWm^{-2}
Sevilla et al. [96]	Bi_2Te_3 and Sb_2Te_3	63	20	Sputtering		0.139 mW cm^{-2}
Cao et al. [88]	BiTe/SbTe	8	20	Screen-printing	36.4 mV	40.3 nW
Khan et al. [84]	Si micro-wires	34	54	photolithography and etching	9.3 mV	
Kim et al. [90]	$Bi_{0.5}Sb_{1.5}Te_3$ and $Bi_2Se_{0.3}Te_{2.7}$	12	15	Dispenser printing	14.2 mV	224 nW
We et al. [94]			50	Screen-printing	85.2 mV	1.2 mW cm^{-2}
Im et al. [101]	Polyethylene terephthalate (PET)		36			0.46 mW m^{-2}
Kim et al. [93]	Bi_2Te_3 and Sb_2Te_3		50	Screen-printing	90 mV	3.8 mW cm^{-2}
Fan et al. [97]	Al-doped ZnO and Zn-Sb	10	180	Direct current (DC) magnetic sputtering	460 mV	246.3 μW
Suemori et al. [102]	Carbon nanotube					413 μW k^{-2} m^{-1}

Table 1.VII. *Comparison of vacuum deposition techniques for TE films* [140, 141, 146].

Techniques	Advantages	Disadvantages
Chemical vapour deposition	Very good materials: High TE performance.	1. Low deposition rate; 2. Expensive and complicated equipment.
Thermal evaporation	1. High TE performance; 2. Good deposition rate; 3. Control of film composition; 4. Simple/inexpensive equipment.	1. Needs precise control of deposition rate and crucible temperature.
Molecular beam epitaxy	1. Substrate temperature is not high; 2. Precisely controllable thermal evaporation; 3. Separate evaporation of each component.	1. Low deposition rate; 2. Expensive facility; 3. Very complicated system; 4. Requirements of ultra-high vacuum.
Pulsed laser deposition	1. Suitable for almost any oxide materials;	1. Not suitable for metals;

	2. Good deposition rate; 3. Good stoichiometry transfer.	2. Splashing causes micro-size particles; 3. Extremely complex models eliminates theory-based improvements.
Sputtering	1. Average TE performance; 2. Good deposition rate; 3. Composition can be controlled with co-sputtering; 4. Easily incorporated into R2R large-scale manufacturing.	Substrate heating or annealing improves TE performance.

1.2.6.1 Sputtering technique

Sputter deposition is a widely used technique to deposit thin films on substrates, which is based on ion bombardments of a source-target material [147]. A controlled amount of gas, typically chemically inert argon (Ar), is fed into a vacuum chamber continuously. Then, the cathode/target is electrically energised to generate a self-sustaining plasma as the injected Ar gas atoms are ionised (e.g. to Ar^{+}). Because the target (cathode) is negatively charged, Ar ions are accelerated to hit the target for sputtering (see Figure 1.6) and thus to dislocate atoms from the target material [148]. Ejected atoms then travel some distance in random directions until they reach the substrate. Through controlling sputtering time, layered thin films can be precisely produced [149].

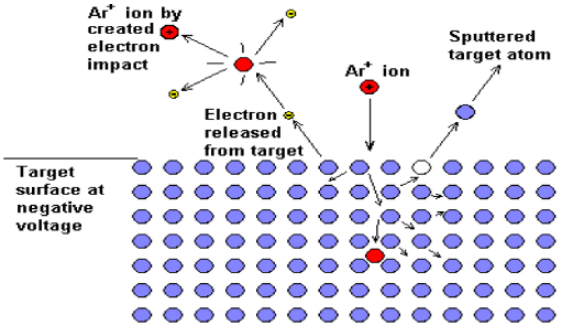


Figure 1.6. *Sputtering deposition* [150].

A direct current (DC) magnetron sputtering system (Figure 1.7) applies a strong magnetic field parallel to the target surface, causing the traveling electrons to follow helical paths along the magnetic flux lines near the target instead of moving towards the substrate [148], and therefore, the magnetic field confines the plasma near the target. A DC power supply is the simplest and least expensive method for magnetron sputtering [147] and is generally used for sputtering of conductive materials. Ionisation of the plasma is improved by further emitted secondary electrons: a stable plasma can be generated with a high density of ions and can be sustained at a low chamber pressure. As more atoms are ejected (sputtered) from the target, if the sputtered atoms can traverse the plasma/discharge space without too many collisions to reach the substrate, this will lead to a high deposition rate [151]. In a DC magnetron sputtering system, the deposition rate (i.e. film thickness deposited per second) is dependent on the electric accelerating field, magnetic field, and gas pressure [152].

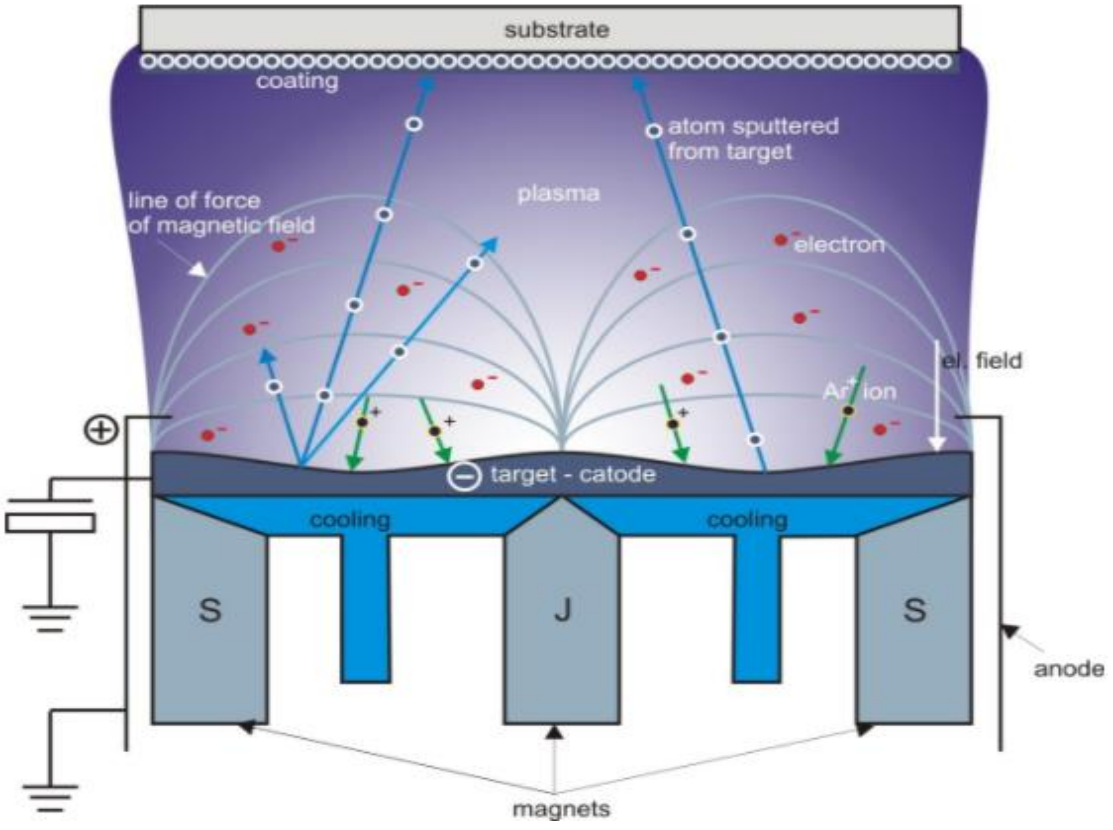


Figure 1.7. *The principle of magnetron sputtering* [153].

1.2.6.2 Sputtering parameters

1.2.6.2.1 Chamber pressure

At a low chamber pressure, the mean free path is large which reduces the probability of collisions between Ar atoms and electrons, thereby the plasma cannot be sustained. At a high pressure (i) due to too many collisions, electrons do not have enough time to gather energy between collisions to be able to ionise the atoms, and thus decreasing the deposition rate [154], (ii) the sputtered atoms undergo more collisions before reaching the substrate, thereby reducing the deposition rate and causing materials waste [155, 156], and (iii) a greater number of ions and neutralised gas atoms may embed on the substrate as impurities, or re-sputter the substrate or the growing film causing etching [157]. Hence, there is an optimum range of working pressure for sputtering. In general, the Ar-flow rate can be used to adjust the pressure.

1.2.6.2.2 Sputter power

The deposition rate is directly proportional to the sputter power applied [158]. As power increases, the ionisation efficiency of Ar atoms increases, and then a denser plasma is generated near the target. This causes more atoms to sputter from the target. If the power-induced denser plasma does not affect too much on the traverse of sputtered atoms to reach the substrate, the sputtering rate will increase.

1.2.6.2.3 Target and substrate temperatures

The target is heated because of the continuous Ar ion bombardment. Although the sputter yield (i.e. the number of ejected atoms per incident ion) increases with the target temperature, the target heat can also cause the problem of outgassing or even target melting [155]. Hence a cooling system is applied behind the target material. In general, the substrate is heated to obtain a high-quality film because the substrate temperature affects film properties of the structure, uniformity, adhesion, surface roughness, etc.

In terms of film morphology, it is significantly affected by the Ar pressure and substrate temperature. The zone model to describe morphology under different conditions was proposed by Thornton in 1973 (see Figure 1.8 [159]). To obtain highly crystalline films, the substrate temperature should be as close as possible to the melting point of the target material. Only low melting-point materials can crystallise at low temperatures close to room temperature [160]. For most semiconductors, a high substrate temperature is required to deposit high-quality films. In case of bismuth telluride films, the optimal substrate temperature is around 270°C to achieve the best TE performance because of changes/improvements in the elemental composition, crystallinity and grain size [146]. However, polymer-substrate TEGs cannot achieve a high-temperature deposition due to the consequent problem of polymer stretching and melting. This is the urgent problem at present to achieve an R2R high-temperature sputtering, or sufficient quality low-temperature deposited layers for polymer-substrate TEGs.

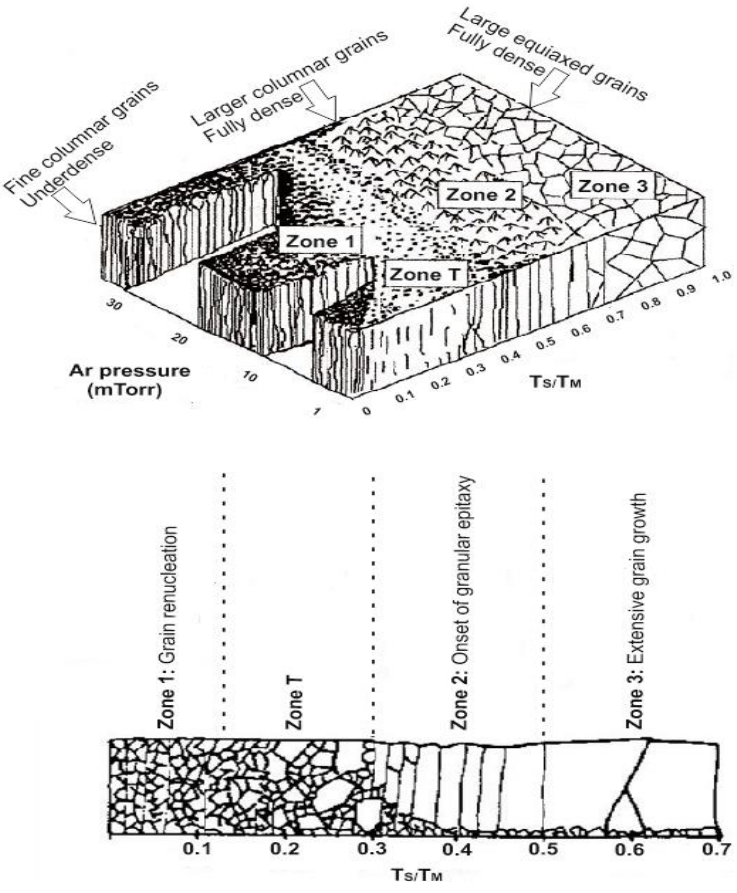


Figure 1.8. *Schematics of coating structure as a function of Ar pressure and substrate temperature (where T_S is substrate temperature, and T_M is melting point of target materials). Adapted from* [159].

1.2.7 Thermoelectric parameters

The dimensionless figure of merit (*ZT*) is the most important parameter to identify the TE conversion efficiency of TE materials [108], as expressed below.

$$ZT = \frac{S^2 T}{\rho\lambda} = \frac{S^2 T\sigma}{\lambda} = PF \cdot \frac{T}{\lambda} \quad (1.2)$$

where *S, T,* ρ, σ, λ and *PF* are Seebeck coefficient, absolute temperature, electrical resistivity, electrical conductivity, thermal conductivity, and power factor, respectively [161]. *PF* is introduced because it is independent of thermal conductivity, and most thin-film studies reported *PF* rather than *ZT* to avoid the difficulty of measuring λ of thin films. A high-efficiency TE material is required to possess a low ρ, λ and high *S*, thereby a high *PF* and *ZT*. A low λ maintains the ΔT between the hot and cold sides, while a high σ increases the ability of electric current to flow through a sample [162]. Although flexible TEGs have been studied for decades, the value of *ZT* remains relatively low (for example, Bi-Te has remained a *ZT* of around 1 for many years [163]) because of the complex inter-dependence of the three parameters (ρ, λ and *S)* that limits *ZT*. It is notable that while the second law of thermodynamics does not put any restrictions on improving *ZT* [164], the commercially available TE materials show *ZT* (~1), where a value above 3 [165] would allow them to directly compete with the traditional techniques, e.g. mechanical power generation and refrigeration.

A typical relationship between ρ, λ and *S* is displayed in Figure 1.9. Because σ and λ nearly vanish for insulators and *S* nearly vanishes for metals, TE materials are mainly focused on semiconductors. A trade-off is required among ρ, λ and *S* to achieve an

optimum *ZT* value, possibly corresponding to the peak of *PF* as shown in Figure 1.9. What is more, wearable TEGs must work well at a low-temperature regime (i.e. near the human-body temperature) [2]. Therefore, challenges still exist to make high-efficiency flexible TE cells.

The problem here is that high electrical conductors have high thermal conductivity (because the carrier can not only carry electric charges but also carry the heat, i.e. the Wiedemann-Franz law), which conflicts with the optimisation of *ZT* (i.e. high σ but low λ). A similar analysis can also be done between *S* and σ or *S* and λ. For semiconductors, as the Fermi level approaches the conduction band, the carrier density/concentration increases and it will behave as metal if the Fermi level lies in the conduction band (i.e. high σ), however, the density of thermally available states decreases and these thermally generated carriers above Fermi level play a significant role on improving *S* [166]. Therefore, high σ is generally accompanied by low *S*. Overall, ρ, λ and *S* are strongly coupled to the carrier concentration [21, 167]. The main challenge remains on how to decouple these three TE parameters to maximise *ZT*. In recent years, nanostructured materials and boundary or defect engineering have increasingly attracted the attention of researchers for improving the *ZT* of TE materials [84-87] because nanostructures can provide a chance to break the linkage among ρ, λ and *S*, and thus potentially enhance the TE performance.

It is ideal to decouple these three properties so that one could be optimised with no (or less) influence on others. *S* and σ can be decoupled by charge carrier induced vibrational softening [168], the density of states tuning [169], interface filtering of charge carrier energies [170], and electronic conduction through hopping mechanisms [171]. Take the interface filtering as an example (see Figure 1.10). In a TE material, electronic states (in a pear-shape energy distribution) above the conduction band at the hot side are filled by

the thermally excited electron carriers, then these energetic carriers tend to move towards the cold side (where the bands above the conduction band are unfilled) creating a potential difference to achieve equilibrium. If there is an energy barrier at the interface of grains/crystals, only high-energy carriers can cross the barrier while others are scattered, which means that only carriers at the peak of the 'pear' at the hot side tend to fill the empty states at the cold side. Due to a smaller number of carriers reaching the bottom of the 'pear' at the cold side, the conduction band at the cold side has to lift up more (i.e. greater potential difference) to get equilibrium. Therefore, the carrier filtering effect can lead to a greater potential difference (i.e. a greater *S*) across the semiconductor from the hot to cold sides. Besides, these high-energy carriers have greater mobility thus σ will not be significantly influenced although the carrier density decreases.

λ and σ can be decoupled by increasing phonon scattering which does not influence electron transport significantly [166] and thus possibly decreasing λ without affecting σ.

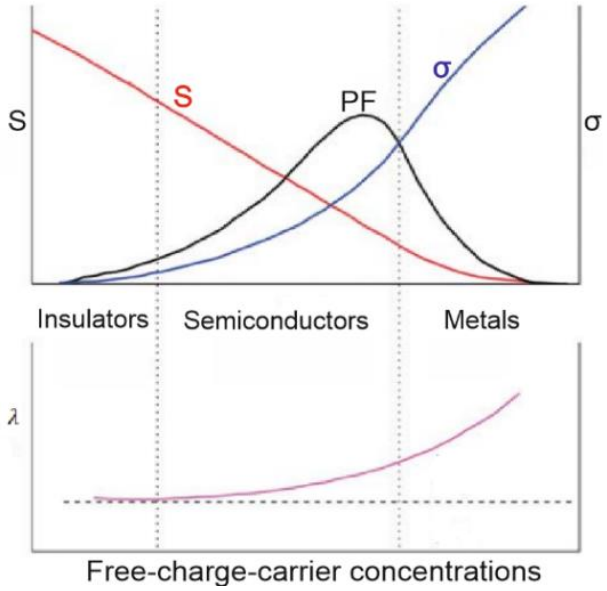


Figure 1.9. *Dependence of ρ, S and λ on different materials (where electrical conductivity $\sigma = 1/\rho$). Adapted from* [21].

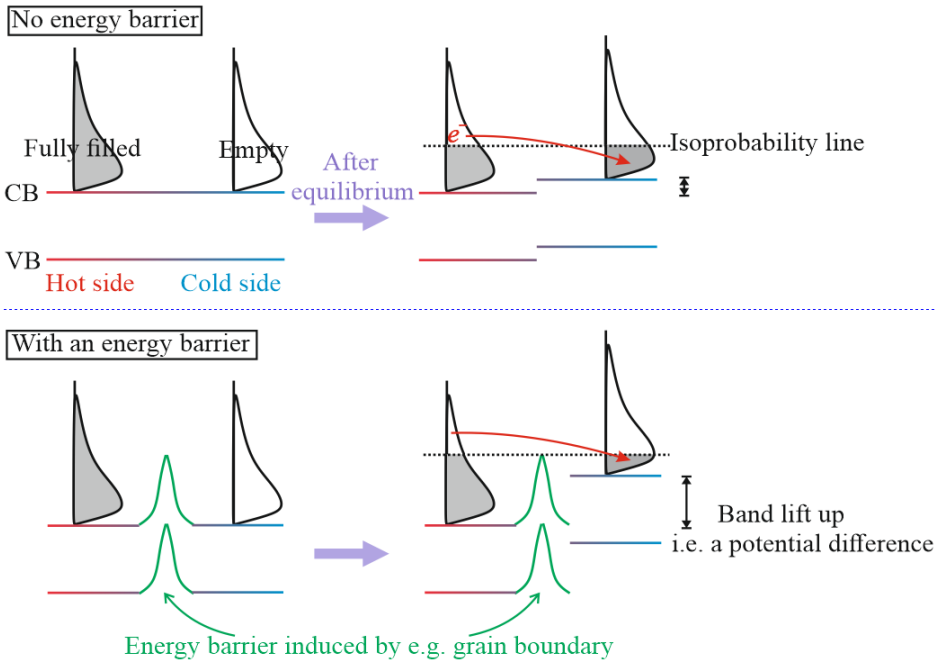


Figure 1.10. *Schematic diagram of the effect of energy barrier on the potential difference generated.*

1.3 Roll-to-roll manufacturability of flexible thin-film TEGs

With the advantages of high throughput and environmental friendliness, R2R coating technology has been widely used at various industrial sites [172], e.g. the food packaging. Hence, the electronics fabrication techniques could be directly set up into the modern industrial system. To move the manufacturability of flexible thin-film devices (in this case TEGs) from laboratory scale to R2R, four aspects of challenges/opportunities are explored in this work:

(1) Exploration of using very thin films to balance the fast R2R web speed and low vacuum-deposition rate --- Chapter 3

For electronics fabrication, an industrial R2R speed could be 10 - 100 m min^{-1} [173] dependent on the technique used, while the typical sputtering rate is in the range of nm s^{-1} [174]. This means, only a very thin coating can be deposited. Hence, the performance of very thin layers is being examined to maximise a great web speed.

Besides, other possible factors are considered to optimise the performance of films at this thickness, e.g. the surface modification on polymer substrates.

(2) Post-deposition radiation treatments to improve TE performance and use of interlayers to improve mechanical resilience --- Chapter 4

The functional material normally requires a very hot substrate during the deposition for the best performance (e.g. Bi_2Te_3: 270°C [175]), but the typical polymer substrate (e.g. PET/PI/PEN) cannot reach such high temperature during R2R. Hence, the performance of film grown at RT is studied. To improve the performance of as-deposited films, other possible approaches are being explored (e.g. post-treatments and selective heating).

Besides, R2R induces stretching and bending strain on the polymer substrate, which could significantly affect the film performance. Also, wearable electronics suffer from mechanical actions thereby affecting their durability, while only a few experimental-type papers were published in this area. Hence, the mechanical resilience of films on polymer web during R2R and in-service operation is of interest. I also investigate the effect of putting a buffer layer in between the function layer and the polymer substrate, to see if it could help maintain the film performance.

(3) Replacing a solid shadow mask by other approaches (compatible with R2R), to make in-line patterns --- Chapter 5

Patterns are required for functional devices. In laboratory research, using a solid shadow mask is a traditional means, however, it is an undesirable route for a continuous R2R process. To make in-line patterning, I further study the in-line oil patterning technique [176] which is a mature and previously published technique in the group. My work is seeking to implement the process with a sputter deposition, rather than evaporation as previously studied/published.

(4) Exploring the preferred architecture of flexible TEG suitable for both wearable applications and R2R --- Chapter 6 & 7

The architecture of TEGs (e.g. the dimension, No./connection of TE strips) significantly affects the device performance. I investigate the best architecture and propose a novel multilayer stacking structure of TEGs that would be compatible with R2R processing.

To study the new sciences listed above, a sputtering source has been well established in an industrial-type Aerre Machine Vacuum R2R web coater (see below). A flexography system is designed/installed (by a previous postdoc. in the group: Bryan Stuart) in this web coater as well to investigate the feasibility of in-line patterning in R2R processing.

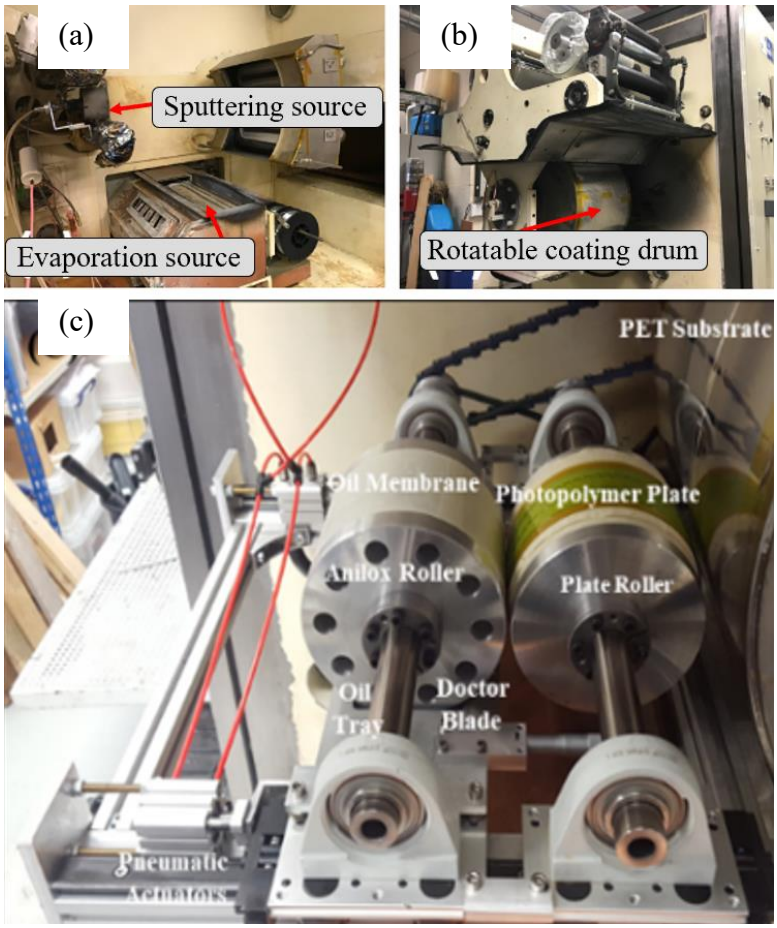


Figure 1.11. *(a) Sputtering source; (b) Roll-to-roll handing; (c) Flexography, inside Aerre Machine Vacuum web coater at Department of Materials, University of Oxford.*

1.4 Summary

The review outlines the basic knowledge of wearable/flexible TEGs including the working principle, device development, classification, materials/nanomaterials trend, and fabrication techniques. A research plan is also listed. The rest of the chapters are introduced following this list.

1.5 Reference

[1] Hatamie, A.; Angizi, S.; Kumar, S.; Pandey, C. M.; Simchi, A.; Willander, M.; Malhotra, B. D. , Review—Textile Based Chemical and Physical Sensors for Healthcare Monitoring, *J. Electrochem. Soc.* 2020, *167*, 37546, https://doi.org/10.1149/1945-7111/ab6827.

[2] Siddique, A. R. M.; Mahmud, S.; Heyst, B. V. , A review of the state of the science on wearable thermoelectric power generators (TEGs) and their existing challenges, *Renew. Sust. Energ. Rev.* 2017, *73*, 730-744, https://doi.org/10.1016/j.rser.2017.01.177.

[3] Arnold, D. P. , Review of Microscale Magnetic Power Generation, *IEEE Transactions on Magnetics.* 2007, *43*, 3940-3951, https://doi.org/10.1109/TMAG.2007.906150.

[4] Ming He, Feng Qiu and Zhiqun Lin , Towards high-performance polymer-based thermoelectric materials, *Environmental Science.* 2013, *6*, 1352-1361, https://doi.org/10.1039/c3ee24193a.

[5] Yoo, B. Y.; Huang, C. -.; Lim, J. R.; Herman, J.; Ryan, M. A.; Fleurial, J. -.; Myung, N. V. , Electrochemically deposited thermoelectric n-type Bi2Te3 thin films, *Electrochimica Acta.* 2005, *50*, 4371-4377, https://doi.org/10.1016/j.electacta.2005.02.016.

[6] Rogers, J. A.; Ghaffari, R.; Kim, D. , Stretchable Bioelectronics for Medical Devices and Systems, 2016, https://doi.org/10.1007/978-3-319-28694-5.

[7] Bahk, J.; Fang, H.; Yazawa, K.; Shakouri, A. , Flexible thermoelectric materials and device optimization for wearable energy harvesting, *J. Mater. Chem. C.* 2015, *3*, 1362-1374, https://doi.org/10.1039/c5tc01644d.

[8] Hendricks, T.; Choate, W. T. , Engineering Scoping Study of Thermoelectric Generator Systems for Industrial Waste Heat Recovery, 2006, https://doi.org/10.2172/1218711.

[9] Williams, N. E.; Silva, H.; Gokirmak, A. , Finite element analysis of scaling of silicon micro-thermoelectric generators to nanowire dimensions, *Journal of Renewable and Sustainable Energy.* 2012, *4*, 43110, https://doi.org/10.1063/1.4738592.

[10] Huesgen, T.; Woias, P.; Kockmann, N. , Design and fabrication of MEMS thermoelectric generators with high temperature efficiency, *Sensors & Actuators: A. Physical.* 2008, *145-146*, 423-429, https://doi.org/10.1016/j.sna.2007.11.032.

[11] Olivo, J. , Remote Powering and Communication of Implantable Biosensors Through Inductive Link, 2013, https://doi.org/10.5075/epfl-thesis-5936.

[12] Hayati M., R. A. , A Review: Thermoelectric Generators in Renewable Energy, *International Journal of Renewable Energy Research.* 2014, *4*, 128-136, http://www.ijrer.org/ijrer/index.php/ijrer/article/view/1040.

[13] Stark, I. , Converting body heat into reliable energy for powering physiological wireless sensors, *Proceedings of the 2nd Conference on Wireless Health.* 2011, 1-2, https://doi.org/10.1145/2077546.2077580.

[14] Yang, Y.; Wei, X.; Liu, J. , Suitability of a thermoelectric power generator for implantable medical electronic devices, *Journal of Physics D: Applied Physics.* 2007, *40*, 5790-5800, https://doi.org/10.1088/0022-3727/40/18/042.

[15] Vullers, R. J. M.; van Schaijk, R.; Doms, I.; Van Hoof, C.; Mertens, R. , Micropower energy harvesting, *Solid State Electronics.* 2009, *53*, 684-693, https://doi.org/10.1016/j.sse.2008.12.011.

[16] Gonçalves, A.; Godart, C. , Alternative Strategies for Thermoelectric Materials Development, *New Materials for Thermoelectric Applications: Theory and Experiment.* 2013, 1-24, https://doi.org/10.1007/978-94-007-4984-9_1.

[17] Wright, D. A. , Materials for direct-conversion thermoelectric generators, *International Materials Reviews.* 1970, *15*, 147-160, https://doi.org/10.1179/imr.1970.15.1.147.

[18] Gould, C. A.; Shammas, N. Y. A.; Grainger, S.; Taylor, I. , A comprehensive review of thermoelectric technology, micro-electrical and power generation properties, *2008 26th International Conference on Microelectronics.* 2008, 329-332, https://doi.org/10.1109/ICMEL.2008.4559288.

[19] Rowe, D. M. , Thermoelectrics Handbook, 2005, 1-10, http://www.crcnetbase.com/isbn/9781420038903.

[20] Nolas, G. S.; Goldsmid, H. J.; Sharp, J. , Thermoelectrics, 2001, *45*, 1-5, http://www.springer.com/gb/book/9783540412458.

[21] C Wood , Materials for thermoelectric energy conversion, *Reports on Progress in Physics.* 1988, *51*, 459-539, https://doi.org/10.1088/0034-4885/51/4/001.

[22] Ismail, Y.; Alaskalany, A. , Thermoelectric Devices: Cooling and Power Generation, 2014, http://arxiv.org/abs/1403.3836.

[23] Doms, I.; Merken; Van Hoof, C. , Comparison of DC-DC-converter architectures of power management circuits for thermoelectric generators, *2007 European Conference on*

Power Electronics and Applications. 2007, 1-5, https://doi.org/10.1109/EPE.2007.4417530.

[24] Singh, R.; Tundee, S.; Akbarzadeh, A. , Electric power generation from solar pond using combined thermosyphon and thermoelectric modules, *Solar Energy.* 2011, *85*, 371-378, https://doi.org/10.1016/j.solener.2010.11.012.

[25] Ahiska, R.; Dişlitaş, S. , Computer controlled test system for measuring the parameters of the real thermoelectric module, *Energy Conversion and Management.* 2011, *52*, 27-36, https://doi.org/10.1016/j.enconman.2010.06.023.

[26] Qu, W.; Plötner, M.; Fischer, W. , Microfabrication of thermoelectric generators on flexible foil substrates as a power source for autonomous microsystems, *Journal of Micromechanics and Microengineering.* 2001, *11*, 146, https://doi.org/10.1088/0960-1317/11/2/310.

[27] Wang, Z.; Leonov, V.; Fiorini, P.; Van Hoof, C. , Micromachined Thermopiles for Energy Scavenging on Human Body, *TRANSDUCERS 2007 - 2007 International Solid-State Sensors, Actuators and Microsystems Conference.* 2007, 911-914, https://doi.org/10.1109/SENSOR.2007.4300279.

[28] Leonov, V.; Torfs, T.; Fiorini, P.; Van Hoof, C. , Thermoelectric Converters of Human Warmth for Self-Powered Wireless Sensor Nodes, *IEEE Sensors Journal.* 2007, *7*, 650-657, https://doi.org/10.1109/JSEN.2007.894917.

[29] Leonov, V.; Vullers, R. J. M. , Wearable electronics self-powered by using human body heat: The state of the art and the perspective, *Journal of Renewable and Sustainable Energy.* 2009, *1*, 062701-14, http://dx.doi.org/10.1063/1.3255465.

[30] Leonov, V. , Simulation of maximum power in the wearable thermoelectric generator with a small thermopile, *Microsystem Technologies.* 2011, *17*, 495-504, https://doi.org/10.1007/s00542-011-1262-6.

[31] Leonov, V. , Thermoelectric energy harvester on the heated human machine, *Journal of Micromechanics and Microengineering.* 2011, *21*, 125013, https://doi.org/10.1088/0960-1317/21/12/125013.

[32] Mitcheson, P. D. , Energy harvesting for human wearable and implantable bio-sensors, *2010 Annual International Conference of the IEEE Engineering in Medicine and Biology.* 2010, *2010*, 3432-3436, https://doi.org/10.1109/IEMBS.2010.5627952.

[33] Nakamura, T.; Funahashi, S.; Kageyama, K.; Ieki, H. , Monolithic oxide-metal composite thermoelectric generators for energy harvesting, *Journal of Applied Physics.* 2011, *109*, 124509-4, http://dx.doi.org/10.1063/1.3599890.

[34] Settaluri, K.; Lo, H.; Ram, R. , Thin Thermoelectric Generator System for Body Energy Harvesting, *Journal of Electronic Materials.* 2012, *41*, 984-988, http://dx.doi.org/10.1007/s11664-011-1834-3.

[35] Wahbah, M.; Alhawari, M.; Mohammad, B.; Saleh, H.; Ismail, M. , Characterization of Human Body-Based Thermal and Vibration Energy Harvesting for Wearable Devices, *IEEE Journal on Emerging and Selected Topics in Circuits and Systems.* 2014, *4*, 354-363, https://doi.org/10.1109/JETCAS.2014.2337195.

[36] Takashiri, M.; Shirakawa, T.; Miyazaki, K.; Tsukamoto, H. , Fabrication and characterization of bismuth–telluride-based alloy thin film thermoelectric generators by flash evaporation method, *Sensors & Actuators: A. Physical.* 2007, *138*, 329-334, https://doi.org/10.1016/j.sna.2007.05.030.

[37] Lee, H. B.; We, J. H.; Yang, H. J.; Kim, K.; Choi, K. C.; Cho, B. J. , Thermoelectric properties of screen-printed ZnSb film, *Thin Solid Films.* 2011, *519*, 5441-5443, https://doi.org/10.1016/j.tsf.2011.03.031.

[38] Kim, S. J.; We, J. H.; Cho, B. J. , A wearable thermoelectric generator fabricated on a glass fabric, *Energy & Environmental Science.* 2014, *7*, 1959-1965, https://doi.org/10.1039/c4ee00242c.

[39] Suemori, K.; Watanabe, Y.; Hoshino, S. , Carbon nanotube bundles/polystyrene composites as high-performance flexible thermoelectric materials, *Applied Physics Letters.* 2015, *106*, 113902, https://doi.org/10.1063/1.4915622.

[40] Bahk, J.; Fang, H.; Yazawa, K.; Shakouri, A. , Flexible thermoelectric materials and device optimization for wearable energy harvesting, *J. Mater. Chem. C.* 2015, *3*, 1362-1374, https://doi.org/10.1039/c5tc01644d.

[41] Du, Y.; Cai, K.; Chen, S.; Wang, H.; Shen, S. Z.; Donelson, R.; Lin, T. , Thermoelectric fabrics: toward power generating clothing, *Scientific Reports.* 2015, *5*, 6411, https://doi.org/10.1038/srep06411.

[42] Hasebe, S.; Ogawa, J.; Toriyama, T.; Sugiyama, S.; Ueno, H.; Itoigawa, K. , Design and fabrication of flexible thermopile for power generation, *MHS2003. Proceedings of 2003 International Symposium on Micromechatronics and Human Science (IEEE Cat. no.03TH8717).* 2003, 287-291, https://doi.org/10.1109/MHS.2003.1249950.

[43] Itoigawa, K.; Ueno, H.; Shiozaki, M.; Toriyama, T.; Sugiyama, S. , Fabrication of flexible thermopile generator, *Journal of Micromechanics and Microengineering.* 2005, *15*, S233-S238, https://doi.org/10.1088/0960-1317/15/9/S10.

[44] Weber, J.; Potje-Kamloth, K.; Haase, F.; Detemple, P.; Völklein, F.; Doll, T. , Coin-size coiled-up polymer foil thermoelectric power generator for wearable electronics, *Sens. Actuators, A.* 2006, *132*, 325-330, https://doi.org/10.1016/j.sna.2006.04.054.

[45] Yadav, A.; Pipe, K. P.; Shtein, M. , Fiber-based flexible thermoelectric power generator, *Journal of Power Sources.* 2008, *175*, 909-913, https://doi.org/10.1016/j.jpowsour.2007.09.096.

[46] Schwyter, E.; Glatz, W.; Durrer, L.; Hierold, C. , Flexible micro thermoelectric generator based on electroplated Bi2+xTe3−x, *2008 Symposium on Design, Test,*

Integration and Packaging of MEMS/MOEMS. 2008, 46-48, https://doi.org/10.1109/DTIP.2008.4752949.

[47] Glatz, W.; Schwyter, E.; Durrer, L.; Hierold, C. , Bi2Te3-based flexible micro thermoelectric generator with optimized design, *Journal of Microelectromechanical Systems.* 2009, *18*, 763, https://doi.org/10.1109/JMEMS.2009.2021104.

[48] Navone, C.; Soulier, M.; Plissonnier, M.; Seiler, A. L. , Development of (Bi,Sb)2(Te,Se)3-Based Thermoelectric Modules by a Screen-Printing Process, *J. Electron. Mater.* 2010, *39*, 1755–1759, https://doi.org/10.1007/s11664-010-1187-3.

[49] Hsiao, C.; Wu, Y. , Fabrication of flexible thin-film thermoelectric generators, *Journal of the Chinese Institute of Engineers.* 2011, *34*, 809-816, https://doi.org/10.1080/02533839.2011.591552.

[50] Francioso, L.; De Pascali, C.; Farella, I.; Martucci, C.; Cretì, P.; Siciliano, P.; Perrone, A. , Flexible thermoelectric generator for ambient assisted living wearable biometric sensors, *Journal of Power Sources.* 2011, *196*, 3239-3243, https://doi.org/10.1016/j.jpowsour.2010.11.081.

[51] Jo, S. E.; Kim, M. K.; Kim, M. S.; Kim, Y. J. , Flexible thermoelectric generator for human body heat energy harvesting, *Electronics Letters.* 2012, *48*, 1015-1017, https://doi.org/10.1049/el.2012.1566.

[52] Yang, Y.; Lin, Z.; Hou, T.; Zhang, F.; Wang, Z. , Nanowire-composite based flexible thermoelectric nanogenerators and self-powered temperature sensors, *Nano Research.* 2012, *5*, 888-895, https://doi.org/10.1007/s12274-012-0272-8.

[53] Delaizir, G.; Monnier, J.; Soulier, M.; Grodzki, R.; Villeroy, B.; Testard, J.; Simon, J.; Navone, C.; Godart, C. , A new generation of high performance large-scale and flexible thermo-generators based on (BiSb)2(Te,Se)3 nano-powders using the Spark Plasma Sintering technique, *Sensors & Actuators: A. Physical.* 2012, *174*, 115, https://doi.org/10.1016/j.sna.2011.11.011.

[54] Madan, D.; Wang, Z.; Chen, A.; Wright, P. K.; Evans, J. W. , High-performance dispenser printed MA p-type Bi(0.5)Sb(1.5)Te(3) flexible thermoelectric generators for powering wireless sensor networks, *ACS Applied Materials & Interfaces.* 2013, *5*, 11872, https://doi.org/10.1021/am403568t.

[55] Cao, Z.; Koukharenko E., Tudor MJ., Torah RN., Beeby SP. , Screen printed flexible Bi2Te3-Sb2Te3 based thermoelectric generator, *Journal of Physics: Conference Series.* 2013, https://doi.org/10.1088/1742-6596/476/1/012031.

[56] Kim, M. K.; Kim, M. S.; Jo, S. E.; Kim, H. L.; Lee, S. M.; Kim, Y. J. , Wearable thermoelectric generator for human clothing applications, *2013 Transducers & Eurosensors XXVII: The 17th International Conference on Solid-State Sensors, Actuators and Microsystems (TRANSDUCERS & EUROSENSORS XXVII).* 2013, 1376-1379, https://doi.org/10.1109/Transducers.2013.6627034.

[57] Francioso, L.; De Pascali, C.; Siciliano, P.; De Risi, A.; D'Amico, S.; Veri, C.; Pasca, M. , Thin film technology flexible thermoelectric generator and dedicated ASIC for energy harvesting applications, *5th IEEE International Workshop on Advances in Sensors and Interfaces IWASI.* 2013, 104-107, https://doi.org/10.1109/IWASI.2013.6576100.

[58] Suemori, K.; Hoshino, S.; Kamata, T. , Flexible and lightweight thermoelectric generators composed of carbon nanotube–polystyrene composites printed on film substrate, *Appl. Phys. Lett.* 2013, *103*, 153902, https://doi.org/10.1063/1.4824648.

[59] Sevilla, G. A. T.; Inayat, S. B.; Rojas, J. P.; Hussain, A. M.; Hussain, M. M. , Flexible and Semi-Transparent Thermoelectric Energy Harvesters from Low Cost Bulk Silicon (100), *Small.* 2013, *9*, 3916-3921, https://doi.org/10.1002/smll.201301025.

[60] Z Cao, E Koukharenko, RN Torah, J Tudor and S P Beeby , Flexible screen printed thick film thermoelectric generator with reduced material resistivity, *Journal of Physics: Conference Series.* 2014, *557*, https://doi.org/10.1088/1742-6596/557/1/012016.

[61] Khan, S.; Dahiya, R. S.; Lorenzelli, L. , Flexible thermoelectric generator based on transfer printed Si microwires, *2014 44th European Solid State Device Research Conference (ESSDERC).* 2014, 86-89, https://doi.org/10.1109/ESSDERC.2014.6948764.

[62] Min-Ki Kim, Myoung-Soo Kim, Seok Lee, Chulki Kim and Yong-Jun Kim , Wearable thermoelectric generator for harvesting human body heat energy, *Smart Materials and Structures.* 2014, *23*, http://dx.doi.org/10.1088/0964-1726/23/10/105002.

[63] We, J. H.; Kim, S. J.; Cho, B. J. , Hybrid composite of screen-printed inorganic thermoelectric film and organic conducting polymer for flexible thermoelectric power generator, *Energy.* 2014, *73*, 506-512, https://doi.org/10.1016/j.energy.2014.06.047.

[64] H. Im , Flexible thermocells for utilization of body heat, *Nano Res.* 2014, *7*, 443-452, https://doi.org/10.1007/s12274-014-0410-6.

[65] Kim, S. J.; We, J. H.; Cho, B. J. , A wearable thermoelectric generator fabricated on a glass fabric, *Energy & Environmental Science.* 2014, *7*, 1959-1965, https://doi.org/10.1039/c4ee00242c.

[66] Fan, P.; Zheng, Z.; Li, Y.; Lin, Q.; Luo, J.; Liang, G.; Cai, X.; Zhang, D.; Ye, F. , Low-cost flexible thin film thermoelectric generator on zinc based thermoelectric materials, *Applied Physics Letters.* 2015, *106*, 73901, https://doi.org/10.1063/1.4909531.

[67] Scholdt, M.; Do, H.; Lang, J.; Gall, A.; Colsmann, A.; Lemmer, U.; Koenig, J.; Winkler, M.; Boettner, H. , Organic Semiconductors for Thermoelectric Applications, *J. Electron. Mater.* 2010, *39*, 1589-1592, https://doi.org/10.1007/s11664-010-1271-8.

[68] Yakuphanoglu, F.; Şenkal, B.; Saraç, A. , Electrical Conductivity, Thermoelectric Power, and Optical Properties of Organo-Soluble Polyaniline Organic Semiconductor, *J. Electron. Mater.* 2008, *37*, 930-934, https://doi.org/10.1007/s11664-008-0404-9.

[69] Tang, X.; Liu, T.; Li, H.; Yang, D.; Chen, L.; Tang, X. , Notably enhanced thermoelectric properties of lamellar polypyrrole by doping with β-naphthalene sulfonic acid, *RSC Adv.* 2017, *7*, 20192-20200, https://doi.org/10.1039/C7RA02302B.

[70] Kemp, N. T.; Kaiser, A. B.; Trodahl, H. J.; Chapman, B.; Buckley, R. G.; Partridge, A. C.; Foot, P. J. S. , Effect of ammonia on the temperature-dependent conductivity and thermopower of polypyrrole, *J. Polym. Sci. B Polym. Phys.* 2006, *44*, 1331-1338, https://doi.org/10.1002/polb.20792.

[71] Yao, Q.; Chen, L.; Zhang, W.; Liufu, S.; Chen, X. , Enhanced Thermoelectric Performance of Single-Walled Carbon Nanotubes/Polyaniline Hybrid Nanocomposites, *ACS Nano.* 2010, *4*, 2445-2451, http://dx.doi.org/10.1021/nn1002562.

[72] Tian, R.; Wan, C.; Wang, Y.; Wei, Q.; Ishida, T.; Yamamoto, A.; Tsuruta, A.; Shin, W.; Li, S.; Koumoto, K. , A solution-processed TiS2/organic hybrid superlattice film towards flexible thermoelectric devices, *J. Mater. Chem. A.* 2017, *5*, 564-570, https://doi.org/10.1039/C6TA08838D.

[73] Wan, C.; Gu, X.; Dang, F.; Itoh, T.; Wang, Y.; Sasaki, H.; Kondo, M.; Koga, K.; Yabuki, K.; Snyder, G. J.; Yang, R.; Koumoto, K. , Flexible n-type thermoelectric materials by organic intercalation of layered transition metal dichalcogenide TiS2, *Nat. Mater.* 2015, *14*, 622-627, https://doi.org/10.1038/nmat4251.

[74] Meng, C.; Liu, C.; Fan, S. , A Promising Approach to Enhanced Thermoelectric Properties Using Carbon Nanotube Networks, *Adv. Mater.* 2010, *22*, 535-539, https://doi.org/10.1002/adma.200902221.

[75] Wang, H.; Yu, C. , Organic Thermoelectrics: Materials Preparation, Performance Optimization, and Device Integration, *Joule.* 2019, *3*, 53-80, https://doi.org/10.1016/j.joule.2018.10.012.

[76] Zhang, Y.; Park, S. , Flexible Organic Thermoelectric Materials and Devices for Wearable Green Energy Harvesting, *Polymers.* 2019, *11*, 909, https://doi.org/10.3390/polym11050909.

[77] Freer, R.; Powell, A. V. , Realising the potential of thermoelectric technology: a Roadmap, *Journal of Materials Chemistry C.* 2020, *8*, 441-463, https://doi.org/10.1039/C9TC05710B.

[78] Jung, Y. S.; Jeong, M. H.; Jeong, D. H.; Kang, S. B.; Kim, J.; Kim, F.; Lee, K.; Son, J. S.; Baik, J. M.; Choi, K. J. , Wearable solar thermoelectric generator driven by unprecedentedly high temperature difference, *Nano Energy.* 2017, *40*, 663-672, https://doi.org/10.1016/j.nanoen.2017.08.061.

[79] Jitthamapirom, P.; Wanarattikan, P.; Nuthongkum, P.; Sakdanuphab, R.; Sakulkalavek, A. , Comparison of thermoelectric properties of flexible bismuth telluride thin films deposited via DC and RF magnetron sputtering, *Ferroelectrics.* 2019, *552*, 64-72, https://doi.org/10.1080/00150193.2019.1653083.

[80] Kianwimol, S.; Wanarattikan, P.; Sakdanuphab, R.; Pluengphon, P.; Bovornratanaraks, T.; Sakulkalavek, A. , Experimental Study on Flexible Bismuth Telluride Thin Films Deposited by DC Sputtering at Different Powers, *Journal of Electronic Materials.* 2019, *48*, 3490-3496, https://doi.org/10.1007/s11664-019-07100-1.

[81] Singkaselit, K.; Sakulkalavek, A.; Sakdanuphab, R. , Effects of annealing temperature on the structural, mechanical and electrical properties of flexible bismuth telluride thin films prepared by high-pressure RF magnetron sputtering, *Ansn.* 2017, *8*, 350021-350027, https://doi.org/10.1088/2043-6254/aa7222.

[82] Oga Norimasa; Takuya Kurokawa; Rikuo Eguchi; Masayuki Takashiri , Evaluation of Thermoelectric Performance of Bi2Te3 Films as a Function of Temperature Increase Rate during Heat Treatment, *Coatings (Basel).* 2021, *11*, 38, https://doi.org/10.3390/coatings11010038.

[83] Y. Shi; Y. Wang; D. Mei; B. Feng; Z. Chen , Design and Fabrication of Wearable Thermoelectric Generator Device for Heat Harvesting, *IEEE Robot. Autom. Lett.* 2018, *3*, 373-378, https://doi.org/10.1109/LRA.2017.2734241.

[84] Zhao, L.; Zhang, B.; Li, J.; Zhou, M.; Liu, W.; Liu, J. , Thermoelectric and mechanical properties of nano-SiC-dispersed Bi2Te3 fabricated by mechanical alloying and spark plasma sintering, *J. Alloys Compd.* 2008, *455*, 259-264, https://doi.org/10.1016/j.jallcom.2007.01.015.

[85] Mun, H.; Choi, S.; Lee, K. H.; Kim, S. W. , Boundary Engineering for the Thermoelectric Performance of Bulk Alloys Based on Bismuth Telluride, *ChemSusChem.* 2015, *8*, 2312-2326, https://doi.org/10.1002/cssc.201403485.

[86] Liu, Y.; Zhou, M.; He, J. , Towards higher thermoelectric performance of Bi2Te3 via defect engineering, *Scripta Materialia.* 2016, *111*, 39-43, https://doi.org/10.1016/j.scriptamat.2015.06.031.

[87] Minnich, A. J.; Dresselhaus, M. S.; Ren, Z. F.; Chen, G. , Bulk nanostructured thermoelectric materials: current research and future prospects, *Energy & Environmental Science.* 2009, *2*, 466-479, https://doi.org/10.1039/b822664b.

[88] Tappura, K. , A numerical study on the design trade-offs of a thin-film thermoelectric generator for large-area applications, *Renew. Energy.* 2018, *120*, 78-87, http://dx.doi.org/10.1016/j.renene.2017.12.063.

[89] Mayer, P. M.; Ram, R. J. , Optimization of Heat Sink-Limited Thermoelectric Generators, *Nanoscale Microscale Thermophys. Eng.* 2006, *10*, 143-155, https://doi.org/10.1080/10893950600643063.

[90] Carmo, J. P.; Goncalves, L. M.; Correia, J. H. , Thermoelectric Microconverter for Energy Harvesting Systems, *IEEE Trans. Ind. Electron.* 2010, *57*, 861-867, https://doi.org/10.1109/TIE.2009.2034686.

[91] Suemori, K.; Hoshino, S.; Kamata, T. , Flexible and lightweight thermoelectric generators composed of carbon nanotube–polystyrene composites printed on film substrate, *Appl. Phys. Lett.* 2013, *103*, 153902, https://doi.org/10.1063/1.4824648.

[92] Kim, C. S.; Lee, G. S.; Choi, H.; Kim, Y. J.; Yang, H. M.; Lim, S. H.; Lee, S.; Cho, B. J. , Structural design of a flexible thermoelectric power generator for wearable applications, *Appl. Energy.* 2018, *214*, 131-138, http://doi.org/10.1016/j.apenergy.2018.01.074.

[93] Strasser, M.; Aigner, R.; Lauterbach, C.; Sturm, T. F.; Franosch, M.; Wachutka, G. , Micromachined CMOS thermoelectric generators as on-chip power supply, *Sens. Actuators, A.* 2004, *114*, 362-370, http://doi.org/10.1016/j.sna.2003.11.039.

[94] Jin Xie; Chengkuo Lee; Hanhua Feng , Design, Fabrication, and Characterization of CMOS MEMS-Based Thermoelectric Power Generators, *J Microelectromech Syst.* 2010, *19*, 317-324, https://doi.org/10.1109/JMEMS.2010.2041035.

[95] Wang, Z.; Leonov, V.; Fiorini, P.; Van Hoof, C. , Realization of a wearable miniaturized thermoelectric generator for human body applications, *Sens. Actuators, A.* 2009, *156*, 95-102, http://doi.org/10.1016/j.sna.2009.02.028.

[96] Su, J.; Leonov, V.; Goedbloed, M.; van Andel, Y.; de Nooijer, M. C.; Elfrink, R.; Wang, Z.; Vullers, R. J. M. , A batch process micromachined thermoelectric energy harvester: fabrication and characterization, *J. Micromech. Microeng.* 2010, *20*, 104005, https://doi.org/10.1088/0960-1317/20/10/104005.

[97] Kim, M.; Oh, T. , Thermoelectric Thin Film Device of Cross-Plane Configuration Processed by Electrodeposition and Flip-Chip Bonding, *Materials Transactions.* 2012, *53*, 2160-2165, https://doi.org/10.2320/matertrans.M2012265.

[98] Colpitts, T.; Venkatasubramanian, R.; Siivola, E.; O'Quinn, B. , Thin-film thermoelectric devices with high room-temperature figures of merit, *Nature.* 2001, *413*, 597-602, http://doi.org/10.1038/35098012.

[99] Harman, T. C.; Taylor, P. J.; Walsh, M. P.; LaForge, B. E. , Quantum Dot Superlattice Thermoelectric Materials and Devices, *Science.* 2002, *297*, 2229-2232, https://doi.org/10.1126/science.1072886.

[100] Sun, X.; Lin, Y. M.; Cronin, S. B.; Dresselhaus, M. S.; Ying, J. Y.; Chen, G. , Theoretical modeling of thermoelectricity in Bi nanowires, *18th ICT.* 1999, 394-397, https://doi.org/10.1109/ICT.1999.843413.

[101] Meijer, G.; Pertijs, M.; Makinwa, K. , Thermoelectric Energy Harvesting, in Smart sensor systems: emerging technologies and applications, 2014, 246-252, http://eu.wiley.com/WileyCDA/WileyTitle/productCd-0470686006.html.

[102] Qu, S.; Chen, Y.; Shi, W.; Wang, M.; Yao, Q.; Chen, L. , Cotton-based wearable poly(3-hexylthiophene) electronic device for thermoelectric application with cross-plane temperature gradient, *Thin Solid Films.* 2018, *667*, 59-63, http://dx.doi.org/10.1016/j.tsf.2018.09.046.

[103] Nguyen Huu, T.; Nguyen Van, T.; Takahito, O. , Flexible thermoelectric power generator with Y-type structure using electrochemical deposition process, *Appl. Energy.* 2018, *210*, 467-476, http://doi.org/10.1016/j.apenergy.2017.05.005.

[104] Sun, T.; Peavey, J. L.; David Shelby, M.; Ferguson, S.; O'Connor, B. T. , Heat shrink formation of a corrugated thin film thermoelectric generator, *Energy Convers. Manag.* 2015, *103*, 674-680, http://doi.org/10.1016/j.enconman.2015.07.016.

[105] Yamamuro, H.; Takashiri, M. , Power Generation in Slope-Type Thin-Film Thermoelectric Generators by the Simple Contact of a Heat Source, *Coatings.* 2019, *9*, 63, https://doi.org/10.3390/coatings9020063.

[106] LeBlanc, S. , Thermoelectric generators: Linking material properties and systems engineering for waste heat recovery applications, *Sustain. Mater. Techno.* 2014, *1-2*, 26-35, http://doi.org/10.1016/j.susmat.2014.11.002.

[107] Ding, Y.; Qiu, Y.; Cai, K.; Yao, Q.; Chen, S.; Chen, L.; He, J. , High performance n-type Ag2Se film on nylon membrane for flexible thermoelectric power generator, *Nat. Commun.* 2019, *10*, 1-7, https://doi.org/10.1038/s41467-019-08835-5.

[108] Elsheikh, M.; Shnawah, D.; Sabri, M.; Said, S.; Hassan, M.; Bashir, M.; Mohamad, M. , A review on thermoelectric renewable energy: Principle parameters that affect their performance, *Renewable & Sustainable Energy Reviews.* 2014, *30*, 337-355, https://doi.org/10.1016/j.rser.2013.10.027.

[109] Dmitriev, A. V.; Zvyagin, I. P. , Current trends in the physics of thermoelectric materials, *Physics-Uspekhi.* 2010, *53*, 789-803, https://doi.org/10.3367/UFNe.0180.201008b.0821.

[110] Liao, M. H.; Huang, K. C.; Tsai, F. A.; Liu, C. Y.; Lien, C.; Lee, M. H. , Thickness dependence of electrical conductivity and thermo-electric power of Bi2.0Te2.7Se0.3/Bi0.4Te3.0Sb1.6 thermo-electric devices, *AIP Advances.* 2018, *8*, 015020-4, http://doi.org/10.1063/1.5017252.

[111] Dheepa, J.; Sathyamoorthy, R.; Subbarayan, A. , Optical properties of thermally evaporated Bi2Te3 thin films, *J. Cryst. Growth.* 2005, *274*, 100-105, https://doi.org/10.1016/j.jcrysgro.2004.09.070.

[112] El-Sayed, H. E. A. , Structural and optical properties of thermally evaporated Bi2Te3 films, *Appl. Surf. Sci.* 2005, *250*, 70-78, https://doi.org/10.1016/j.apsusc.2004.12.025.

[113] Ren, P.; Liu, Y.; He, J.; Lv, T.; Gao, J.; Xu, G. , Recent advances in inorganic material thermoelectrics, *Inorganic Chemistry Frontiers.* 2018, *5*, 238-2398, https://doi.org/10.1039/c8qi00366a.

[114] G. D. Deshmukh; S. M. Patil; S. S. Patil; P. H. Pawar. , Effect of Film Thickness on Structural and Optical Properties of Bi2Te3 Thin Films, *J. Chem. Biol. Phys. Sci.* 2015, *5*, 2769-2779, https://www.jcbsc.org/admin/get_filephy.php?id=335.

[115] Ohta, H. , Thermoelectrics based on strontium titanate, *Materials Today.* 2007, *10*, 44-49, https://doi.org/10.1016/S1369-7021(07)70244-4.

[116] Tritt, T. M.; Subramanian, M. A. , Thermoelectric Materials, Phenomena, and Applications: A Bird's Eye View, *MRS Bulletin.* 2006, *31*, 188-198, https://doi.org/10.1557/mrs2006.44.

[117] Nptel , Metal-semiconductor junctions, *NOC: Fundamentals of Electronic Materials and Devices.* , https://nptel.ac.in/content/storage2/courses/113106065/Week%204/Lesson9.pdf.

[118] Kasap, S. O. , Principles of electronic materials and devices, 2006.

[119] Lüth, H. , Solid Surfaces, Interfaces and Thin Films, 2015, 380, https://doi.org/10.1007/978-3-319-10756-1.

[120] Zhao, L.; Zhang, B.; Li, J.; Zhou, M.; Liu, W.; Liu, J. , Thermoelectric and mechanical properties of nano-SiC-dispersed Bi2Te3 fabricated by mechanical alloying and spark plasma sintering, *J. Alloys Compd.* 2008, *455*, 259-264, https://doi.org/10.1016/j.jallcom.2007.01.015.

[121] Prokhorov, V. M.; Pivovarov, G. I. , Detection of internal cracks and ultrasound characterization of nanostructured Bi_2Te_3-based thermoelectrics via acoustic microscopy, *Ultrasonics.* 2011, *51*, 715, https://doi.org/10.1016/j.ultras.2011.02.005.

[122] J. Yao and D. W. Hewak , Chalcogenide flexible thin film thermoelectric device fabricated by co-sputtering, 2015, https://chalcogenide.files.wordpress.com/2015/03/champ-2015-poster-jin-yao-chalcogenide-flexible-thin-film-thermoelectric.pdf.

[123] Kim, T.; Chun, B. , Microstructure and thermoelectric properties of n- and p-type Bi2Te3 alloys by rapid solidification processes, *Journal of Alloys and Compounds.* 2007, *437*, 225-230, https://doi.org/10.1016/j.jallcom.2006.07.090.

[124] Zhu, T.; Li, J. , Ultra-strength materials, *Progress in Materials Science.* 2010, *55*, 710-757, https://doi.org/10.1016/j.pmatsci.2010.04.001.

[125] Colpitts, T.; Venkatasubramanian, R.; Siivola, E.; O'Quinn, B. , Thin-film thermoelectric devices with high room-temperature figures of merit, *Nature.* 2001, *413*, 597-602, http://doi.org/10.1038/35098012.

[126] Chen, T.; Yu, P.; Chou, R.; Pan, C. , Phonon thermal conductivity suppression of bulk silicon nanowire composites for efficient thermoelectric conversion, *Optics Express.* 2010, *18 Suppl 3*, A467, https://doi.org/10.1364/OE.18.00A467.

[127] Hicks, L.; Dresselhaus, M. , Effect of quantum-well structures on the thermoelectric figure of merit, *Physical Review B.* 1993, *47*, 12727-12731, https://doi.org/10.1103/PhysRevB.47.12727.

[128] Dresselhaus, M. S.; Chen, G.; Tang, M. Y.; Yang, R.; Lee, H.; Wang, D.; Ren, Z.; Fleurial, J.; Gogna, P. , New Directions for Low-Dimensional Thermoelectric Materials, *ChemInform.* 2007, *38*, https://doi.org/10.1002/chin.200726202.

[129] Snyder, G. J.; Toberer, E. S. , Complex thermoelectric materials, *Nat. Mater.* 2008, *7*, 105-114, http://doi.org/10.1038/nmat2090.

[130] Chen, X.; Dai, W.; Wu, T.; Luo, W.; Yang, J.; Jiang, W.; Wang, L. , Thin Film Thermoelectric Materials: Classification, Characterization, and Potential for Wearable Applications, *Coatings.* 2018, *8*, 244, https://doi.org/10.3390/coatings8070244.

[131] He, Z.; Chen, Y.; Zheng, Z.; Li, F.; Liang, G.; Luo, J.; Fan, P. , Enhancement of thermoelectric performance of N-type Bi2Te3 based thin films via in situ annealing during magnetron sputtering, *Ceramics International.* 2020, https://doi.org/10.1016/j.ceramint.2020.02.117.

[132] Tao, X.; Wan, K.; Deru, J.; Bilotti, E.; Assender, H. E. , Thermoelectric behaviour of Bi-Te films on polymer substrates DC-sputtered at room-temperature in moving web deposition, *Surf. Coat. Technol.* 2020, *385*, 125393, http://doi.org/10.1016/j.surfcoat.2020.125393.

[133] Huang, H.; Luan, W.; Tu, S. , Influence of annealing on thermoelectric properties of bismuth telluride films grown via radio frequency magnetron sputtering, *Thin Solid Films.* 2009, *517*, 3731-3734, https://doi.org/10.1016/j.tsf.2009.01.015.

[134] Kim, D.; Byon, E.; Lee, G.; Cho, S. , Effect of deposition temperature on the structural and thermoelectric properties of bismuth telluride thin films grown by co-sputtering, *Thin Solid Films.* 2006, *510*, 148-153, https://doi.org/10.1016/j.tsf.2005.12.306.

[135] Pilaipon Nuthongkum; Rachsak Sakdanuphab; Mati Horprathum; Aparporn Sakulkalavek. , [Bi]:[Te] Control, Structural and Thermoelectric Properties of Flexible Bi^sub x^Te^sub y^ Thin Films Prepared by RF Magnetron Sputtering at Different Sputtering Pressures, *J. Electron. Mater.* 2017, *46*, 6444–6450, https://doi.org/10.1007/s11664-017-5671-x.

[136] Bahk, J.; Fang, H.; Yazawa, K.; Shakouri, A. , Flexible thermoelectric materials and device optimization for wearable energy harvesting, *J. Mater. Chem. C.* 2015, *3*, 1362-1374, https://doi.org/10.1039/c5tc01644d.

[137] Boulouz, A.; Boulouz, M.; Giani, A.; Pascal-Delannoy, F.; Foucaran, A.; Boyer, A. , Preparation and characterization of MOCVD bismuth telluride thin films, *J. Cryst. Growth.* 1998, *194*, 336-341, https://doi.org/10.1016/S0022-0248(98)00690-3.

[138] Zou, H.; Rowe, D. M.; Min, G. , Growth of p- and n-type bismuth telluride thin films by co-evaporation, *J. Cryst. Growth.* 2001, *222*, 82-87, https://doi.org/10.1016/S0022-0248(00)00922-2.

[139] Duan, X.; Jiang, Y. , Annealing effects on the structural and electrical transport properties of n-type Bi2Te2.7Se0.3 thin films deposited by flash evaporation, *Appl. Surf. Sci.* 2010, *256*, 7365-7370, https://doi.org/10.1016/j.apsusc.2010.05.069.

[140] Cho, S.; Kim, Y.; DiVenere, A.; Wong, G. K.; Ketterson, J. B.; Meyer, J. R. , Antisite defects of Bi2Te3 thin films, *Appl. Phys. Lett.* 1999, *75*, 1401-1403, https://doi.org/10.1063/1.124707.

[141] Bailini, A.; Donati, F.; Zamboni, M.; Russo, V.; Passoni, M.; Casari, C. S.; Li Bassi, A.; Bottani, C. E. , Pulsed laser deposition of Bi2Te3 thermoelectric films, *Appl. Surf. Sci.* 2007, *254*, 1249-1254, https://doi.org/10.1016/j.apsusc.2007.09.039.

[142] Noro, H.; Sato, K.; Kagechika, H. , The thermoelectric properties and crystallography of Bi-Sb-Te-Se thin films grown by ion beam sputtering, *Journal of Applied Physics.* 1993, *73*, 1252-1260, https://doi.org/10.1063/1.353266.

[143] Zhou, Y.; Li, L.; Tan, Q.; Li, J. , Thermoelectric properties of Pb-doped bismuth telluride thin films deposited by magnetron sputtering, *J. Alloys Compd.* 2014, *590*, 362-367, https://doi.org/10.1016/j.jallcom.2013.12.136.

[144] Madou, M. J. , Manufacturing techniques for microfabrication and nanotechnology, *CRC Press.* 2011, 403-404, https://doi.org/10.1201/9781439895306.

[145] Taylor; Cliffordl; Bjornard; Erikj; Valiska; Michaelj , Film thickness uniformity control apparatus for in-line sputtering systems, *US Patents.* 1992, 1-7, https://patents.google.com/patent/US5156727.

[146] Gonçalves, L. M. , The deposition of Bi2Te3 and Sb2Te3 thermoelectric thin-films by thermal co-evaporation and applications in energy harvesting, 2012, https://doi.org/10.1201/b11891-19.

[147] Depla, D.; Mahieu, S.; Greene, J. E. , Sputter Deposition Processes, *Handbook of Deposition Technologies for Films and Coatings.* 2010, 253-296, https://doi.org/10.1016/B978-0-8155-2031-3.00005-3.

[148] Micro Magnetics , Magnetron sputtering technology, , http://micromagnetics.com/pdfs/what_is_sputtering.pdf.

[149] Liu, H.; Liu, X.; Xiong, L.; Zhao, W. , Packaging of High Power Semiconductor Lasers, 2015, https://doi.org/10.1007/978-1-4614-9263-4.

[150] Anonymous, Sputtering deposition, *Oxford Vacuum Science.* , http://www.oxford-vacuum.com/background/thin_film/sputtering.htm.

[151] Adachi, H.; Wasa, K.; Kanno, I.; Kotera, H. , Handbook of sputter deposition technology, 1-Thin Films and Nanomaterials, 2012, https://doi.org/10.1016/B978-1-4377-3483-6.00001-2.

[152] G. Monaco. , Coating technology: evaporation vs sputtering, *Satisloh Italy S.R.L.* 2016, http://www.satisloh.com/fileadmin/contents/Whitepaper/Evaporation-vs-Sputtering-Coating_EN.pdf.

[153] Anonymous, Physical vapor deposition, *Advanced Technologies, Coating Techniques, Institute of Materials and Machine Mechanics.* , http://www.umms.sav.sk/6493-en/physical-vapor-deposition/.

[154] Anonymous, Sputtering, , http://users.wfu.edu/ucerkb/Nan242/L07-Sputtering_a.pdf.

[155] Anonymous, Thin Film Deposition, , http://shodhganga.inflibnet.ac.in/bitstream/10603/79579/12/12_chapter%202.pdf.

[156] Anonymous, Deposition of Thin TiO2 Films by DC Sputtering Method, , http://shodhganga.inflibnet.ac.in/bitstream/10603/44513/12/12_chapter%204.pdf.

[157] Anonymous, Sputtering. , http://users.wfu.edu/ucerkb/Nan242/MT2-Review.pdf.

[158] Kelly, P. J.; Arnell, R. D. , Magnetron sputtering: a review of recent developments and applications, *Vacuum.* 2000, *56*, 159-172, http://doi.org/10.1016/S0042-207X(99)00189-X.

[159] Thornton, J. A. , Influence of apparatus geometry and deposition conditions on the structure and topography of thick sputtered coatings, *Journal of Vacuum Science and Technology.* 1974, *11*, 666-670, https://doi.org/10.1116/1.1312732.

[160] Musil, J.; Matouš, J.; Vlček, J.; Koydl, L.; Müller, K. , Surface morphology of sputter deposited low melting point metallic thin films, *Czechoslovak Journal of Physics.* 1994, *44*, 565-574, https://doi.org/10.1007/BF01689604.

[161] Goldsmid, H. J. , Thermoelectric refrigeration, *Springer.* 1964, 133-161, http://www.springer.com/gb/book/9781489957252.

[162] Shakouri, A.; Bian, Z. , Enhanced solid-state thermionic emission in nonplanar heterostructures, *Applied Physics Letters.* 2006, *88*, 012102-3, http://doi.org/10.1063/1.2159574.

[163] Yucheng, L.; Minnich, A. J.; Gang, C.; Zhifeng, R. , Enhancement of Thermoelectric Figure of Merit by a Bulk Nanostructuring Approach, *Advanced Functional Materials.* 2010, *20*, 357-376, https://doi.org/10.1002/adfm.200901512.

[164] Alam, H.; Ramakrishna, S. , A review on the enhancement of figure of merit from bulk to nano-thermoelectric materials, *Nano Energy.* 2013, *2*, 190-212, https://doi.org/10.1016/j.nanoen.2012.10.005.

[165] Casati, G.; Mejía-Monasterio, C.; Prosen, T. , Increasing Thermoelectric Efficiency: A Dynamical Systems Approach, *Physical Review Letters.* 2008, *101*, 016601, https://doi.org/10.1103/PhysRevLett.101.016601.

[166] Mason, S. J. , Nanoscale Thermoelectrics: A Study of the Absolute Seebeck Coefficient of Thin Films, 2014, https://search.proquest.com/docview/1625052273.

[167] Mi-Kyung Han; Yingshi Jin; Da-Hee Lee; Sung-Jin Kim , Thermoelectric Properties of Bi2Te3: CuI and the Effect of Its Doping with Pb Atoms, *Materials*. 2017, *10*, 1235, https://doi.org/10.3390/ma10111235.

[168] Aselage, T. L.; Emin, D.; McCready, S. S.; Duncan, R. V. , Large Enhancement of Boron Carbides' Seebeck Coefficients through Vibrational Softening, *Physical Review Letters*. 1998, *81*, 2316-2319, https://doi.org/10.1103/PhysRevLett.81.2316.

[169] Pei, Y.; Wang, H.; Snyder, G. J. , Band engineering of thermoelectric materials, *Advanced Materials (Deerfield Beach, Fla.)*. 2012, *24*, 6125-6135, https://doi.org/10.1002/adma.201202919.

[170] G. Homm; F. Gather; A. Kronenberger; S. Petznick; T. Henning; M. Eickhoff; B. K. Meyer; C. Heiliger; P. J. Klar , Effects of interface geometry on the thermoelectric properties of laterally microstructured ZnO-based thin films, *Physica Status Solidi. A, Applications and Materials Science*. 2013, *210*, 119-124, https://doi.org/10.1002/pssa.201228463.

[171] Baily, S. A. , Transport properties of amorphous antimony telluride, *Physical Review B*. 2006, *73*, https://doi.org/10.1103/PhysRevB.73.165211.

[172] Park, J.; Shin, K.; Lee, C. , Roll-to-Roll Coating Technology and Its Applications: A Review, *International Journal of Precision Engineering and Manufacturing*. 2016, *17*, 537-550, https://doi.org/10.1007/s12541-016-0067-z.

[173] Roth, B.; Søndergaard, R. R.; Krebs, F. C. , 7 - Roll-to-roll printing and coating techniques for manufacturing large-area flexible organic electronics, *Handbook of Flexible Organic Electronics*. 2015, 171-197, http://doi.org/10.1016/B978-1-78242-035-4.00007-5.

[174] Ekpe, S. D.; Bezuidenhout, L. W.; Dew, S. K. , Deposition rate model of magnetron sputtered particles, *Thin Solid Films*. 2005, *474*, 330-336, https://doi.org/10.1016/j.tsf.2004.09.007.

[175] Goncalves, L. M.; Couto, C.; Alpuim, P.; Rolo, A. G.; Völklein, F.; Correia, J. H. , Optimization of thermoelectric properties on Bi2Te3 thin films deposited by thermal co-evaporation, *Thin Solid Films*. 2010, *518*, 2816-2821, http://doi.org/10.1016/j.tsf.2009.08.038.

[176] Cosnahan, T.; Watt, A. A. R.; Assender, H. E. , Modelling of a vacuum metallization patterning method for organic electronics, *Surface and Coatings Technology*. 2018, *336*, 128-132, https://doi.org/10.1016/j.surfcoat.2017.09.058.

Chapter 2 Coating fabrication and characterisation

This chapter describes the sputtering technique for the fabrication of Bi-Te based TE thin films and TEGs. Various measurements and characterisation techniques are described in detail.

2.1 Thin-film fabrication in roll-to-roll

All deposition processes were conducted in either an Edwards Vacuum Coater Auto 306 system or an Aerre Machines R2R vacuum web coater. As shown in Figure 2.1, both are equipped with a thermal evaporation system and a magnetron sputtering cathode, which is to one side (horizontally/vertically 'directed') of the rotating drum that supports the polymer substrate.

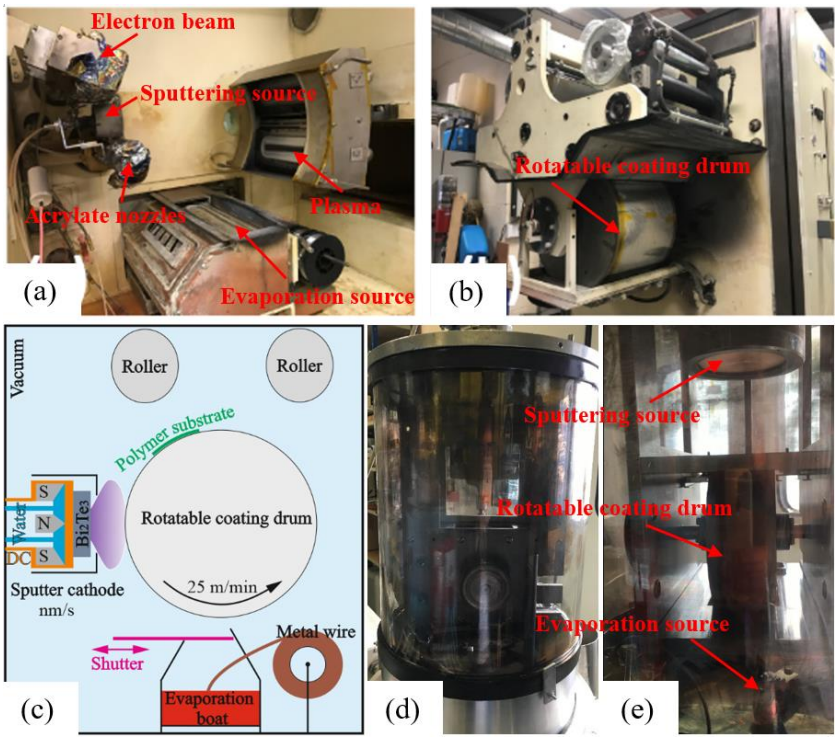


Figure 2.1. *Aerre Machine web coater (a) left side (b) right side (the right side inserts into the left side to allow the deposition source towards the rotatable drum); (c) a schematic diagram of incontinuous processes in web coater; Edwards 306 system (d) side view (e) face view.*

In the Oxford Aerre Machine R2R web coater, Bi-Te thin films were deposited onto flexible polymer substrates (e.g. ~125-µm PET sheets) at RT using a three-inch Bi_2Te_3 target (in a 0.25-inch thickness, indium bonded to a 0.125-inch thick Cu backing plate, 99.999% purity, Mi-Net Tech. Ltd.) with a target-substrate distance of ~6 cm. A typical Ar flow rate I used was 250 sccm. The power applied to the target source was maintained as 0.25 kW. Polymer sheets were attached to a coating drum (circumference 1.8 m) rotated at 25 m min^{-1} during sputtering, allowing multiple rotations for increased thickness. A pre-sputtering was conducted for three mins to clean the target surface before deposition. Films with various thicknesses can be obtained by varying the deposition time (1 – 10 mins), and hence the number of passes of the deposition source.

An Edwards 306 system was used to deposit various electrode materials in TEGs because the evaporation of raw metal material in the Edward 306 system was more convenient. Four different metals: Ag (99.99%, Kurt J. Lesker Co. Ltd.), Al (99.8%, Speedmet®), Cu (99.0%, Sigma-Aldrich®), Au (99.99%, Testbourne Ltd.), were thermally evaporated onto a static solid-mask covered PET (~125-µm thick) substrate in an Edwards Vacuum Coater Auto 306 system under a vacuum condition of 2×10^{-5} mbar. Evaporation was stopped once a quartz crystal microbalance placed at the same level as the substrate holder indicated a thickness of ~60 nm. Ag, Cu, and Au were slowly deposited (3 - 4 min deposition) to achieve a uniform/dense film, while Al was evaporated in a flash (~28 s) to limit oxidation during deposition.

The same three-inch Bi_2Te_3 target can also be used in an Edwards 306 system under a vacuum of $\sim 8 \times 10^{-5}$ mbar ($\sim 2 \times 10^{-5}$ mbar base pressure with 20 sccm Ar flow rate) and 0.1 kW power. The substrates were attached to a rotating drum at an in-line speed of 11.3 m min^{-1}, and the drum-to-target distance was maintained as 6 cm. A pre-cleaning process was also conducted.

2.2 Acrylate-layer fabrication

The acrylate coating is of interest in this study as a smoothing layer (Chapter 3), a buffer layer (Chapter 4), and an electrically insulating layer (Chapter 7). As can be seen in Figure 2.2, the acrylate layer was made by tripropyleneglycol diacrylate monomer (TPGDA Sigma–Aldrich [1]) injected into a hot tank (preheated at ~240°C, for ~3 – 6 mins according to the amount of monomer, under an injection rate of ~0.5 mL/min) and then vacuum-flash evaporated (~1.8×10^{-4} mbar) through nozzles (preheated at ~240°C) onto a PET substrate (rotating under an in-line speed of ~25 m/min), followed by an *in situ* polymerised cure by a 1-min exposure to an Ar plasma (270 V, 5.8 A).

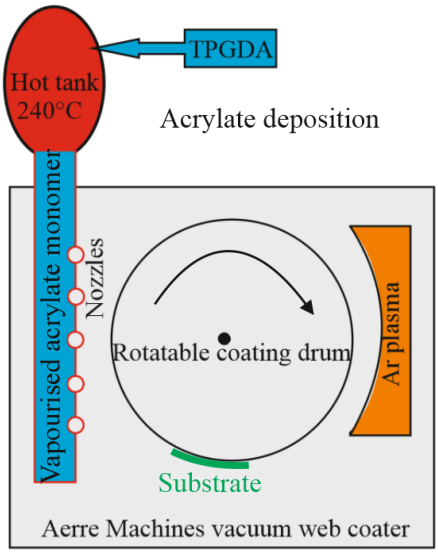


Figure 2.2. *Vacuum jet deposition of acrylate.*

2.3 Characterisation techniques

A variety of typical material characteristics are used to assess as-prepared specimens, as summarised below. More details are explained in the corresponding section.

Table 2.I. *Materials characterisations used in this project.*

Techniques	Characteristics
Thermoelectric/Seebeck system	Seebeck coefficient
Dektak stylus profiler	Film thickness

Four-point probe	Electrical resistivity
Tensile/buckling test	Mechanical property
Contact resistance measurement	Contact resistance at the interface
X-ray diffraction	Crystal structure
Atomic force microscope	Surface morphology
Scanning electron microscope/Energy-dispersive x-ray Analysis	Surface morphology & Elemental composition
UV-Vis spectroscopy	Absorbance spectra & Bandgap
Fourier-transform infrared spectroscopy	IR absorbance spectra
X-ray Photoelectron Spectrometer	Elemental composition & Valance band
Hall measurement system/van der Pauw	Carrier concentration and mobility
Optical profilometer MicroXAM	Surface morphology
Scanning Kelvin probe	Work function

2.3.1 Thermoelectric characterisation

Both a commercial (MMR Tech. Inc.) Seebeck system and an in-house custom Seebeck setup are used to measure S of TE films and TEGs. The output voltage (ΔV) is recorded corresponding to each ΔT applied between two ends of the TE film. S is determined by the slope of fit line in the plot of ΔT *vs* ΔV.

The experiment in the MMR Tech. Seebeck effect system (Figure 2.3 a) was conducted by a PhD student (Kening Wan) at Queen Mary University of London. S of TE films was measured along the in-plane direction at 300 K under nitrogen atmosphere applying ΔT from 0.1 to 0.45 K, determined by the ratio of ΔV generated across the film surface to ΔT. Similar to most studies of flexible thin-film TEGs, this project does not characterise λ of TE films. PF is used to quantify the TE efficiency of a TE film, which is calculated by combining effects of both S and ρ ($PF = S^2/\rho$).

This commercial MMR Seebeck system cannot be used for TEGs (the hot-cold distance, i.e. the sample length > cm) because the sample size (length: 5 mm; width: 3 mm) in

MMR Seebeck system is smaller than the TEGs. TE efficiency of a TEG was assessed *via* an in-house custom Seebeck setup using two Peltier modules (RS No.: 693-7080) to apply a ΔT between two opposing sides of a TEG. The thermocouples were placed on top of the polymer substrate and close to the ends of a thermoelectric strip, to emulate the real temperature reaching at the Bi-Te. The open-circuit voltage (V_{OC}) and short-circuit current (I_{SC}) were recorded by applying ΔT from 5 – 31°C, and then S was calculated by the ratio of V_{OC} generated across the device and a ΔT applied between two sides. The power output was measured using a simple Ohm's circuit: Power (P) = Current (I) × Voltage (V), recorded using two Keithley 2400 source meters, as shown in Figure 2.3 b, by applying a ΔT of 11.4 ± 0.2°C (a little smaller than the real temperature difference, 14 - 17°C, between the human body and room temperature, as it was considered that there would be a temperature loss at the contact between TEGs and the human body in a real wearable condition). Many studies [2-4] reported that a maximum power output of TEGs could be obtained if the load resistance (R_L) was equal to the internal resistance of TEGs (R_{TEG}). In this study, R_L was varied using a rheostat from 0.84 Ω to 50.5 kΩ, containing the R_{TEG} in this project.

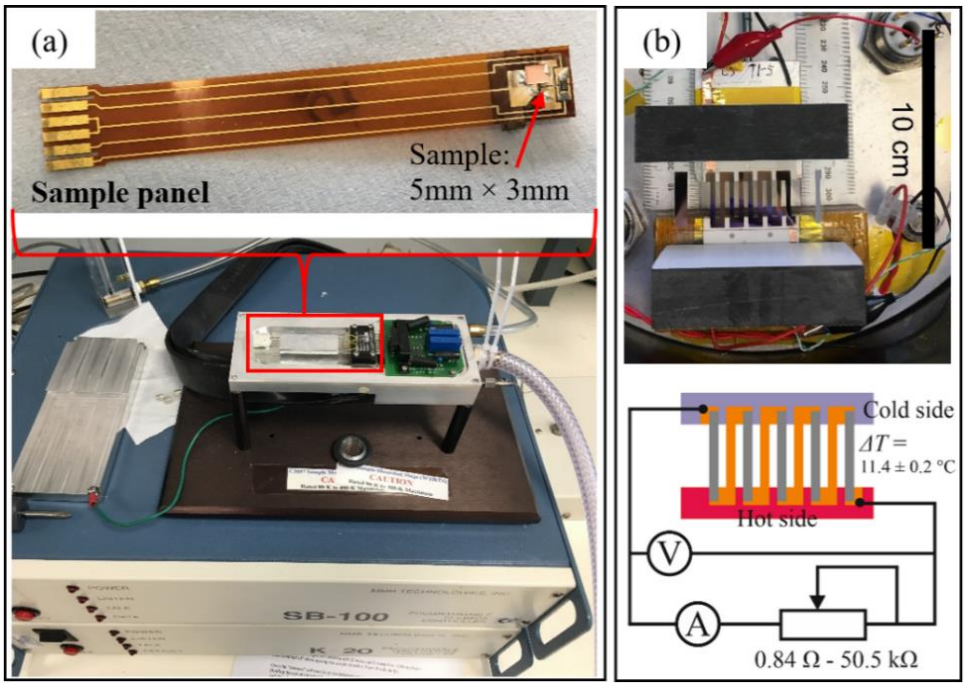


Figure 2.3. *(a) An MMR Tech. Seebeck effect system for characterisation of TE films (i.e. Bi-Te films were grown on polymer substrates); (b) A home-built Seebeck setup with a schematic diagram for characterisation of TEGs (i.e. '\|' shape Bi-Te strips were connected by 'ʃ' shape metal contacts).*

Error analysis of Seebeck setup

Measurements on the home-built system were compared with the MMR Tech. Seebeck system (Figure 2.4).

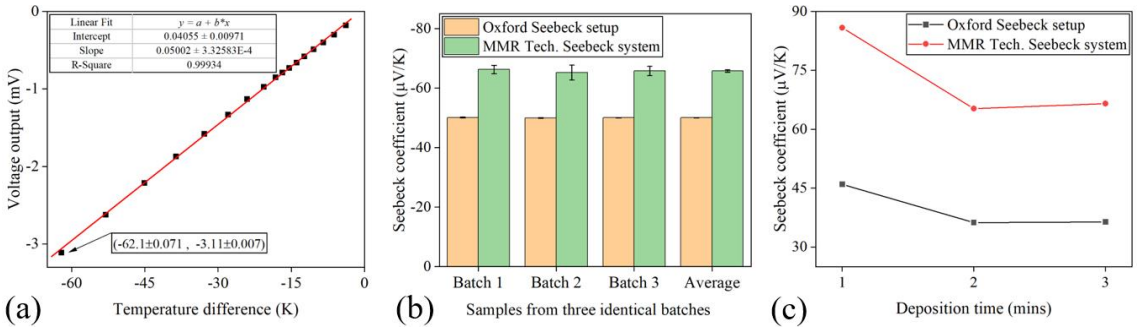


Figure 2.4. *(a) A plot of V_{OC} vs ΔV for S, i.e. the slope of linear fit; (b) Comparison of results between Oxford home-build Seebeck setup and a commercial Seebeck system (in three identical batches, three samples in each batch were tested); (c) Comparison*

between these two Seebeck systems (three different batch samples were tested). All error bars denote standard deviation from three identical measurements.

In Figure 2.4 a, the fit line has an R^2 approaching 1, i.e. a perfect linear fit, hence the obtained slope (i.e. S) is reliable. Figure 2.4 b reveals great repeatability between samples and batches not only for the Seebeck measurement but also for the fabrication process in Oxford web coater. A constant difference in results between the Oxford Seebeck setup and MMR Tech. Seebeck system is observed, which could come from the differences of sample sizes, ΔT range, standard meters and heaters for applying/measuring ΔT (the Oxford setup could have an overestimated ΔT due to the position of thermocouples), etc. Importantly, results from two Seebeck systems show the same trend for a series of films in Figure 2.4 c, so comparisons between samples showing the effect of variations with various parameters (the film thickness, sputter pressure, etc.) can be made with confidence. The results suggest that the performance of the films measure on the home-built system are an underestimate compared with the measurements from the commercial system.

2.3.2 Film thickness measurement

The film thickness was obtained using a Veeco DekTak 6 M stylus profiler, which measured, in at least 5 locations, the step height (using contact profilometry technique) between the film and the substrate made by masking the substrate with polyimide tapes.

2.3.3 Electrical resistivity measurement

The electrical resistance of a TEG is directly obtained from a two-probe ohmmeter, while ρ of a thin-film specimen is obtained from an in-house custom four-point probe system. An in-line four-point probe is a typical type of ρ measurement for thin films, in which four probes are collinear with equal spacing between them on the specimen surface. Compared with the two-probe method, the current and voltage electrodes are separated

[5]. As seen in Figure 2.5 (4 point probe), the current is applied to flow through the sample *via* the outer two probes while the inner probes are used to measure the resulting voltage drop across the sample surface. Because of quite high electrical impedance in the voltmeter, there is no current flowing through the inner probes, and thus eliminating the contact and wire resistance contribution onto the measurement results of a voltmeter. Hence, the measured voltage entirely arises from the sample resistance.

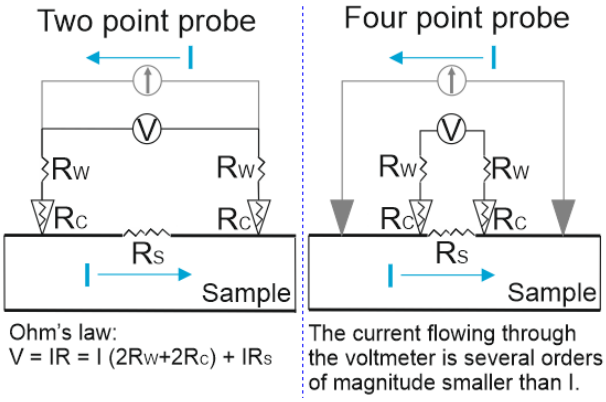


Figure 2.5. *Comparison between the two-point probe and four-point probe.*

The electrical resistivity was calculated using equation (2.1) by the film thickness and the sheet resistance obtained from an in-house custom four-point probe system (measured from 5 different locations). Under applied current of 10^{-2} - 10^{-5} A in the outer two probes, the voltage was measured in two inner probes *via* an Agilent 34420 A Nano Volt/Micro Ohm meter. In this case, the sample size is very large compared to the probe spacing, so the correction of geometry is neglected.

$$\rho = Rs \cdot t = \frac{\pi}{ln2}\left(\frac{V}{I}\right) \cdot t \qquad (2.1)$$

where ρ is electrical resistivity, Rs is sheet resistance, t is film thickness, V is voltage and I is current.

2.3.4 Mechanical test

Tensile tests were conducted to check the mechanical performance of polymer substrates after e-beam or IR radiation (see Chapter 4 & 5). Tensile tests were performed in a

Linkam Scientific TST350 using a 200 N load cell (requiring samples of a dog bone-like shape: width 10 mm × length 20 mm with a semicircle of 2 mm radius in the middle at each side). A dog-bone shape is used to concentrate the stress in the middle section and to avoid failure at the edge of the grips. The measured difference of Young's modulus between the straight sample and the dog-bone shape sample is very small [6].

Buckling tests were conducted to investigate the effect of bending during R2R manufacture and in wearable device operation (see Chapter 4). The buckling test was carried using a rectangle-shape sample (5 mm × 37 mm) in an in-house custom system (Figure 2.6) within the Oxford Seebeck testing apparatus, where the cold-side bulk was moved at a speed of 0.3 mm s^{-1} by a 24 V DC geared motor. The strain applied to the functional coating was affected by the displacement of the cold side which thus was accurately controlled according to a calculation method as reported in [7]. This model calculated the strain considering factors of the displacement, the sample thickness and length. Because the buckling test was built within the Oxford Seebeck system, an *in situ* Seebeck measurement can be acquired during buckling tests. In addition, an automated cycling of buckling was conducted for a number (~ 50 - 140) of cycles.

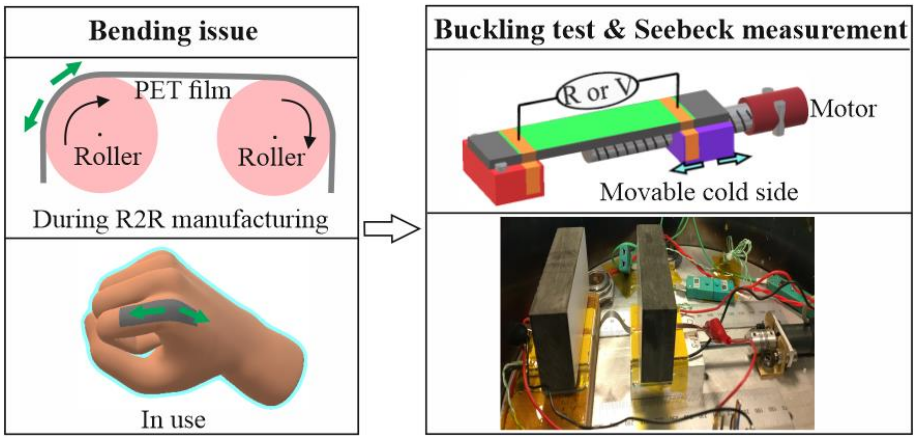


Figure 2.6. *Buckling test.*

2.3.5 Contact resistance measurement

The electrical contact resistance (R_C) at the M-S interface was measured, using the method as reported in [8], in a probe station with two Keithley 2400 source meters (one for applying current; another for voltage measurement). Unlike using a scanning probe as in [8], I selected 10 locations with a fixed distance in metal and semiconductor strips, as shown in Figure 2.7. The R_C was determined from the averaged voltage jump using Equation (2.2).

$$R_c = A \cdot \frac{V_{jump}}{I} \tag{2.2}$$

where A is the contact area between semiconductor and metal (6 mm^2), V_{jump} is the voltage jump between points 3&4 or points 7&8 as shown in Figure 2.7, I is the current applied passing through the element (0.5 mA).

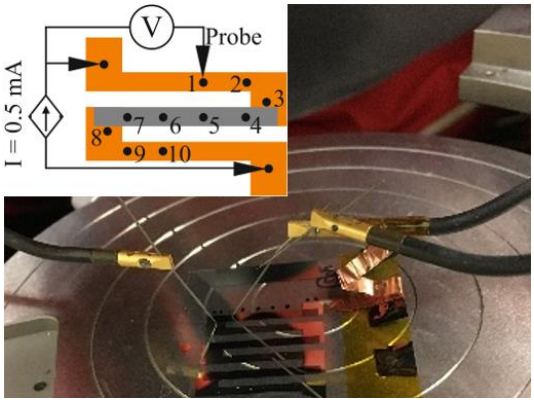


Figure 2.7. *Schematic diagram of contact resistance measurement.*

2.3.6 X-ray diffraction

XRD is a rapid analytical technique for investigating crystalline solids including ceramics, metals, and polymers [9]. X-rays have a correct order of magnitude of wavelength for diffraction by atoms (i.e. a few angstroms, which is the typical interatomic distance in crystalline solids). As x-rays are exposed to crystalline solids, interference happens among the waves scattered by atoms, and a diffracted beam is produced along directions

of constructive interference (i.e. the scattered waves with the same frequency and amplitude overlap one another, Figure 2.8). The constructive interference results in diffraction patterns with the angles of diffraction defined by Bragg's law, equation (2.3). Based on the constructive interference of monochromatic x-rays reflecting off internal crystal planes [10], the arrangement of atoms and atomic spacings can be characterised and thus identifying the phase by comparing the XRD patterns with the reference database in ICDD (International Centre for Diffraction data [11]) because each material has a unique diffraction pattern (i.e. a unique crystalline structure) [12].

$$n\lambda = 2dsin\theta \tag{2.3}$$

where d is the spacing between diffracting planes, θ is the incident angle, n is any integer, and λ is the wavelength of an x-ray beam.

The crystallite size and lattice strain were calculated from the broadening of XRD peaks using the Williamson-Hall method [13] in X'pert Highscore Plus software, with removal of instrumental broadening by assuming a Gaussian profile and using a polycrystalline Si bulk as a standard reference.

$$\beta \cos(\theta) = \frac{K\lambda}{D} + 4\eta sin(\theta) \tag{2.4}$$

where θ is the Bragg diffraction angle, β is the full width of the Bragg peak at half maximum (FWHM), λ is the radiation wavelength (0.154 nm), D is the crystallite size, η is the lattice strain and K is the Scherrer constant (0.91). With the plot of $\beta cos(\theta)$ and $4sin(\theta)$, the slope of fitting line estimates the average lattice strain and the y-intercept estimates the average crystallite size.

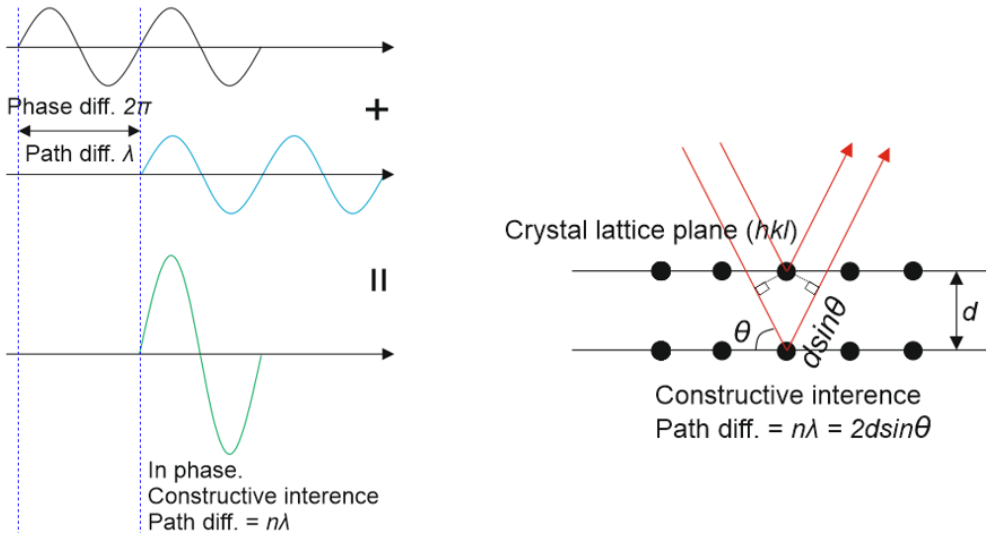


Figure 2.8. *Constructive interference and diffraction of x-rays from planes of atoms in a crystal.*

The crystal-structural analysis of films was performed by x-ray diffraction XRD (Rigaku Miniflex diffractometer) using Cu kα radiation (λ = 0.154 nm) at 30 kV and 30 mA over a range of 2θ between 10° and 80° with a step size of 0.007°.

2.3.7 Atomic force microscope

As a high-resolution type of scanning probe microscopy, AFM can image the objective on the scale of angstrom [14]. In Figure 2.9, the specimen surface is scanned by a cantilever with a sharp tip. As the tip approaches the specimen surface, the cantilever is attracted by the surface, while if the tip approaches too closely there is an increasing repulsive force [15]. The cantilever deflection that arises from these forces, which depends upon the 'stiffness of the cantilever [14]', is detected by a laser beam and the slight direction change of the reflected laser beam is captured by a photodiode to measure the deflection and hence the force between tip and surface. According to the interaction between the tip and the specimen surface, there are typically three-type AFM modes: contact, non-contact, and tapping modes.

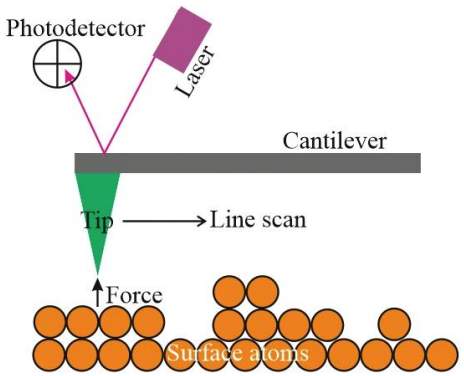


Figure 2.9. *The principle of AFM.*

In this study, AFM (Agilent 5400) using tips (NCHV-A, Bruker Ltd.) in tapping mode was used to analyse the film surface morphology, and to determine the surface roughness of films.

2.3.8 Scanning electron microscope/Energy dispersive x-ray

As a traditional electron microscopy technique, SEM is widely used for the analysis of microstructure morphology and chemical composition characterisations in material science [16]. SEM measurement requires a vacuum chamber to eliminate the interference from air particles. A collimated e-beam is generated from a field emission gun (or a tungsten filament) then apertures and electromagnetic lenses. When the finely focused e-beam scans the specimen surface, various types of signals from the specimen-ebeam interaction volume [17] are constantly emitted and captured by the suitably positioned detectors. Secondary and backscattered electrons are generated by the inelastic collision (scattering of incident electrons with the sample), and elastic collision (i.e. no loss of kinetic energy in the collision), respectively [18]. The detected image depends on the acquisition of signals. The surface topography will change the local interaction volume, so can be analysed from the intensity of signals (e.g. electrons) as detected. SEM requires the specimen to be conductive to avoid sample damage and the charging issue that affects

the SEM image. Hence, for characterising insulator samples, Au coating on the specimen surface is commonly used.

EDX is an analytical technique, typically attached to an SEM, based on the interaction of x-ray excitation and the sample for the elemental analysis or chemical characterisation [19]. In Figure 2.10, as the e-beam hits the specimen, the beam energy is partially transferred to atoms of the sample, causing the electron of an atom to be knocked off from the atom. A hole is generated as the electron leaves and thus attracting electrons from a higher-energy shell. The energy, in the form of an x-ray, is released in this transition. Such energy (i.e. x-ray) is unique for each element, thus can be used to identify the type of elements in the specimen. An EDX result presents the elemental distribution mapping in the specimen as well as peaks in a spectrum corresponding to elements in the sample.

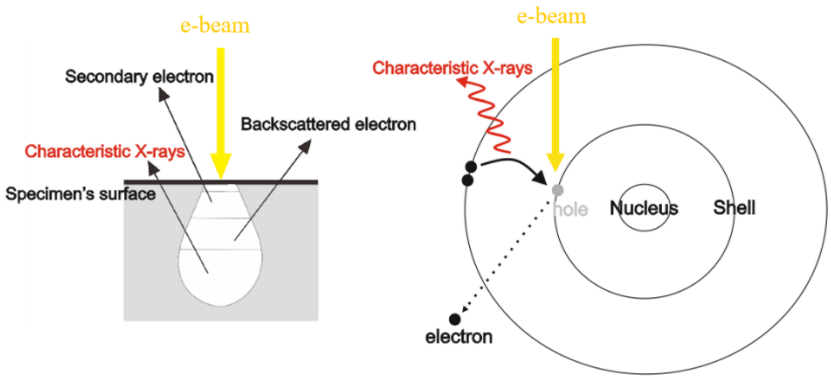


Figure 2.10. *Signals and their regions are generated by e-beam-sample interaction in SEM and x-ray generation process: 1) The energy transferred to the atomic electron knocks it off leaving behind a hole; 2) Its position is filled by another electron from a higher energy shell and the characteristic x-ray is released.*

The surface morphology of thin film was characterised using a field-emission SEM Zeiss Merlin, with 50 k × magnification, 3 kV voltage, 100 pA probe, and 5 mm working distance. The elemental composition was obtained by EDX using point ID mode over 12 independent locations.

2.3.9 UV-Vis spectroscopy

UV-Vis [190 – (400) – 800 nm] spectroscopy measures the attenuation of electromagnetic radiation by an absorbing substance [20]. In material science, it is used for the quantitative measurements of absorbance or reflectance and the characterisation of optical and electronic properties, applicable for metal, semiconductor, and insulator. Electronic excitations or transitions can occur in the UV-Vis range. Single bonding molecular orbitals σ tend to be lower energy than others hence large energy is required to excite electrons to the anti-bonding states (σ* π*). Most of the absorptions (electronic transitions, Figure 2.11) involve π → π*, n→ σ*, and n → π* transitions [21].

Because the energy of orbitals for electronic transitions is quantised, the absorption peak should be sharp. However, that is rare, instead the peaks are broad which should be attributed to the vibrational and rotational energy levels in the absorbing materials [21], giving a combination of overlapping lines and appearing as a continuous absorption band. For example, the energy of UV-Vis photons is absorbed by matter (e.g. semiconductor), the valence electrons are excited and promoted from their ground states to higher energy excited states, hence both electronic and optical properties of the matter can be obtained by the UV-Vis spectroscopy.

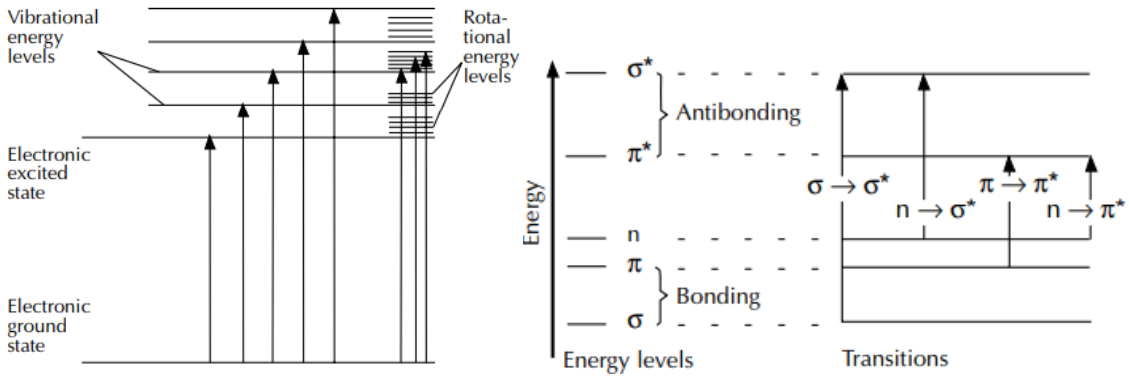


Figure 2.11. *UV-Vis transitions* [21].

E_g of the TE film was obtained from a Tauc plot of the absorbance spectra (200 – 3300 nm wavelength) measured using a Cary Varian 5000 UV-visible-NIR spectrometer. Tauc plot shows the energy of light ($h\nu$) at x-axis and the quantity $(\alpha h\nu)^{1/r}$ at y-axis (where α is the absorption coefficient of the material [$\alpha = 2.303(A/t)$ where A is the absorbance and t is the thickness of sample], h is Planck's constant, ν is the frequency of wave [$\nu = c/\lambda$, where c is the speed of light and λ is the wavelength], the exponent r means the nature of the transition [r = 0.5 for directly allowed transitions and r = 2 for indirectly allowed transitions]).

2.3.10 Fourier-transform infrared spectroscopy

Similarly to UV-Vis, FTIR measures the light absorbed by a specimen. For FTIR light of wavelength 2.5 to 25 μm is absorbed by the vibration of specific molecular bonds.

In this study, FTIR spectra were recorded using a Varian Excalibur FTS 3500 FTIR Spectrometer with attenuated total reflection in the mid IR range 7000 to 350 cm^{-1}, obtaining 16 scans for co-averaged results.

2.3.11 X-ray photoelectron spectrometry

XPS is a surface analytical technique based on the photoelectric effect [22]. The surface of a specimen is irradiated by a beam of x-rays to simultaneously measure the kinetic energy of electrons that are emitted from the top (a few nm) of the sample surface. The energy of the x-ray photon is absorbed by the electron of an atom to enable the electron to escape from the atom and then emit out of the surface. The emitted electron is referred as a photoelectron and a photoelectron spectrum records photoelectron over a range of electron kinetic energies. Peaks in the photoelectron spectrum indicate particular characteristic energy and the corresponding kinetic energy and intensity could be used to identify and quantify elements on the sample surface.

The kinetic energy of photoelectron is determined by the photoelectric-effect equation:

$$E_{kinetic} = hv - E_{binding} - \Phi \quad (2.5)$$

where $E_{kinetic}$ is the measured kinetic energy of emitted electron; hv is the energy of an x-ray with a particular wavelength (typically 1486.7 eV for monochromatic Al Kα x-rays); $E_{binding}$ is the binding energy of electron measured relative to the chemical potential; Φ is the work function for the specific surface of a material and induced by the instrumental analyser.

A ThermoFisher Scientific Al Kα XPS system was used to check the composition/oxidation of metal films, and the position of the valance band of the film (n = 4) using a valence scan by finding the intersection of two linearly fitting lines of the leading edge of the valence band and the flat energy distribution [23]. The work was conducted by Dr. Philip Holdway, Oxford Materials Characterisation Services, Department of Materials, University of Oxford.

2.3.12 Hall effect measurement system/van der Pauw

The purpose of Hall effect measurement is to characterise the carrier concentration (n) and mobility (μ) of TE films. The Hall effect is a generation of a voltage difference (Hall voltage) across an electrical conductor, transverse to an electric current in a conductor when a magnetic field (B) is applied perpendicular to the current [24]. As an electric current is applied to a conductor (Figure 2.12 a), charges follow a curved path because of a B perpendicular to the direction of the current which generates the Lorentz force. Thus, charges accumulate on one side of the conductor causing a potential difference (i.e. Hall voltage). The carrier type of a semiconductor can be represented by the sign of Hall voltage.

Hall coefficient is the ratio of the induced electric field to the product of the applied *B* and the current density.

$$R_H = \frac{V_H t}{IB} = \frac{1}{ne} \tag{2.6}$$

where R_H is Hall coefficient, V_H is Hall voltage; t is the sample thickness; I is the applied current; B is the applied magnetic field; n is the carrier concentration and e is the elementary charge ($1.602176634\times10^{-19}$ C).

Thus, n can be calculated through R_H. In the Hall effect setup (Figure 2.12 a), the measured voltage does not represent the real Hall voltage because it contains three undesirable voltages (errors):

Table 2.II. *Undesirable voltages in Hall effect measurement.*

Errors	**Descriptions**	**Removal**
Misalignment voltage	• Due to imperfect geometry of sample; • Independent of field.	Removed using field reversal by subtraction
Thermal electric voltage	• Due to the effect of temperature; • Independent of current.	Removed using current reversal by subtraction
System noise	• Due to the error of setup.	Error calibration

Thus to eliminate these errors, Hall effect experiments could be conducted by reversing directions of the current and magnetic field.

Table 2.III. *Hall effect measurements ($I_{13\uparrow}$ means applying current from 1 to 3 with a positive magnetic field↑).*

The applied current	The applied magnetic field	The measured voltage
$I_{13\uparrow}$	Positive (↑)	$V_{24\uparrow}$
$I_{31\uparrow}$	Positive (↑)	$V_{42\uparrow}$
$I_{13\downarrow}$	Negative (↓)	$V_{24\downarrow}$

$I_{31\downarrow}$	Negative (↓)	$V_{42\downarrow}$

R equals to the current-reversed resistance in the positive field minus the current reversed resistance in the negative field:

$$R_H = \frac{V_H t}{IB} = \frac{t}{B} R = \frac{t}{B}\left[\left(\frac{V_{24\uparrow} - V_{42\uparrow}}{I_{13\uparrow} - I_{31\uparrow}}\right) - \left(\frac{V_{24\downarrow} - V_{42\downarrow}}{I_{13\downarrow} - I_{31\downarrow}}\right)\right] \tag{2.7}$$

Finally, the calculated R_H can be used to obtain n, see equation (2.6).

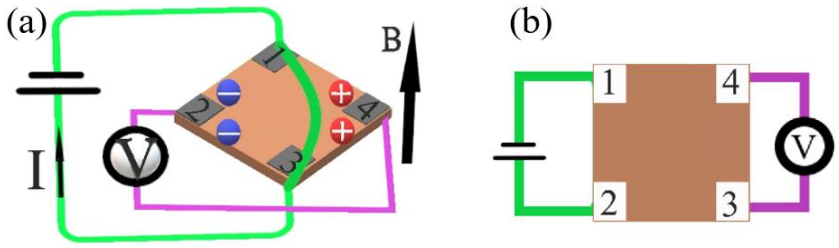


Figure 2.12. *(a) Hall effect measurement and (b) van der Pauw method. (where B is a magnetic field, 1234 are electrical contacts where electrical leads are attached, I is the applied current, V is the measured Hall voltage).*

μ is also of interest in this project which can be calculated by the following equation:

$$\mu = \frac{R_H}{\rho} \tag{2.8}$$

Researchers prefer the van der Pauw method rather than an in-line four-point probe to get ρ because the sample used in van der Pauw can be placed *in situ* for Hall measurements. Besides, the van der Pauw method places four probes around the sample thus measuring the average resistivity of the sample while the in-line four-point probe only measures a resistivity in the direction of probes. In Figure 2.12 b, as the current is applied from 1 to 2 ($I_{1\rightarrow2}$), and the voltage is measured across the opposite edges 3 and 4 ($V_{3\rightarrow4}$), and thus a resistance can be calculated according to Ohm's law. Accuracy and repeatability of measurements are improved by averaging eight measurements that apply an identical current around the periphery of the sample: from 1 to 2, 2 to 3, 3 to 4, 4 to 1, and 2 to 1, 3 to 2, 4 to 3, 1 to 4 with the measured the corresponding voltages between the two corners

at another side [25] (see below). In this case, the correction factor for the sample thickness is 1 (because of the sample thickness/the probe spacing < 10^{-5}), while the geometrical factor is 0.5 [26].

The applied current (I)	The measured voltage
$I_{1\to2}$	V_{34}
$I_{2\to1}$	V_{43}
$I_{2\to3}$	V_{41}
$I_{3\to2}$	V_{14}
$I_{3\to4}$	V_{12}
$I_{4\to3}$	V_{21}
$I_{4\to1}$	V_{23}
$I_{1\to4}$	V_{32}

$$\rho_a = \frac{\pi}{ln2} f_a t \frac{(V_{34}-V_{43}+V_{41}-V_{14})}{4I} \quad \rho_b = \frac{\pi}{ln2} f_b t \frac{(V_{12}-V_{21}+V_{23}-V_{32})}{4I} \Rightarrow \rho_{average} = \frac{\rho_a+\rho_b}{2}$$

Figure 2.13. *Calculation of ρ using van der Pauw method (where $I_{1\to2}$ defines applying a current from 1 to 2 in Figure 2.12 b; t is the sample thickness; f_a and f_b are geometrical factors based on the sample symmetry).*

In this project, Hall effect and van der Pauw measurements were carried out in collaboration with the Semiconductor and Silicon Photovoltaics Group, Department of Materials, University of Oxford. n, μ, and ρ were evaluated for thin films. An in-house custom Hall measurement system (magnet: 0.165 T) with van der Pauw configuration using Keysight Technologies B2901A at RT was used to measure the n and μ of a square-size TE film (1 cm × 1 cm) with an evaporated silver layer (110 ± 5 nm) at the four corners (0.1 cm × 0.1 cm).

2.3.13 Optical profilometer MicroXAM

MicroXAM is a white light scanning interferometer (a non-contact optical method) for surface topographic measurements using the interference effect. Figure 2.14 (top left) shows the optical setup of a MicroXAM. The main components are a coherence light source, a beam splitter, a reference plane and a camera. A simplified setup is displayed in Figure 2.14 (top right). The light toward the beam splitter is divided: one goes to the

reference mirror and another one strikes the sample surface. Lights reflected from the mirror and the sample surface then recombined at the beam splitter and goes toward the camera generating the resulting pattern. The interference effect (Figure 2.14 bottom) occurs when the measurement beam and the reference beam recombine. The optical path difference determines the type (i.e. constructive or destructive) of interference.

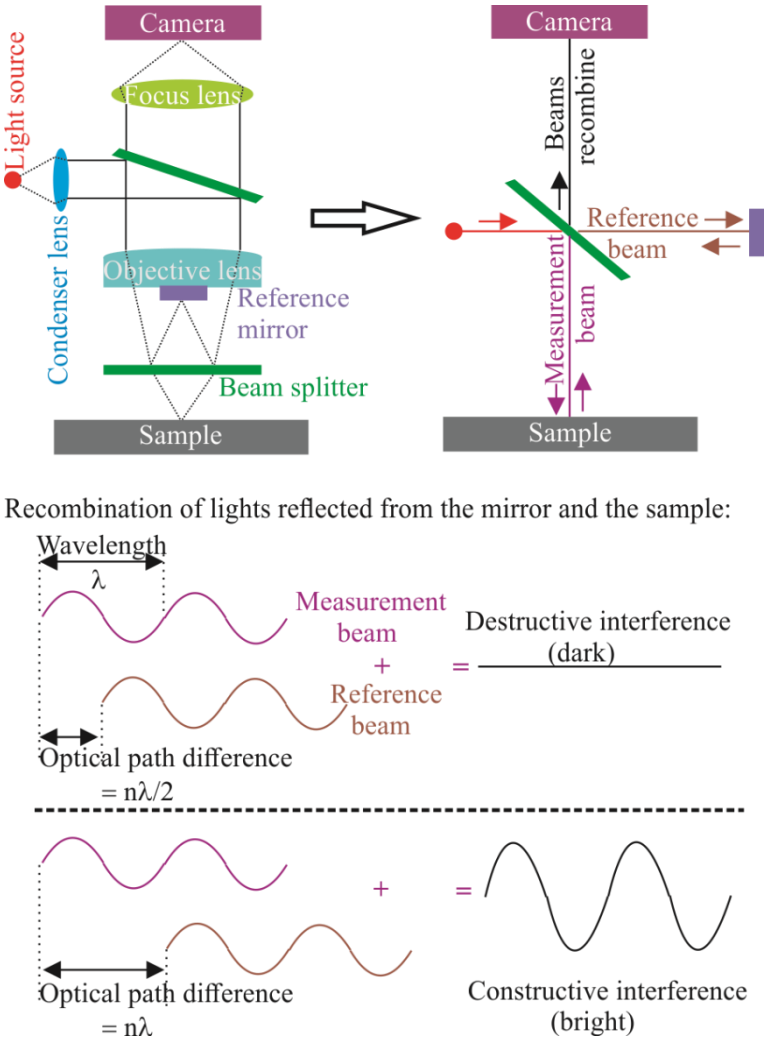


Figure 2.14. *The optical setup of MicroXAM (top left) and a simple white light interferometer (top right), and the theory of interference effect: constructive/destructive interference (bottom).*

In this study, an Omniscan MicroXAM 5000B Optical profiler (Magnification: 50), with a lateral resolution of ~1 μm and a vertical resolution of ~1 nm, was used to characterise the surface morphology of coatings.

2.3.14 Scanning Kelvin probe

Scanning Kelvin probe microscopy measures the local contact potential difference between the scanning tip (typically based on AFM) and the sample surface, thus mapping the surface potential of the sample. In Figure 2.15, as the tip approaches the sample surface (i.e. the distance, *d*, decreases), there is an electrical force generated between the tip and the sample because of the differences in E_F. Under an equilibrium state, the E_F align through the electron current flow, thus both the tip and the sample are charged generating a contact potential difference (V_{CPD}), see Figure 2.15 b. If an external bias (V_{DC}) with the same magnitude but opposite direction to V_{CPD}, this electrical force is eliminated (see Figure 2.15 c). The value of V_{DC} represents the difference of work functions between the tip ($\Phi 2$) and the sample ($\Phi 1$). Hence, the $\Phi 1$ can be calculated if the $\Phi 2$ is known.

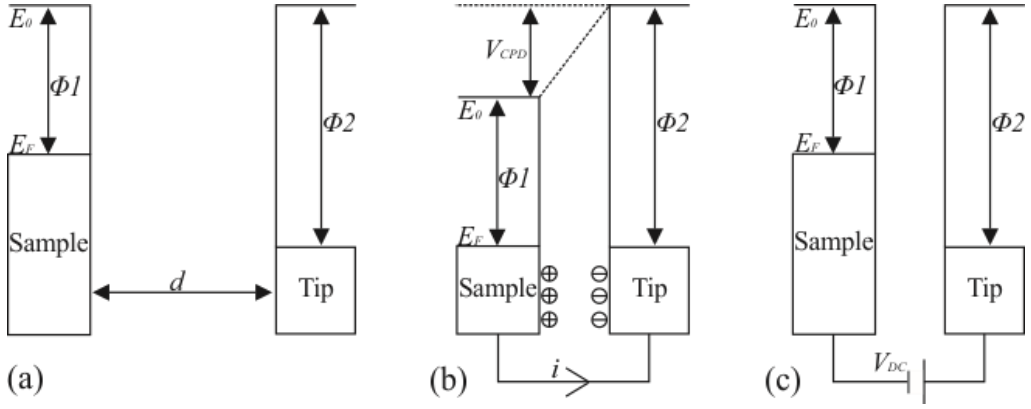


Figure 2.15. *The electronic energy level of the sample and tip for three cases (a) separated with no electrical contact, (b) electrically contacted, (c) external bias applied.*

In this project, the Kelvin probe measurement was done by a PhD student, Daniel Gregory, at Solar Energy Materials Group, Department of Materials, University of Oxford. The Φ of the metal coating was obtained from a KP Technology SKP5050 Scanning Kelvin Probe, with reference electrodes of Au and Al for calibration (average results calculated from 75 arbitrarily chosen points on the film and following a

correlation). The collected relative work functions were then calculated to their absolute work function.

2.6 Summary

This chapter summarises the fabrication methodologies and the characterisation techniques to be used in this project, including the working principle of each technique and the experimental details in this study.

2.7 Reference

[1] Ding, Z.; Abbas, G. A. W.; Assender, H. E.; Morrison, J. J.; Yeates, S. G.; Patchett, E. R.; Taylor, D. M. , Vacuum production of OTFTs by vapour jet deposition of dinaphtho[2,3-b:2′,3′-f]thieno[3,2-b]thiophene (DNTT) on a lauryl acrylate functionalised dielectric surface, *Org. Electron.* 2016*, 31*, 90-97, https://doi.org/10.1016/j.orgel.2016.01.024.

[2] Suarez, F.; Nozariasbmarz, A.; Vashaee, D.; Öztürk, M. C. , Designing thermoelectric generators for self-powered wearable electronics, 2016*, 9*, 299-2113, https://doi.org/10.1039/c6ee00456c.

[3] Hodes, M. , Optimal Pellet Geometries for Thermoelectric Power Generation, *IEEE Transactions on Components and Packaging Technologies.* 2010*, 33*, 307-318, https://doi.org/10.1109/TCAPT.2009.2039934.

[4] Enescu, D. , Thermoelectric Energy Harvesting: Basic Principles and Applications, *Green Energy Advances.* 2019, https://doi.org/10.5772/intechopen.83495.

[5] Panta, G.; Subedi, D. , Electrical characterization of aluminum (Al) thin films measured by using four- point probe method, *Kathmandu University Journal of Science, Engineering and Technology.* 2013*, 8*, 31-36, https://doi.org/10.3126/kuset.v8i2.7322.

[6] Yoshihara, H.; Yoshinobu, M. , Effects of specimen configuration and measurement method of strain on the characterization of tensile properties of paper, *Journal of Wood Science.* 2014*, 60*, 287-293, https://doi.org/10.1007/s10086-014-1398-y.

[7] Chen, Z.; Cotterell, B.; Wang, W. , The fracture of brittle thin films on compliant substrates in flexible displays, *Eng. Fract. Mech.* 2002*, 69*, 597-603, https://doi.org/10.1016/S0013-7944(01)00104-7.

[8] Liu, W.; Wang, H.; Wang, L.; Wang, X.; Joshi, G.; Chen, G.; Ren, Z. , Understanding of the contact of nanostructured thermoelectric n-type Bi2Te2.7Se0.3 legs for power generation applications, *Journal of Materials Chemistry A.* 2013*, 1*, 13093, https://doi.org/10.1039/c3ta13456c.

[9] T. Thilak , Growth and investigation of third order nonlinear optical properties of PUR and doped metal nitroaniline potassium dichromate laslnine single crystal, *B S Abdur Rahman University.* 2015, http://hdl.handle.net/10603/49453.

[10] Cullity, B. D. , Elements of x-ray diffraction, 2001, https://doi.org/10.1107/S0567739479000917.

[11] Zhong Zhan, Y.; Du, Y.; Hong Zhuang, Y. , Chapter four - Determination of phase diagrams using equilibrated alloys, *Methods for Phase Diagram Determination.* 2007, 108-150, https://doi.org/10.1016/B978-008044629-5/50004-5.

[12] Janssens, K.; Van Grieken, R.; Van Grieken, R. , X-ray based methods of analysis - Non-Destructive Microanalysis of Cultural Heritage Materials, 2004, 186-190, https://ebookcentral.proquest.com/lib/[SITE_ID]/detail.action?docID=269523.

[13] Williamson, G. K.; Hall, W. H. , X-ray line broadening from filed aluminium and wolfram, *Acta Metall.* 1953*, 1*, 22-31, https://doi.org/10.1016/0001-6160(53)90006-6.

[14] Vahabi, S.; Nazemi Salman, B.; Javanmard, A. , Atomic force microscopy application in biological research: a review study, *Iranian Journal of Medical Sciences.* 2013*, 38*, 76-83, https://www.ncbi.nlm.nih.gov/pubmed/23825885.

[15] Kudelka, J.; Martinek, T.; Navratil, M.; Kresalek, V. , Quality control in microelectronics using scanning probe microscopy, *2016 21st International Conference on Microwave, Radar and Wireless Communications (MIKON).* 2016, 1-4, https://doi.org/10.1109/MIKON.2016.7492107.

[16] Yi Wang; Vania Petrova , Scanning Electron Microscopy, *In Nanotechnology Research Methods for Foods and Bioproducts (Eds G. W. Padua and Q. Wang).* 2012, https://doi.org/10.1002/9781118229347.ch6.

[17] Zhou, W.; Apkarian, R.; Wang, Z.; Joy, D. , Fundamentals of Scanning Electron Microscopy (SEM), *Scanning Microscopy for Nanotechnology.* 2007, 1-40, https://doi.org/10.1007/978-0-387-39620-0_1.

[18] Joy, D. C. , Beam interactions, contrast and resolution in the SEM, *Journal of Microscopy.* 1984*, 136*, 241-258, https://doi.org/10.1111/j.1365-2818.1984.tb00532.x.

[19] Prasad, P. S.; Sam, J. E.; Kumar, A.; Kannan , The effect of 5% sodium hypochlorite, 17% EDTA and triphala on two different rotary Ni-Ti instruments: An AFM and EDS analysis, *Journal of Conservative Dentistry : JCD.* 2014*, 17*, 462-466, https://doi.org/10.4103/0972-0707.139842.

[20] Brian M. Tissue , Ultraviolet and Visible Absorption Spectroscopy, *In Characterization of Materials, E. N. Kaufmann (Ed.).* 2012, https://doi.org/10.1002/0471266965.com059.pub2.

[21] Royals society of chemistry , UV/visible spectroscopy, , http://www.liskeard.cornwall.sch.uk/images/Liskeard-Sixth-Form/UV-Visible-Spectroscopy.pdf.

[22] Oswald, S. , X-Ray Photoelectron Spectroscopy in Analysis of Surfaces, 2013, https://doi.org/10.1002/9780470027318.a2517.pub2.

[23] Chambers, S. A.; Droubay, T. C.; Kaspar, T. C.; Gutowski, M. S. , Experimental Determination of Valence Band Maxima for SrTiO3, TiO2, and SrO and the Associated Valence Band Offsets with Si(001), *Journal of Vacuum Science and Technology B--Microelectronics and Nanometer Structures, 22(4):2205-2215.* 2004, *22*, https://doi.org/10.1116/1.1768525.

[24] Sun, J.; Kosel, J. , Finite-Element Modelling and Analysis of Hall Effect and Extraordinary Magnetoresistance Effect, 2012, http://dx.doi.org/10.5772/47777.

[25] Tektronix Keithley , Techniques for measuring resistivity for materials characterization, , https://download.tek.com/document/1KW-60826-0_4200AMaterialsAppsGuide.pdf.

[26] I. Miccoli, F. Edler, H. Pfnur and C. Tegenkamp, The 100th anniversary of the four-point probe technique: the role of probe geometries in isotropic and anisotropic systems, http://dx.doi.org/10.1088/0953-8984/27/22/223201

Chapter 3 Exploration of using very thin films to balance the fast roll-to-roll web speed and low vacuum-deposition rate

This chapter explores the issue of vary fast R2R speed against the relatively low vacuum-deposition speed. Specifically, the very thin TE coating is studied to achieve a maximum R2R speed. Besides, an industrial-type PET roll could contain scratches on the surface, so a smoothing acrylate layer is used to smoothen the surface of polymer substrates to examine the TE performance of film grown on it.

3.1 Introduction

Bi_2Te_3 is predicted to be a topological insulator, and has shown topological surface states that are protected by time-reversal symmetry [1, 2]. The expected conducting surface and insulating bulk would theoretically give rise to a linear decrease in ρ with a decrease in the thickness of a film [3]. A range of recent thickness studies [4-8], although not showing a linear relationship with thickness explicitly, do show an increase of resistivity with thickness, as would be expected. A lower ρ benefits *PF*, but the change in *S* with thickness is not established for Bi-Te film sputtered at RT. Materials of very small dimensions are predicted to show significant increases in *PF* due to quantum confinement effects [9]. For example, Mingo *et al.* [10] showed an increase in *PF* of TE nanowires of various materials (InP, GaAs, InAs, and InSb) as the wire thickness became smaller (from 15 nm to a few nm). By far the thinnest Bi_2Te_3 thin-film study, around 18 nm with $S \approx 100$ μV/K, was reported by Rogacheva *et al.* [11] using thermal evaporation onto a hot substrate as the deposition method. This can be compared with a μm thick Bi-Te film ($S \approx 50$ μV/K) fabricated by RF magnetron sputtering [12]. Such a relationship opens up the exciting possibility of improved TE properties for very thin films, which would also have the manufacturing advantage of high deposition throughputs, to keep down the

manufacturing cost. Therefore, in this study, I explore the TE properties of Bi_2Te_3 thin films, particularly down to very thin layers, by RT sputter deposition onto polymer substrates.

3.2 Results and discussion

3.2.1 Film thickness

A series of thin films with varying thicknesses were obtained as shown in Table 3.I. To manufacture ultra-thin films, PET substrates were also placed towards the edge of the drum, i.e. not passing directly underneath the sputter target as the cathode/target is much smaller than the drum's width. This oblique deposition can produce thinner films compared to those passing directly under the sputter target.

Table 3.I. *Bi-Te samples obtained by varying deposition times. The thickness of the thinnest layers '~' are estimated, as they form non-continuous layers. Note that the 'deposition time' is the time that the sample is rotating on the drum during deposition: the time spent under the sputter cathode is substantially less. The film thickness was obtained from the measurements at five different locations.*

Position of target and substrate	**Directly opposite deposition**					**Oblique deposition**		
Deposition time (mins)	10	5	3	2	1	5	3	1
Film thickness (nm)	370	170	100	70	20	55	~33	~11
Standard deviation	3	4	5	3	1	3	-	-

3.2.2 Surface topography

During the initial deposition, grains of the deposited material can form isolated islands on the substrate, depending on the wetting of the substrate [13], and the sputtering power and species mobility [14]. Under deposition onto a heated substrate, Bi_2Te_3 films grow

by a 2D layer-by-layer growth mode [15-17] or a 2D step flow growth mode [18, 19]. The surface roughness should remain constantly that of the substrate for step-flow growth mode. In layer-by-layer growth, the roughness should oscillate between the highest, just before island coalescence in each layer, and the lowest, at the formation of the next integer layer [20]. In contrast, 3D island growth mode is often observed for metal deposition onto polymer substrates at RT e.g. [21, 22]. In this study, I consider the effect of RT deposition with short deposition times and characterise the layers to establish confidently the nature of the first stages of growth of the films in this case. Figure 3.1 shows the surface morphology for Bi-Te films grown by RT sputtering. AFM images reveal a process of the initial small islands combining to form larger, subdivided, grains. The line profiles show how the islands of deposition become taller and merge as more material is deposited. The root mean square roughness (RMSR), as shown in Figure 3.2, provides a simple quantification of this effect. The thinnest films are deposited through oblique deposition: the 1-min sample shows a significantly higher RMSR than the uncoated substrate because the film is partially coated with islands of coated material protruding a couple of nm above the uncoated substrate surface leading to an increase in roughness over that of the substrate, while after 3-min coating the islands are impinging, giving rise to an overall slightly smoother surface which then roughens again as the film thickens further after 5 minutes deposition. These cannot be compared directly to the samples mounted directly opposite the target as the angle of deposition may influence the morphology and properties, but from the samples mounted directly opposite the target, it is clear that as the film thickness grows further, the surface roughness then increases, as previously reported for island-growth mode [23].

For the shortest deposition times, therefore, the layers may not form a complete coating with the islands fully impinged. To further examine this, both SEM and AFM phase

images are obtained for a 1-min coating (Figure 3.3), as contrasted with a much thicker layer (5-min deposition sample) that is expected to form a complete layer. SEM images clearly demonstrate the morphological difference of films under different thicknesses. Unlike the big grains observed in the thick film, the 1-min coating shows a small-island structural morphology. The AFM phase image strongly suggests an island-growth period for a 1-min coating due to the strong contrast between the coating and the relatively compliant substrate. The acrylate layers will tend to smooth over the larger-scale defects on the polymer substrate to smooth the film (Figure 3.2 a). The relationship between RMSR and the film thickness is summarised in the schematic in Figure 3.2 b. At a very high film thickness, the film surface roughness is assumed to tend towards some equilibrium value (dashed line).

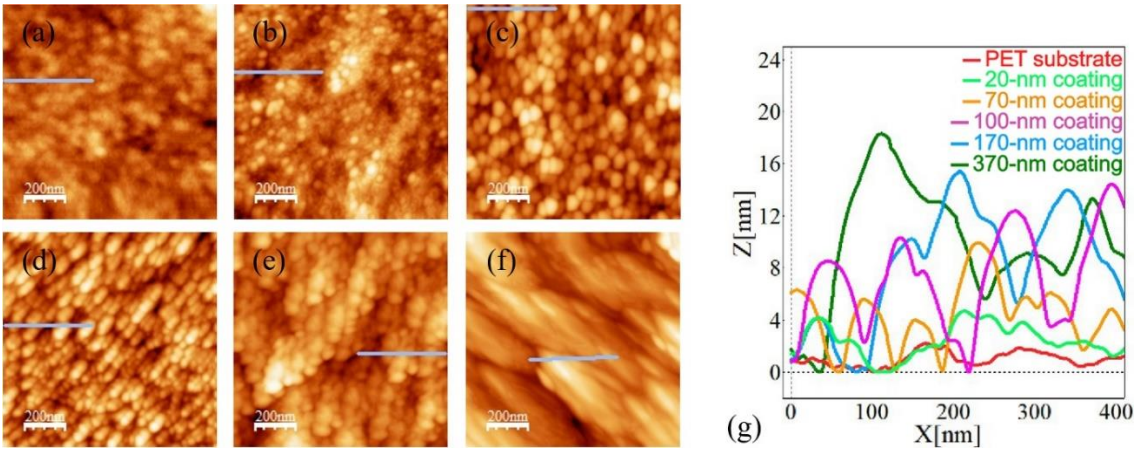
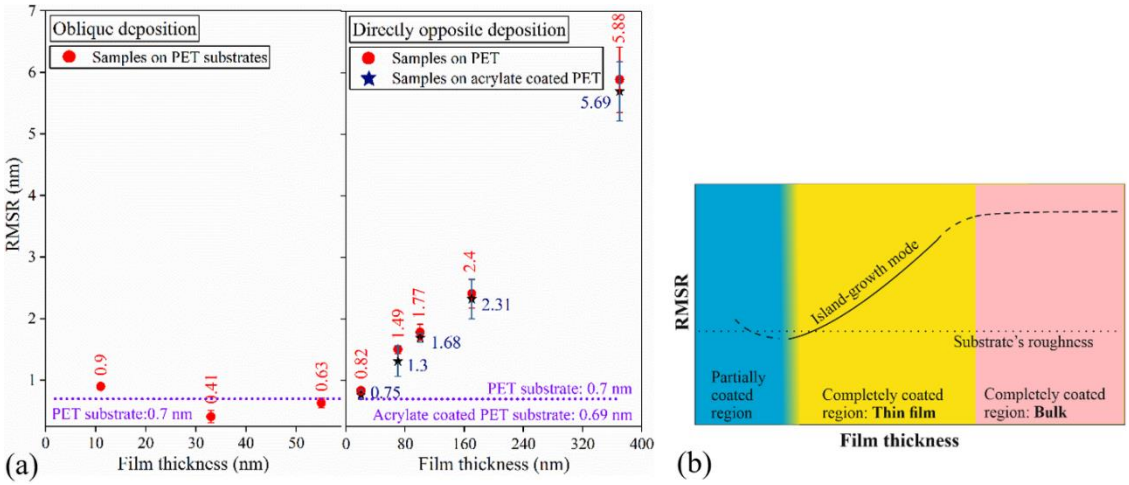


Figure 3.1. *(a-f) AFM topography images and (g) example line profiles (from positions indicated by grey lines in the images) with the image size of 1μm×1μm for Bi-Te films deposited directly opposite the target: (a) the polymer substrate, (b) 1-min coating, (c) 2-min coating, (d) 3-min coating, (e) 5-min coating, (f) 10-min coating.*

Part A



Part B

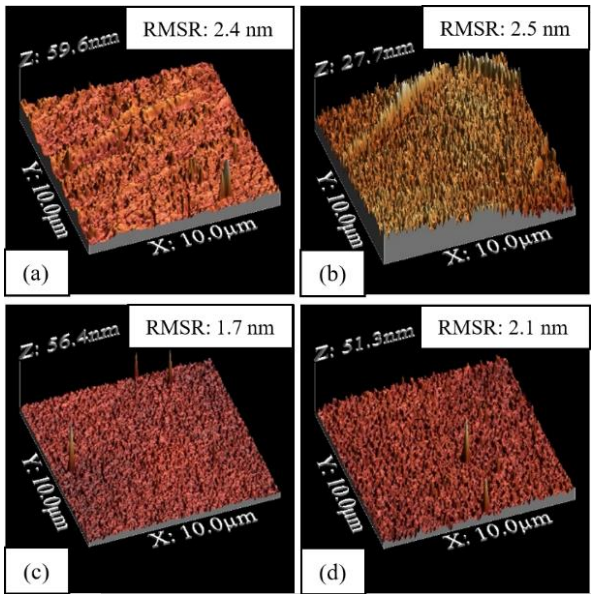


Figure 3.2. *Part A: (a) RMSR of Bi-Te films (The error bars represent a standard deviation, which are obtained from at least eight 1μm×1μm images); (b) Schematic of the variation of RMSR with the thickness of films grown by RT sputtering (The solid line is analysed from the experimental results, while the dashed line is estimated. The dotted line indicates the roughness of the substrate). Part B: AFM images of substrates and coatings: (a) PET substrate; (b) films on PET substrates; (c) acrylate smoothing layer on PET substrates; (d) films on acrylate substrates. (RMSR is average roughness from three different locations, with standard deviations of ~ ± 0.1 nm).*

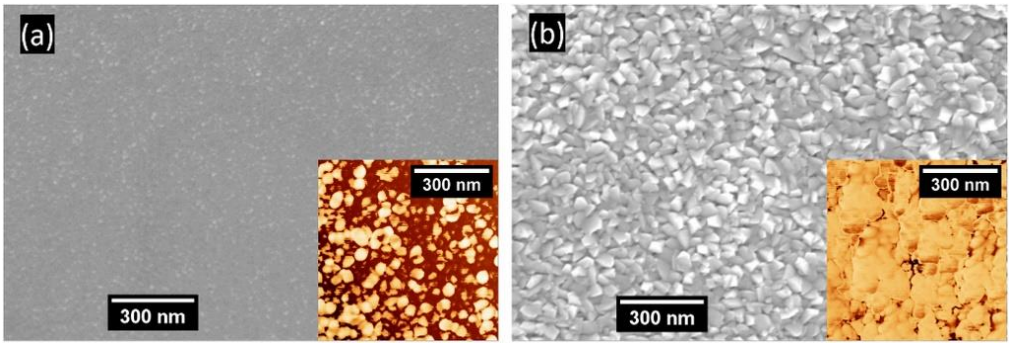


Figure 3.3. *SEM images and AFM phase images (inset) of (a) 1-min and (b) 5-min films deposited directly opposite the target.*

To decrease the effect of scratches on the industrial PET sheet, an acrylate layer (600 ± 30 nm) is considered to smoothen the substrate's surface. From AFM images in Figure 3.2, an acrylate layer, which is easily achieved R2R in vacuum, and hence could be formed in the same process as the Bi-Te layer, can help smoothen scratches on PET sheets, hence there are no scratches on the film that coated on acrylate substrates. For 10×10 μm^2 images, RMSR of the acrylate-smoothed substrate is much lower than that of blank PET substrate because most scratches on PET sheets are covered and smoothened by acrylate layers. Therefore, the acrylate-smoothed substrate is desirable when typical, low-cost polymer substrates are used (NB for the other devices reported in this thesis a high-quality smooth PET supplied in single A4 sheets is used to minimise any influence of substrate roughness). The next thing is to find out the effect of smoothing layers on electrical properties and TE behaviours, particularly for very thinner layers.

3.2.3 Elemental composition

When considering the properties of a layer as a function of thickness it is important to consider any possible change in stoichiometry. Figure 3.4 shows a change in elemental ratio, as measured by EDX, of Te and Bi with deposition time (i.e. the film thickness). All the as-deposited films were found to be Te-rich compared to the sputtering target as reported elsewhere [24], in this case for RF sputtering, where for high powers Te content

could reach as high as 90%. An off-stoichiometric Bi-Te film does not directly produce poor TE properties because the excess Te content acts as a major source of e^- donors [25]. The Te: Bi ratio changes with thickness (Figure 3.4) as the Te content decreases with thickness. The reasons could be (1) there is a different sticking coefficient of Bi and Te to the substrate, giving a rise in Te near the interface which is averaged over the different thicknesses as measured by the penetration depth of the EDX. (2) time spent passing under the sputter target (i.e. deposition time) may result in preferential removal of one element from the coating [26]. Such etching process could be either from the plasma region or from the high energy backscattered Ar neutrals from the sputter target. It is expected that the Te atoms in the film will be preferentially removed due to its poorer binding energy, smaller atomic size, and atomic mass. (3) the preferential removal of Te could also happen on the Bi_2Te_3 target for the initial sputtering process i.e. the Te is the first to be removed from the sputter target at the initial stage.

The effect of stoichiometry on electrical properties is worth considering for the Bi-Te films. Goncalves *et al.* [27] carried out a stoichiometric study of Bi_2Te_3 films and found that, at low-temperature deposition (in their case by evaporation), as the Te content of the film increases in the approximate range of Te: Bi ratio 1.5-2.5, the magnitude of S decreases and ρ increases leading to a decrease in PF. However, my results are the reverse of their observation. Goncalves *et al.* used a constant film thickness, so the reversed trend with stoichiometry suggests that the origin of the change in electrical behaviour observed here is the variation in film thickness and/or morphology, not the stoichiometry. Although the difference in deposition method may preclude a direct comparison with Goncalves' films, my measurements of carrier concentration (Figure 3.9 a) also suggest that stoichiometry is not a dominant effect: I would expect to see a significant increase in

carrier concentration with Te content [25], but in this case, the thinnest sample has both the greatest Te content and lowest carrier concentration.

Due to sputtering under a high vacuum condition (rather than an ultra-high vacuum), oxygen impurity in the film is of concern, e.g. acting as a dopant [28]. Since the interaction depth of SEM is larger than the film thickness, measuring oxygen content by EDX in the film means that oxygen signals from the polymer substrate cannot be avoided. A high oxygen content (7 at.% to as much as 54 at.% for the thinnest films) is detected in samples on the polymer substrate. Hence, I made Bi-Te films on a Si wafer for EDX analysis, and no oxygen signal was detected from these samples on Si. However, it is noted that oxygen reading could be within the noise background and detection of EDX for a light element such as oxygen is poor. In addition, since the TE performance of the fabricated films is consistent with [12, 29], oxygen is not an overriding influence on the film even with these more modest vacuums, and the trends with thickness reported here are unlikely to be explained by the oxygen content.

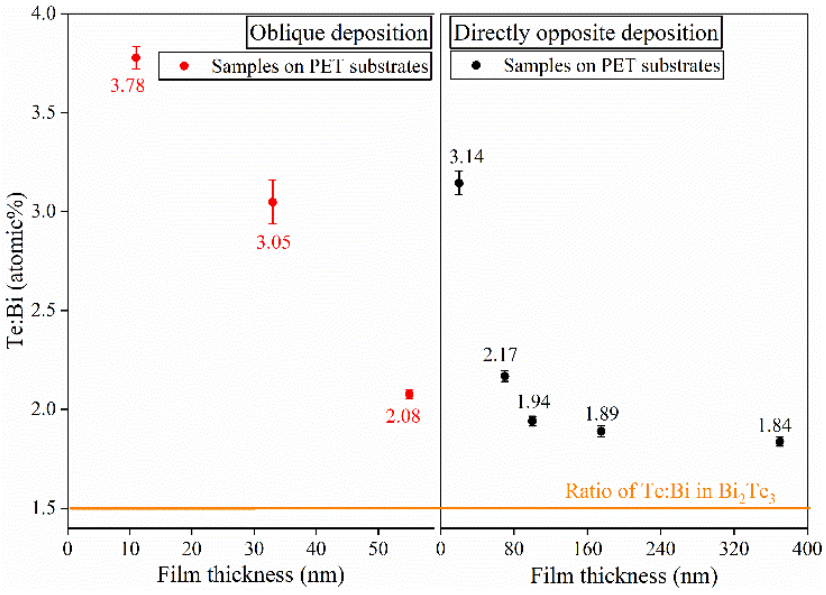


Figure 3.4. *Elemental ratio of Te and Bi as a function of deposition time (The error bars are standard error from at least six independent points in six different locations on a large-area sample).*

3.2.4 Thermoelectric parameters

3.2.4.1 Electrical resistivity

The variation of ρ, *S,* and *PF* as a function of film thickness has been measured (Figure 3.5). Both Seebeck and Hall measurements confirm all the films to be n-type. Both deposition conditions show a sharp increase in ρ for the very thinnest films, commensurate with islands of material not fully connected to one another. Under this condition, any conductivity is due to a small number of paths of connectivity between the islands, with poorly conducting, disordered, or extremely thin/no material between. Dheepa *et al*. [30] concluded that the resistivity of Bi-Te films deposited at RT, as a result of island-growth, depended upon the tunnelling of charge carriers between the islands once they were separated by only a few angstroms, but for the thinnest layers, where there are relatively few such connections, the resistivity would sharply increase in layers that are not made up of fully impinged islands. A sharp increase in resistance for very thin films observed in PbTe thermoelectric layers [31] was similarly linked to percolation and linking of islands of material as the amount of deposited material increased.

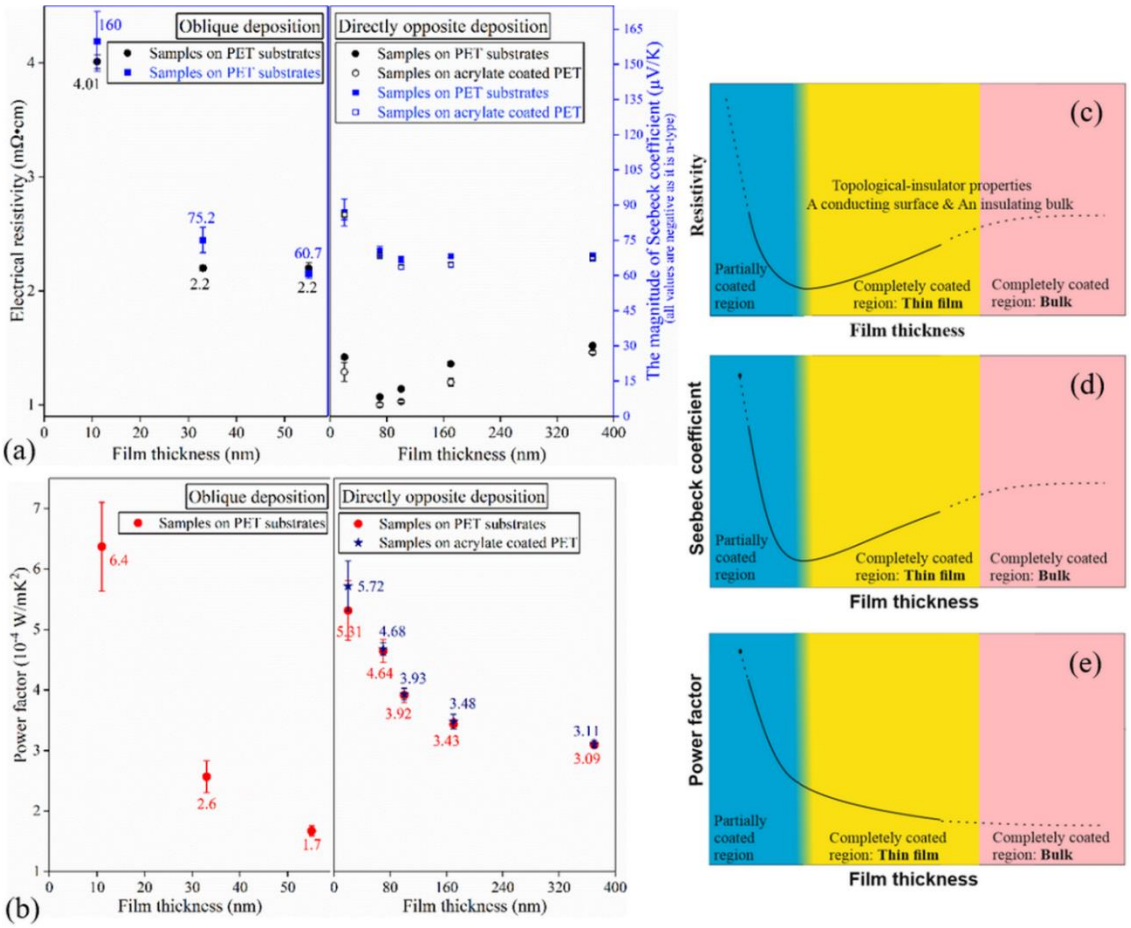


Figure 3.5. *Plots of ρ, S (a) and PF (b) for Bi-Te films with various deposition time, and schematic representations of the relationship between film thickness and ρ (c), S (d), and PF (e) (The solid lines are analysed from the experimental result, while the dashed lines are estimated. The error bars are the standard deviation of at least six and three measurements at different locations for S and ρ, respectively).*

After a complete layer is formed, ρ gradually increases in an approximately linear fashion, as represented in Figure 3.5 c, as would be expected for a topological insulator until such thickness as the overall resistivity reflects that of the bulk. Changes in conductivity might also be influenced by changes in the contact with the four-point probe as the topography and morphology change, or changes in carrier mobility as a function of grain size [32] and degree of crystallinity [30, 33].

3.2.4.2 Seebeck coefficient

The relationship between *S* and film thickness can be described as illustrated in Figure 3.5 d. *S* is observed to increase sharply for the thinnest layers as was also observed for PdTe [31]. In this region, the film thickness is small compared to the Bohr exciton radius of Bi_2Te_3 (57 nm [34]). Indeed the E_g, as determined by Tauc plots from UV-Vis data (Figure 3.6), is seen to increase significantly for the thinnest films, as would be expected from the effect of quantum confinement. A greater E_g would be associated with a lower density of charge carriers (from intrinsic carrier generation) for a given temperature, which is expected to increase *S*. Quantum confinement in one dimension (for a thin film) would also lead to a change in density of states near the Fermi level which would change TE performance, and Dmitriev *et al.* 2010, [35] ascribed the higher *PF* for thinner nanowires (confinement in two dimensions) to sharp features in the density of states resulting from the effect of quantum confinement. However, the trends in *S* and E_g observed do not correlate well (i.e. the increase in *S* is only observed for deposition time less than 3 mins), so this is not shown to be the primary explanation. The effect of barrier scattering should also be considered, which is established as a reason for larger *S* in thin films than bulk samples [36, 37]. This scattering arises from potential barriers in the material, such as at grain boundaries, which stop the carriers of lower energy, thus increasing *S*.

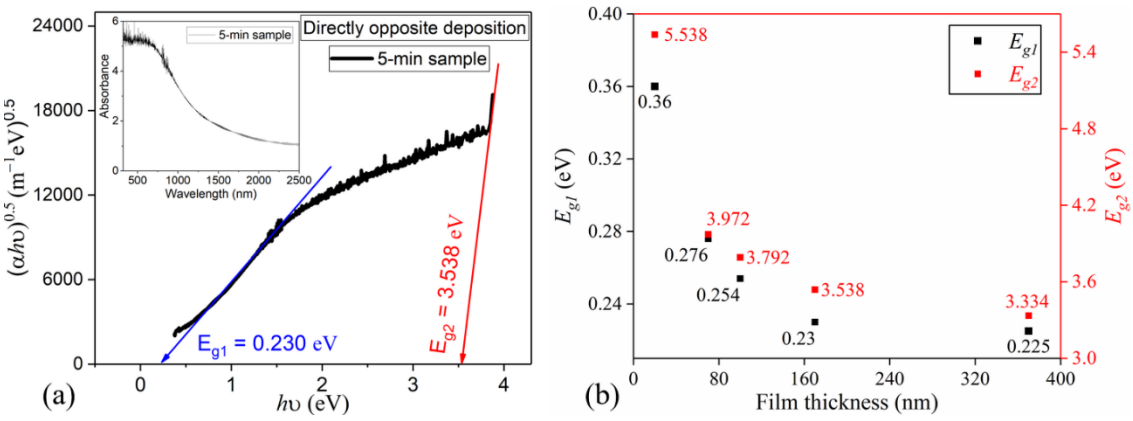


Figure 3.6. *(a) Tauc plot of Bi-Te films under 5-min opposite deposition with (inset) corresponding absorbance spectra (where α is absorbance coefficient, hv is photon energy). The primary E_g is observed at around 0.23 eV, similar to other reports* [38-41] *and a second E_g is seen corresponding to a gap of 3.54 eV that has been reported by* [42]*; (b) The variation of two types of E_g as a function of deposition time/film thickness.*

The thinner films will have fewer high-quality connections between grains (good conducting material), with potentially poorly ordered material between (which would serve as a potential barrier). In this study, the XRD measurement was not obtained because the film is too thin to obtain sufficient signal (the signal from the polymer substrate is too strong), however, the room-temperature sputtered Bi-Te film is not expected to be highly crystalline [33].

To explore the crystallinity of Bi-Te film that grows under RT, a very thin (~80 nm) Bi-Te film grown on Si wafer and a thick (~1 μm) film grown on polymer substrate were fabricated/characterised using XRD, as shown in Figure 3.7. Besides, a very thin film (~70 nm) was directly deposited onto lacey carbon-supported copper grids (300 mesh, Agar Scientific) to be characterised in TEM (this was conducted by a PhD student in the group, Botao Hao). High-resolution TEM (HRTEM) and fast Fourier transform (FFT) images are analysed (Figure 3.8), in which four d-spacings (0.3282, 0.2357, 0.2025, and 0.1498 nm) are identified and a polycrystalline structure can be observed. XRD confirms these d-spacings in the ~1-μm thick Bi-Te film (Table 3.II), corresponding to miller indices of (0 1 5), (1 0 10), (1 1 6) and (1 1 15), respectively. The HRTEM result here indicates that the very thin Bi-Te film is also crystallised. However, the XRD profile of the ~80-nm thick Bi-Te film does suggest a poor crystallinity even though it is crystallised.

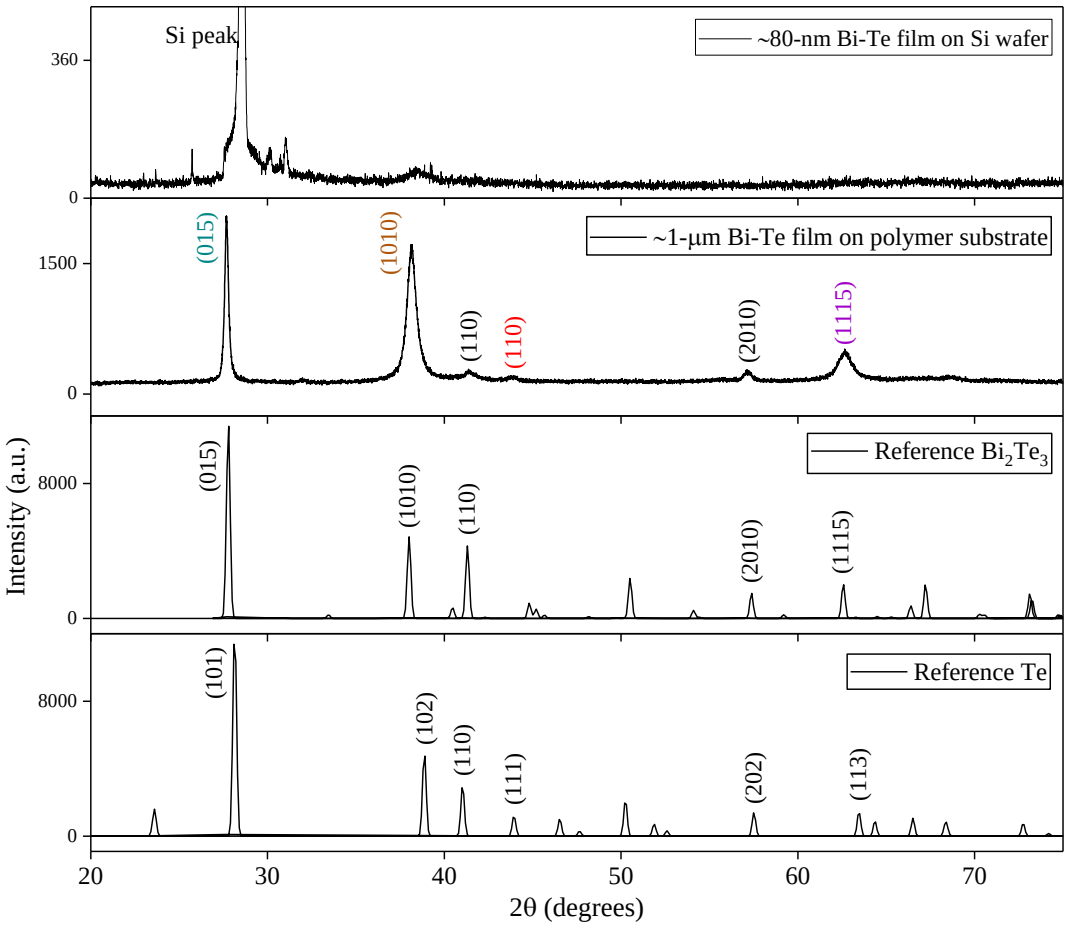


Figure 3.7. *XRD pattern of ~80-nm film grown Si wafer and ~1-µm Bi-Te film grown on polymer substrate, with the references of Te (ICSD #40042) and Bi2Te3 (ICSD #193330) powders.*

Table 3.II. *XRD details of a ~1-µm thick Bi-Te film (where FWHM and Rel. Int. are the full width at half maximum and relative intensity of diffraction peaks, respectively).*

Position [°2θ]	Height [counts]	FWHM Left [°2θ]	d-spacing [Å]	Rel. Int. [%]
27.69	1704.06	0.51	3.220	100.00
37.96	467.79	0.71	2.368	27.45
41.14	379.49	0.77	2.192	22.27
44.85	67.80	0.85	2.019	3.98
57.24	81.74	1.12	1.608	4.80
62.51	94.31	1.24	1.485	5.53

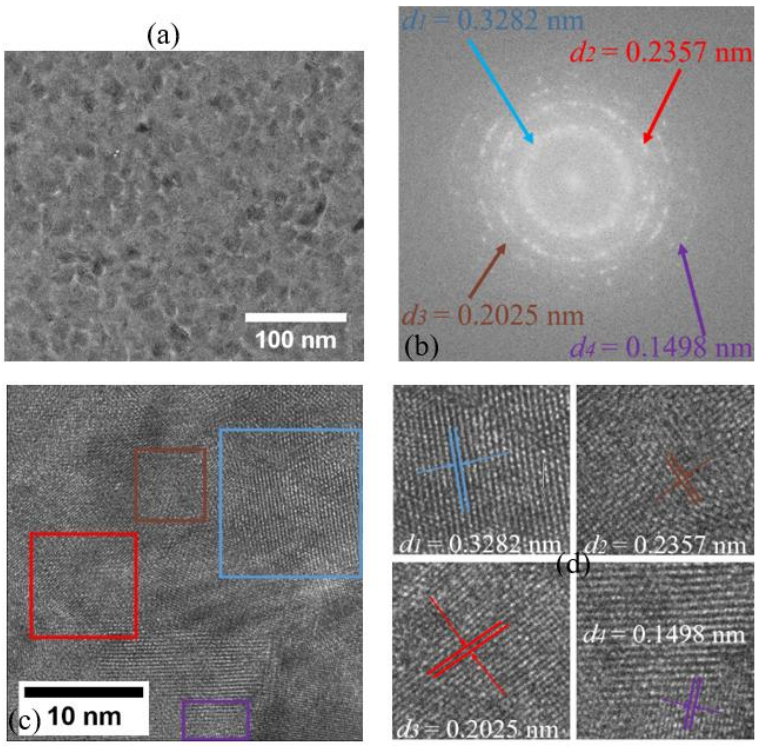


Figure 3.8. *(a) TEM image of Bi-Te film; (b) TEM diffraction pattern of a Bi-Te film; (c-d) HRTEM images of a Bi-Te film. (TEM was conducted by a PhD student in the group: Botao Hao.)*

In the thinnest, partially coated, films, the material relies on a relatively low number of percolation pathways for conduction, and the intimate, ideal, electronic connection between neighbouring grains will not be made in many cases, thus a relatively large proportion of the moving charge will need to pass through higher potential barriers. To describe it in another way, the thinnest layers might be considered as an incomplete layer of a nanocomposite material of Bi-Te with inclusions of poor quality/no/high Te/oxidized-phase material between that would serve to give an energy filtering effect, stopping the low energy carriers, as above, as reported for nanocomposites [43, 44]. Thus, *S* increases as the carrier concentration decreases (the inverse relationship between *S* and the carrier concentration has been reported by many studies [35, 45, 46]).

As a continuous layer is formed for thicker films, the carrier pathways become multitudinous (continuous) and so the sample no longer depends on such, imperfect,

connections, as good connectivity between the better-quality material will be much more common with a reduction or removal of the carrier filtering effect.

3.2.4.3 Carrier concentration and mobility

The measured carrier concentration and carrier mobility taken from Hall measurements, Figure 3.9, do confirm a very substantial decrease in carrier concentration for the thinnest layer (i.e. an incomplete layer with inclusions of poor quality/no/high Te/oxidized-phase material acting as energy barrier), due to the carrier filtering effect. The trends for thicker films, observed in both carrier concentration and mobility do give rise to an increase in resistivity with deposition time, as observed in Figure 3.5, and are expected to be influenced by stoichiometry (doping: increased Te doping in the thinner films is a source of electron donors [25]; oxygen doping could increase TE performance [28]), and grain size and crystallinity (larger grains [40, 42, 47] and better crystallinity [33] have been observed in thicker layers). The observed decrease in carrier concentration (Figure 3.9 a) with increased deposition time for the thicker films is consistent with the observed increase in *S* (Figure 3.5 a).

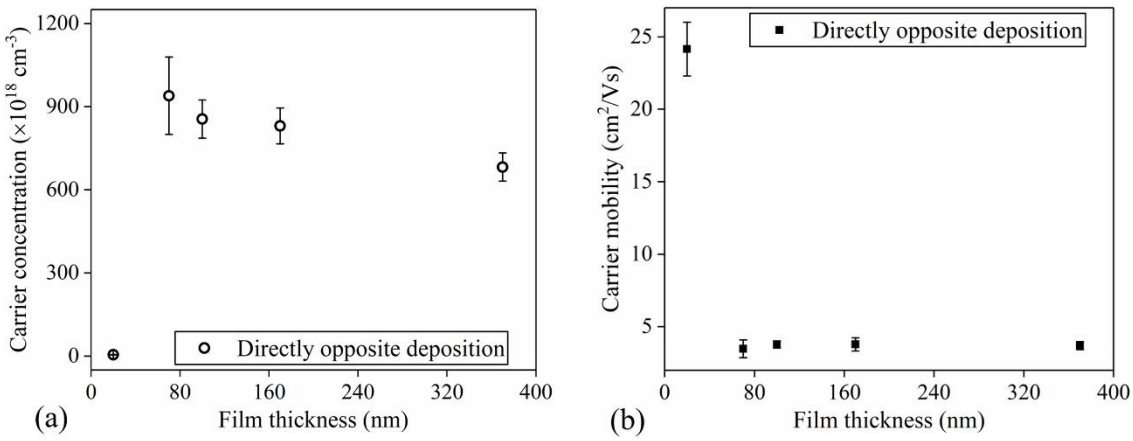


Figure 3.9. *Variation of (a) carrier concentration and (b) carrier mobility of Bi-Te films as a function of sputtering time i.e. film thickness (The error bars represent a standard error, which are obtained from three measurements).*

3.2.5 Thermoelectric behaviour: Power factor

The samples deposited directly opposite the target show much better *PF* (product of S^2 and σ) than those deposited obliquely, even when in the same range of thickness, because of their lower ρ but higher *S*. This can be attributable to a difference in the morphology (e.g. RMSR), uniformity and potentially stoichiometry of films deposited at different positions on the drum. Those films deposited on acrylate-coated PET have better *PF* than those deposited directly onto PET: the acrylate layer helps to smooth over scratches and other micro-scale defects on the PET surface that are likely to break the carrier's percolation path, as is reflected in their lower resistivity. It is noted that the effect of acrylate smoothing layer on *PF* (Figure 3.5 b) is more obvious for a thinner Bi-Te film but even then, it only makes a small difference on *PF*.

I have observed that very thin Bi-Te films exhibit better *PF* behaviour (Figure 3.5 b). This is significant and encouraging, given that very thin layers are favoured for high-throughput manufacture. This is the first such study for very thin Bi-Te films grown at RT in moving web deposition. From the experimental result, the relationship between *PF* and the film thickness is proposed as shown in Figure 3.5 e. The competition between the change in ρ and the change in *S* is the key. In the completely coated region, *PF* increases as the film becomes thinner because the decrease in ρ is larger, hence the change in ρ dominates the change in *PF*. In the partially coated region, *PF* increases as the film becomes thinner because the change in *S* dominates the change in *PF*. Hence the coupling between ρ and *S* is different for the thinnest layers due to the different mechanisms involved, giving rise to the relatively high *PF* observed for the thinnest layer.

3.3 Summary

An experimental study has been carried out to investigate the TE behaviour of RT-sputtered Bi-Te thin films on polymer substrates in the thickness range of a few nm – 370

nm. AFM analysis revealed an island-growth mode of Bi-Te films deposited at RT by DC magnetron sputtering. ρ was found to be the lowest as a complete coating is formed, and an almost linear relationship between ρ and the film thickness was observed thereafter, as expected for topological-insulator films. In addition to a possible low-dimensional quantum confinement effect, an energy barrier mechanism was proposed to explain the extremely high *S* at the partially coated region. The island-growth behaviour observed in these RT-deposited layers facilitated forming coatings which showed this energy barrier effect, as the layer-by-layer growth reported for high substrate temperature deposition would tend to give rise to good connectivity across the layer. *PF* was shown to increase substantially in very thin films, which has been explained by a quasi-decoupling of *S* and ρ. Therefore, both a high deposition throughput and a high *PF* could be fulfilled by using very thin TE materials, giving a boost to the commercialisation of flexible TEGs even though the film sputtered at room temperature under high vacuum level is not highly crystallised and possibly involves oxidized phases resulting from sputtering at such vacuum level (not an ultra-high vacuum level). The film surface features were improved by applying an acrylate smoothing layer to the substrate which could enhance the power factor by improving the electrical resistivity of films.

3.4 Reference

[1] Wang, G.; Zhu, X.; Sun, Y.; Li, Y.; Zhang, T.; Wen, J.; Chen, X.; He, K.; Wang, L.; Ma, X.; Jia, J.; Zhang, S. B.; Xue, Q. , Topological insulator thin films of Bi2Te3 with controlled electronic structure, *Advanced Materials (Deerfield Beach, Fla.).* 2011*, 23*, 2929-2932, https://doi.org/10.1002/adma.201100678.

[2] Zhang, H.; Liu, C.; Qi, X.; Dai, X.; Fang, Z.; Zhang, S. , Topological insulators in Bi2Se3, Bi2Te3 and Sb2Te3 with a single Dirac cone on the surface, *Nature Physics.* 2009*, 5*, 438-442, https://doi.org/10.1038/nphys1270.

[3] Barua, S.; Rajeev, K. P. , Status of surface conduction in topological insulators, *AIP Advances.* 2014*, 4*, 017135-6, http://dx.doi.org/10.1063/1.4864058.

[4] Analytis, J. G.; Chu, J.; Chen, Y.; Corredor, F.; McDonald, R. D.; Shen, Z. X.; Fisher, I. R. , Bulk Fermi surface coexistence with Dirac surface state inBi2Se3: A comparison of photoemission and Shubnikov–de Haas measurements, *Physical Review B.* 2010*, 81*, https://doi.org/10.1103/PhysRevB.81.205407.

[5] Taskin, A. A.; Ren, Z.; Sasaki, S.; Segawa, K.; Ando, Y. , Observation of dirac holes and electrons in a topological insulator, *Physical Review Letters.* 2011*, 107*, 016801, https://doi.org/10.1103/PhysRevLett.107.016801.

[6] Kim, Y. S.; Brahlek, M.; Bansal, N.; Edrey, E.; Kapilevich, G. A.; Iida, K.; Tanimura, M.; Horibe, Y.; Cheong, S.; Oh, S. , Thickness-dependent bulk properties and weak antilocalization effect in topological insulator Bi2Se3, *Physical Review B.* 2011*, 84*, https://doi.org/10.1103/PhysRevB.84.073109.

[7] Bansal, N.; Kim, Y. S.; Brahlek, M.; Edrey, E.; Oh, S. , Thickness-independent transport channels in topological insulator Bi2Se3 thin films, *PhysRevLett.* 2011, https://doi.org/10.1103/PhysRevLett.109.116804.

[8] Xia, B.; Ren, P.; Sulaev, A.; Liu, P.; Shen, S.; Wang, L. , Indications of surface-dominated transport in single crystalline nanoflake devices of topological insulator Bi1.5Sb0.5Te1.8Se1.2, *Physical Review B.* 2013*, 87*, https://doi.org/10.1103/PhysRevB.87.085442.

[9] Osterhage, H.; Gooth, J.; Hamdou, B.; Gwozdz, P.; Zierold, R.; Nielsch, K. , Thermoelectric properties of topological insulator Bi2Te3, Sb2Te3, and Bi2Se3 thin film quantum wells, *Applied Physics Letters.* 2014*, 105*, 123117, https://doi.org/10.1063/1.4896680.

[10] Mingo, N. , Thermoelectric figure of merit of II-VI semiconductor nanowires, *Appl. Phys. Lett.* 2004*, 85*, 5986-5988, http://dx.doi.org/10.1063/1.1829391.

[11] Rogacheva, E. I.; Budnik, A. V.; Nashchekina, O. N.; Meriuts, A. V.; Dresselhaus, M. S. , Quantum Size Effects in Transport Properties of Bi2Te3 Topological Insulator Thin Films, *Journal of Electronic Materials.* 2017*, 46*, 3949-3957, http://dx.doi.org/10.1007/s11664-017-5561-2.

[12] Singkaselit, K.; Sakulkalavek, A.; Sakdanuphab, R. , Effects of annealing temperature on the structural, mechanical and electrical properties of flexible bismuth telluride thin films prepared by high-pressure RF magnetron sputtering, *Ansn.* 2017*, 8*, 350021-350027, https://doi.org/10.1088/2043-6254/aa7222.

[13] Lazzari, R.; Jupille, J. , Silver layers on oxide surfaces: morphology and optical properties, *Surface Science.* 2001*, 482-485*, 823-828, https://doi.org/10.1016/S0039-6028(01)00935-9.

[14] Je, J. H.; Kang, T. S.; Noh, D. Y. , Epitaxial and island growth of Ag/Si(001) by rf magnetron sputtering, *Journal of Applied Physics.* 1997*, 81*, 6716-6722, https://doi.org/10.1063/1.365213.

[15] Liu, H. W.; Yuan, H. T.; Fukui, N.; Zhang, L.; Jia, J. F.; Iwasa, Y.; Chen, M. W.; Hashizume, T.; Sakurai, T.; Xue, Q. K. , Growth of topological insulator Bi2Te3 ultrathin films on Si (111) investigated by low-energy electron microscopy, *Crystal Growth & Design.* 2010*, 10*, 4491-4493, https://doi.org/10.1021/cg1007457.

[16] Li, Y. Y.; Guang, W.; Zhu, X. G.; Liu, M. H.; Cun, Y.; Xi, C.; Wang, Y. Y.; Ke, H.; Wang, L. L.; Ma, X. C.; Zhang, H. J.; Xi, D.; Zhong, F.; Xie, X. C.; Ying, L.; Qi, X. L.; Jia, J. F.; Zhang, S. C.; Xue, Q. K. , Intrinsic Topological Insulator Bi2Te3 Thin Films on Si and Their Thickness Limit, *Advanced Materials.* 2010*, 22*, 4002-4007, https://doi.org/10.1002/adma.201000368.

[17] Krumrain, J.; Mussler, G.; Borisova, S.; Stoica, T.; Plucinski, L.; Schneider, C. M.; Grtzmacher, D. , MBE growth optimization of topological insulator Bi2Te3 films, *J. Cryst. Growth.* 2011*, 324*, 115-118, https://doi.org/10.1016/j.jcrysgro.2011.03.008.

[18] Borisova, S.; Krumrain, J.; Luysberg, M.; Mussler, G.; GruÌˆtzmacher, D. , Mode of growth of ultrathin topological insulator Bi2Te3 films on Si (111) substrates, *Crystal Growth & Design.* 2012*, 12*, 6098-6103, https://doi.org/10.1021/cg301236s.

[19] Schönherr, P.; Tilbury, T.; Wang, H.; Haghighirad, A. A.; Srot, V.; van Aken, P. A.; Hesjedal, T. , Step-flow growth of Bi2Te3 nanobelts, *Crystal Growth & Design.* 2016*, 16*, 6961-6966, https://doi.org/10.1021/acs.cgd.6b01147.

[20] Brune, H. , Growth Modes, *Encyclopedia of Materials: Science and Technology, Sect. 1.9, Physical Properties of Thin Films and Artificial Multilayers.* 2001, 3683-3693, https://infoscience.epfl.ch/record/135795/.

[21] Ruffino, F.; Torrisi, V.; Marletta, G.; Grimaldi, M. , Growth morphology of nanoscale sputter-deposited Au films on amorphous soft polymeric substrates, *Applied Physics A.* 2011*, 103*, 939-949, https://doi.org/10.1007/s00339-011-6413-1.

[22] Matthias Schwartzkopf; Gonzalo Santoro; Calvin J Brett; André Rothkirch; Oleksandr Polonskyi; Alexander Hinz; Ezzeldin Metwalli; Yuan Yao; Thomas Strunskus; Franz Faupel; Peter Müller-Buschbaum; Stephan V Roth , Real-Time Monitoring of Morphology and Optical Properties during Sputter Deposition for Tailoring Metal–Polymer Interfaces, *ACS Applied Materials & Interfaces.* 2015*, 7*, 13547-13556, https://doi.org/10.1021/acsami.5b02901.

[23] Petrov, I.; Barna, P. B.; Hultman, L.; Greene, J. E. , Microstructural evolution during film growth, *Journal of Vacuum Science & Technology A: Vacuum, Surfaces, and Films.* 2003*, 21*, S117-S128, http://dx.doi.org/10.1116/1.1601610.

[24] Goto, M.; Sasaki, M.; Xu, Y.; Zhan, T.; Isoda, Y.; Shinohara, Y. , Control of p-type and n-type thermoelectric properties of bismuth telluride thin films by combinatorial sputter coating technology, *Applied Surface Science.* 2017*, 407*, 405-411, https://doi.org/10.1016/j.apsusc.2017.02.187.

[25] Cho, S.; Kim, Y.; DiVenere, A.; Wong, G. K.; Ketterson, J. B.; Meyer, J. R. , Antisite defects of Bi2Te3 thin films, *Appl. Phys. Lett.* 1999*, 75*, 1401-1403, https://doi.org/10.1063/1.124707.

[26] Gregoire, J. M.; Lobovsky, M. B.; Heinz, M. F.; DiSalvo, F. J.; van Dover, R. B. , Resputtering phenomena and determination of composition in codeposited films, *Physical Review B.* 2007*, 76*, https://doi.org/10.1103/PhysRevB.76.195437.

[27] Goncalves, L. M.; Couto, C.; Alpuim, P.; Rolo, A. G.; Völklein, F.; Correia, J. H. , Optimization of thermoelectric properties on Bi2Te3 thin films deposited by thermal co-evaporation, *Thin Solid Films.* 2010*, 518*, 2816-2821, http://doi.org/10.1016/j.tsf.2009.08.038.

[28] Van Quang, T.; Kim, M. , Enhancement of the thermoelectric performance of oxygen substituted bismuth telluride, *Journal of Applied Physics.* 2017*, 122*, 245104, http://dx.doi.org/10.1063/1.5006233.

[29] Huang, H.; Luan, W.; Tu, S. , Influence of annealing on thermoelectric properties of bismuth telluride films grown via radio frequency magnetron sputtering, *Thin Solid Films.* 2009*, 517*, 3731-3734, https://doi.org/10.1016/j.tsf.2009.01.015.

[30] Dheepa, J.; Sathyamoorthy, R.; Velumani, S.; Subbarayan, A.; Natarajan, K.; Sebastian, P. J. , Electrical resistivity of thermally evaporated bismuth telluride thin films, *Solar Energy Materials and Solar Cells.* 2004*, 81*, 305-312, https://doi.org/10.1016/j.solmat.2003.11.008.

[31] Rogacheva, E. I.; Krivulkin, I. M.; Nashchekina, O. N.; Sipatov, A. Y.; Volobuev, V. A.; Dresselhaus, M. S. , Percolation transition of thermoelectric properties in PbTe thin films, *Applied Physics Letters.* 2001*, 78*, 3238-3240, https://doi.org/10.1063/1.1357809.

[32] Bouderbala, M.; Hamzaoui, S.; Amrani, B.; Reshak, A. H.; Adnane, M.; Sahraoui, T.; Zerdali, M. , Thickness dependence of structural, electrical and optical behaviour of undoped ZnO thin films, *Physica B: Condensed Matter.* 2008*, 403*, 3326-3330, https://doi.org/10.1016/j.physb.2008.04.045.

[33] Morgan, K. A.; Tang, T.; Zeimpekis, I.; Ravagli, A.; Craig, C.; Yao, J.; Feng, Z.; Yarmolich, D.; Barker, C.; Assender, H.; Hewak, D. W. , High-throughput physical vapour deposition flexible thermoelectric generators, *Scientific Reports.* 2019*, 9*, 1-9, https://doi.org/10.1038/s41598-019-41000-y.

[34] Panmand, R. P.; Kumar, G.; Mahajan, S. M.; Shroff, N.; Kale, B. B.; Gosavi, S. W. , Growth of Bi2Te3 quantum dots/rods in glass: a unique highly stable nanosystem with novel functionality for high performance magneto optical devices, *Physical Chemistry Chemical Physics : PCCP.* 2012*, 14*, 16236, https://doi.org/10.1039/c2cp43169f.

[35] Dmitriev, A. V.; Zvyagin, I. P. , Current trends in the physics of thermoelectric materials, *Physics-Uspekhi.* 2010*, 53*, 789-803, https://doi.org/10.3367/UFNe.0180.201008b.0821.

[36] Atakulov, S. B. A.; Shamsiddinov, A. N. , The problem of transport phenomena in polycrystalline semiconductor thin films with potential barriers in the case where the carriers gas degenerated, *Solid State Communications.* 1985*, 56*, 215-219, https://doi.org/10.1016/0038-1098(85)90744-6.

[37] Kishimoto, K.; Tsukamoto, M.; Koyanagi, T. , Temperature dependence of the Seebeck coefficient and the potential barrier scattering of n-type PbTe films prepared on heated glass substrates by rf sputtering, *Journal of Applied Physics.* 2002*, 92*, 5331, https://doi.org/10.1063/1.1512964.

[38] Shaik, M.; Motaleb, I. A. , Investigation of the optical properties of PLD-grown Bi2Te3 and Sb2Te3, *IEEE International Conference on Electro-Information Technology, EIT 2013.* 2013, 1-6, https://doi.org/10.1109/EIT.2013.6632708.

[39] Liao, M. H.; Huang, K. C.; Tsai, F. A.; Liu, C. Y.; Lien, C.; Lee, M. H. , Thickness dependence of electrical conductivity and thermo-electric power of Bi2.0Te2.7Se0.3/Bi0.4Te3.0Sb1.6 thermo-electric devices, *AIP Advances.* 2018*, 8*, 015020-4, http://doi.org/10.1063/1.5017252.

[40] Dheepa, J.; Sathyamoorthy, R.; Subbarayan, A. , Optical properties of thermally evaporated Bi2Te3 thin films, *J. Cryst. Growth.* 2005*, 274*, 100-105, https://doi.org/10.1016/j.jcrysgro.2004.09.070.

[41] El-Sayed, H. E. A. , Structural and optical properties of thermally evaporated Bi2Te3 films, *Appl. Surf. Sci.* 2005*, 250*, 70-78, https://doi.org/10.1016/j.apsusc.2004.12.025.

[42] Elahi, S. M.; Taghizadeh, A.; Hadizadeh, A.; Dejam, L. , Effect of Thickness and Annealing on Structural and Optical Properties of Bi2Te3 Thin Films Prepared from Bi2Te3 Nanoparticels, *International Journal of Thin Films Science and Technology.* 2014*, 3*, 13, http://dx.doi.org/10.12785/ijtfst/030103.

[43] Yang, X. H.; Qin, X. Y.; Zhang, J.; Li, D.; Xin, H. X.; Liu, M. , Enhanced thermopower and energy filtering effect from synergetic scattering at heterojunction potentials in the thermoelectric composites with semiconducting nanoinclusions, *Journal of Alloys and Compounds.* 2013*, 558*, 203-211, https://dx.doi.org/10.1016/j.jallcom.2012.12.048.

[44] Zou, T. H.; Qin, X. Y.; Li, D.; Sun, G. L.; Dou, Y. C.; Wang, Q. Q.; Ren, B. J.; Zhang, J.; Xin, H. X.; Li, Y. Y. , Simultaneous enhancement in thermoelectric power factor and phonon blocking in hierarchical nanostructured β-Zn4Sb3-Cu3SbSe4, *Applied Physics Letters.* 2014*, 104*, 13904, https://doi.org/10.1063/1.4861156.

[45] C Wood , Materials for thermoelectric energy conversion, *Reports on Progress in Physics.* 1988*, 51*, 459-539, https://doi.org/10.1088/0034-4885/51/4/001.

[46] Elsheikh, M.; Shnawah, D.; Sabri, M.; Said, S.; Hassan, M.; Bashir, M.; Mohamad, M. , A review on thermoelectric renewable energy: Principle parameters that affect their performance, *Renewable & Sustainable Energy Reviews.* 2014*, 30*, 337-355, https://doi.org/10.1016/j.rser.2013.10.027.

[47] G. D. Deshmukh; S. M. Patil; S. S. Patil; P. H. Pawar. , Effect of Film Thickness on Structural and Optical Properties of Bi2Te3 Thin Films, *J. Chem. Biol. Phys. Sci.* 2015*, 5*, 2769-2779, https://www.jcbsc.org/admin/get_filephy.php?id=335.

Chapter 4 Post-deposition radiation treatments to improve TE performance and use of interlayers to improve mechanical resilience

The performance of Bi-Te film grown at RT was analysed in the last chapter. To enhance the performance of the as-deposited film, two possible approaches of post-deposition anneal (e-beam and IR treatments) are described in this chapter. In addition, two types of substrate-to-coating interlayers are trialled to improve the mechanical resilience.

4.1 Post-deposition anneal

In laboratory-scale studies of TE materials, the focus has been on high-temperature deposition techniques because a columnar growth of Bi_2Te_3 films can be achieved, significantly increasing the figure of merit, *ZT*, e.g. by ~50% [1-4]. However, for high-throughput R2R processing, increasing the substrate temperature is a substantial challenge for flexible TEGs based on a deformable polymer substrate. Hence, for R2R processing at RT, a post-annealing treatment is of interest because it can have a positive effect on the structural, electrical, and TE properties of Bi-Te films [5-8].

As well as morphology, stoichiometry can affect TE performance as discussed in chapter 3, and annealing can adjust the stoichiometry of the deposited Bi-Te films by re-evaporation of Te under various annealing temperatures [5], because of its higher vapour pressure *P* (P_{Bi} = 1 Pa <<< P_{Te} = 1 kPa, at around 600°C [63,64]). I have undertaken a study of films RT deposited onto a moving polymer substrate by DC magnetron sputtering, followed by a range of post-deposition annealing processes, to understand the impact upon materials TE properties.

To anneal Bi-Te films, a vacuum oven [9-13] is the most common and simple method. However, it is not a favourable approach for in-line R2R processing, for example, annealing a wound roll of material will lead to the danger of the roll 'blocking' and being difficult to unwind. In recent years, more novel techniques have been proposed to enhance TE properties of Bi-Te films such as e-beam irradiation treatment [12, 14], which is an R2R compatible method, and could improve the film's crystallisation by raising the temperature within the coating over a suitable depth (e-beam irradiation depth: ~ 50 μm [15]). As a comparison, in addition to e-beam treatment, I also use IR as another R2R compatible annealing technique. As the IR absorption regions of Bi-Te films [16, 17] and polymer substrates [18, 19] differ, it is possible to raise the coating temperature with the radiation whilst maintaining a minimally affected bulk polymer substrate. If either e-beam and/or IR treatment methods are demonstrated to improve the coating properties, the challenges associated with post-rolling annealing could be eliminated whilst improving process efficacy for industrial manufacturing of flexible TEGs. Therefore, in this chapter, I explored the feasibility of various R2R compatible annealing strategies, particularly IR and e-beam irradiations, for RT sputtered Bi-Te films grown on polymer substrates (i.e. PI sheets with a T_g of 360°C) and their effect on TE properties.

4.2 Annealing strategies in roll-to-roll

To better observe the XRD peak of as-deposited films, thicker (~1 μm) Bi-Te films were fabricated at RT in an Edwards 306 system (see Chapter 2 for details). Then, these as-deposited films were annealed *via* four methodologies, as summarised in Table 4.I. The first two approaches were static i) in a vacuum oven and ii) e-beam irradiation as static standard references. The static vacuum oven was a custom-built high-vacuum furnace (capable of reaching ~1300 °C at 1×10^{-5} mbar, with an approximate ramp rate of ~5.5°C min^{-1}). Static annealing *via* e-beam irradiation was carried out with a pulsed electron

source using a Sodick PF32A electron beam machining system in 5×10^{-4} mbar of argon with an irradiation distance and accelerating voltage of 300 mm and (10 & 13 kV), respectively. This low-energy (<40 keV) high current (10 - 25 kA) pulsed electron beam irradiation could give a rapid and homogenous application of energy density 0.3 - 20 J/cm^2 over an area of ~60 mm diameter with a pulse duration of 2 - 4 µs, and penetration depth up to 10 µm [20].

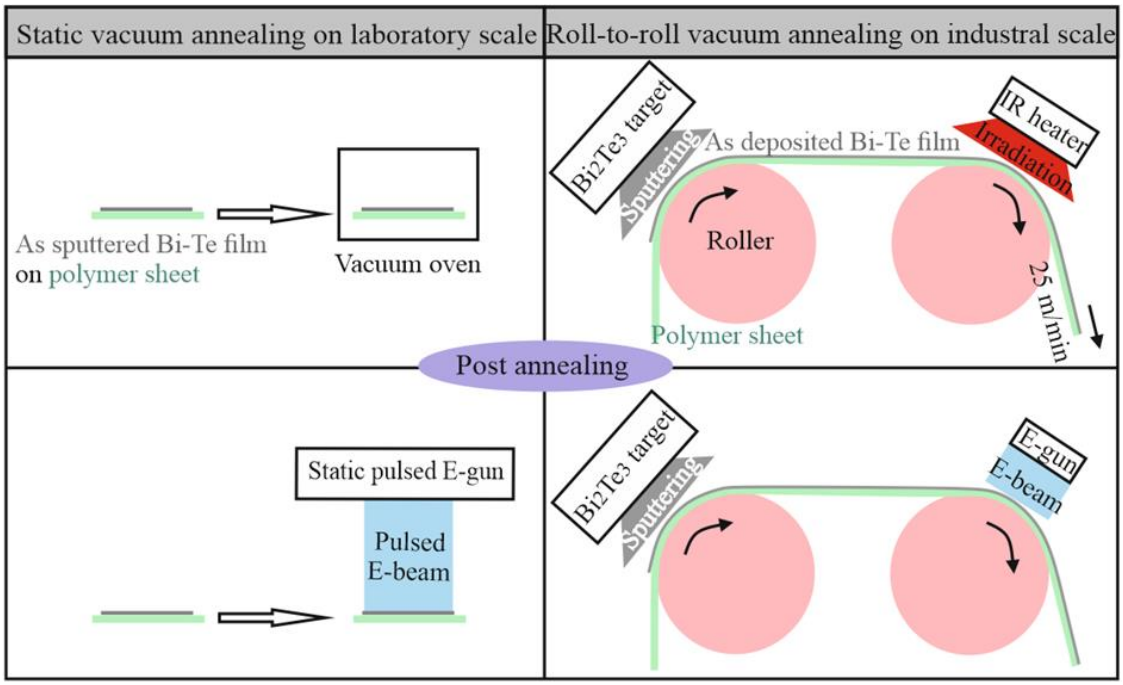


Figure 4.1. *Schematics of four different post-annealing strategies: static vacuum oven, static e-beam irradiation, dynamic IR irradiation, and dynamic e-beam irradiation, under conditions of 250/350 ℃ (1 × 10^{-5} mbar), 10/13 kV (5 × 10^{-4} mbar), 250/350 ℃ (1.5 × 10^{-4} mbar, 25 m min^{-1}), and 5.8/7.3 kV (1.5 × 10^{-4} mbar, 25 m min^{-1}), respectively.*

To further investigate the feasibility of annealing approaches in R2R processing, two dynamic strategies (IR and e-beam irradiations) were trialled at 1.5×10^{-4} mbar (a typical vacuum level for a low-cost high throughput R2R process) with samples fixed to a rotating drum (25 m min^{-1}) in the Oxford webcoater with e-beam current: 100 mA (5.8 kV) and 170 mA (7.3 kV). The IR annealing (0.5 kW IR source: 1500 – 5600 nm, i.e.

0.2214 – 0.8266 eV, corresponding to ~20000 – 100000 cm^{-1} of absorption coefficient on Bi-Te film [21, 22]) was initially conducted in the same condition but with the sample held statically under the IR source to determine the effect of maximum irradiation temperature. To measure the dynamic temperature on the film surface (i.e. the temperature variation as the drum rotates), a temperature data logger (EL-USB-TC-LCD EasyLog) measured a Bi-Te coated thermocouple, attached to the rotating roller.

Table 4.I. *Conditions of various annealing approaches.*

Annealing means	**Vacuum base pressure (mbar)**	**Anneal temp. /condition**	**Time to setting condition (min)**	**Anneal time (min)**	**Take-out temp. /time**	**Drum speed (m/min)**
Comparison of different methods (section 4.3.1 & 4.3.2)						
Static vacuum oven	1×10^{-5}	250°C	~60	60	50°C	Static
		350°C				
Static pulsed e-beam	5×10^{-4}	10 kV	-	60	-	
		13 kV				
Static IR	1.5×10^{-4}	250°C	~8	60	50°C	
		350°C				
Dynamic e-beam	1.5×10^{-4}	5.8 kV	~3	60	5 mins	25
		7.3 kV				
Time-dependency (section 4.3.3)						
Dynamic	1.5×10^{-4}	145°C	~8	1 - 60	50°C	25
Dynamic	1.5×10^{-4}	7.3 kV	~3	1 - 60	5 mins	25

*Note that for the dynamic processes the samples are attached to a rotating drum of approx. 1.8 m circumference, rotating at 25 m min^{-1}, thus the sample, during the annealing process is not continuously underneath the annealing source, but passes underneath it multiple times.

4.3 Results and discussion

4.3.1 Structural properties of as-deposited/annealed Bi-Te films

The XRD patterns and elemental compositions of as-deposited and post-annealed Bi-Te films are shown in Figure 4.2 a & b. The average crystal size and strain were obtained from Williamson-Hall plots (see Figure 4.2 c), as summarised in Table 4.II. Figure 4.3 shows the SEM micrographs of as-deposited and post-annealed Bi-Te films. The effect of post-deposition anneal is clearly revealed through these SEM images, although the impact varies for different annealing techniques.

4.3.1.1 As-deposited film

The as-deposited film showed characteristic diffraction peaks at 2θ of 27.7°, 38.2°, 57.1°, and 62.7°, corresponding to (0 1 5), (1 0 10), (2 0 10) and (1 1 15) planes, respectively, as expected in a standard Bi_2Te_3 phase (ICSD #193330). XRD peaks (0 1 5) and (1 0 10) were observed for both hot and RT deposition of Bi_2Te_3 film on polymer/rigid substrates [9, 12, 14, 23-32], due to their inherently strong reflection. Unlike with hot deposition on rigid substrates [14, 23, 33], orientated growth (beneficial to the electrical property of films) was not observed in this study, consistent with the literature for RT deposition [25, 34].

The as-deposited film showed low/broad peaks indicative of small crystallites [9, 12], as well as a possibility of overlapping peaks [35] of different phases with a similar crystallographic structure to Bi_2Te_3, e.g. BiTe and Te (Figure 4.2 a). In addition, some minor diffraction peaks (e.g. 43.8°) were indexed as metallic Te [13]. Therefore, other

phases, including Te-rich phases [15] could coexist with the Bi_2Te_3 phase, forming structural defects between different phases [30]. This could have a significant influence on TE behaviours.

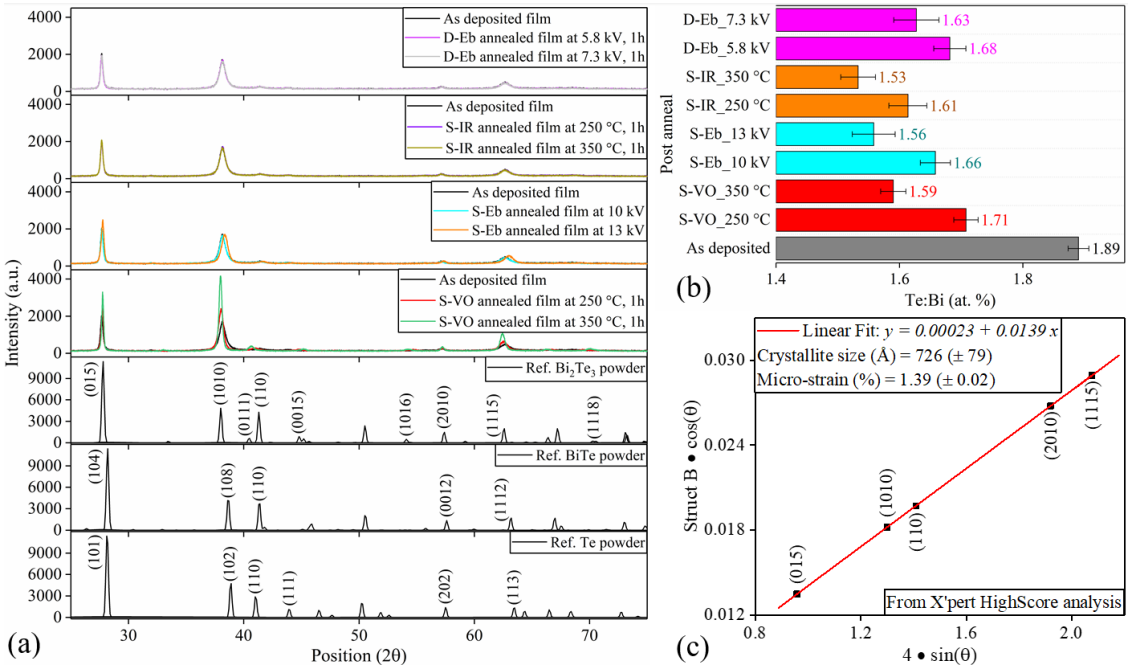


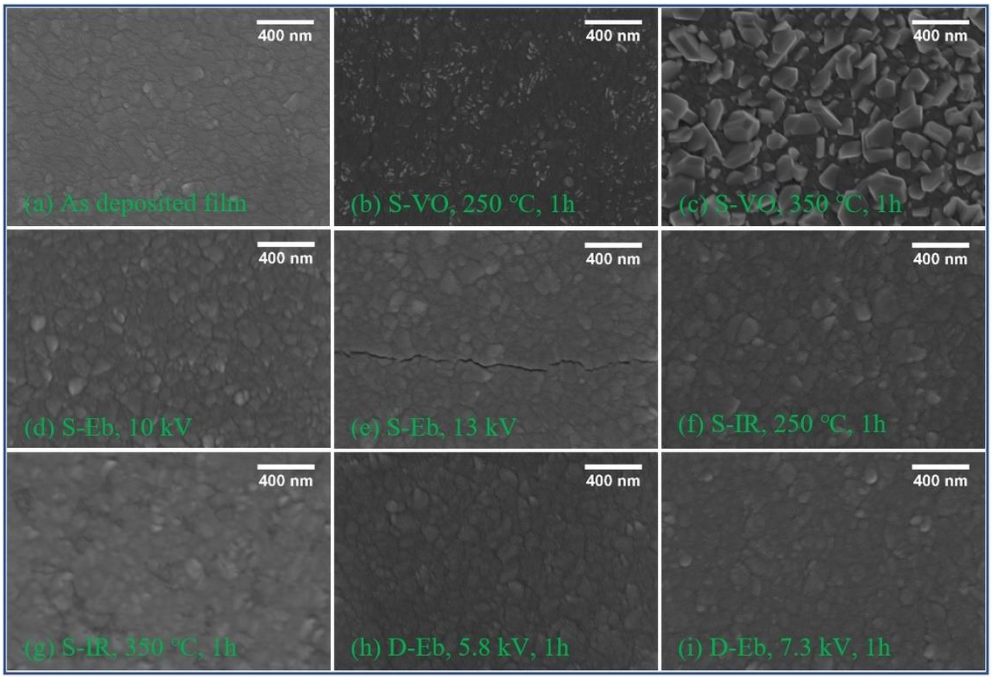
Figure 4.2. *(a) XRD patterns of as-deposited and post-annealed Bi-Te films, with the reference traces: Te (ICSD #40042), BiTe (ICSD #30526), and Bi_2Te_3 (ICSD #193330) powders; (b) Te/Bi ratio determined from EDX before and after various treatments; (c) Example Williamson-Hall analysis (as-deposited film), where Struct B = the observed FWHM – the instrumental broadening, θ is the Bragg diffraction angle. (S-VO denotes static vacuum oven system in laboratory-scale; S-Eb denotes static pulsed e-beam system in laboratory-scale; while S-IR and D-IR denote static and dynamic infrared radiation, respectively; D-Eb denotes dynamic e-beam system in an R2R web coater).*

Table 4.II. *The average crystallite size, micro-strain, and lattice parameters of as-deposited and post-annealed films from Williamson-Hall plot in X'pert Highscore Plus software.*

Specimens	Crystallite size [Å]	Micro-strain [%]	Lattice parameters [Å]	
			a = b (± 0.003)	c (± 0.03)
As-deposited	726 (± 79)	1.39 (± 0.02)	4.36	30.31
S-VO_250 °C	1333 (± 284)	1.06 (± 0.02)	4.43	30.35
S-VO_350 °C	1341 (± 252)	0.81 (± 0.01)	4.46	30.25
S-Eb_10 kV	1031 (± 153)	1.63 (± 0.01)	4.39	30.37
S-Eb_13 kV	848 (± 48)	1.75 (± 0.07)	4.37	30.20
S-IR_250 °C	740 (± 87)	1.39 (± 0.02)	4.36	30.31
S-IR_350 °C	742 (± 98)	1.39 (± 0.02)	4.35	30.35
D-Eb_5.8 kV	788 (± 87)	1.39 (± 0.01)	4.37	30.30
D-Eb_7.3 kV	814 (± 77)	1.44 (± 0.01)	4.37	30.32

From the EDX result (Figure 4.2 b), the as-deposited film was more Te-rich (1.9 at.%) than the Bi_2Te_3 target (1.5 at.%). Also after heat or radiation treatments, the films were Te rich, but to a lesser extent due to preferential vaporisation of Te elements in the film during the annealing process [5, 10, 13]. In this study, the Te-rich film was n-type, confirmed by both Seebeck and Hall results, consistent with the literature [36, 37], remaining n-type even after heat or radiation treatments.

Part A:



Part B:

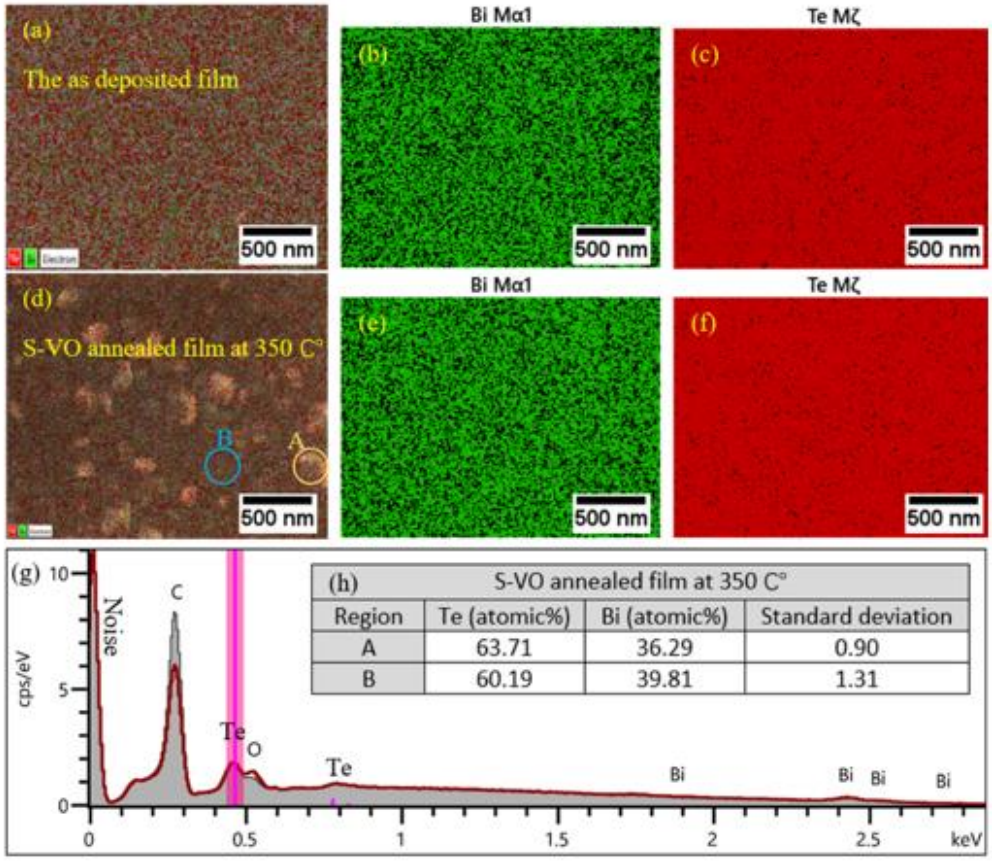


Figure 4.3. *Part A: SEM images of the as-deposited and post-treated Bi-Te films: (a) the as-deposited film; (b-c) films annealed in a static vacuum oven at 250°C and 350°C; (d-*

e) films annealed in a static e-beam system at 10 kV and 13 kV; (f-g) films annealed in static IR radiation at 250°C and 350°C; (h-i) films annealed in a dynamic e-beam treatment at 5.8 kV and 7.3 kV. Part B: The elemental mapping of: (a-c) the as-deposited film and (d-f) the film annealed in a vacuum oven at 350°C; (g) EDX spectra of the as-deposited film (the grey profile line) and the film annealed in a vacuum oven at 350°C (the red profile line); (h) the composition in regions 'A' and 'B' in (d) (an average of 6 different locations) of the film annealed in a vacuum oven.

4.3.1.2 Static vacuum-oven annealed film

Films annealed in a vacuum oven showed a significant enhancement in crystallinity, with more intense crystalline peaks. The peak of the as-deposited film at 38.17° (FWHM = 0.358°) narrowed to 0.248° and shifted to 37.99°, approaching the expected position for reference Bi_2Te_3, for a 350°C anneal. The same phenomenon was observed for the 62.7° peak. These observations reflect an increase in crystal size to 134.1 nm and a decrease in lattice strain from 1.39% to 0.81% (Table 4.II), associated with the annealing. After annealing, the relative intensity of (0 1 5), (1 0 10), and (1 1 15) peaks changed and the (1 0 10) plane gradually showed the strongest intensity, indicating a change in the preferential orientation of crystallites [9, 38]. In addition, the minor diffraction peak (1 1 0) at 41.5° (possibly corresponding to Te phase since the film was Te-rich) completely vanished while a new peak at 40.6° appeared to match the (0 1 11) plane in reference Bi_2Te_3, indicating a decrease in Te content with annealing [10] and more or differently orientated crystallites in the Bi_2Te_3 phase.

From the SEM imaging (Figure 4.3 A b & c), after annealing in the vacuum oven, protruding large crystals appeared on the film surface and appeared to grow with the annealing temperature. This kind of phenomenon has already been observed and reported as Sb-rich/Te-rich crystalloid precipitates in annealing Bi-Sb-Te and Sb-Te films [28, 39,

40], but not yet observed for Te-rich precipitates in annealing Bi-Te films [9, 10, 13, 32]. EDX maps (Figure 4.3 B d & h) indicated that the protruding grains were modestly Te-rich. Te-rich precipitates formed when annealing as the Te atoms became mobile and tended to migrate/precipitate at the grain boundaries and to the surface of annealing films.

4.3.1.3 Static electron beam annealed film

In terms of annealing using a static pulsed e-beam system, there were some increases in grain size from the XRD pattern, greater for the sample annealed at 10 kV (Table 4.II). Both e-beam-treated specimens showed an increased lattice strain, as observed in [14]. Some reports of e-beam treatment suggested little or no modification [12] of the crystallinity of Bi-Te, although one report of Bi-Sb-Te [15] noted a small increase in crystallite size with e-beam treatment.

The 13 kV e-beam irradiation was shown to damage the film (for example due to thermal expansion) as shown by cracks observed on the film surface (see Figure 4.3 A e), which dramatically affected the electrical properties (see part 3.2) giving a very high resistance.

4.3.1.4 Dynamic infrared and electron beam annealed films

Regarding both IR and e-beam treatments in the web coater, there was no substantial change in XRD peak positions. This modest increase in crystallite size perhaps seen from the XRD was also observed in the SEM (Figure 4.3 A f-i), though the grain growth is less obvious at the surface than for the vacuum oven-treated samples.

These observed changes in crystal size and stoichiometry will be discussed below, in the context of the TE characteristics of the material.

4.3.2 Thermoelectric behaviour of as-deposited/annealed films

Figure 4.4 A shows ρ, S and PF of as-deposited and post-annealed Bi-Te films. To analyse the variation of ρ and S, I also plotted the carrier concentration (n), mobility (μ) and E_g of films. To achieve a high PF, a low ρ but a high S are required. The data fit the

expected relations $\rho \propto \frac{1}{\mu \bullet n}$ [41], $S \propto \frac{1}{n^{2/3}}$ [42] and $S \propto \mu^{0.2}$ [43] well (except the damaged S-Eb 13 kV), as shown in Figure 4.4 B (a-c).

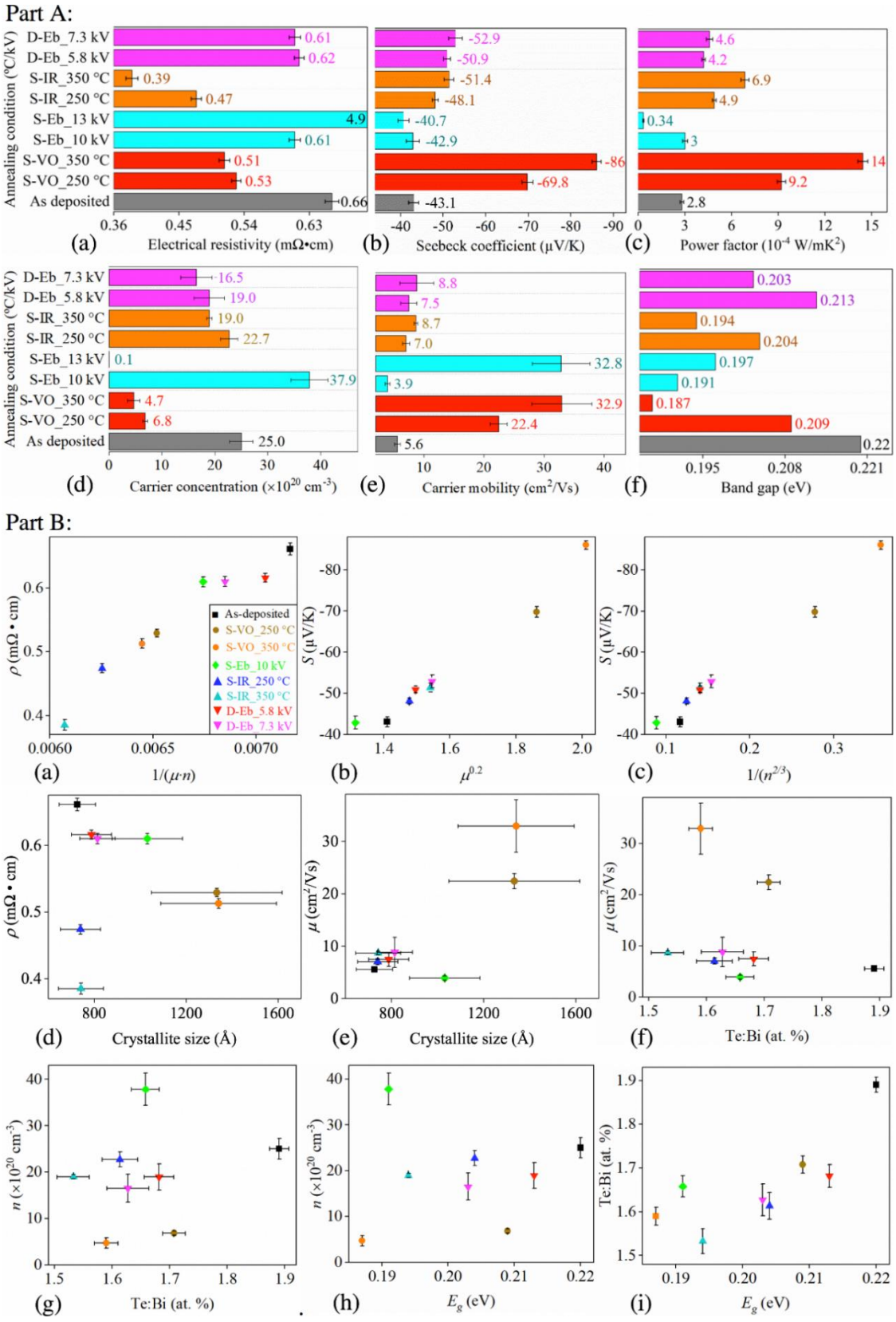


Figure 4.4. *Part A: (a) ρ, (b) S, (c) PF, (d) n, (e) μ and (f) E_g of as-deposited and post-annealed films; Part B: (a-c) the expected relations of S and ρ with n and μ; Plots of (d) ρ vs crystallite size, (e) μ vs crystallite size, (f) μ vs ratio of Te: Bi, (g) n vs ratio of Te: Bi and (h) n vs E_g; and (i) ratio of Te: Bi vs E_g.*

4.3.2.1 Electrical resistivity and Seebeck coefficient

The as-deposited film exhibited the highest ρ (0.66 mΩ·cm) and a relatively small S (43.1 μV/K). The vacuum-oven annealing at 350°C decreased ρ to 0.51 mΩ·cm while significantly increased S to 86 μV/K. The static pulsed e-beam annealing at 13 kV increased ρ tenfold due to cracks formed in the film, while the 10 kV e-beam treatment kept ρ and S approximately unchanged. In terms of the IR annealing, a significant decrease in ρ (from 0.66 to 0.39 mΩ·cm) was observed, accompanied with a slight increase in S (from 43.1 to 51.4 μV/K). After e-beam annealing in the web coater, there was no obvious change in ρ but an increase in S was observed from 43.1 to 52.9 μV/K. The variation in both ρ and S is a complicated competitive relation between n and μ. We can consider the following factors that could affect both n and μ.

(1) The change in grain size on boundary scattering mechanism [32];

(2) The improvement of crystallinity on scattering mechanism [14, 44];

(3) The change in film composition [45, 46];

(4) The content variation of defects as donors [32];

(5) The variation in bandgap with annealing process [47];

(6) The modification of the energy barrier at a grain boundary [48].

Results related to these effects are plotted in Figure 4.4 B (d-i).

(1 - 3) These three effects have significant impacts on μ. Figure 4.4 B (e) shows that μ broadly increases as crystallite size increases because of a reduced crystallite boundary

carrier scattering. There does not appear to be a strong correlation between mobility and composition (Figure 4.4 B f). A low μ for S-Eb could be due to the observed sample damage by the e-beam treatment.

(4 - 6) These effects significantly influence *n*. Post annealing treatments do tend to lead to a lower Te content, as expected from the greater volatility of Te. With Te_{Bi} defects removed, *n* would expect to decrease with lower Te content, because Te_{Bi} antisite defects (i.e. the substitution of Te atoms into Bi vacancies) act as the major source of electron donors [49] in Te-excess Bi-Te films. The variation of *n* with Te: Bi ratio, shown in Figure 4.4 B (g), does not show a strong trend as expected from this defect model. It may be that the very high Te content of these films reflects the formation of regions of the material that are predominantly Te (for which there are indications in the XRD data), which themselves would not act as defects in the Bi-Te material. The E_g of the material is shown to increase with increasing Te: Bi (Figure 4.4 B i), i.e. it is lower for the annealed materials. This may be due to doping effects introducing carrier levels in the E_g, or from changes in ordering/confinement length in the material. One might expect *n* to increase with decreasing E_g because of the dual effect of the increased number of intrinsic carriers with a lower E_g, and any extrinsic carriers formed by increased dopant levels that would have the effect of decreasing the observed E_g. However, if anything, a slight decrease in *n* with decreasing E_g, is observed (Figure 4.4 B h), suggesting that (1) any decrease in E_g does not lead to useful charge carriers e.g. due to the formation of trapped charge levels, or (2) the observed decrease in E_g may originate from material that does not contribute significantly to the charge conduction as measured by the Hall effect e.g. in highly disordered or non-stoichiometric material. Indeed, there is little or no correlation observed between *n* and the average stoichiometry of the film (Te: Bi), as observed in Figure 4.4 B g). In addition to the consideration of extrinsic (due to doping) and intrinsic

(due to a reduction in E_g) carriers, we should also consider the energy barrier to carrier transport at grain boundaries (6), which will act to decrease the effective n. Room-temperature sputtered Bi-Te film is Te-rich and poorly crystalline, and most likely, the excess/amorphous Te phases exist at the grain boundaries, acting as an energy barrier to filter the carriers moving in the plane. If Te precipitates form at grain boundaries on annealing (Figure 4.3 A c), this could increase the energy barrier leading to a significant decrease in measured n (Figure 4.4 A d).

This analysis of trends in μ and n demonstrates that a number of factors come together to give rise to the observed changes in TE performance, and that these can be related to the observed changes in microstructure and composition of the films as a result of annealing. It also serves to demonstrate how not only the deposition processes but also any subsequent treatments are factors in the TE performance of the material.

4.3.2.2 Power factor

All annealing approaches tried here showed an enhancement in *PF*. The film annealed in the vacuum oven at 350°C exhibited the highest *PF* (14×10^{-4} W/mK^2), ~5-times greater than that of the as-deposited film. Such a *PF* is also higher than the latest reported values of post-annealed/hot-deposited Bi-Te films fabricated by sputtering (11.45×10^{-4} W/mK^2, 2017, [10]). However, a vacuum oven is not a feasible method for R2R processing. Considering annealing approaches compatible with an R2R process, a dynamic e-beam treatment (7.3 kV) showed an increase in *PF* by 64% compared to the as-deposited film while a static IR irradiation (350°C) increases *PF* by 146%. According to the irradiation/penetration depth of e-beam (~ 50 μm [15]) and IR (~400 - 700 nm [50]) on Bi-Te films, the e-beam treatment can directly anneal the whole thickness of the coating, while the IR treatment is only expected to directly treat the top region, thus the underlying material will only be annealed by any conduction of heat from the top. If this is the case,

then it opens up the possibility that IR annealing would be able to significantly improve the TE behaviour of thinner layers that may be more appropriate for R2R-deposited material [51]. A study of the effect of film thickness on the effectiveness of the post-deposition annealing is beyond the scope of this study but would be an important consideration for further work on optimising a preferred annealing method.

Although both e-beam and IR techniques each could improve the TE property of the as-deposited Bi-Te film, IR irradiation performed better. However, these results were obtained from a 60-min anneal which was a long time for a fast R2R process (requiring 833 rotational passes in this case), and the IR irradiation was performed in a static condition rather than a dynamic condition. The effectiveness of an anneal will decrease as the annealing time decreases [52, 53]. To achieve a real R2R post-annealing process, investigating the extent of the effect of treatment time in R2R processing is necessary.

4.3.3 Decreasing the treatment time for R2R anneals

To achieve the highest temperature during drum rotation, a full power (500 W) was applied to the IR source. In Figure 4.5, the approximate temperature varied between ~150°C and ~138°C as the drum rotated.

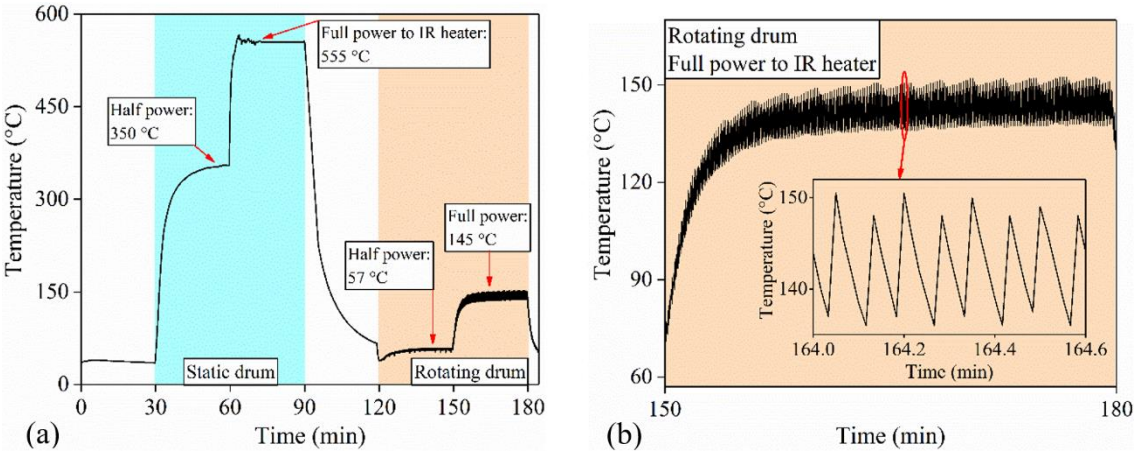


Figure 4.5. *(a) The variation of temperature on the drum in static and dynamic situations under half/full powers of an IR source, and (b) The temperature on a rotating drum under*

full power to the IR heater (the temperature reached the highest when facing the IR heater but reached the lowest when rotated away from the heater).

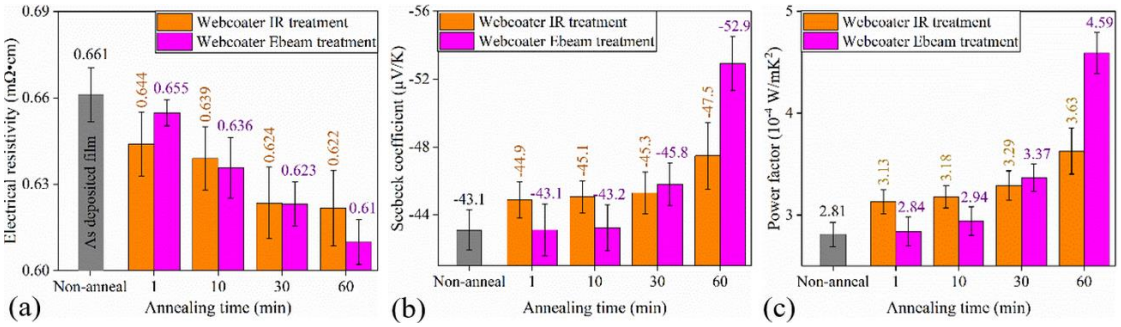


Figure 4.6. *Plots of (a) ρ, (b) S and (c) PF for Bi-Te films with various annealing times of dynamic IR (145°C) and e-beam (7.3 kV) irradiations in web coater (moving drum: 25 m min^{-1}).*

The variations of ρ, *S,* and *PF* as a function of annealing time have been obtained, as shown in Figure 4.6. Similar to previous reports [52, 53], the property improvement increases with annealing time. I did not consider very long annealing times as this is incompatible with the R2R process.

The dynamic IR annealing is less effective to enhance *PF* compared with the static IR annealing, most likely due to the lower temperature achieved (Figure 4.4 A c and Figure 4.6 c). Comparing dynamic e-beam and IR, although the dynamic e-beam treatment could achieve a higher *PF* than the dynamic IR after 1 hour of treatment, IR annealing could increase *PF* even for 1-min irradiation after the stable temperature was reached, while dynamic e-beam annealing did not improve *PF* until 30 mins of treatment. The shorter treatment time is more desirable for in-line treatment during an R2R process. Therefore, dynamic IR post-deposition treatment seems to be a better approach, to be compatible with a real high-throughput R2R process in an industrial context. Further improvements could be envisaged with a higher power IR source, applied to thinner layers, or between successively sputtered layers as might be envisaged for an R2R sputtered process.

To check any effect of the IR treatment on the underlying substrate, the tensile mechanical properties and FTIR spectra (Figure 4.7) of the materials (blank PI substrate and Bi-Te films on PI with/without IR anneal at 350°C for 1 hour) were measured. The results in Figure 4.7 suggests no significant effect on the substrate.

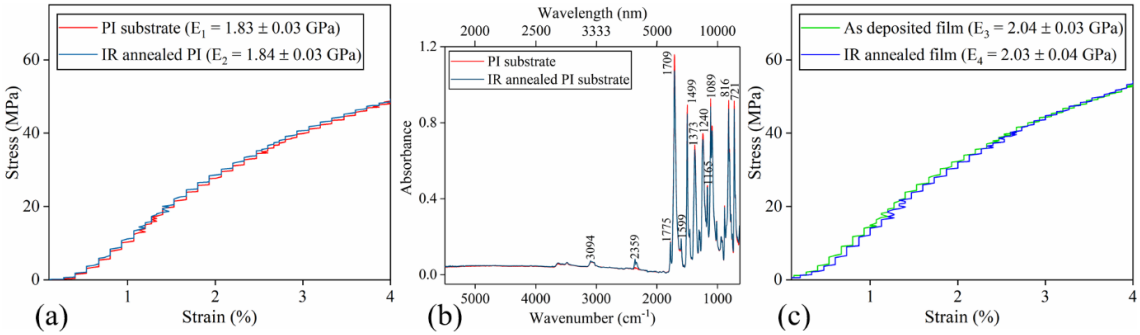


Figure 4.7. *(a) Stress-strain relations of polymer substrate and post static IR annealed polymer substrate (E is the modulus which comes from the strain below 2%); (b) FTIR spectra of polymer substrate and a 1-hour post static IR annealed polymer substrate (the peak at around 2359 cm^{-1} comes from CO_2 in the air); (c) Stress-strain relations of the as-deposited and post dynamic IR annealed films on polymer substrates.*

4.4 Mechanical deformation

TEGs on flexible substrates must be resilient to bending both during production and application (e.g. a wristband). Zhang *et al.* [54] reported an analytical method to investigate the crack formation in inorganic TE materials (without substrates), and found that the crack size affected the electrical and thermal conductivities whilst showing that the TE conversion efficiency was independent of the crack size. Cao *et al.* [55] carried out an experimental study of bending properties for a screen-printed TE coating (~70 - 250 μm thick Bi-Te and Sb-Te) on textile by flexing the sample at a fixed bend radius over a roller. They observed an increase in sheet resistance of 200 % (over ten bending cycles passing a 60 mm diameter roller and a 4 mm diameter roller), and also some debonding. To date, there are few research reports about the experimental observation of

mechanical behaviours of TE thin films (in nm range) on polymer substrates. Singkaselit *et al.* [56] reported that annealing could improve the hardness of ~1.5 μm thick TE films on polyimide sheets due to a change in the film density. A recent work (Kong *et al.* 2019 [57]) reported that coating a PDMS layer on the Bi_2Te_3 surface (grown on a polyimide sheet) could significantly improve the flexibility of the film. They observed <5% change in resistance after bending 2000 cycles (radius: 7 mm).

During R2R coating (Figure 2.1, Chapter 2), the polymer web bends around a series of rollers (typically with a core radius of ~15 cm), and a fixed tension (e.g. ~24 N/mm^2, applying 1% strain) is applied to keep the web tight.

To improve the mechanical resilience of the TE film grown on polymer substrates, coating a PDMS layer on *top* of the TE film has been found to be effective (Kong *et al.* 2019 [57]). However, this method fabricates the PDMS coating after the deposition of TE films on polymer substrates, so it does not solve the induced strain in TE films during the process of R2R manufacture. Therefore, a further study to put a PDMS layer before depositing TE films on the polymer substrate is worth considering. In addition to PDMS, an R2R manufacturable acrylate coating is also explored in this study, as a buffer layer in between the PET substrate and the functional film, expected to help improve the mechanical resilience of the functional materials during R2R processing and during operation.

4.5 Buffer-layer fabrication

Two types of buffer layers (acrylate and PDMS) were deposited onto the PET substrate before Bi-Te deposition, as contrasted with a blank PET substrate. The fabrication process of the acrylate layer has been described in Chapter 2. The acrylate thickness was controlled by varying the amount (0.6 – 10 mL) of acrylic monomer (TPGDA Sigma–

Aldrich) injected into the hot tank with a constant injection speed: ~0.5 mL/min. The thickness of the acrylate coating was then measured using DekTak.

A PDMS layer was made using a spin coater (Laurell Technologies Corporation). Similar as in reference [58], PDMS and curing agent (SYLGARD® 184) were mixed in ratio 10 : 1 and stirred for ~5 mins and under vacuum (~4 × 10^{-2} mbar) for ~1 hour to remove bubbles. Sufficient PDMS mixture (~200 mg) was dropped on a PET substrate and then spun with varying spinning rates (1000 – 8000 rpm) in a spin coater, followed by curing in an oven under ~55°C for ~16 hours. The mass difference was measured before and after deposition using a laboratory balance (Mettler Toleto), so the film thickness could be roughly calculated using the relation: mass = density (0.98 g/mL in this case) × volume = density × (the film thickness × the substrate area). The PDMS thickness was controlled by varying the spinning rate.

4.6 Results and discussions

4.6.1 Film thickness and surface morphology

Figure 4.8 a shows the thickness of buffer layers: acrylate coatings: 0.4 (± 0.01) – 7.7 (± 0.09) μm; PDMS coatings: 2.5 (± 0.01) – 16.8 (± 0.01) μm. The Bi-Te film has a thickness of 92 (± 6) nm. These thicknesses can be used to calculate the strain applied to the film during buckling tests, using the model reported in [59]. The displacements of all samples are given in Table 4.III.

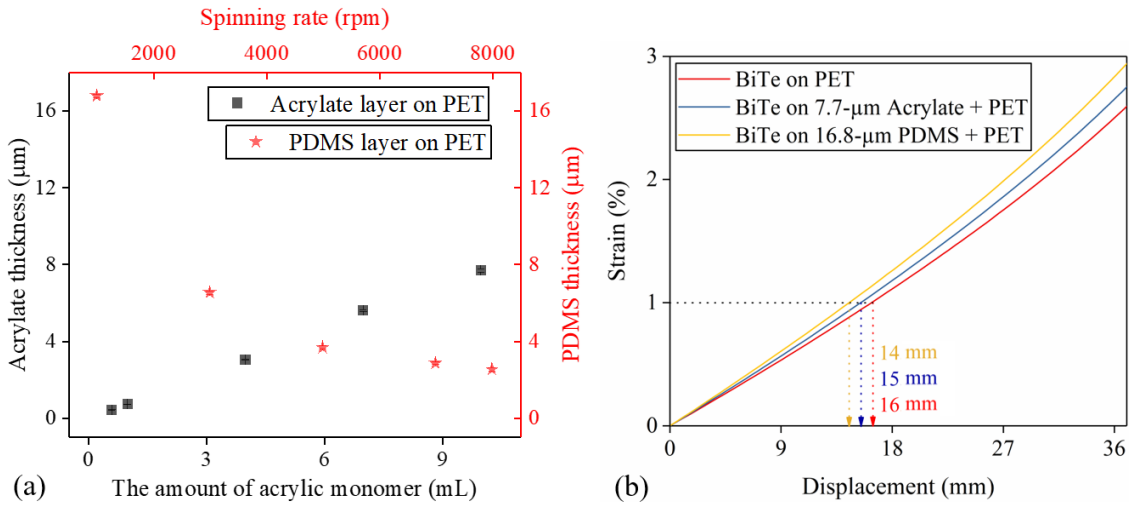


Figure 4.8. *(a) The thickness of buffer coatings (the error bars are standard deviations from eight and three measurements for acrylate and PDMS, respectively); (b) the calculated relation between the strain applied to the Bi-Te film as a result of the applied displacement during buckling tests.*

Table 4.III. *The relation between strain (on the upper surface of the buckling film) and displacement during buckling tests for all samples, using a calculation method considering the thickness of Bi-Te film, the buffer layer, and PET substrate (where the assigned nomenclature of 7.7A means Bi-Te grown on 7.7-µm thick acrylate + PET and 16.8P means Bi-Te grown on 16.8-µm thick PDMS + PET).*

Sample / Strain [%]	Displacement [mm]										
	PET	**0.4A**	**0.7A**	**3A**	**5.5A**	**7.7A**	**2.5P**	**2.8P**	**3.5P**	**6.5P**	**16.8P**
0.6	9.84	9.81	9.78	9.62	9.45	9.31	9.66	9.63	9.58	9.38	8.74
1.0	15.90	15.87	15.82	15.57	15.30	15.07	15.62	15.59	15.50	15.19	14.19
1.8	28.02	27.99	27.91	27.47	27.01	26.60	27.54	27.51	27.36	26.82	25.07
2.0	31.05	31.02	30.93	30.45	29.94	29.48	30.52	30.49	30.32	29.73	27.79

AFM imaging (Figure 4.9) indicates modest changes to the roughness of the Bi-Te on different buffer layers. The Bi-Te film grown on PDMS presents a quite rough surface even though the substrate is smoother than some of the acrylate substrates.

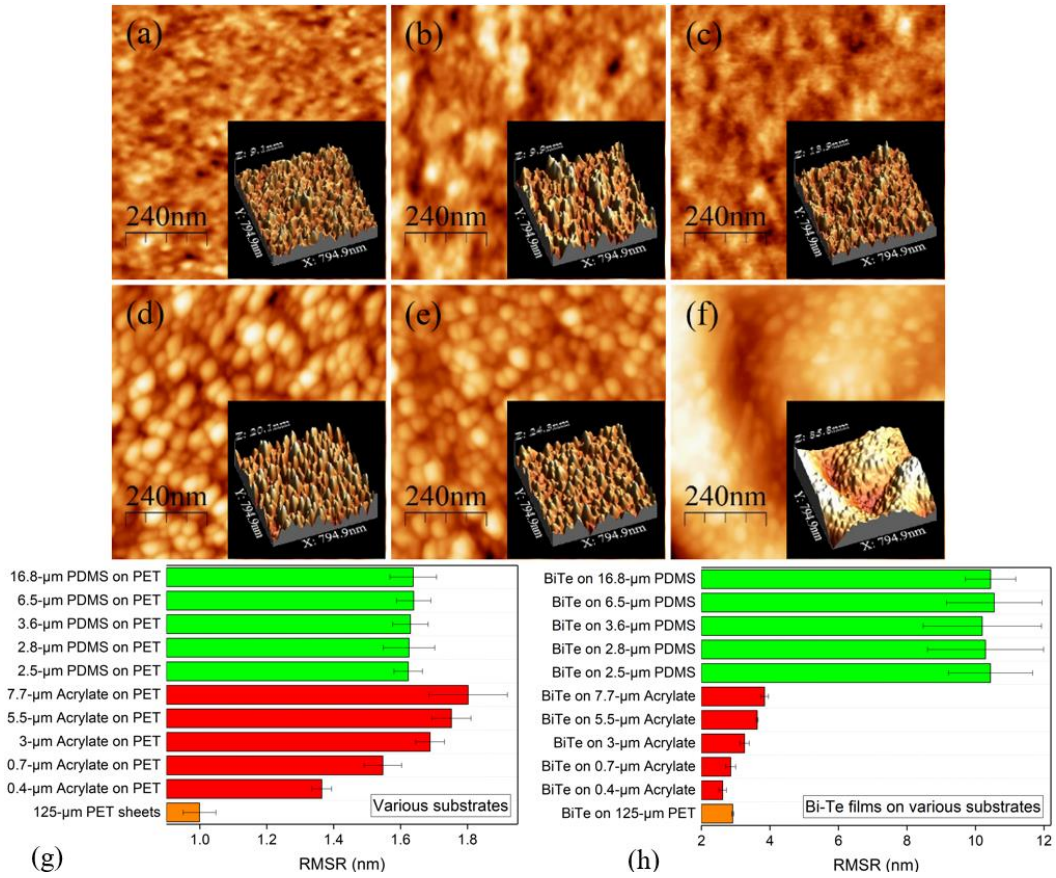


Figure 4.9. *AFM images of substrates (a) blank PET, (b) 0.4-μm acrylate layer on PET, (c) 16.8-μm PDMS layer on PET; and Bi-Te film grown on (a) (b) (c) corresponding to (d) (e) (f), respectively; RMSR of (g) PET substrates and buffer layers coated on PET substrates; (h) Bi-Te film grown on different substrates. (Inset of a-g: 3D images. The error bars in RMSR represent standard deviations from 6 AFM images: 0.5 μm×0.5 μm).*

4.6.2 Buckling test

Buckling tests were carried out using a rectangular sample (5 mm × 37 mm), see Chapter 2. The samples were taped to the rig on a region of the PET without coating see Figure 4.13 b inset. Both S and ρ were measured *in situ* while the sample was buckled.

Figure 4.10 illustrates two possible mechanisms that could help to maintain the functional performance of Bi-Te while the substrate is under strain and the strain is then transferred to the Bi-Te: (a) a sliding phenomenon (i.e. the frictional sliding at the interface [60]) that would depend on the interfacial adhesion strength between the coating and substrate [61]; (b) if a buffer layer is deformable, there will be less strain on top of the buffer layer (and thus on the Bi-Te coating) than that on the bottom.

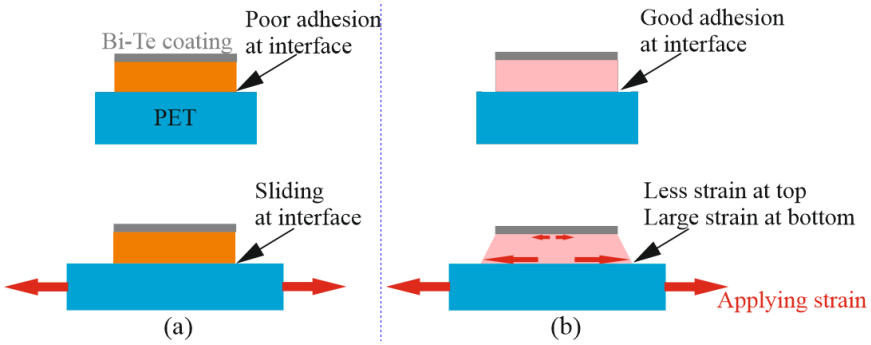


Figure 4.10. *Two mechanisms by buffer layers (in between PET and Bi-Te) to maintain the Bi-Te coating under tension.*

4.6.2.1 Changes in morphology during buckling strain

To observe the morphology clearly, the sample was imaged during buckling strain by MicroXAM. Figure 4.11 shows the cracking induced in the coating. All observed cracks are perpendicular to the buckling direction.

The 'PET sample' shows greater crack density compared with the 'acrylate sample' and the 'PDMS sample' under the same strain. As the thickness of the buffer layer decreases, both the 'acrylate and PDMS samples' show an increasing number of much more severe cracks. As the buckling strain increases, there is no crack observed until 1% buckling strain for the 'PET sample' (Figure 4.11 a, d, g, and j) and the 'acrylate sample' (Figure 4.11 b, e, f and k). In terms of the 'PDMS sample' (Figure 4.11 c, f, i and l), cracks are not easily observed especially under the feature of furrows, however, it should be noted

that one quite tiny crack starts to appear (in the middle section of Figure 4.11 c) under a buckling strain of 0.6%.

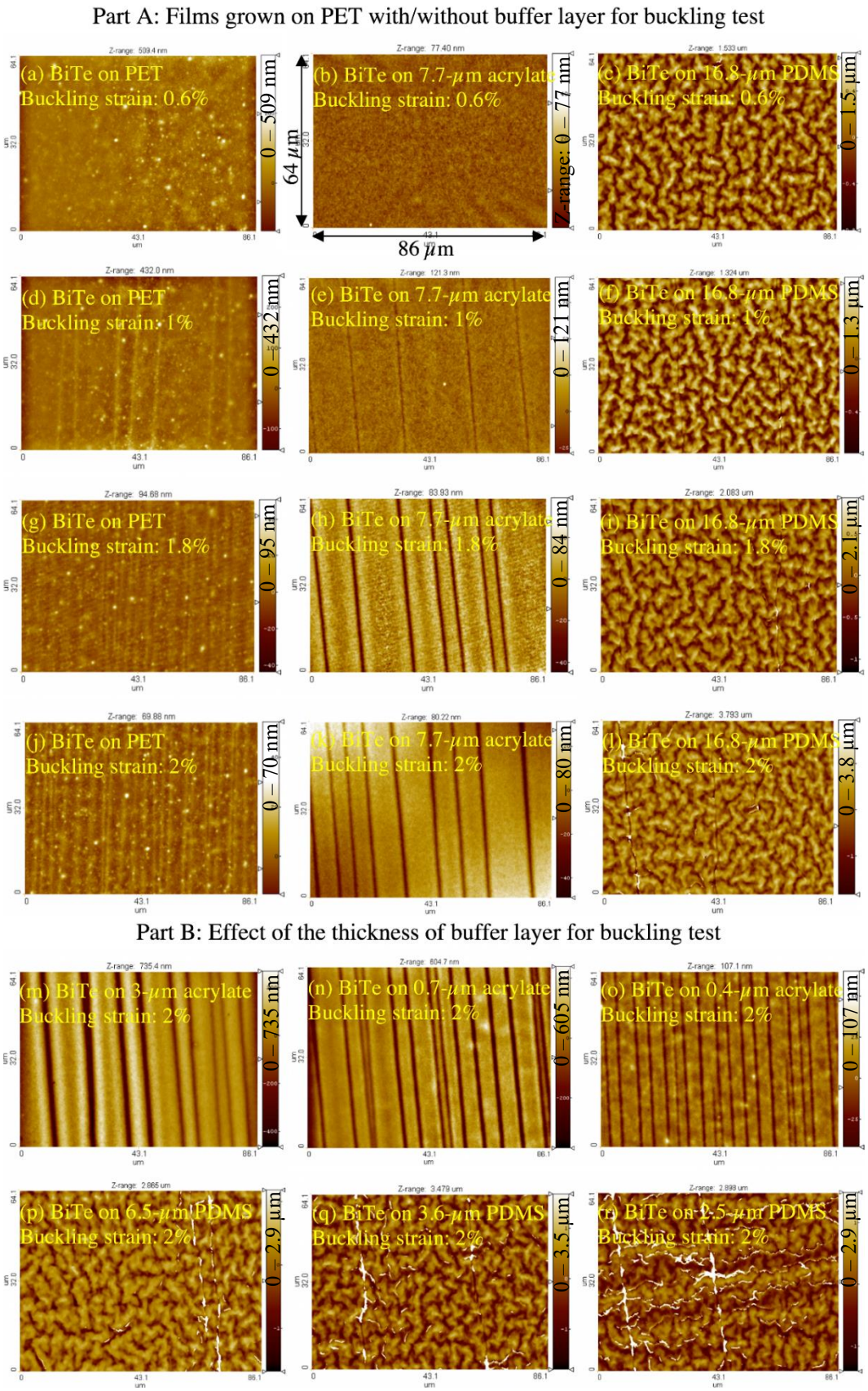


Figure 4.11. *MicroXAM images of during-buckling-strained Bi-Te films on PET sheets with/without buffer layers. Bi-Te film grown: on PET with buckling stains of (a) 0.6%, (d) 1%, (g) 1.8% and (j) 2%; on 7.7-μm acrylate/PET with buckling stains of (b) 0.6%, (e) 1%, (h) 1.8% and (k)2%; on 16.8-μm PDMS/PET with buckling stains of (c) 0.6%, (f) 1%, (i) 1.8% and (l) 2%. A variation of buffer-layer thickness: (m-o) acrylate; (p-r) PDMS.*

4.6.2.2 Changes in thermoelectric behaviours during buckling strain

The 'PET sample', in response to a rise in the buckling strain (see Figure 4.12 a), presents a decreasing trend in *PF* because of a slight decrease in *S* (3%) and a significant increase in ρ (2951%),

In Figure 4.12 b, the 'PDMS sample' behaves the best under 2% buckling strain indicating the thick PDMS buffer layer (16.8 μm) has more ability to maintain the film performance, as expected from Figure 4.10 b.

Figure 4.12 e, f, and g depict the effect of thickness of buffer layer. The *S* is changed by less than -3% so the change in ρ dominates the change in *PF*. It is observed that only the samples with the thicker acrylate (95.2%) or PDMS (93.8%) layers possess the ability to maintain *PF*, as contrasted to the 'PET sample' (96.9%). For the thinner samples, it is speculated that the buffer layer could be delaminated under the long-time buckling required to take electrical measurements, which makes the ρ worse than the pristine PET sample. This would strongly depend on the adhesion toughness of the coating, as reported [59]: with a small adhesion toughness, the delamination could occur at a lower buckling strain than under tension. In both manufacturing process and in-use condition, samples will not permanently stay under strain, hence the cyclical-buckling test is also of interest.

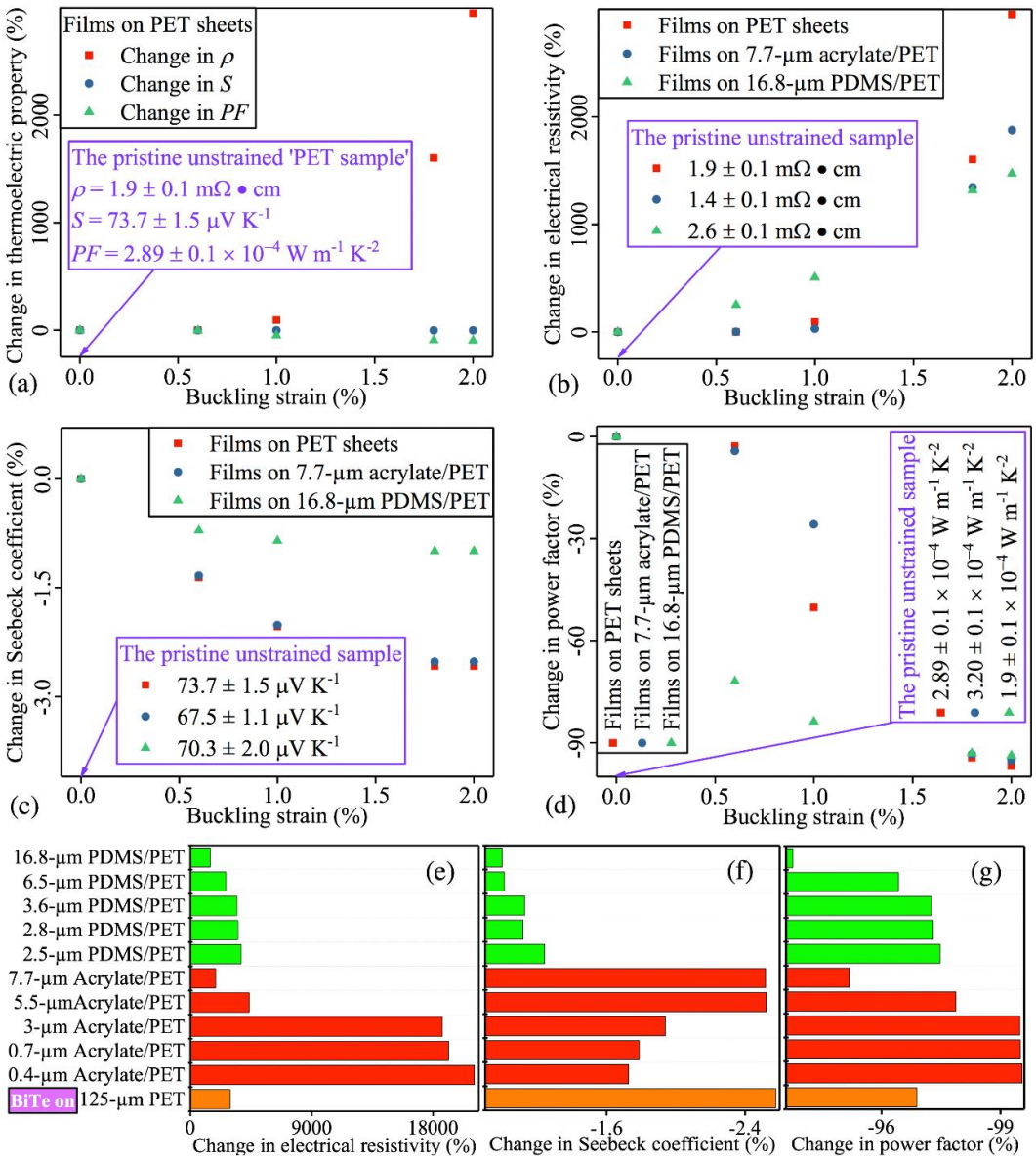


Figure 4.12. *(a) Changes in ρ, S and PF of Bi-Te film on PET under various strains during buckling test; (b-d) Changes in ρ, S and PF of Bi-Te film on PET with/without buffer layers under various strains; (e-g) Changes in ρ, S and PF of Bi-Te film on PET with various-thickness buffer layers during a buckling strain of 2%. (NB: all Bi-Te film in this study is n-type and the S herein is the magnitude of S. Hence, the change in S herein represents the change in the magnitude of S)*

4.6.2.3 Power measurements during cyclical buckling test

Cycles of bending increase the resistance of Bi-Te samples (Figure 4.13), consistent with the observation in [55], because the number of cracks increases with increasing bending

cycles [62]. There is negligible change in resistance under a buckling strain of 0.6%, and even 1%, which describes an elastic region. Under 1.8% strain, the resistance can come back to the original level after 3 cycles, but after this, the resistance (1.56 ± 0.05 kΩ) gradually increases and stabilises at 105 ± 2 kΩ in ~50 cycles, which indicates that more cracks can develop over the initial cycles until there are no more cracks formed under this strain (i.e. an equilibrium of cracking condition under a specific strain). The situation is even worse when the buckling strain is 2% (3-cycle come-back, 306 ± 6 kΩ at equilibrium).

As discussed, a strain within 1% is of principal interest in both manufacturing and in-use situations. Figure 4.13 a shows a ~15% increase in resistance under a strain of 1% after 80 cycles. Figure 4.13 c, e, and g present current, voltage, and calculated power (at 1.5 kΩ load, close to the maximum power point with ΔT = 14°C) during cyclical bending tests (1% strain). Each bending cycle (buckling + relaxing) requires 106, 100, and 96 s to apply equivalent strain (1%), for the 'PET, acrylate, and PDMS samples', respectively due to the different displacements required to accommodate the thickness differences. The 'PET sample' failed (i.e. zero current output) at around 1000 s (4 cycles), the 'acrylate sample' almost failed at around 2000 s (14 cycles), and the 'PDMS sample' still worked after 8000 s (80 cycles). This is also the case for voltage output, and thus the power calculated from current and voltage. As can be seen in Figure 4.13 g, the 'PDMS sample' has a stable power output between 6000 – 8000 s (~0.02 nW which is about 90% less than the starting point 0.2 nW). Overall, the cyclical fatigue behaviour of the 'acrylate sample' is very poor because of its poor recovery capability, while the 'PDMS sample' can improve the cyclical fatigue significantly and still work after 80 cycles of buckling tests.

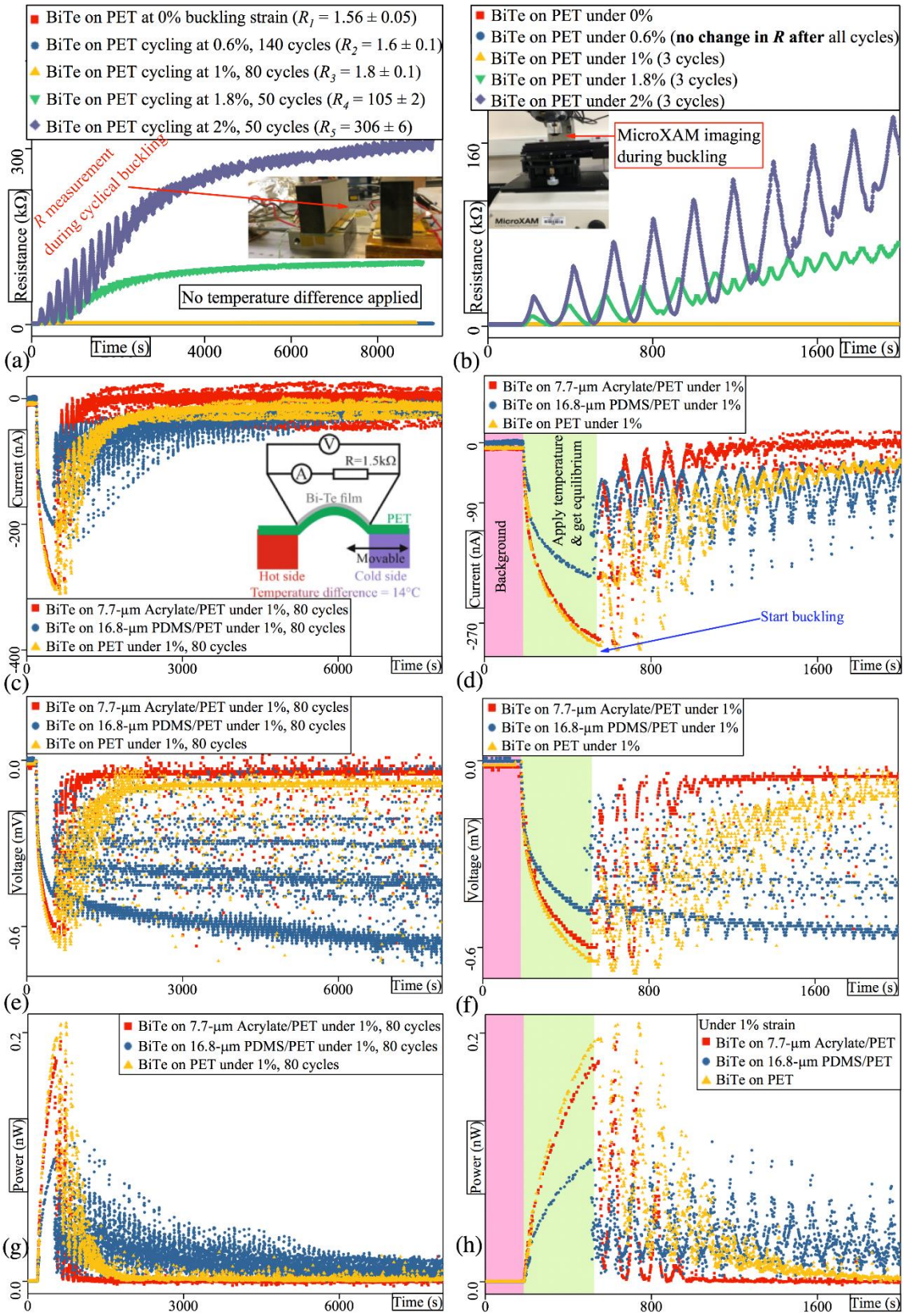


Figure 4.13. *(a) Resistance measurement for Bi-Te film grown on PET sheets under various buckling strains in cycling fatigue testing; (c) Current, (e) Voltage and (g) Power*

measurements of Bi-Te film on PET substrates (strip: 5-mm width × 37-mm length) with/without buffer layers in cycles of 1%-strain buckling tests. (b)(d)(f)(h) are zoomed-in regions from (a)(c)(e)(g), respectively.

4.7 Summary

To investigate feasible post-deposition annealing approaches suitable for R2R processing, I fabricated 1-μm thick Bi-Te films at RT using DC magnetron sputtering onto 125-μm thick PI film, and then post-annealed the coatings using IR and e-beam irradiation in the webcoater. In addition, static post-annealing strategies that are commonly used in the laboratory (i.e. vacuum oven and pulsed e-beam irradiation) were studied as control groups. The static pulsed e-beam irradiation was found to be too aggressive showing micro-cracks on the film's surface, confirmed in SEM images, while, as expected/reported, annealing in a vacuum oven significantly improved the film's crystallinity (increasing crystallite size and decreasing micro-strain) and decreased Te content in the film, and *PF* was enhanced by 400%.

Both IR and e-beam irradiations were compatible with R2R processes. After these two treatments, there was no observed change in the film's crystallinity but the average crystallite size slightly increased. *PF* was improved by 146% and 64% after IR and e-beam irradiations, respectively. The effect of annealing time was further investigated to guide the design of an R2R process. After a 1-min treatment on a rotating drum, the film annealed with IR irradiation had a much better improvement on *PF* (improved 11.4%) than that annealed in e-beam irradiation. Hence, IR treatment is more feasible to anneal Bi-Te films in a high throughput R2R process, also because it does not have a significant effect on the mechanical property of PI film.

This study investigated a feasible post-deposition annealing method for flexible TE films to be compatible with high-throughput R2R processes, and achieved an improvement on

TE performance by post-deposition annealing Bi-Te films, demonstrating a step forward for commercialisation of flexible TEGs.

An experimental study was carried out to investigate the mechanical stability of ~90-nm thick Bi-Te film grown on flexible polymer sheets (~125 μm PET), and two types of buffer layers (0.4-7.7 μm-thick Acrylate and 2.5-16.8 μm-thick PDMS) were proposed to improve the mechanical resilience.

During buckling, samples with acrylate buffer layers show an ability to maintain thermoelectric performance, while samples with PDMS layers show a larger change in resistivity once the strain is applied, indicating an elastic behaviour of PDMS, however in cyclical-bending tests, the sample with PDMS shows much better ability to recover than others, maintaining good performance over many cycles.

4.8 Reference

[1] Shen, J.; Zhu, T.; Zhao, X.; Zhang, S.; Yang, S.; Yin, Z. , Recrystallization induced in situ nanostructures in bulk bismuth antimony tellurides: a simple top down route and improved thermoelectric properties, *Energy Environ. Sci.* 2010*, 3*, 1519-1523, https://doi.org/10.1039/C0EE00012D.

[2] Manzano, C. V.; Abad, B.; Rojo, M. M.; Koh, Y. R.; Hodson, S. L.; Martinez, A. M. L.; Xu, X.; Shakouri, A.; Sands, T. D.; Borca-Tasciuc, T. , Anisotropic effects on the thermoelectric properties of highly oriented electrodeposited Bi2Te3 films, *Sci. Rep.* 2016*, 6*, 19129, https://doi.org/10.1038/srep19129.

[3] Antonova, E. E.; Looman, D. C. , Finite elements for thermoelectric device analysis in ANSYS, 2005, 215-218, https://doi.org/10.1109/ICT.2005.1519922.

[4] Fleurial, J. P.; Gailliard, L.; Triboulet, R.; Scherrer, H.; Scherrer, S. , Thermal properties of high quality single crystals of bismuth telluride—Part I: Experimental characterization, *J Phys Chem Solids.* 1988*, 49*, 1237-1247, https://doi.org/10.1016/0022-3697(88)90182-5.

[5] Duan, X.; Jiang, Y. , Annealing effects on the structural and electrical transport properties of n-type Bi2Te2.7Se0.3 thin films deposited by flash evaporation, *Appl. Surf. Sci.* 2010*, 256*, 7365-7370, https://doi.org/10.1016/j.apsusc.2010.05.069.

[6] Zheng, Z.; Fan, P.; Liang, G.; Zhang, D.; Cai, X.; Chen, T. , Annealing temperature influence on electrical properties of ion beam sputtered Bi2Te3 thin films, *J Phys Chem Solids.* 2010*, 71*, 1713-1716, https://doi.org/10.1016/j.jpcs.2010.09.012.

[7] Lee, D.; Lim, C.; Cho, D.; Lee, Y.; Lee, C. , Effects of annealing on the thermoelectric and microstructural properties of deformed n-type Bi2Te3-based compounds, *Journal of Electronic Materials.* 2006*, 35*, 360-365, https://doi.org/10.1007/BF02692457.

[8] Huang, H.; Luan, W.; Tu, S. , Influence of annealing on thermoelectric properties of bismuth telluride films grown via radio frequency magnetron sputtering, *Thin Solid Films.* 2009*, 517*, 3731-3734, https://doi.org/10.1016/j.tsf.2009.01.015.

[9] Sudarshan, C.; Jayakumar, S.; Vaideki, K.; Sudakar, C. , Effect of vacuum annealing on structural, electrical and thermal properties of e-beam evaporated Bi2Te3 thin films, *Thin Solid Films.* 2017*, 629*, 28-38, https://doi.org/10.1016/j.tsf.2017.03.043.

[10] Singkaselit, K.; Sakulkalavek, A.; Sakdanuphab, R. , Effects of annealing temperature on the structural, mechanical and electrical properties of flexible bismuth telluride thin films prepared by high-pressure RF magnetron sputtering, *Ansn.* 2017*, 8*, 350021-350027, https://doi.org/10.1088/2043-6254/aa7222.

[11] Nishino, T.; Suzuki, T. , Flexible thermoelectric generator with efficient vertical to lateral heat path films, *Journal of Micromechanics and Microengineering.* 2017*, 27*, 35011, https://doi.org/10.1088/1361-6439/aa5aad.

[12] Takemori, D.; Okuhata, M.; Takashiri, M. , Thermoelectric Properties of Electrodeposited Bismuth Telluride Thin Films by Thermal Annealing and Homogeneous Electron Beam Irradiation, *ECS Trans.* 2017*, 75*, 123-131, https://doi.org/10.1149/07552.0123ecst.

[13] Kim, J.; Choi, J.; Bae, J.; Kim, M.; Oh, T. , Thermoelectric Characteristics of n-Type Bi2Te3 and p-Type Sb2Te3 Thin Films Prepared by Co-Evaporation and Annealing for Thermopile Sensor Applications, *Mater. Trans.* 2013*, 54*, 618-625, https://doi.org/10.2320/matertrans.M2013010.

[14] Kudo, S.; Tanaka, S.; Miyazaki, K.; Nishi, Y.; Takashiri, M. , Anisotropic Analysis of Nanocrystalline Bismuth Telluride Thin Films Treated by Homogeneous Electron Beam Irradiation, *Mater. Trans.* 2017*, 58*, 513-519, https://doi.org/10.2320/matertrans.M2016295.

[15] Takashiri, M.; Uyama, M.; Imai, K. , Comparison of crystal growth and thermoelectric properties of n-type Bi-Se-Te and p-type Bi-Sb-Te nanocrystalline thin films: Effects of homogeneous irradiation with an electron beam, *J. Appl. Phys.* 2014*, 115*, 2143111-2143117, https://doi.org/10.1063/1.4881676.

[16] Chatterjee, K.; Suresh, A.; Ganguly, S.; Kargupta, K.; Banerjee, D. , Synthesis and characterization of an electro-deposited polyaniline-bismuth telluride nanocomposite — A novel thermoelectric material, *Mater. Charact.* 2009*, 60*, 1597-1601, https://doi.org/10.1016/j.matchar.2009.09.012.

[17] Carroll, E.; Buckley, D.; Mogili, N. V. V.; McNulty, D.; Moreno, M. S.; Glynn, C.; Collins, G.; Holmes, J. D.; Razeeb, K. M.; O'Dwyer, C. , 2D Nanosheet Paint from Solvent-Exfoliated Bi2Te3 Ink, *Chem. Mater.* 2017*, 29*, 7390-7400, https://doi.org/10.1021/acs.chemmater.7b02321.

[18] Mohammed Khalaf, E. , Improvement of Chemical and Thermal Properties of Polyethylene Terephthalate (PET) by Using Multi-walled Carbon Nanotubes (MWCNTs), *Ijmsa.* 2016*, 5*, 297-301, https://doi.org/10.11648/j.ijmsa.20160506.20.

[19] Maurer, M. L.; Tooker, A. C.; Felix, S. H. , Characterization of polyimide via FTIR analysis, *SciTech Connect.* 2014, 1-8, https://www.pdffiller.com/101226832-780487pdf-Characterization-of-polyimide-via-FTIR-analysis-e-reports-ext-llnl-.

[20] Ozur, G. E.; Proskurovsky, D. I. , Generation of Low-Energy High-Current Electron Beams in Plasma-Anode Electron Guns, *Plasma Phys. Rep.* 2018*, 44*, 18-39, https://doi.org/10.1134/S1063780X18010130.

[21] Greenaway, D. L.; Harbeke, G. , Band structure of bismuth telluride, bismuth selenide and their respective alloys, *J Phys Chem Solids.* 1965*, 26*, 1585-1604, http://dx.doi.org/10.1016/0022-3697(65)90092-2.

[22] Kaddouri, E. H.; Maurice, T.; Gratens, X.; Charar, S.; Benet, S.; Mefleh, A.; Tedenac, J. C.; Liautard, B. , Optical Properties of Bismuth Telluride Thin Films, Bi2Te3/Si(100) and Bi2Te3/SiO2/Si(100), *Phys. Status Solidi.* 1999*, 176*, 1071-1076, http://dx.doi.org/10.1002/(SICI)1521-396X(199912)176:23.0.CO;2-E.

[23] Deng, Y.; Liang, H.; Wang, Y.; Zhang, Z.; Tan, M.; Cui, J. , Growth and transport properties of oriented bismuth telluride films, *J. Alloys Compd.* 2011*, 509*, 5683-5687, https://doi.org/10.1016/j.jallcom.2011.02.123.

[24] Zhang, J. X.; Li, Q.; Niu, P. J.; Yang, Q. X.; Tan, B. M.; Niu, X. H.; Gao, B. H. , Effect of annealing temperature on microstructure and thermoelectric properties of bismuth–telluride multilayer thin films prepared by magnetron sputtering, *Mater. Res. Innov.* 2015*, 19*, S10-412, https://doi.org/10.1179/1432891715Z.0000000002209.

[25] Vieira, E.; Figueira, J.; Pires, A. L.; Grilo, J.; Silva, M. F.; Pereira, A. M.; Goncalves, L. M. , Bi2Te3 and Sb2Te3 Thin Films with Enhanced Thermoelectric Properties for Flexible Thermal Sensors, *Proceedings.* 2018*, 2*, 8151-8154, https://doi.org/10.3390/proceedings2130815.

[26] El-Sayed, H. E. A. , Structural and optical properties of thermally evaporated Bi2Te3 films, *Appl. Surf. Sci.* 2005*, 250*, 70-78, https://doi.org/10.1016/j.apsusc.2004.12.025.

[27] G. D. Deshmukh; S. M. Patil; S. S. Patil; P. H. Pawar. , Effect of Film Thickness on Structural and Optical Properties of Bi2Te3 Thin Films, *J. Chem. Biol. Phys. Sci.* 2015*, 5*, 2769-2779, https://www.jcbsc.org/admin/get_filephy.php?id=335.

[28] Liao, C.; Liou, K. , Electric current enhanced defect elimination in thermally annealed Bi-Sb-Te and Bi-Se-Te thermoelectric thin films, *J. Appl. Phys.* 2010*, 108*, 537111, http://dx.doi.org/10.1063/1.3477184.

[29] Faraji, L. S.; Singh, R. P.; Allahkarami, M. , Pulsed laser deposition of bismuth telluride thin film and annealing effects, *EPJ Appl. Phys.* 2009*, 46*, 205011-205015, https://doi.org/110.1051/epjap/2009053.

[30] Kim, H.; Yim, J.; Choi, W.; Park, C.; Kim, J. , The Effect of Annealing in Controlled Vapor Pressure on the Thermoelectric Properties of RF-Sputtered Bi2Te3 Film, *J. Electron. Mater.* 2012*, 41*, 1519-1523, https://doi.org/10.1007/s11664-012-1938-4.

[31] Navone, C.; Soulier, M.; Plissonnier, M.; Seiler, A. L. , Development of (Bi,Sb)2(Te,Se)3-Based Thermoelectric Modules by a Screen-Printing Process, *J. Electron. Mater.* 2010*, 39*, 1755–1759, https://doi.org/10.1007/s11664-010-1187-3.

[32] Miyazaki, K.; Kurosaki, J.; Takashiri, M.; Tsukamoto, H.; Tanaka, S.; Nagai, D. , Effect of grain size on thermoelectric properties of n -type nanocrystalline bismuth-telluride based thin films, *J. Appl. Phys.* 2008*, 104*, 843021, http://dx.doi.org/10.1063/1.2990774.

[33] Krumrain, J.; Mussler, G.; Borisova, S.; Stoica, T.; Plucinski, L.; Schneider, C. M.; Grtzmacher, D. , MBE growth optimization of topological insulator Bi2Te3 films, *J. Cryst. Growth.* 2011*, 324*, 115-118, https://doi.org/10.1016/j.jcrysgro.2011.03.008.

[34] Pilaipon Nuthongkum; Rachsak Sakdanuphab; Mati Horprathum; Aparporn Sakulkalavek , [Bi]:[Te] Control, Structural and Thermoelectric Properties of Flexible Bi^sub x^Te^sub y^ Thin Films Prepared by RF Magnetron Sputtering at Different Sputtering Pressures, *J. Electron. Mater.* 2017*, 46*, 6444–6450, https://doi.org/10.1007/s11664-017-5671-x.

[35] Lanson, B. , Decomposition of Experimental X-ray Diffraction Patterns (Profile Fitting): A Convenient Way to Study Clay Minerals, *Clays Clay Miner.* 1997*, 45*, 132-146, https://doi.org/10.1346/CCMN.1997.0450202.

[36] Na, J.; Kim, Y.; Park, T.; Park, C.; Kim, E. , Preparation of Bismuth Telluride Films with High Thermoelectric Power Factor, *ACS Appl. Mater. Interfaces.* 2016*, 8*, 32392-32400, https://doi.org/10.1021/acsami.6b10188.

[37] Kim, Y.; Cho, S.; DiVenere, A.; Wong, G. K. L.; Ketterson, J. B. , Composition-dependent layered structure and transport properties in BiTe thin films, *Phys. Rev. B.* 2001*, 63*, 1553061-1553065, https://doi.org/10.1103/PhysRevB.63.155306.

[38] Arunachalam, A.; Dhanapandian, S.; Manoharan, C.; Sivakumar, G. , Physical properties of Zn doped TiO2 thin films with spray pyrolysis technique and its effects in antibacterial activity, *Spectrochim. Acta A Mol. Biomol. Spectrosc.* 2015*, 138*, 105-112, https://doi.org/10.1016/j.saa.2014.11.016.

[39] Park, N.; Lee, W.; Hong, J.; Park, T.; Yoon, S.; Im, H.; Kim, H.; Lee, S. , Effect of grain size on thermal transport in post-annealed antimony telluride thin films, *Nanoscale Res. Lett.* 2015*, 10*, 1-9, https://doi.org/10.1186/s11671-015-0733-6.

[40] Chu, H.; Liou, K.; Liao, C. , Enhancement of thermoelectric properties of sputtered Bi-Sb-Te thin films by electric current stressing, *Appl. Phys. Lett.* 2008*, 93*, 421031, http://dx.doi.org/10.1063/1.2965487.

[41] Snyder, G. J.; Toberer, E. S. , Complex thermoelectric materials, *Nat. Mater.* 2008*, 7*, 105-114, http://doi.org/10.1038/nmat2090.

[42] Levin, E. M. , Charge carrier effective mass and concentration derived from combination of Seebeck coefficient and Te125 NMR measurements in complex tellurides, *Phys. Rev. B.* 2016*, 93*, 2452021-2452025, https://doi.org/10.1103/PhysRevB.93.245202.

[43] Petsagkourakis, I.; Pavlopoulou, E.; Cloutet, E.; Chen, Y. F.; Liu, X.; Fahlman, M.; Berggren, M.; Crispin, X.; Dilhaire, S.; Fleury, G.; Hadziioannou, G. , Correlating the Seebeck coefficient of thermoelectric polymer thin films to their charge transport mechanism, *Org. Electron.* 2018*, 52*, 335-341, http://dx.doi.org/10.1016/j.orgel.2017.11.018.

[44] Damodara Das, V.; Soundararajan, N.; Pattabi, M. , Electrical conductivity and thermoelectric power of amorphous Sb2Te3 thin films and amorphous-crystalline transition, *J. Mater. Sci.* 1987*, 22*, 3522-3528, https://doi.org/10.1007/BF01161452.

[45] H Julian Goldsmid , Bismuth Telluride and Its Alloys as Materials for Thermoelectric Generation, *Materials.* 2014*, 7*, 2577-2592, https://doi.org/10.3390/ma7042577.

[46] K Sharma; M Lal; V K Gumber; A Kumar; N Chaudary; N Goyal. , Effect of Composition on Optical and Thermoelectric Properties of Microstructured p-type (Bi2Te3)x(Sb2Te3)1 - x Alloys, *J. Nano- Electron. Phys.* 2014*, 6*, 1007-1, https://doi.org/2077-6772/2014/6(1)01007(6).

[47] Gibbs, Z. M.; Kim, H.; Wang, H.; Snyder, G. J. , Band gap estimation from temperature dependent Seebeck measurement—Deviations from the 2e|S|maxTmax relation, *Appl. Phys. Lett.* 2015*, 106*, 221121-221125, http://dx.doi.org/10.1063/1.4905922.

[48] M. Bachmann, M. Czerner, and C. Heiliger. , Ineffectiveness of energy filtering at grain boundaries for thermoelectric materials, *Phys. Rev. B. , 86*, 1153201- 1153206, https://doi.org/10.1103/PhysRevB.86.115320.

[49] Cho, S.; Kim, Y.; DiVenere, A.; Wong, G. K.; Ketterson, J. B.; Meyer, J. R. , Antisite defects of Bi2Te3 thin films, *Appl. Phys. Lett.* 1999*, 75*, 1401-1403, https://doi.org/10.1063/1.124707.

[50] Hada, M.; Norimatsu, K.; Tanaka, S.; Keskin, S.; Tsuruta, T.; Igarashi, K.; Ishikawa, T.; Kayanuma, Y.; Miller, R. J. D.; Onda, K.; Sasagawa, T.; Koshihara, S.; Nakamura, K. G. , Bandgap modulation in photoexcited topological insulator Bi2Te3 via atomic displacements, *J. Chem. Phys.* 2016*, 145*, 245041, https://doi.org/10.1063/1.4955188.

[51] Tao, X.; Wan, K.; Deru, J.; Bilotti, E.; Assender, H. E. , Thermoelectric behaviour of Bi-Te films on polymer substrates DC-sputtered at room-temperature in moving web deposition, *Surf. Coat. Technol.* 2020*, 385*, 125393, http://doi.org/10.1016/j.surfcoat.2020.125393.

[52] Lal, S.; Gautam, D.; Razeeb, K. M. , Optimization of annealing conditions to enhance thermoelectric performance of electrodeposited p-type BiSbTe thin films, *APL Mater.* 2019*, 7*, 311021, https://doi.org/10.1063/1.5049586.

[53] Lu, J.; Guo, R.; Dai, W.; Huang, B. , Enhanced thermoelectric figure-of-merit in boron-doped SiGe thin films by nanograin boundaries, *Nanoscale.* 2014*, 7*, 7331-7339, https://doi.org/10.1039/c5nr00181a.

[54] Zhang, A. B.; Wang, B. L.; Wang, J.; Du, J. K.; Xie, C. , Effect of cracking on the thermoelectric conversion efficiency of thermoelectric materials, *Journal of Applied Physics.* 2017*, 121*, 45105, http://dx.doi.org/10.1063/1.4974848.

[55] Zhuo Cao; Tudor, M. J.; Torah, R. N.; Beeby, S. P. , Screen Printable Flexible BiTe-SbTe-Based Composite Thermoelectric Materials on Textiles for Wearable Applications, *IEEE Transactions on Electron Devices.* 2016*, 63*, 4024-4030, https://doi.org/10.1109/TED.2016.2603071.

[56] Singkaselit, K.; Sakulkalavek, A.; Sakdanuphab, R. , Effects of annealing temperature on the structural, mechanical and electrical properties of flexible bismuth telluride thin films prepared by high-pressure RF magnetron sputtering, *Ansn.* 2017*, 8*, 350021-350027, https://doi.org/10.1088/2043-6254/aa7222.

[57] Kong, D.; Zhu, W.; Guo, Z.; Deng, Y. , High-performance flexible Bi2Te3 films based wearable thermoelectric generator for energy harvesting, *Energy.* 2019*, 175*, 292-299, https://doi.org/10.1016/j.energy.2019.03.060.

[58] Cosnahan, T.; Watt, A. A. R.; Assender, H. E. , Flexography Printing for Organic Thin Film Transistors, *Materials Today: Proceedings.* 2018*, 5*, 16051-16057, https://doi.org/10.1016/j.matpr.2018.05.050.

[59] Chen, Z.; Cotterell, B.; Wang, W. , The fracture of brittle thin films on compliant substrates in flexible displays, *Eng. Fract. Mech.* 2002*, 69*, 597-603, https://doi.org/10.1016/S0013-7944(01)00104-7.

[60] Collino, R. R.; Philips, N. R.; Rossol, M. N.; McMeeking, R. M.; Begley, M. R. , Detachment of compliant films adhered to stiff substrates via van der Waals interactions: role of frictional sliding during peeling, *Journal of the Royal Society, Interface.* 2014*, 11*, 20140453, https://doi.org/10.1098/rsif.2014.0453.

[61] Chen, Z.; Zhou, K.; Lu, X.; Lam, Y. , A review on the mechanical methods for evaluating coating adhesion, *Acta Mechanica.* 2014*, 225*, 431-452, https://doi.org/10.1007/s00707-013-0979-y.

[62] Hsu, J.; Lee, C.; Wen, B.; Huang, P.; Xie, C. , Experimental and Simulated Investigations of Thin Polymer Substrates with an Indium Tin Oxide Coating under Fatigue Bending Loadings, *Materials (Basel, Switzerland).* 2016*, 9*, 720, https://doi.org/10.3390/ma9090720.

[63] J. Szabo, M. Robin, V. Hruby, Bismuth Vapor Hall Effect Thruster Performance and Plume Experiments, 2017, http://electricrocket.org/IEPC/IEPC_2017_25.pdf

[64] P. Michelato, E. Cavaliere, C. Pagani, E. Bari & A. Bonucci, Vacuum Interface Analysis of a Windowless Spallation Target for Accelerator-Driven Systems, 2007, 157, https://doi.org/10.13182/NSE07-A2715

Chapter 5 Replacing a solid shadow mask by selective metallisation technique (compatible with R2R), to make in-line patterns

A real industrial R2R process with selective metallization technique (i.e. a combination of flexography and physical vapour deposition techniques) is explored for large-scale manufacture of flexible TEGs.

5.1 Introduction

This study focuses on an engineering challenge for large-scale manufacture in commercialisation: how to make in-line patterns for a flexible TEG in industry. R2R manufacture of flexible electronics is a developing field as a low-cost and high throughput means for technology transfer from laboratory to industry. Flexible TEGs can be printed onto flexible substrates on rollers in a fast R2R process using e.g. screen-printing [1, 2], inkjet printing [3], dispenser printing [4]. However, these solution-based printing techniques have an inherent drawback to fabricate thin-film TEGs: the film thickness cannot reach nano-size range. However, nanostructured TEGs give the prospect to significantly improve the device performance. Recent advances in a combination of flexography oil masking technique and thermal evaporation (as called selective metallization technique, SMT [5]) proposed a new idea to fabricate in-line patterns of nano-thick metals in a fast R2R process. In SMT, vacuum oil masking is printed onto a polymer web, then metal is vapour deposited during which the oil is evaporated by source radiative heating and the metallisation.

In addition to evaporation, sputtering is another promising technique for large-scale manufacture because of its easy incorporation in R2R [6] and compatibility with in-line

fabrication [7, 8]. Typically, evaporation of functional materials (e.g. Bi-Te) requires multiple co-evaporation boats and power systems for each element, while sputtering is much easier for accurate process control of deposition functional thin films. Often superior functional properties can be achieved with sputtered layers and hence it is widely industrially applied despite typically being slower than evaporation. Further study using SMT by sputtering [9] demonstrated a successful in-line pattern of flexible electrodes for TEGs, however, the sputtering deposition provided insufficient energy to completely remove the residual oil and thus a post-cleaning process (with isopropanol washing) was required. Obviously, chemical solution washing is not the desired method in a thin-film fabrication because of the inevitable damage to nanostructures and the economics of the process. Hence, I carried out a further study of the combination of SMT with sputtering. In this study, SMT employs Krytox® vacuum oil as the liquid mask. The oil has a vapour temperature in a vacuum as shown in Figure 0.1. Hence, post-deposition heat treatment is considered to remove residual oil. A vacuum oven [10-14] is the most simple and common method but it is not compatible with flexible polymer substrates in R2R as considered the blocking/melting issue of polymer roll. Two feasible post-annealing strategies, IR and e-beam irradiations, are proposed in this study to remove the residual oil without damage to the functional coating and polymer substrate. If either of these two methods are demonstrated to work, more physical vapour deposition techniques could be considered to integrate into SMT. This would make a step closer to a real R2R high-throughput manufacture of flexible electronics for commercialisation.

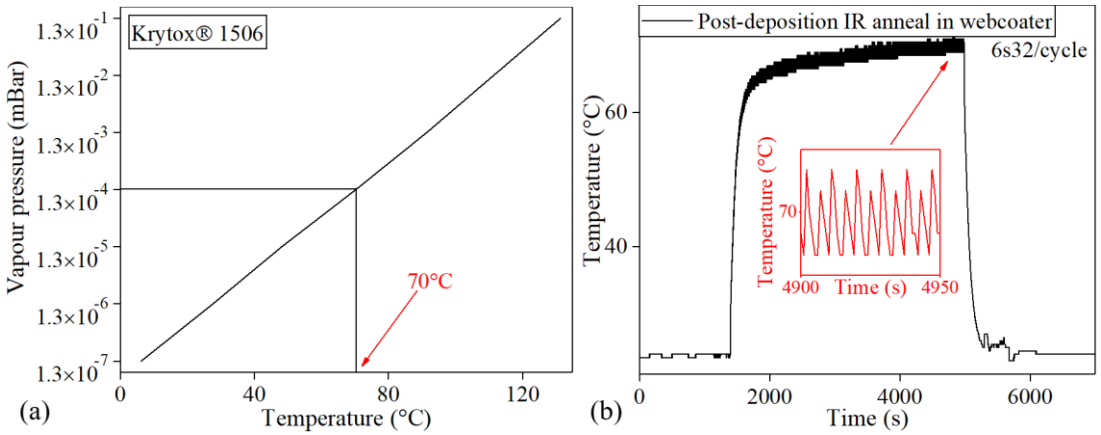


Figure 0.1. *(a) Plot of vapour pressure and temperature of Krytox® 1506 vacuum oil; (b) Temperature recording of IR source in web coater (a thermocouple was attached on the drum and the temperature number fluctuates around 70 ℃ as the drum rotates).*

5.2 Roll-to-roll manufacture of flexible TEGs using SMT

A continuous R2R process was broken into stepwise processes as shown in Figure 0.2 a. SMT with evaporation was used to make in-line patterns of Cu electrodes, followed by IR or e-beam irradiation. Then, the oil printing pattern plate was replaced for TE materials. SMT with sputtering was used to make patterns of Bi-Te film aligned to the previously deposited Cu patterns, followed by post-deposition treatments. The flexography part was pulled back after the 1st rotation of the drum to deposit the oil pattern, then multiple passes of the oiled substrate over the vapour source for the film deposition and simultaneous removal of oil, following an IR or e-beam treatments for completion of oil removal.

All films were fabricated onto 125 µm-thick PET webs (in-line speed: 25 m/min) under a base pressure of 1.3 × 10^{-4} mbar. The sputtering condition has been optimized from previous chapters (Ar flow rate: 250 sccm, DC power: 0.25 kW). In terms of the evaporation, Cu wire (1.2 mm diameter, Speedmet 98 Welding Alloys) was fed into two resistively heated ceramic boats (Sintec Ceramics) for thermal evaporation under a power of ~500 A and a source-to-substrate distance of 180 mm.

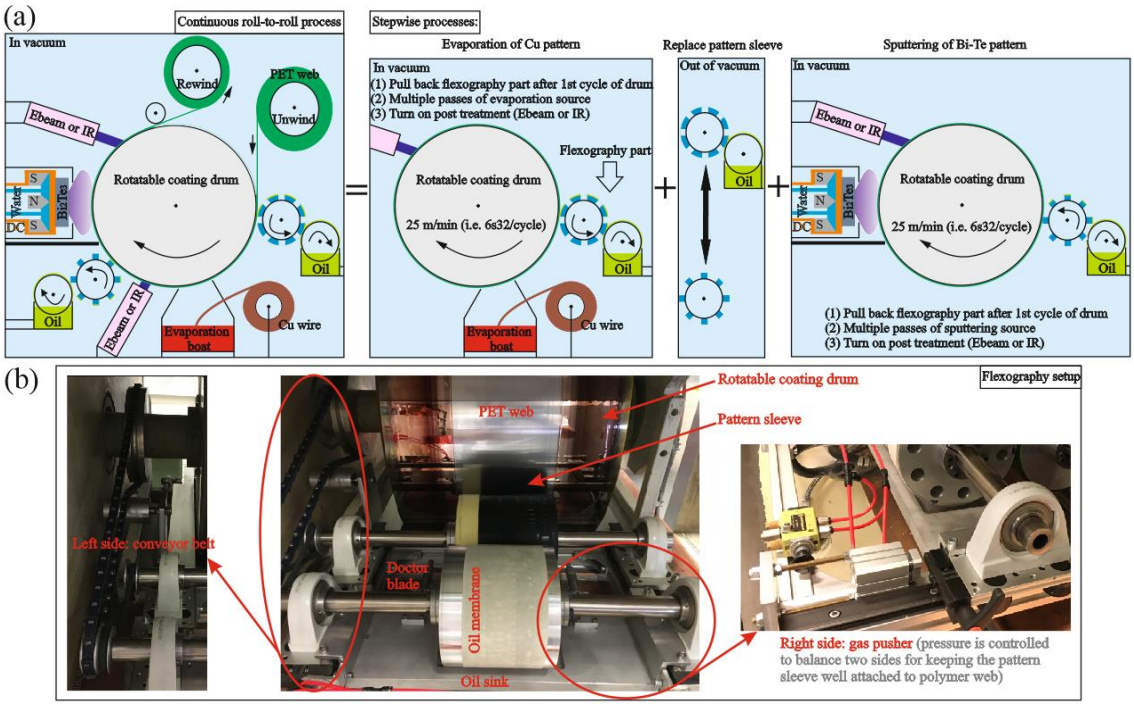


Figure 0.2. *(a) Schematics of continuous R2R setups and stepwise processes used in this work where SMT with evaporation of Cu was made in three individual processes: flexography + evaporation (2 cycles) + post-deposition treatment; The oil pattern plate of Cu was placed with one for the Bi-Te pattern; SMT with sputtering (20 cycles) of Bi-Te was also made followed by post-deposition treatment to remove oil. (b) A real image of flexography setup (left side with conveyor belt at left side and gas pusher at right side to balance the pattern plate).*

5.3 Results and discussion

5.3.1 Non-SMT fabricated samples

5.3.1.1 Phase identification

The purpose of using post-deposition treatments is to only remove the residual oil after SMT, without any damage to the functional coating and polymer substrate (NB: a strong post anneal could improve the film performance but also could damage the polymer substrate). Thus, to start with, non-SMT samples (films manufactured without oil patterns) were characterised to identify the material phase and to assess the effect of the potential

oil removal treatments on the electrical performance of the films. The thicknesses of as-deposited (evaporated) Cu and (sputtered) Bi-Te films were 105 (± 6) nm and 63 (± 6) nm, respectively. Unlike the 80-nm Bi-Te film (in Chapter 3) that the (1 0 10) peak observed, there is no peak in the 60-nm Bi-Te film in Figure 0.3 b although the XPS result confirms the presence of Bi and Te elements.

In Figure 0.3 a, both XRD and XPS results confirm the phase of Cu in the evaporated film. Because the film is very thin, there is not much intensity to the (1 1 1) peak. After an IR treatment under ~70°C, there is no obvious change with increasing the annealing time (see Figure 0.3 c). Short-time e-beam treatment can slightly increase the (1 1 1) peak of Cu films, revealing that this e-beam system is strong enough to enhance the crystallinity of as-evaporated Cu films, similar as observed in [15]. The depth of e-beam irradiation was reported as ~50 μm [16], which could anneal the whole thickness of Cu films in this case. However, due to such a strong e-beam, a long-time (50-min) irradiation destroys the (1 1 1) peak, indicating that the film is damaged. This is also observed in an image inset Figure 0.4, in which a 50-min e-beam irradiation partially removes the coating of Cu, and a significant increase in resistivity is measured. These suggest that the Cu coating can be removed by a 50-min e-beam irradiation until the polymer substrate is exposed. The sputtered Bi-Te film seems to be less etched, perhaps because of the covalent nature of Bi-Te [17].

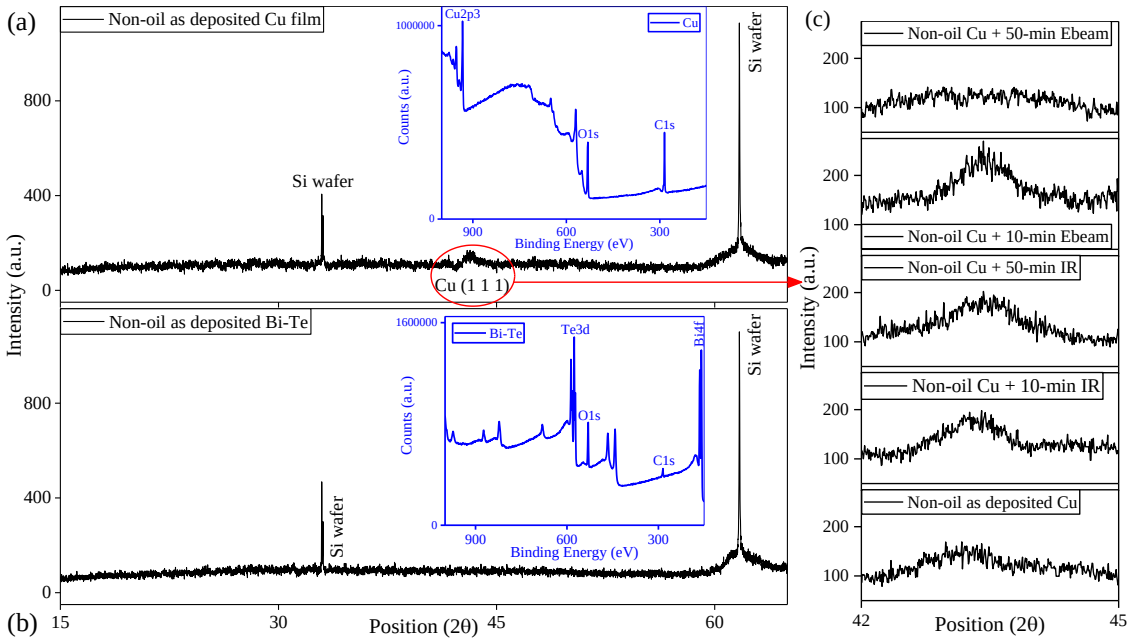


Figure 0.3. *(a) XRD and XPS results of evaporated Cu films; (b) XRD, XPS and TEM results of Bi-Te films; (c) Variations of the (1 1 1) peak in XRD of Cu films under 10 and 50 mins under e-beam or IR treatments. (XPS was conducted by Dr. Philip Holdway.)*

5.3.1.2 Electrical performance

Both IR and e-beam irradiations improved the measured electrical conductivity of as-evaporated Cu films, and the e-beam treatment seems to be more effective (see Figure 0.4 a). However, a 50-min e-beam irradiation appears to etch the Cu film and thus increasing the electrical resistivity. In terms of as-sputtered Bi-Te films, there is no obvious enhancement after these post-deposition treatments. A slight apparent increase in resistivity is observed for >10-min e-beam irradiations because such a strong e-beam could also etch Bi-Te films, making them thinner. A negligible change in electrical resistivity of Bi-Te films predicts that R_{TEG} will not change too much after IR or e-beam irradiations, which is expected in this study (i.e. the post-deposition treatment should only remove the residual oil rather than degrading the performance of TEGs).

This could be regarded as a further study to post-anneal a thinner Bi-Te film (~100 nm), as contrasted to Chapter 4 in which ~1-μm thick Bi-Te film are dynamically post-

annealed in Oxford webcoater by e-beam (170 mA, 7.3 kV) or IR (~145°C). In this study, the treatment conditions are 100 mA 4 kV (e-beam) and ~70°C (IR, see Figure 0.1) because the purpose is to only remove the residual without affecting the functional coating. Unlike Chapter 4, the IR temperature in this study is not high enough to anneal the Bi-Te film hence there is not an obvious enhancement in the film conductivity. In terms of the e-beam treatment, again unlike Chapter 4, it does not seem to decrease (there is even a slight increase) the electrical resistivity of the ~100 nm thick Bi-Te film, because (1) the e-beam condition in this study is not as strong as used in Chapter 4 (see above); (2) ~100 nm is close to the so-called threshold between the partially coated region and completely coated region (Chapter 3), hence, if the e-beam etches the film to the partial-coating region, the electrical resistivity will increase.

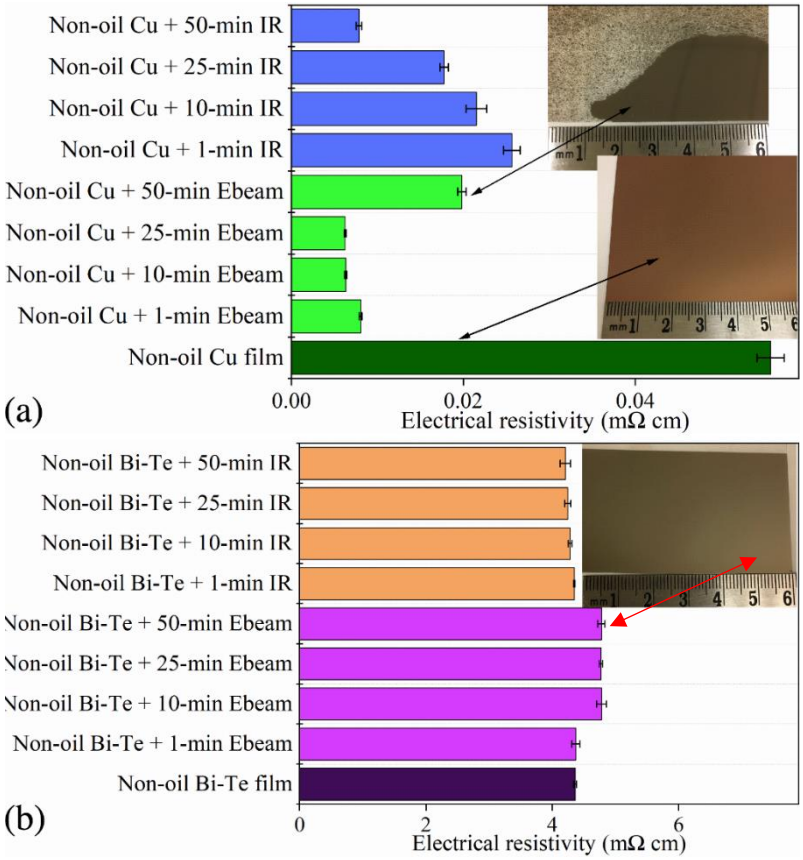


Figure 0.4. *Electrical resistivity of as-deposited and post-treated (a) Cu films and (b) Bi-Te films (inset: the image of the arrow pointed specimen. An etching phenomenon is only visually observed for a Cu film after a 50-min e-beam treatment).*

5.3.1.3 Mechanical performance

~1% strain capacity is of interest to wearable electronics for stretchability without significant degradation on the electronic performance [18]. In terms of the flexible thin-film TEG grown on polymer sheets, the mechanical performance is dominated by the polymer substrate. In this study, post-deposition treatments, IR and e-beam, are not expected to influence polymer substrate too much. Figure 0.5 shows the result of the tensile test for untreated PET, and PET after IR and e-beam irradiations for ~50 mins. After the irradiations by IR or e-beam on the PET sheet, a similar Young's modulus indicates a negligible influence on the mechanical performance, as expected.

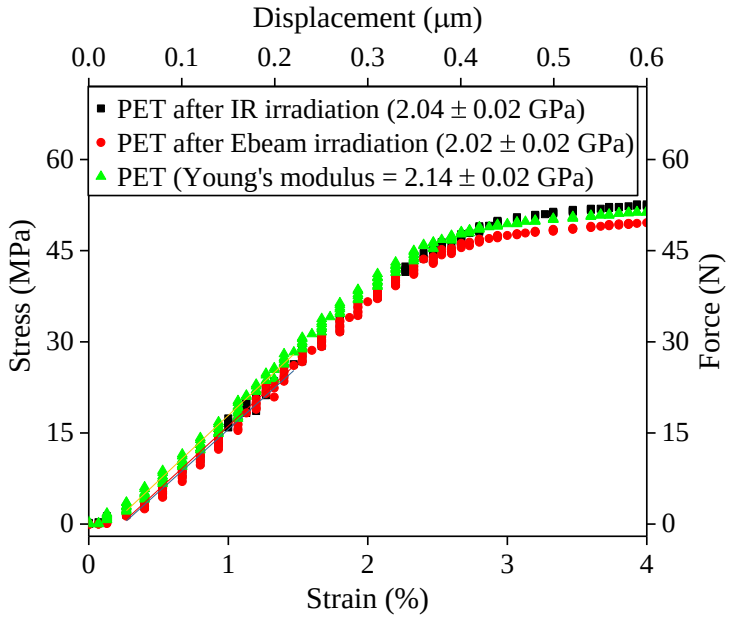


Figure 0.5. *Tensile stress-strain or force-displacement plot of PET with/without post-deposition treatments for ~50 mins (Young's modulus is the slope below 2% strain).*

5.3.2 SMT-fabricated TEGs

5.3.2.1 Images of Cu/Bi-Te patterns

Figure 0.6 a shows a clear in-line-deposited pattern of as-evaporated Cu film fabricated using SMT. A small amount of residual oil can be seen by visual observation towards a light. This is further confirmed by optical microscopy (Figure 0.6 e). The residual oil

could even coat the deposited film region (see the colourful area). Both IR (Figure 0.6 f-i) and e-beam (Figure 0.6 j-m) irradiations demonstrate a gradual removal process of the residual oil, indicating that these two treatments work well for the removal of oil from SMT-evaporated Cu films.

Sputtered layers tend to overcoat the patterned oil Figure 0.6 b, as previously reported in [9]. A series of subsequent experiments were trialled to figure out this phenomenon, for example, varying the sputtering time (i.e. the film thickness), the sputtering power (i.e. increasing energy of sputter source) to thermally remove the oil during deposition. Only increasing the target-to-substrate distance is found to work (see Figure 0.6 c). A clear pattern is observed for SMT-sputtered Bi-Te films as the target-to-substrate distance increases from 6 cm to 12 cm, suggesting that, a short distance could make the substrate completely within the central plasma region during sputtering, thereby all oil pattern is under the pressure of plasma and thus there is too much local pressure for the oil to leave. This phenomenon is reduced (see Figure 0.6 c) as the distance increases i.e. the substrate is out of the central plasma region. It should be noted that a long target-to-substrate distance would decrease the sputtering rate and increase material waste. Post-deposition treatments of IR and e-beam are also effective to remove the residual oil in SMT-sputtered Bi-Te films (see Figure 0.6 n-v).

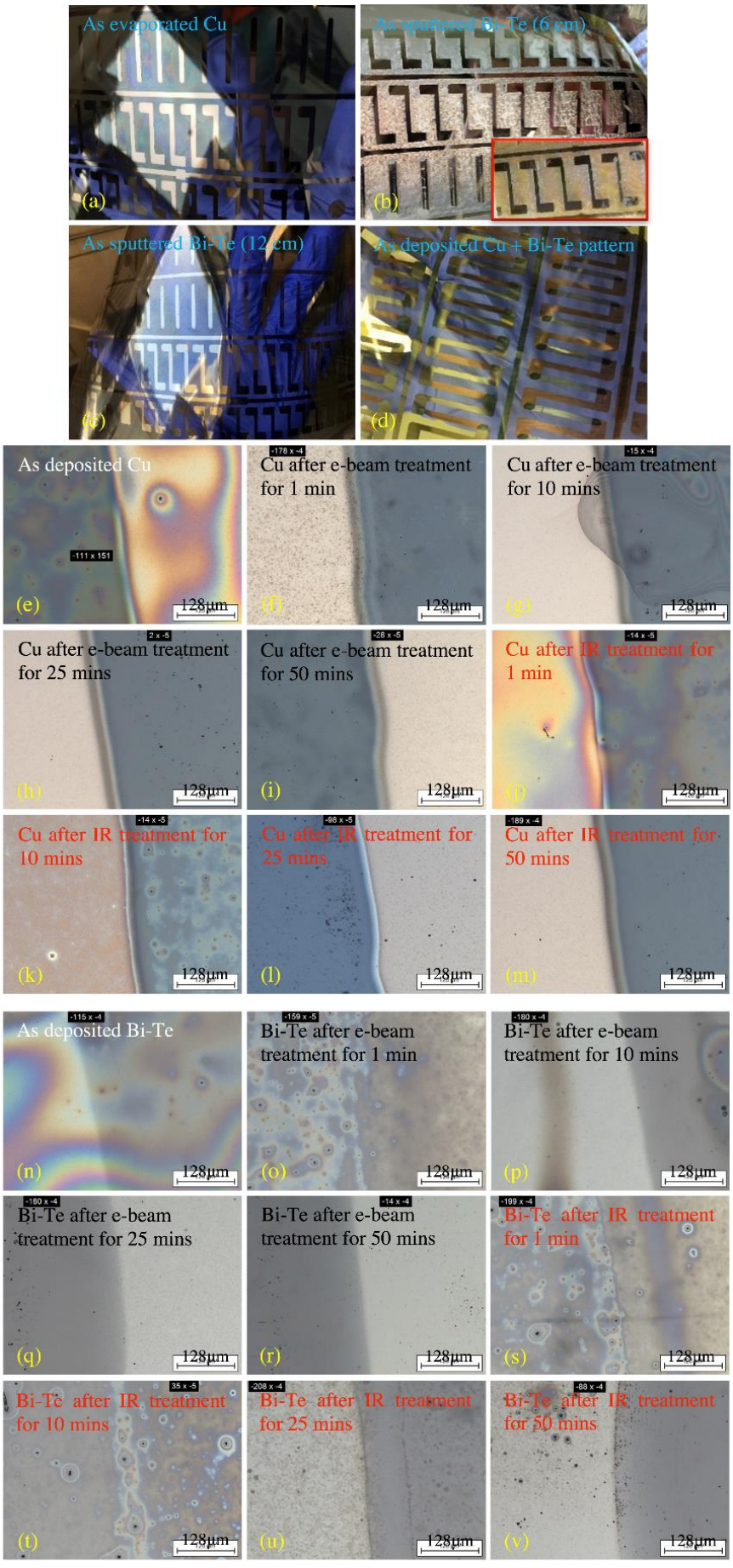

As evaporated Cu
(a)
As sputtered Bi-Te (6 cm)
(b)
As sputtered Bi-Te (12 cm)
(c)
As deposited Cu + Bi-Te pattern
(d)
As deposited Cu
(e)
Cu after e-beam treatment for 1 min
(f)
Cu after e-beam treatment for 10 mins
(g)
Cu after e-beam treatment for 25 mins
(h)
Cu after e-beam treatment for 50 mins
(i)
Cu after IR treatment for 1 min
(j)
Cu after IR treatment for 10 mins
(k)
Cu after IR treatment for 25 mins
(l)
Cu after IR treatment for 50 mins
(m)
As deposited Bi-Te
(n)
Bi-Te after e-beam treatment for 1 min
(o)
Bi-Te after e-beam treatment for 10 mins
(p)
Bi-Te after e-beam treatment for 25 mins
(q)
Bi-Te after e-beam treatment for 50 mins
(r)
Bi-Te after IR treatment for 1 min
(s)
Bi-Te after IR treatment for 10 mins
(t)
Bi-Te after IR treatment for 25 mins
(u)
Bi-Te after IR treatment for 50 mins
(v)
128µm

Figure 0.6. *Images of patterns using SMT (the width of the strip is 2 mm): (a) as evaporated Cu films; (b-c) as sputtered Bi-Te films with the source-to-substrate distances of 6-cm and 12-cm; (d) SMT-fabricated TEGs; (e-v) Cu and Bi-Te patterns before/after e-beam/IR treatments for 1, 10, 25, 50 mins, imaged by optical microscopy.*

5.3.2.2 Seebeck performance of SMT-fabricated TEGs with post-deposition treatment to remove oil

Open-circuit voltage (V_{OC}) and short-circuit current (I_{SC}) are displayed with varying ΔT, showing a linear relationship where slopes of fit lines are Seebeck coefficient and Seebeck current in Figure 0.7 a and b, respectively. In this study, the Seebeck current describes how the I_{SC} changes with the ΔT, which is a measure of the magnitude of an induced I_{SC} in response to a ΔT across the sample. There is no significant change in Seebeck coefficient, while Seebeck current significantly decreases for SMT-fabricated TEGs after either IR or e-beam irradiation, compared to a standard TEG (made by a shadow mask, i.e. non-oil fabrication). The oil seems to damage the performance of functional coatings. The internal resistance of the TEG (R_{TEG}) measured using a probe station at room temperature is: 270 kΩ (a standard TEG is fabricated by solid shadow masks without any post-deposition treatments), 25 MΩ (an SMT-ebeam TEG), 20 MΩ (an SMT-IR TEG). These high resistances were not observed (Figure 0.4) for samples exposed to the radiation treatment without oil. In terms of P output (Figure 0.7 c), the SMT-fabricated TEG works even though P is three-time poorer than the standard TEG. It is noted that the external load resistance is closer to R_{TEG} of the SMT-fabricated TEG, thus the measured P is approximately the maximum to the SMT-fabricated TEG rather than the standard TEG.

R_{TEG} measured using a probe station may be not very precise because there could be an oil gap between the probe and the coating. Seebeck measurement uses a silver paste to

join the leads and Cu contacts in TEGs, which may be less prone to the effects of residual oil at the contact. To further confirm R_{TEG}, the data of P is used to calculate R_{TEG} under a ΔT, using the following equation [19]:

$$P = I^2 \cdot R_L = \left(\frac{S_{TEG} \cdot \Delta T}{R_{TEG} + R_L}\right)^2 \cdot R_L \quad (0.1)$$

Rearranged to:

$$\sqrt{\frac{P}{R_L}} = \frac{S_{TEG}}{R_{TEG} + R_L} \Delta T \quad (0.2)$$

where R_L is the load resistance (18.45 MΩ), S_{TEG} is Seebeck coefficient of the whole device (i.e. the slope in Figure 0.7 a), ΔT is the temperature difference (11.4 °C), R_{TEG} is the internal resistance of the whole device.

The calculated R_{TEG} under ΔT again indicates that oil significantly affects the performance of functional films. Figure 0.7 a and c reveal that the R2R SMT-manufactured TEG has a comparable voltage output to the standard TEG, and thus can be used for portable devices requiring a voltage-dominant source. To behave as a power source, the SMT-fabricated TEG is more suitable for portable devices with an extremely large resistance (in MΩ range).

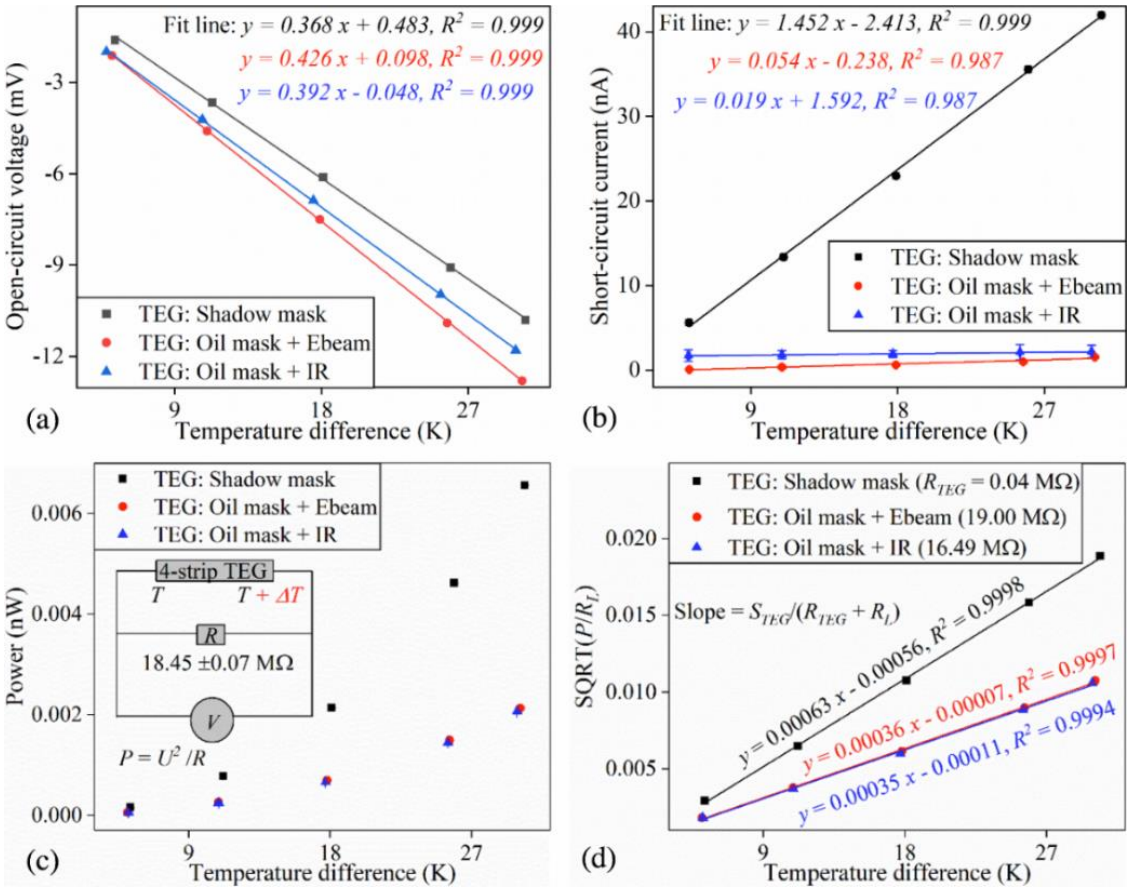


Figure 0.7. *(a) A plot of V_{OC} vs ΔT (slope of the linear fit is Seebeck coefficient); (b) Plot of I_{SC} vs ΔT (slope of the linear fit is defined as Seebeck current herein); (c) P output of TEGs (the dimension of TE strip is 13 mm × 2 mm); (d) Plot to calculate R_{TEG} through the linear fit. (Specimens are four-strip TEG using shadow mask, and SMT-fabricated TEGs after 25-min e-beam and IR irradiations.)*

5.3.2.3 Why does R_{TEG} increase using SMT?

IR and e-beam treatments are not expected to significantly affect R_{TEG}, as analysed from Figure 0.4 for non-SMT-fabricated samples. However, R_{TEG} changes a lot for SMT-fabricated and cleaned samples. Resistances of SMT-fabricated strips (2 mm × 13 mm) were measured using a probe station, as shown in Figure 0.8 a and b. The oiled Cu film (67 Ω) has a much higher (~10 times) resistance than non-oiled Cu film (7 Ω). Post-deposition treatments (IR and e-beam) should gradually decrease the resistance of oiled Cu film with the annealing time. However, the trend is not obvious, and some samples

with a long-time anneal even has a higher resistance than the original oiled Cu film. Diffusion of oil into the film region is observed in Figure 0.6. Given the scatter in the result in Figure 0.8 a, it is speculated that the diffusion of oil into the film is random and the oil thickness is not even. This is particular to the case in which a single drum rotates. It is predicted that, in a real R2R case, the residual oil will uniformly cover the film region because the polymer web passes a series of rollers, rapidly moving away from the oiling region. Hence, it is predicted that the thickness of residual oil could likely be removed at a linear speed with the annealing time, and thus reducing resistance.

The resistance of the Cu film is not that significant in TEGs because R_{TEG} is dominated by the TE (semiconductor) part. In Figure 0.8 b, it is seen that resistance of the Bi-Te strip dramatically increases for SMT/oiled Bi-Te films (in MΩ range), compared to non-oiled films (the standard sample in kΩ range). Some Bi-Te strips are even unmeasurable (due to a random distribution of diffused oil on Bi-Te films and a very thick oil between the probe and the film will lead to an open circuit).

The reaction between the Krytox® oil and Bi-Te are considered for SMT-fabricated films. Krytox® oil contains carbon, oxygen and fluorine. It is speculated that the evaporated source and the sputtered source/plasma could break the bonds of the oil molecules leading to free oxygen and fluorine species which could react with the incoming evaporated/sputtered atoms to deposit on the substrate.

XPS was used to check the residual (Fluorine) F on films after post anneals (see Figure 0.9 and Table 0.I). The detected oil elements (C, O and F) could be from (1) the residual oil on top of the film (2) the reacted component in the film. F exists for both Cu and Bi-Te films even after 50-min post-deposition treatments. e-beam irradiation can gradually decrease the amount of F (see atomic% in Table 0.I) with treatment time for both Cu and Bi-Te films. This could illustrate a removal process of the residual oil on top of the film.

Removal of the F using IR seems to work for the Cu film but not well for the Bi-Te film, so a reaction could happen for the Bi-Te film with either F or O. Although an oxidation peak (Figure 0.9 e and f) is observed for the Bi-Te sample (the positions of these oxidation peaks are agreed with the reference [21]), further studies are required to confirm this kind of reaction. The existence of F for the Cu sample does not change too much in the electrical performance, because TEGs only require the Cu contacts to be conductive in the Ω range. However, it is a severe phenomenon for Bi-Te semiconductor because there is a significant degradation on the electrical performance, R_{TEG} (see Figure 0.7 b and d).

The junction between Cu and Bi-Te films is also analysed. Images inset Figure 0.8 c indicate the region of oil pattern is not uniform. After SMT-evaporated Cu patterns are post annealed, the residual oil may not be completely removed, which affects the following deposition of Bi-Te patterns. A breakage in the Bi-Te pattern of the strip was observed (Figure 5.8 c inset image) because the Bi-Te film cannot grow onto the residual oil region. Only clear patterns of SMT-fabricated TEGs are selected for analysis through this study. In terms of the Cu/Bi-Te junction, oil could also exist at the interface. The contact resistance between Cu and Bi-Te was measured using the method as described in Chapter 2. R_c of SMT-fabricated TEG is about 200-times larger than that of the standard TEG (Figure 0.8 c). Hence, a layer of oil or F possibly exists between Cu and Bi-Te coatings.

Overall, there could be reaction between the oil and the functional coating, especially in Bi-Te films. A sandwich structure, Cu/Oil/Bi-Te, could exist at the interface. These two phenomena result into an increase in R_{TEG} for the SMT-fabricated TEG.

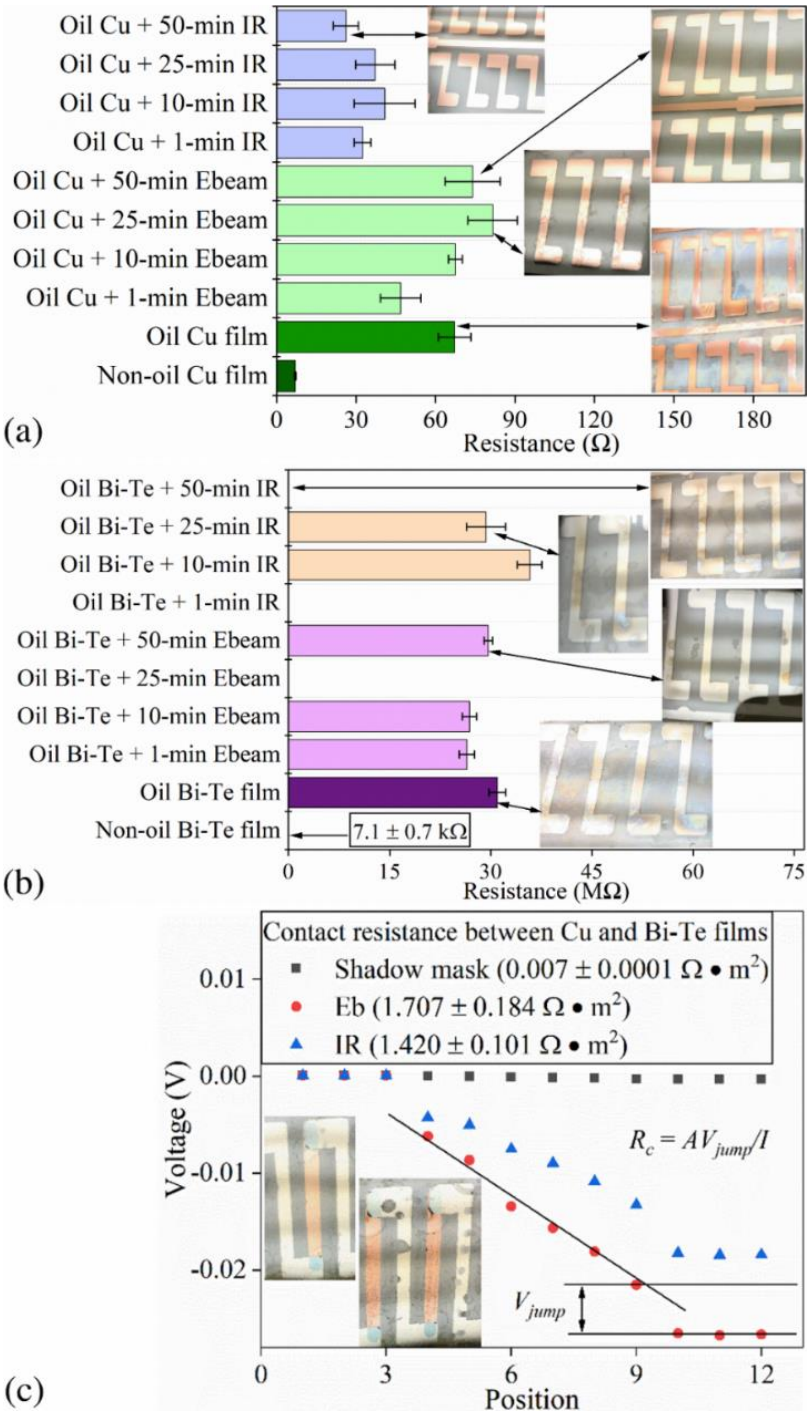


Figure 0.8. *(a & b) Resistances of SMT-fabricated Cu and Bi-Te strips (13 mm × 2 mm), following IR or e-beam irradiations with different annealing times; (c) R_C of Cu/Bi-Te interface of a standard TEG and SMT-fabricated TEGs following 25-min IR and e-beam treatments.*

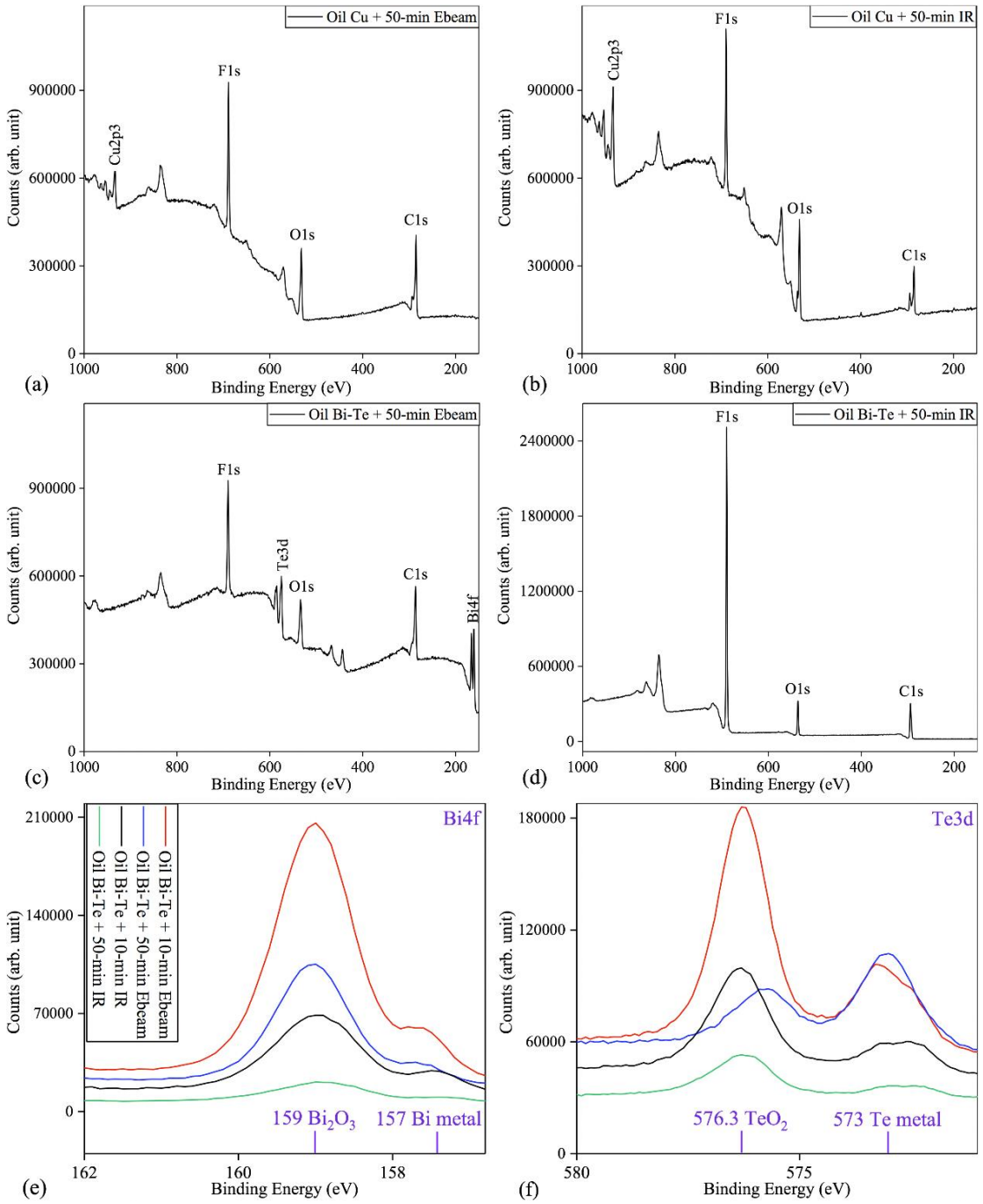


Figure 0.9. *XPS results of SMT-fabricated patterns after IR or e-beam treatment. (XPS was conducted by Dr. Philip Holdway).*

Table 0.I. *Elemental compositions for SMT-fabricated patterns after IR and e-beam treatments.*

Atomic%	F	Cu	Bi	Te	O	C
Oil Cu + 10-min e-beam	44.33	4.24	-	-	18.19	33.27
Oil Cu + 50-min e-beam	26.55	3.47	-	-	52.38	17.6
Oil Cu + 10-min IR	61.42	0.35	-	-	9.6	28.63
Oil Cu + 50-min IR	28.97	7.38	-	-	26.39	37.27
Oil Bi-Te + 10-min e-beam	54.52	-	2.2	2.17	14.67	26.45
Oil Bi-Te + 50-min e-beam	23.85	-	1.51	1.78	15.25	57.61
Oil Bi-Te + 10-min IR	62.16	-	0.07	0.19	9.34	28.24
Oil Bi-Te + 50-min IR	62.52	-	0.03	0.08	9.4	28.01

5.4 Summary

The selective metallisation technique was explored to fabricate flexible thermoelectric generators in a roll-to-roll process. The fabricated TEG works and behaves as a voltage-dominant source, comparable to a standard TEG fabricated using a shadow mask, but the power performance is much poorer than the standard device because the internal resistance increases dramatically. This could be ascribed to (1) a reaction between the oil and the functional coatings; (2) the residual oil at the metal-semiconductor interface. Further investigations about the oil type, precise control of oil pattern and a stronger e-beam or IR irradiations are considered in the future.

5.5 Reference

[1] Cao, Z.; Koukharenko, E.; Tudor, M. J.; Torah, R. N.; Beeby, S. P. , Screen printed flexible Bi2Te3-Sb2Te3 based thermoelectric generator, 1970, https://doi.org/10.1088/1742-6596/476/1/012031.

[2] Shin, S.; Kumar, R.; Roh, J. W.; Ko, D.; Kim, H.; Kim, S. I.; Yin, L.; Schlossberg, S. M.; Cui, S.; You, J.; Kwon, S.; Zheng, J.; Wang, J.; Chen, R. , High-Performance Screen-Printed Thermoelectric Films on Fabrics, *Scientific Reports.* 2017*, 7*, 7317-9, https://doi.org/10.1038/s41598-017-07654-2.

[3] Chen, B.; Kruse, M.; Xu, B.; Tutika, R.; Zheng, W.; Bartlett, M. D.; Wu, Y.; Claussen, J. C. , Flexible thermoelectric generators with inkjet-printed bismuth telluride nanowires and liquid metal contacts, *Nanoscale.* 2019*, 11*, 5222-5230, https://doi.org/10.1039/c8nr09101c.

[4] Madan, D.; Wang, Z.; Wright, P. K.; Evans, J. W. , Printed flexible thermoelectric generators for use on low levels of waste heat, *Applied Energy.* 2015*, 156*, 587-592, https://doi.org/10.1016/j.apenergy.2015.07.066.

[5] Cosnahan, T.; Watt, A. A. R.; Assender, H. E. , Modelling of a vacuum metallization patterning method for organic electronics, *Surface & Coatings Technology.* 2018*, 336*, 128-132, https://doi.org/10.1016/j.surfcoat.2017.09.058.

[6] Madou, M. J. , Manufacturing techniques for microfabrication and nanotechnology, *CRC Press.* 2011, 403-404, https://doi.org/10.1201/9781439895306.

[7] Taylor; Cliffordl; Bjornard; Erikj; Valiska; Michaelj , Film thickness uniformity control apparatus for in-line sputtering systems, *US Patents.* 1992, 1-7, https://patents.google.com/patent/US5156727.

[8] Wei, Z.; Bobbili, P. R.; Senthilarasu, S.; Shimell, T.; Upadhyaya, H. M. , Design and optimisation of process parameters in an in-line CIGS evaporation pilot system, *Surf. Coat. Technol.* 2014*, 241*, 159-167, https://doi.org/10.1016/j.surfcoat.2013.10.033.

[9] Stuart, B. W.; Tao, X.; Gregory, D.; Assender, H. E. , Roll-to-Roll Patterning of Al/Cu/Ag Electrodes on Flexible Polyethylene by Oil Masking: A comparison of Thermal Evaporation and Magnetron Sputtering, *Appl. Surf. Sci.* 2019*, 505*, 144294, https://doi.org/10.1016/j.apsusc.2019.144294.

[10] Kim, J.; Choi, J.; Bae, J.; Kim, M.; Oh, T. , Thermoelectric Characteristics of n-Type Bi2Te3 and p-Type Sb2Te3 Thin Films Prepared by Co-Evaporation and Annealing for Thermopile Sensor Applications, *Mater. Trans.* 2013*, 54*, 618-625, https://doi.org/10.2320/matertrans.M2013010.

[11] Sudarshan, C.; Jayakumar, S.; Vaideki, K.; Sudakar, C. , Effect of vacuum annealing on structural, electrical and thermal properties of e-beam evaporated Bi2Te3 thin films, *Thin Solid Films.* 2017*, 629*, 28-38, https://doi.org/10.1016/j.tsf.2017.03.043.

[12] Singkaselit, K.; Sakulkalavek, A.; Sakdanuphab, R. , Effects of annealing temperature on the structural, mechanical and electrical properties of flexible bismuth telluride thin films prepared by high-pressure RF magnetron sputtering, *Ansn.* 2017*, 8*, 350021-350027, https://doi.org/10.1088/2043-6254/aa7222.

[13] Nishino, T.; Suzuki, T. , Flexible thermoelectric generator with efficient vertical to lateral heat path films, *Journal of Micromechanics and Microengineering.* 2017*, 27*, 35011, https://doi.org/10.1088/1361-6439/aa5aad.

[14] Takemori, D.; Okuhata, M.; Takashiri, M. , Thermoelectric Properties of Electrodeposited Bismuth Telluride Thin Films by Thermal Annealing and Homogeneous Electron Beam Irradiation, *ECS Trans.* 2017*, 75*, 123-131, https://doi.org/10.1149/07552.0123ecst.

[15] Kudo, S.; Tanaka, S.; Miyazaki, K.; Nishi, Y.; Takashiri, M. , Anisotropic Analysis of Nanocrystalline Bismuth Telluride Thin Films Treated by Homogeneous Electron Beam Irradiation, *Mater. Trans.* 2017*, 58*, 513-519, https://doi.org/10.2320/matertrans.M2016295.

[16] Takashiri, M.; Uyama, M.; Imai, K. , Comparison of crystal growth and thermoelectric properties of n-type Bi-Se-Te and p-type Bi-Sb-Te nanocrystalline thin films: Effects of homogeneous irradiation with an electron beam, *J. Appl. Phys.* 2014*, 115*, 2143111-2143117, https://doi.org/10.1063/1.4881676.

[17] Ludwig, T.; Guo, L.; McCrary, P.; Zhang, Z.; Gordon, H.; Quan, H.; Stanton, M.; Frazier, R. M.; Rogers, R. D.; Wang, H.; Turner, C. H. , Mechanism of Bismuth Telluride Exfoliation in an Ionic Liquid Solvent, *Langmuir.* 2015*, 31*, 3644-3652, http://doi.org/10.1021/acs.langmuir.5b00239.

[18] Kim, D.; Rogers, J. A. , Stretchable Electronics: Materials Strategies and Devices, *Adv. Mater.* 2008*, 20*, 4887-4892, https://doi.org/10.1002/adma.200801788.

[19] Enescu, D. , Thermoelectric Energy Harvesting: Basic Principles and Applications, *Green Energy Advances.* 2019, https://doi.org/10.5772/intechopen.83495.

[20] Horio, Y.; Inoue, A. , Effect of Oxygen Content on Thermoelectric Properties of n-Type (Bi,Sb)2(Te,Se)3 Alloys Prepared by Rapid Solidification and Hot-Pressing Techniques, *Materials Transactions.* 2006*, 47*, 1412-1416, https://doi.org/10.2320/matertrans.47.1412.

[21] Denis M., Keke C., Paul S., Felix N B., Martin H., Steffen H., Peter J P., Till S. and Cedric W., On atomic mechanisms governing the oxidation of Bi2Te3, *J. Phys.: Condens. Matte*r 2017, *29*, 485705, https://doi.org/10.1088/1361-648X/aa945f

Chapter 6 Device optimisation and large-scale roll-to-roll manufacturability of flexible TEGs

This chapter investigates the structure of TEGs suitable for R2R processing for scale-up. The dimensions of TE strips and cheap/high-performance contact materials are studied, then, a possible R2R means to fabricate flexible TEGs is proposed.

In previous chapters, the focus was on the TE material and its deposition. In this chapter, I take forward the application of the deposited TE material into TEG devices. The optimisation of a flexible TEG suitable for large area R2R processing is investigated. The selection of suitable contact electrode materials (cost and performance), in-line patterning of connections (in-series or in-parallel), and dimensions of the in-line TE strips (length and width) are investigated. In addition, an industrially-feasible/continuous process is proposed for large-scale manufacture of flexible thermoelectric generators, by roll-to-roll sputtering thermoelectric materials on a polymer web, inkjet printing contact electrodes, and segmenting using a laser.

6.1 Introduction

Exploration of TE materials is always of primary importance in the development of flexible TEGs, while the selection of contact materials (cost, performance, and manufacturability) is also a crucial factor for commercialisation of flexible TEGs. In a TEG, contacts, typically metals because of their good electrical/thermal conductivity to avoid internal electrical and heat power losses, are used to join thermoelectric legs in-series or in-parallel. Joining the contact strips and TE legs is the main task in assembling TEGs. A recent report reviewed on the challenge at the interface between metal contacts and TE materials [1]. The interface is the contact between the metal and TE materials, i.e. an M-S junction, which plays a significant role in heat and charge transport in TEGs [2].

Low thermal resistance as well as a low thermal contact resistance with TE materials is required for good TEG performance [3]. In addition, a good contact should also possess good bonding strength and stability with the TE leg. For commercialisation, a cheap and easy-to-manufacture contact is desired.

For a good interface, one needs to consider the oxidation, roughness, gas absorption, diffusion, doping, thermal/electrical mismatch between two dissimilar materials, etc. In flexible thin-film TEGs, studies on electrode contacts are rare, while there are many contact studies about bulk TEGs.

(1) Stability (reaction and diffusion passivation): Liu *et al.* [4] investigated the contact properties between contact Ni and TE material Bi-Te(-Sb)-Se alloys, and they observed a clear interface reaction layer between the TE leg and contact material, which was formed through the diffusion of Ni along the grain boundary and significantly increased the contact resistance. A similar phenomenon, diffusion of Fe into the TE leg was also observed in [5], which resulted into an increase in contact resistance and a loss of device strength.

(2) Interface resistance (thermal and electrical): In terms of thermal contact resistance, many studies [6, 7] reported that phonon scattering at the interface is a mixture of acoustic and diffusive scattering, and in thin-film TEGs, the thermal contact resistance could be a dominant factor for wearable applications [8]. Considering a simple contact interface without notable diffusion or reaction of the materials, there are two main mechanisms for electrical carrier transport at an M-S interface: a) energy barrier and b) contact gap for carrier tunnelling. Jie *et al.* [9] studied the band alignment evolution of an M-S interface as the contact gap decreased. The tunnelling potential decreased to zero as the contact gap reduced to zero. A potential barrier (Schottky or Ohmic) was generated due to a mismatch between work functions of metal and semiconductor. However, in a real case,

diffusion and reaction processes with the dissimilar materials at the interface are unavoidable and lead to a new interface state, making the energy barrier more complex. Ebling *et al.* [10] reported that the figure of merit of a TEG decreased as the contact resistance increased.

(3) Bonding strength: The bonding strength can be a significant factor in bulk TEGs. As reported in [11], big cracks can be observed at the interface due to a local thermal-expansion difference at an M-S joint, when applying a big thermal shock (550°C). To increase the bonding strength, a surface cleaning approach was reported in [12-14]. Hot pressing [4] and thermal spray processes [15] were also reported to increase the bonding strength. In terms of wearable thin-film TEGs, there is not a big thermal shock and the physical sputtering technique likely will make the bonding sufficiently strong.

In addition to the selection of electrode contact, a TEG design also considers the in-line pattern of connections and dimensions of the legs. The connection of legs is crucial for the performance of TEGs. TE strips can be either in-series or in-parallel connected, leading to a voltage-dominant and current-dominant output power, respectively. There are few studies of the connection configuration of thin-film TEGs. Wang *et al.* [16] carried out a numerical modelling performance comparison between in-series and in-parallel connected TEGs. They predicted that both series- and parallel-connected systems had a linear relationship between output current and voltage; the series-connected system could reach the highest voltage while the parallel-connected system could reach the maximum current; the two systems had almost the same output power. This still needs to be experimentally demonstrated.

The dimension of the legs also plays a crucial role in optimizing the performance of flexible TEGs. Again, many studies report on bulk TEGs but few report thin-film TEGs. Several modelling studies of the effect of leg dimensions have drawn a range of

conclusions, for example, that the leg length showed an influence on electrical performance but little on thermal performance [17], that a leg width-induced increase in the cross-sectional area would increase the power output [18], that electrical current and temperature difference were increasing functions of the ratio of cross-sectional area and length of TE strip, with decaying improvement in performance as this ratio increased [19]. Kim *et al.* [20] argued that a short leg length generated a large power because of reduced electrical resistance, and that there was less consumption of materials, however, short legs might cause large shear stress at the interface and large contact resistance. A finite element and artificial neural network model [21] concluded that the effect of cross-sectional area is more prominent than that of leg length and there was an optimal cross-section area for the highest power output. Ebling *et al.* [10] used a model to predict that the figure of merit increased with the leg length, whereas Suarez *et al.* [22] found that there was an optimum leg length after which the overall power decreased, and Seebeck voltage increased as the cross-sectional area decreased (which also allowed more legs). Again, these studies above are mainly modelling studies based on bulk TEGs. Experimental studies will thus be important and necessary, especially for TEGs in thin-film configuration.

In addition to the electrode contact and design of the in-line pattern, this study also considers a feasible approach for the large-scale manufacture of flexible TEGs. Continuous production of segmented strips is the key to the industrial manufacture of flexible TEGs. A segmented structure could contain different TE materials to improve the performance of TEGs compared with a non-segmented structure [23, 24], while a few studies reported that a segmented structure could also relieve the strain in real applications (e.g. to assemble a flexible TEG into a wristband). Bending flexible TEGs into a ring, e.g. the radius of a bracelet: ~32 mm, will generate >> 2% strain in the film,

which could lead to device failure (see chapter 4). Thus, this chapter will study the bending resilience of a segmented structure based on the TEG device design studied early in the chapter. Laboratory studies used a solid mask to make segmented strips or in-line patterns of TEGs, while a solid mask is not desirable in large-scale manufacture roll-to-roll (R2R). R2R processing is the most attractive means to scale up the manufacture of flexible TEGs, and the previous study [25] and chapter 5 has successfully achieved a flexography + evaporation approach to make in-line patterns of electrodes in flexible TEGs. However, obstacles still exist to make flexography compatible with the sputtering of TE materials, and to produce the uniform coating and accurate process control (because of multiple boats and power systems) for evaporation of functional materials (e.g. Bi_2Te_3 TE materials). At this stage, using flexography techniques to make flexible TEGs is still not very mature. So in this chapter, I trialled a new approach to scale up the manufacture of flexible TEGs: 1) R2R sputtering of TE materials in moving web; 2) laser cutting TE materials into segmented strips; 3) Printing of electrodes to contact the TE strips. Compared with the in-line patterns made by flexography, the laser-cut sample has less difficulty to achieve clarity/resolution between two adjacent strips, and only a small distance (i.e. diameter of laser: 100 μm) is generated between two adjacent strips that significantly increases the fill efficiency in a specific area (i.e. a small area allows more strips involved) and thus more power output. An inkjet printing technique in high-throughput R2R production has been widely reported in many electronic applications [26-28]. Considering the production speed of these three techniques (Aerre Machine R2R vacuum web coater at Oxford: 1-30 m min^{-1} in-line speed; TS 3040 Laser cutter: 0-50 m min^{-1} engraving speed; Inkjet printing: 10 m min^{-1} [26]), it is very likely that a real R2R continuous manufacture of flexible TEGs can be achieved.

Therefore, this chapter aims to optimize flexible TEGs in aspects of contact electrode materials, in-line patterning connection, and the dimension of the TE strip. In addition, I propose a feasible approach to scale up the manufacture of flexible TEGs for commercialisation.

6.2 Device fabrication

6.2.1 Patterning by solid mask

As shown in Figure 5.1 a, Bi-Te strips (in different dimensions) were sputtered through solid shadow masks. Then, with alignment, (the Bi-Te ends contact with the metal strips by an in-series or in-parallel mode, see Figure 5.1 b), metal strips (Ag, Al, Cu or Au) were thermally evaporated through solid shadow masks. The deposition conditions (sputtering and evaporation) have been described in Chapter 2. Connection of parallel strips rather than a wider strip is applied because (1) a segmented structure could also relieve the strain (see Figure 6.9) during wearable applications; (2) this is to be prepared for some special designs for TEG, e.g. the stacking design (see Figure 7.2 d): in-parallel build-up of strips out of plane.

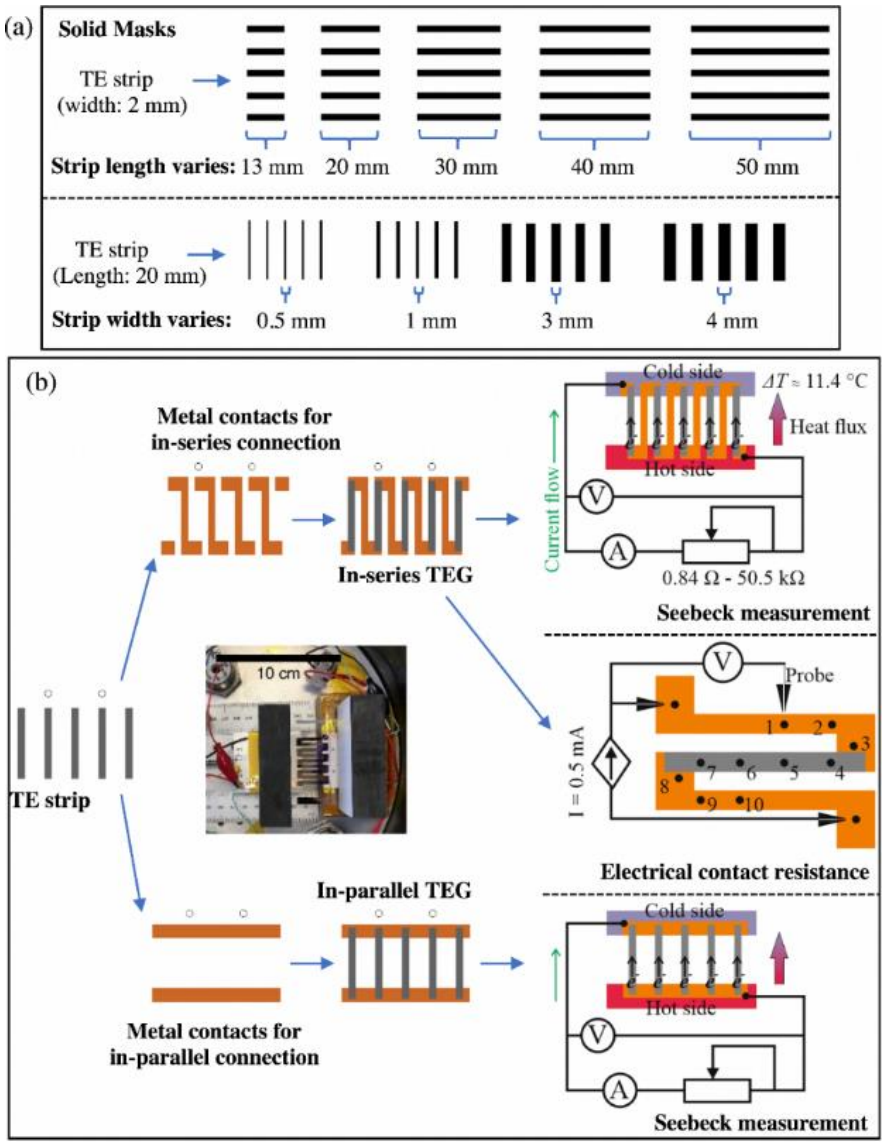


Figure 5.1. *(a) Solid shadow masks for patterning of TEGs with different dimensions; (b) Schematic diagram of making in-series (or in-parallel) connected TEGs, following characterization setups: electrical contact resistance at the metal-semiconductor interface, and Seebeck system (carriers, electron e^- in case of Bi-Te, are generated at the hot side and move towards the cold side. The direction of current is opposite to that of e^- movement).*

6.2.2 Patterning by laser cutter and printing technique

Rather than having a continuous R2R process of film deposition, laser cutting, and inkjet printing (Figure 5.2), the process was step-by-step whereby I sputtered bismuth telluride

film onto a moving polymer web, followed by laser cutting in a TS 3040 40W Laser Cutter and then inkjet printing of silver to connect the segmented TE strips. Various powers were trialled in the Laser Cutter to find an optimum condition, which removed only the Bi-Te coating without visible damage to the PET substrate.

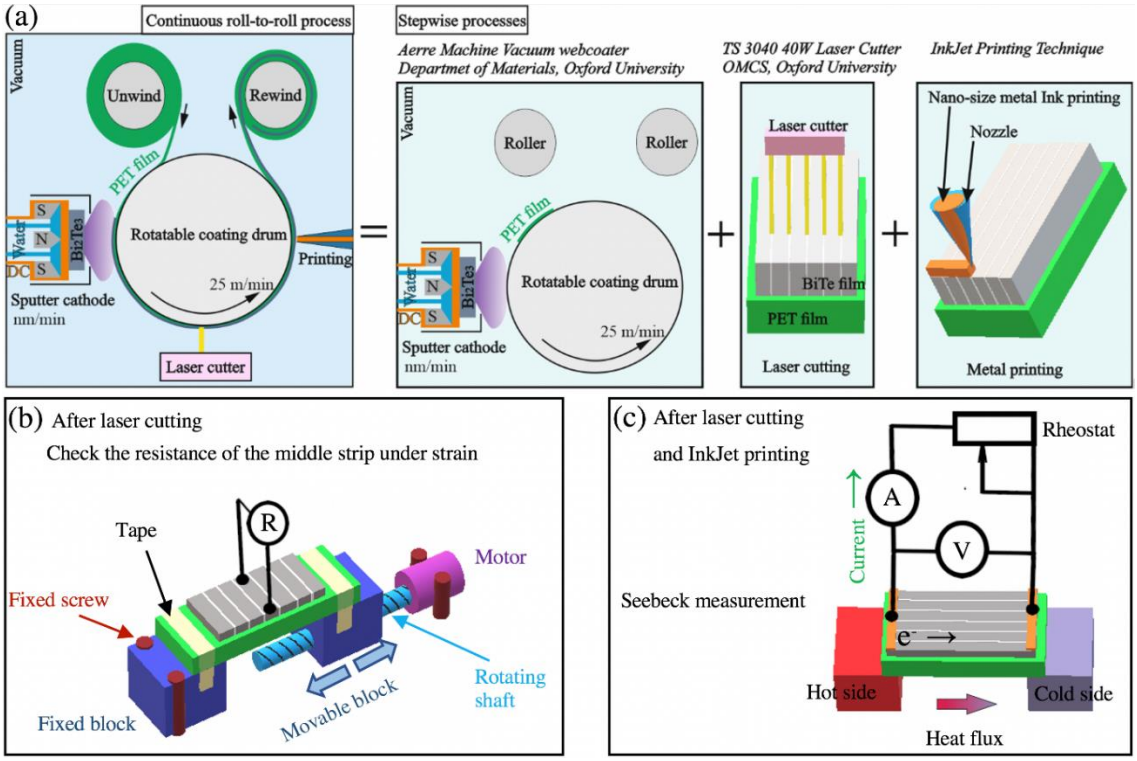


Figure 5.2. *(a) Schematics of continuous R2R setups and stepwise processes used in this work to make laser cut samples where the sample was made by three individual processes (NB: this manufacturing process can only make in-parallel connected TEGs at this stage. The segmented sample using laser cutting is of interest to release the stress in the device under an application e.g. a wrist/watch band); (b) Setup to measure a change in resistance of a segmented sample during bending (to simulate a situation on the strain while assembling TEGs in a wristband, the middle strip is mainly checked because it is under the maximum strain during bending. This is to say, if the middle strip still works under strain, the others will also work. Besides, a non-segmented sample is also measured as a control group); (c) Seebeck measurement of a segmented sample.*

6.3 Results and discussions

6.3.1 Surface morphology, electrical performance, and uniformity

The film morphologies comparing various electrode metals and the Bi-Te are shown in Figure 5.3 a-f, in which metal/Bi-Te films' surface features strongly depend on the surface of the PET substrate, which contains many protrusions of some 10s of nm in height. SEM images reveal a granular texture (fine and uniform), resulting from an island growth mechanism for RT deposition onto the polymer. XRD measurement was conducted on a specimen grown onto a Si wafer because films are too thin to obtain a signal from the coating alone, and the PET substrate has a very broad peak overlapping the peaks of the coating. Even so, the film peaks are still very low intensity, Figure 5.3 g, (the full/original intensity at (1 1 1) of Si wafer is ~42840 a. u.) due to their thinness. XRD patterns confirm the metal phase: Ag, Cu, and Au, while no peak was observed in Al film grown on Si wafer which might be attributed to flash evaporation (to avoid oxidation during deposition) during making Al films. The presence of the Al element was confirmed in the XPS result (Figure 5.5 d). Sputtered Bi-Te film shows a very broad peak at 38.4° corresponding to a plane (1 0 10), attributed to a poor crystallinity/nucleation process while sputtering the Bi-Te source at RT. Surface roughnesses, RMSR (Figure 5.3 h), of all films are almost the same as that of PET sheets, at around 4-5 nm. The electrical resistivity of Ag, Al, Cu, and Au are 7.0 (± 0.2), 23.4 (± 2.1), 11.8 (± 1.1), and 8.6 (± 0.8) μΩ • cm, respectively, in the same range as expected [29-33]. In terms of Bi-Te films, Figure 5.3 (i-l) indicates uniform distributions of Bi and Te, with 35.1 at.% and 64.9 at.%, respectively.

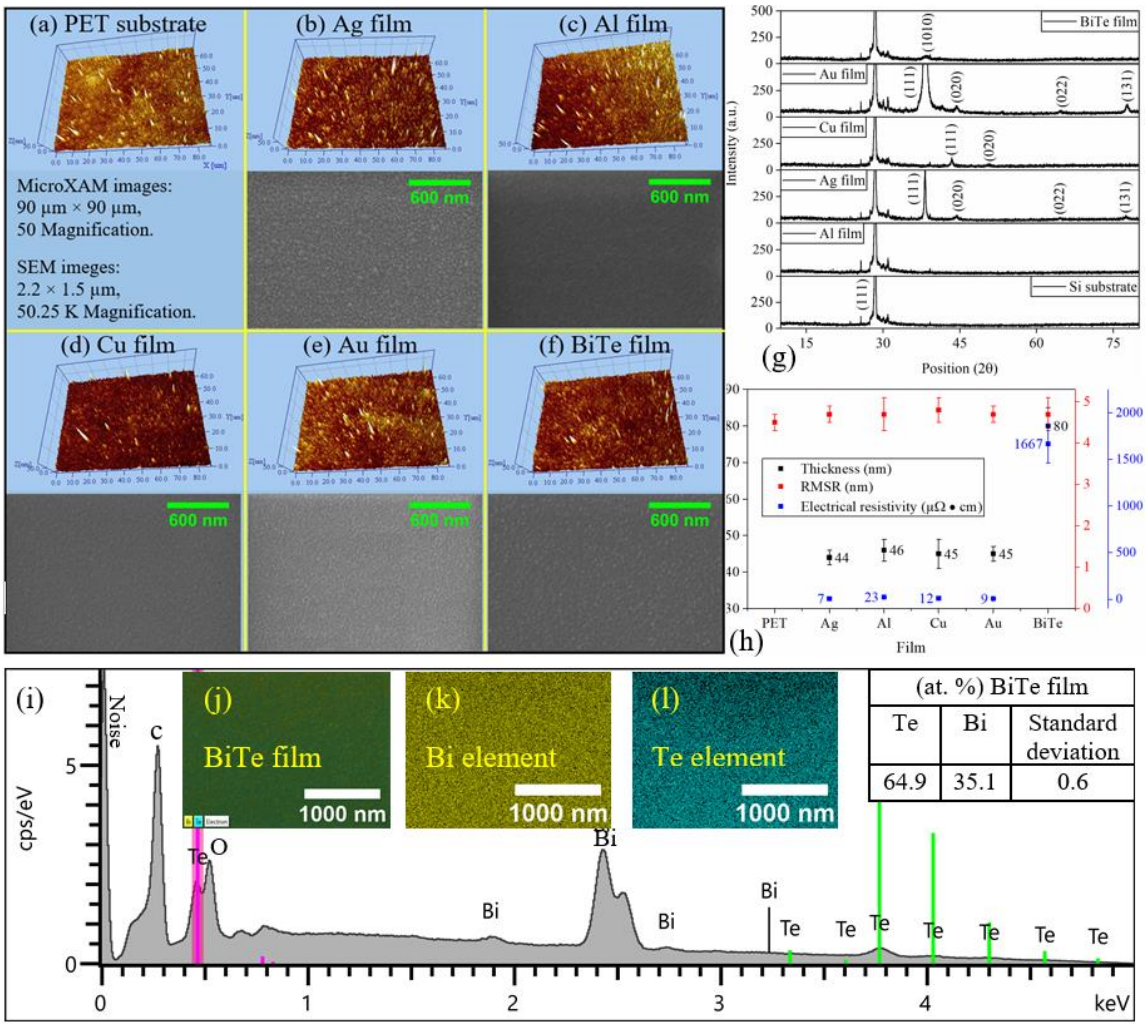


Figure 5.3. *(a-f) MicroXAM (the size of a-b plane is 90 µm × 90 µm and z-scale is ~50 nm) and SEM images of PET substrate and films grown on PET sheets; (g) XRD results of evaporated metal films, sputtered Bi-Te film, and Si wafer substrate (References: Si* [34], *Ag* [35], *Cu* [36], *Au* [35] *and* Bi_2Te_3 [37]*); (h) Roughness, film thickness and electrical resistivity of films grown on PET sheets (The error bars in RMSR, thickness and resistivity represent standard deviations from five 90 µm × 90 µm MicroXAM images, and six measurements in DekTak and four-point probe,); (i) EDX spectrum of Bi-Te film (inset: the compositions of Bi and Te in mapping analysis from three 2.35 µm × 1.95 µm images); Elements (k) Bi and (l) Te distribution in (j) Bi-Te film.*

6.3.2 Band-diagram predication

An aligned band diagram is predicted according to results of work function (*WF*), bandgap (E_g), and maximum valance band (E_{VBM}) of Bi-Te and metal films, as shown in Figure 5.4. This is an idealized prediction of band alignment without consideration of any new phase (e.g. oxidation or new reacted product) formed at the M-S interface. After M-S contact, the Fermi level (E_F) keeps constant at an equilibrium [38] allowing energy bands in the semiconductor to bend up or down, thus forming a Schottky or Ohmic junction depending on the offset between the *WF* of the semiconductor and metal [39]. Any energy barrier formed at these junctions will significantly affect the electrical properties (electron transport) [40]. In Figure 5.4, an Ohmic junction is formed at Al/Bi-Te and Ag/Bi-Te, while a Schottky junction is formed at Cu/Bi-Te and Au/Bi-Te. The height of the energy barrier is almost negligible for the Ohmic junction (i.e. 0.1 eV, between E_F and minimum conduction band E_{CBM}), while a significant barrier is observed in the Schottky junction (Cu/Bi-Te: 0.37 eV; Au/Bi-Te: 0.59 eV). In the Ohmic junction (Al/Bi-Te and Ag/Bi-Te), the band bending region is an accumulation region with many carriers accumulated. Guo *et al.* [41] reported that the electrical resistivity in the accumulation region was much lower than that of bulk materials. Hence, I expect a very small contact resistance at the interface of Al/Bi-Te and Ag/Bi-Te, which could lead to an improvement in power output [3]. For the Schottky junction, the band bending region is a depletion region or a space charge region, which is expected to have a very high resistivity due to a lack of charge carriers. However, this high energy barrier at the interface also provides a potential carrier filtering mechanism [42, 43] which may improve *S*.

Figure 5.4 is only an ideal prediction because a real M-S interface could be more complex. In these experiments, the vacuum was broken before depositing a secondary Bi-Te layer

onto the metal layers, which gives an opportunity for oxidation, especially in Al film. What is more, there is a possible reaction between Bi-Te and Al, Ag, Cu, or Au.

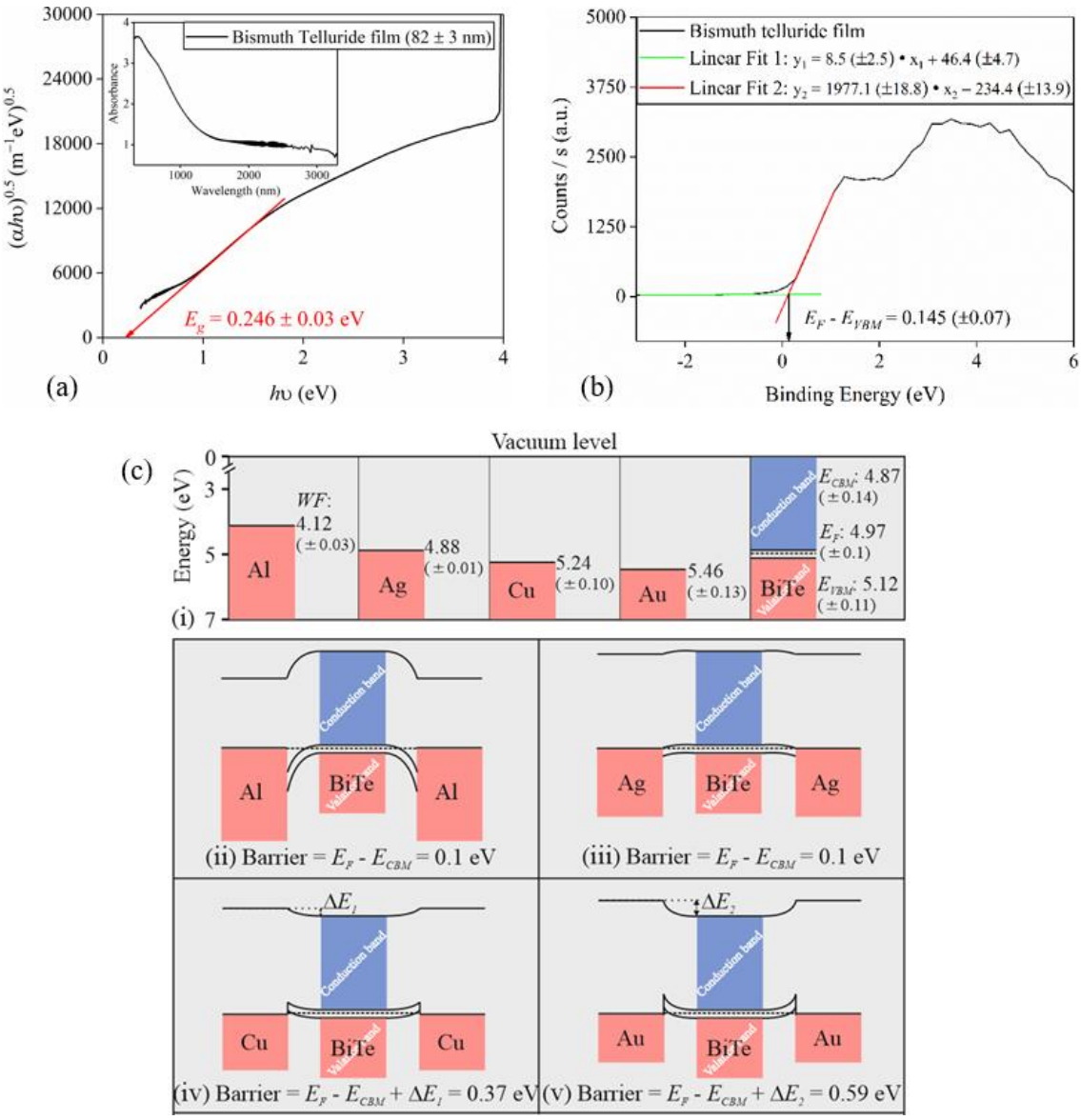


Figure 5.4. *(a) Tauc plot of ~80-nm thick Bi-Te film with (inset) corresponding absorbance spectrum (where α is absorbance coefficient, hν is photon energy, E_g is bandgap. Error of E_g is from three identical measurements); (b) XPS valence scan to determine WF by an intersection of the linear extrapolations to the cutoff regions of E_F and E_{VBM}; (c) i: Positions of WF, E_g, and valance/conduction bands of Bi-Te and metal films, ii-v: Vacuum aligned band diagram, without consideration of any new phase formed at M-S interface.*

6.3.3 Analysis of reactions at interface

The measured resistances of the junctions (using two probes to across the junction) are presented in Figure 5.5 a. A larger resistance is observed at the interface of Al/Bi-Te than the Cu and Au cases, and the Ag/Bi-Te interface is highly resistive, with measurement of a resistance value, close to the upper limit for the meter, only possible in one direction. These observations are confirmed by a contact resistance (R_C) measurement (Figure 5.5 b), using the method as described in Chapter 2. Au/Bi-Te and Cu/Bi-Te have a similar R_C, while Al/Bi-Te has a much higher R_C and Ag/Bi-Te/Ag is measured as an open circuit because of the very high contact resistance. A high R_C at Al/Bi-Te interface is likely due to the expected oxidation layer on the Al. XPS results (Figure 5.5 d) also provide evidence of oxidation of the Al film, where a large content of oxygen (42.2 ± 0.9 %) and an Al oxide peak at 75.4 eV are observed. The expected positions of metal oxide peaks in Ag, Cu, and Au are also labelled in Figure 5.5 c-f. There is no obvious oxide peak observed in Ag and Au although small peaks may not be resolvable from the main metal peak. There is likely a small peak of Cu oxide observed at 934.5 eV (Figure 5.5 e). XPS results of all the metal films indicate the presence of oxygen because XPS always picks up adventitious carbon with C-O and C=O characteristics. Overall, the XPS results (oxidation peak and oxygen content) indicate that Al film is much more oxidized than the others, explaining the high R_C. However, the oxidation phenomenon cannot explain the unusually high resistance at the Ag/Bi-Te interface.

To view the cross-section clearly, thicker metal and Bi-Te films were deposited on Si wafers and then analysed using FIB-SEM and EDX line-scans across an interface, as shown in Figure 5.6 (a-d). Only in the case of the Ag sample is metal diffusion into Bi-Te films observed, and there is also a slight Te diffusion into the Ag films. The Al sample

contains a small amount of oxygen in the Al region, consistent with XPS results in Figure 5.5 d.

In terms of films grown on PET sheets, a cross-sectional image of Bi-Te and Ag was made using a Gatan PECS II AJW Unit and then characterized in EDX mapping as shown in Figure 5.6 (e-h). A partition between Ag and Bi can be clearly seen in the elemental distributions, while Te is observed in the Ag region. Te also appears to extend to the PET region because of an overlapping phenomenon of peaks of Te and O in EDX analysis (see Figure 5.3 i), and similarly Ag peaks do overlap with others such as Bi peaks. A quantitative analysis (Figure 5.6 i) of Ag, Bi, and Te (at positions 1, 2, 3, 4, 5 in Figure 5.6 e) further shows that more Te than Bi exists at the interface between Ag and Bi-Te and in the Ag (i.e. positions 3 and 4). A reaction between Ag and Bi-Te could occur: in an electroplating experiment, Lin *et al.* [13] observed a severe inter-diffusion between Bi_2Te_3 and Ag and confirmed a new Ag_2Te phase formed at the interface following an annealing process at 250°C for 10 h. In my case (a RT deposition), a new phase formed at the interface could involve one or more of several possible phases from the Bi/Te/Ag system [44]. Silver Telluride is reported as a thermoelectric material with a small E_g [45], and there is also a report showing Ag doping to improve the TE performance of Bi-Se-Te compounds [46]. However, in this case, it would seem that the interaction of the Ag with the Bi-Te leads to a very high resistance junction.

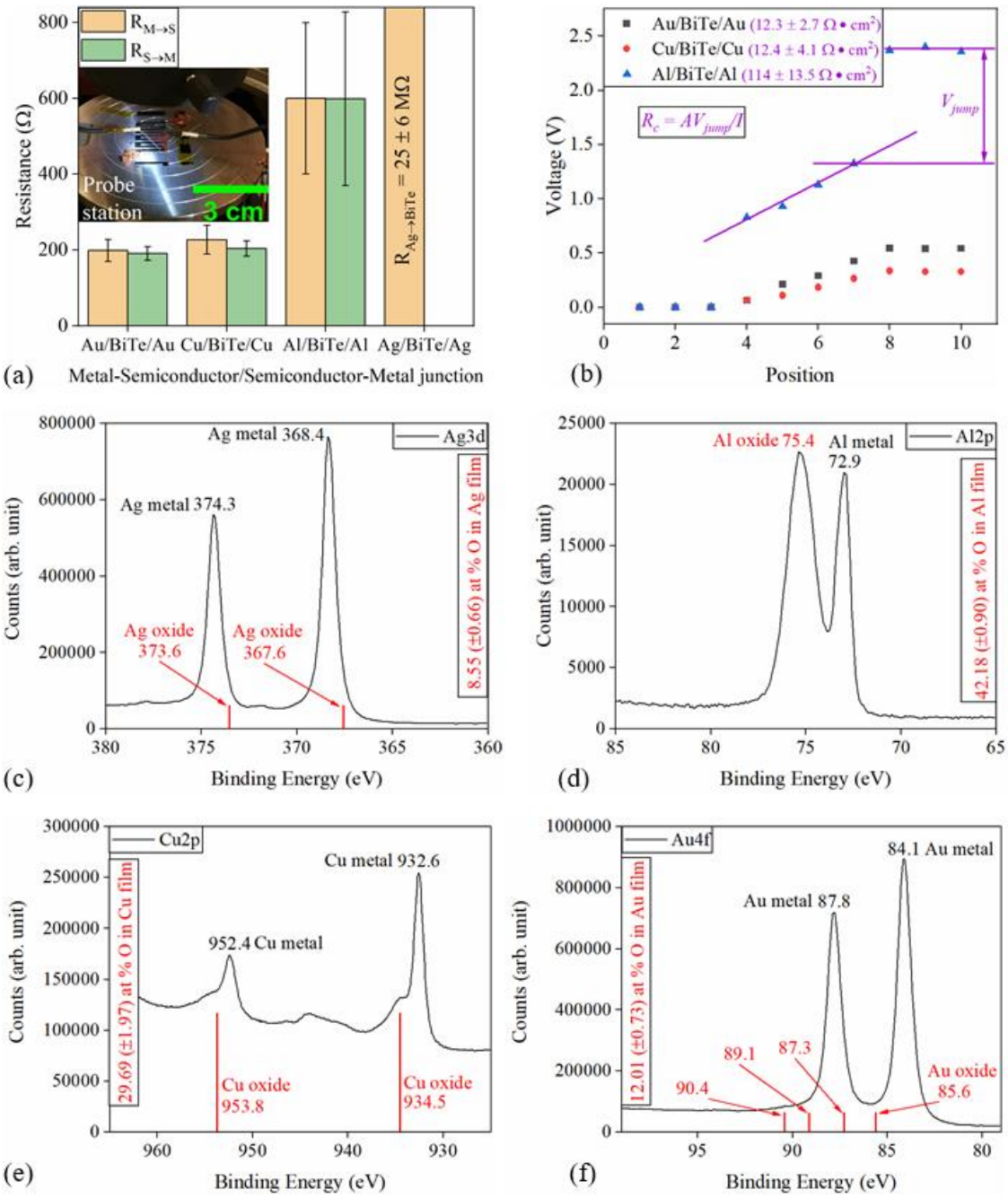


Figure 5.5. *(a) Resistance measurements from metal to semiconductor or from semiconductor to metal, inset: testing setup in a probe station; (b) Contact resistance measurement of the interface between Bi-Te and metal films; (c-f) XPS spectrum of Ag, Al, Cu, and Au films.*

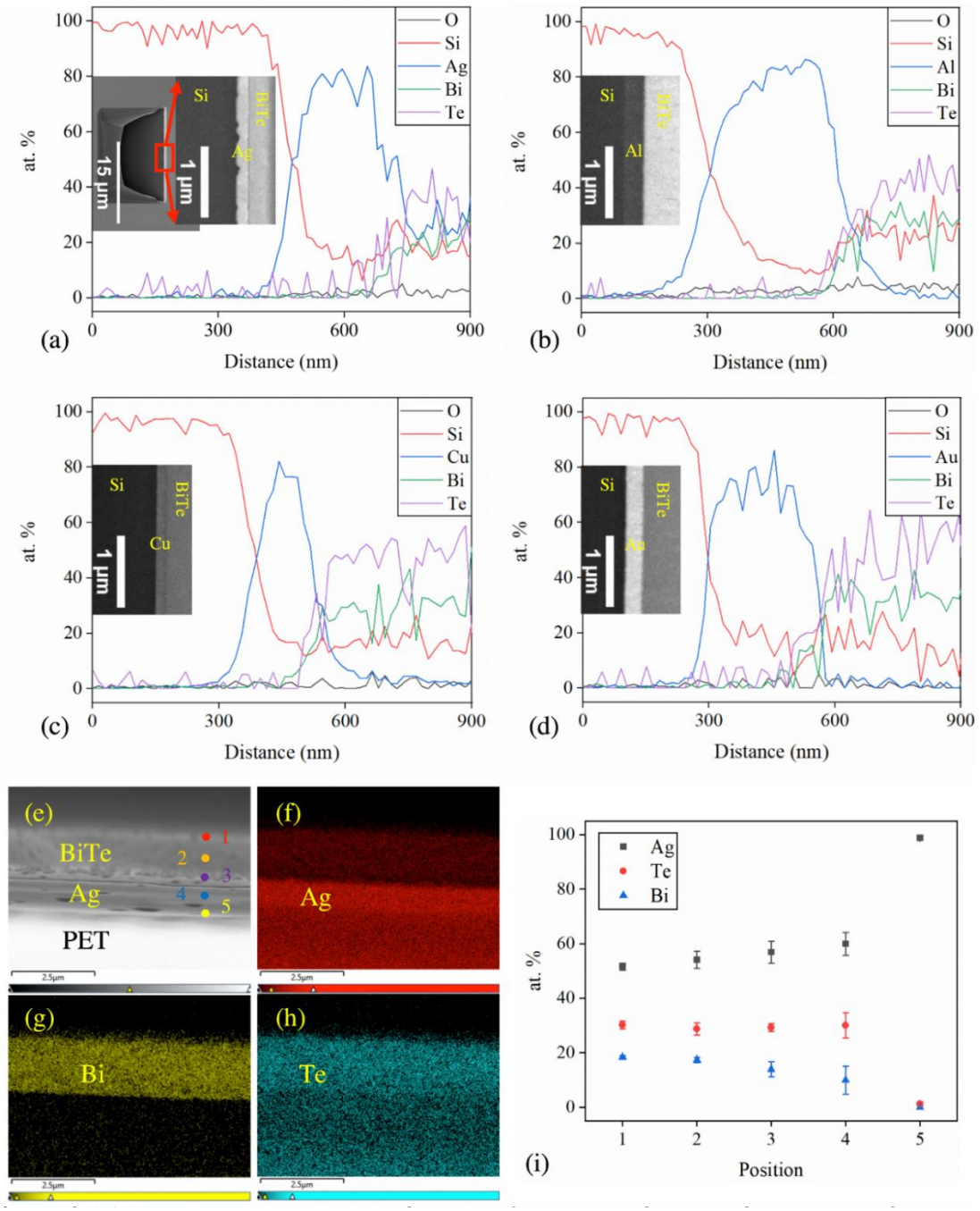


Figure 5.6. *(a-d) Elemental profiles of line scale at cross-sections of Bi-Te film/metal films on Si wafers (inset: cross-section images made by FIB-SEM); (e-h) Elemental mappings of Bi-Te film/Ag film on PET substrate (cross-section made by Gatan PECS II system and FE-SEM); (i) Elemental ratio of Ag, Bi, and Te at positions 1, 2, 3, 4 and 5 in (e). The error bars represent standard errors from three measurements.*

6.3.4 Seebeck characterisation of Al/, Cu/ and Au/Bi-Te based TEGs

Figure 5.7 a and b show V_{OC} and I_{SC} of Bi-Te-based TEGs with three different electrode contacts: Al, Cu, and Au, with a corresponding fit line (inset table: R^2 of 1 means a perfect fitting). The slope of the fit line in a plot of V_{OC} *vs* ΔT is S (238.2, 285.2, 310.2 μV K^{-1}, corresponding to 5-strip Al-, Cu- and Au-TEGs, respectively). A slightly larger S is observed in Au- and Cu-TEGs than Al-TEGs, which could be attributed to a small barrier effect at the Schottky junction, as analysed in Figure 5.4 c. In the plot of I_{SC} *vs* ΔT, there is a slope for each device describing how I changes with ΔT. Again Au- and Cu-TEGs show better behaviours because the resistance of Al-TEGs is very large (consistent with R_C results). Au-TEGs possess the best I_{SC} because it has the lowest internal resistance (measured at an ambient temperature).

In terms of power measurements, changes in I, V, and P are shown in Figure 5.7 (c-e). With increasing resistance of an external load resistor, I decreases, and V increases. As expected [47], there is a maximum P output (P_{max}) when a load resistance is equal to the internal resistance of TEG (i.e. $R_L = R_{TEG}$).

Equation (5.1) in Chapter 5 can be rearranged to give:

$$\sqrt{\frac{R_L}{P}} = \frac{R_{TEG}}{S_{TEG} \cdot \Delta T} + \frac{1}{S_{TEG} \cdot \Delta T} R_L \qquad (5.1)$$

where R_L is the resistance of load resistor; S_{TEG} is the Seebeck coefficient of the whole device; R_{TEG} is the internal resistance of the whole device.

Hence, by plotting $\sqrt{R_L/P}$ *vs* R_L (Figure 5.7 f) using data from Figure 5.7 e, R_{TEG} and S_{TEG} can be extracted from slope and intercept of the linear fit. It is clear that the extracted S_{TEG} values (Figure 5.7 f) are consistent with S derived from the slope of the ΔT relationship (Figure 5.7 a).

Compared with Cu-TEG, Au-TEG has a slightly higher *P* output with $S_{Au\text{-}TEG}$ being greater (Figure 5.7 a f) and $R_{Au\text{-}TEG}$ smaller (Figure 5.7 b f). A larger $S_{Au\text{-}TEG}$ is attributed to a higher barrier (Figure 5.4 c v) to carry carrier filtering effect, and a smaller $R_{Au\text{-}TEG}$ is due to the electrical performance of Au. Although the Cu-TEG shows a slightly lower *P* output than Au-TEG, the copper raw material is much cheaper than gold, thus Cu is suggested as the electrode in this study, and the following investigations are carried out using Cu-TEGs.

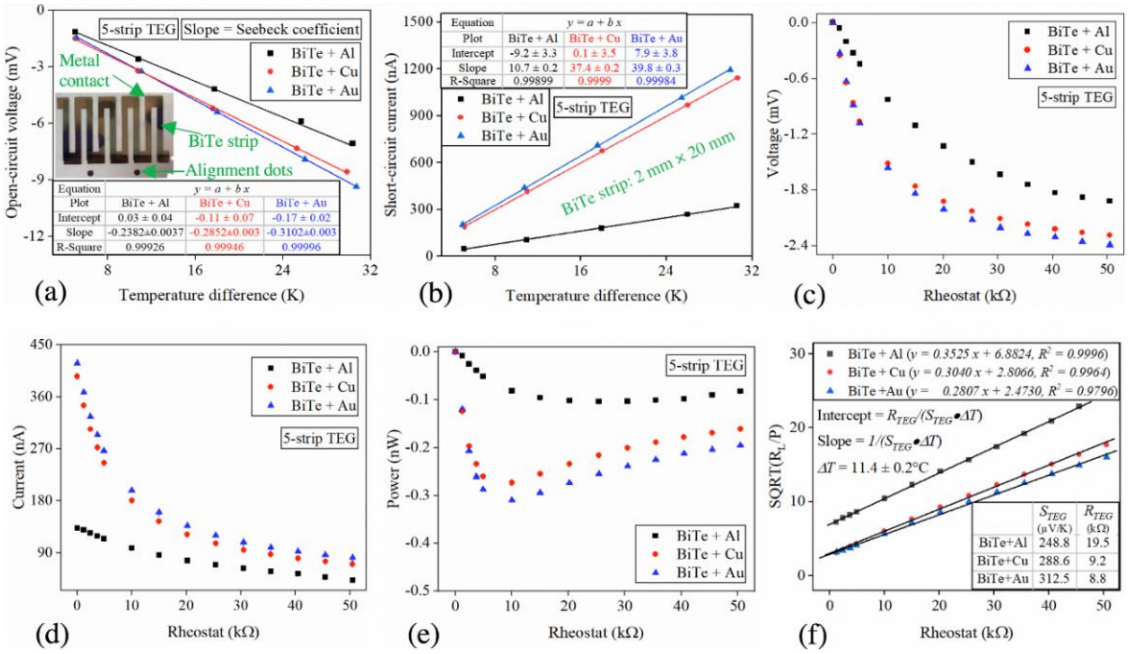


Figure 5.7. *(a-b) V_{OC} and I_{SC} of five-strip TEGs using three different electrodes: Al, Cu, Au by applying ΔT of 5.5, 11.4, 18.2, 26.2, 30.8 ± 0.2°C (inset picture: a real image of a TEG with five Bi-Te strips. The 'ʃ' shape metal contacts are deposited followed by the deposition of '\|' shape Bi-Te strips: 2 mm × 20 mm, with the help of alignment dots. inset table: details of fit lines. a: the slope denotes Seebeck coefficient at a unit of mV K^{-1}, and the negative value means an n-type TE material; b: the slope denotes Seebeck behaviour in current with ΔT, nA K^{-1}); (c-e) Output V, I and calculated P of five-strip TEGs in an Ohm's circuit at a ΔT of 11.4 ± 0.2 °C (An external load resistor (rheostat) varies from 0.84 Ω to 50.5 kΩ); (c) A plot to deduce S_{TEG} and R_{TEG} using data from Figure 5.7 e*

through Equation (5.1). The n-type Bi-Te generates a negative value of voltage output. In this study, the power is calculated by a product of voltage and current as measured, so the power data presented in the figure is also negative values.

6.3.5 Cu/Bi-Te based TEGs

6.3.5.1 In-line patterning connection

In a series connection, power output is expected to increase as the number of strips increases [3]. Voltage output is expected to be proportional to the number of strips and adversely R_{TEG} is proportional to the number of strips connected in series [48]. Consequently, current output should be constant according to Ohm's law [16].

In a parallel connection, power output should also increase with the number of strips. The current output is predicted to be proportional with the number of strips [16] as the effective cross-section area of TE material increases. Voltage is expected to be constant with the number of strips because each TE strip generates the same potential difference between the hot side and cold side, so for an in-parallel connection, there is no change in the potential difference generated. Similar to R_{TEG} in series mode, R_{TEG} should be inversely proportional to the number of strips, according to the rule of parallel circuits.

Note: R_{TEG} is the resistance of a whole TEG which depends on the balance between the number of thermally excited carriers (in TE semiconductor) and scattering phenomena of those carriers (in both metal and semiconductor), depending on ΔT.

Figure 5.8 A shows variations of V_{OC}, $I_{SC,}$ and P output of in-series connected and parallel-connected Cu-TEGs as a function of the number of strips. Using data of P output in Figure 5.8 A b c, S_{TEG} and R_{TEG} can be deduced, Figure 5.8 C a, to be a supplementary explanation for the measured results of V_{OC}, $I_{SC.}$ In Figure 5.8 A a, linear fits of V_{OC} in series ($y = 0.56x + 0.02$) and I_{SC} in parallel ($y = 311x - 63$) show an R^2 approaching 1,

indicating the expected linear relationship of V_{OC} or I_{SC} output with the number of strips in a TEG (consistent with the observations of S_{TEG} and R_{TEG} in Figure 5.8 C a).

There seems to be an unexpected (even though tiny) change in V_{OC} of in-parallel connected device ($y = 0.002x - 0.46$) as the number of strips increases, as also observed in S_{TEG} (Figure 5.8 C a). This could be understandable by a variation of each TE-Cu pair because the pair with the lowest electrical resistivity dominates the overall S of TEG in the case of in parallel connection. A supplementary experiment using probe station confirms a ~5.8% variation of resistance for TE-Cu pairs, including the variations of Bi-Te strip, Cu strip, and TE-Cu interface.

In terms of in-series connected TEGs (Figure 5.8 A a), I shows a slight increase ($y = 20x + 336$) with the number of strips, which is inconsistent with the simplest prediction (a constant current output). However, this increase is consistent with a decreasing trend in calculated R_{TEG} (Figure 5.8 C a). For the in-series mode, R_{TEG} is expected to increase with the number of strips (all strips have a same dimension: 2 mm × 20 mm). A possible reason could be: as more strips work under a ΔT, the number of charge carriers increases, thus decreasing R_{TEG} and increasing I. To confirm this, a further study is required.

In terms of P output (Figure 5.8 A b and c), both in-series and in-parallel connected TEGs show an increasing trend of P output as more TE strips are connected. The choice of in-line connection (in-parallel or in-series) in TEGs allows the device to be tailored for particular applications, depending on whether a current- or voltage- dominant power source is required and what the load on the device will be. For example, a high-resistance portable device needs an in-series connected TEG to reach P_{max}, rather than an in-parallel connected TEG with a small internal resistance.

6.3.5.2 Dimensions of the thermoelectric strip

Figure 5.8 B shows the data from a series of TEGs with differing strip dimensions, all connected in series. The strip width is fixed at 2 mm when the strip length varies 13 – 50 mm (Figure 6.8 B a-c), and the strip length is fixed at 20 mm when the strip width varies 0.5 – 4 mm (Figure 6.8 C d-f). In Figure 5.8 C b c, S_{TEG} and R_{TEG} are calculated through Equation (5.1) using data of P. $S_{\mathrm{TEG}}^2/R_{TEG}$ is a description of power for a given ΔT. In Figure 5.8 B c f, P output increases with the strip width while decreasing with the strip length, as more obviously observed in $S_{\mathrm{TEG}}^2/R_{TEG}$ (Figure 5.8 C b c). The peak of P profile is slightly shifted according to the changes in R_{TEG}, which increases (from 9 to 50 kΩ) with the strip length (from 13 to 50 mm) but decreases (from 55 to 9 kΩ) with the strip width (from 0.5 to 4 mm). Figure 5.8 B a, b, d, and e show changes in output current and voltage as a function of strip length and width. Current decreases with the strip length, attributed to the increase in R_{TEG}, and increases with the strip width because of more TE materials on the hot side to generate more carriers, consistent with the change of R_{TEG} in Figure 5.8 C b c. Voltage is expected to be the same for all devices because ΔT and the number of strips are the same and the voltage output of each strip theoretically only depends on ΔT rather than the geometry of the strips. However, I observed a decrease in voltage with strip length and an increase in voltage with strip width. The geometry of TEG can affect the actual ΔT across a TEG and its internal resistance. Some simulation studies of bulk TEGs [22, 49] reported that a longer and narrower TE element increases the device thermal resistance because it can maintain a larger actual ΔT across a TEG and thus keeping a maximum voltage output. In this study, S_{TEG} is observed to apparently first decrease and then increase with both strip length and strip width. This means some competitive mechanisms could exist, and more data are required to confidently describe this phenomenon, that is a combination of factors as discussed by McEnaney *et al.* [50]:

1) intrinsic thermal resistances of a TE element; 2) the parasitic heat loss at interfacial resistance and contact electrodes; 3) the effect of sidewall radiative loss. The first one is the prime explanation for bulk TEG studies as discussed above [22, 49]. The second one is considered to be a constant in this study as the number of strips and nature of the electrodes is constant. The third one might be expected to be more important in a thin-film device (high surface area to volume ratio).

It is predicted that there is an optimal strip length to achieve the highest P output [50, 51]. There are studies [22, 49] that confirm an upward trend of P with increasing strip length. This study observed a downward trend of P with increasing strip length. It is speculated that as the strip length decreases further, it will reach the length limitation (see Figure 7.7 B b) so that the ΔT is affected, then the P will decrease. (I did not further decrease the strip length because of the practical constraint of the Seebeck measurement if a TE strip is too short.)

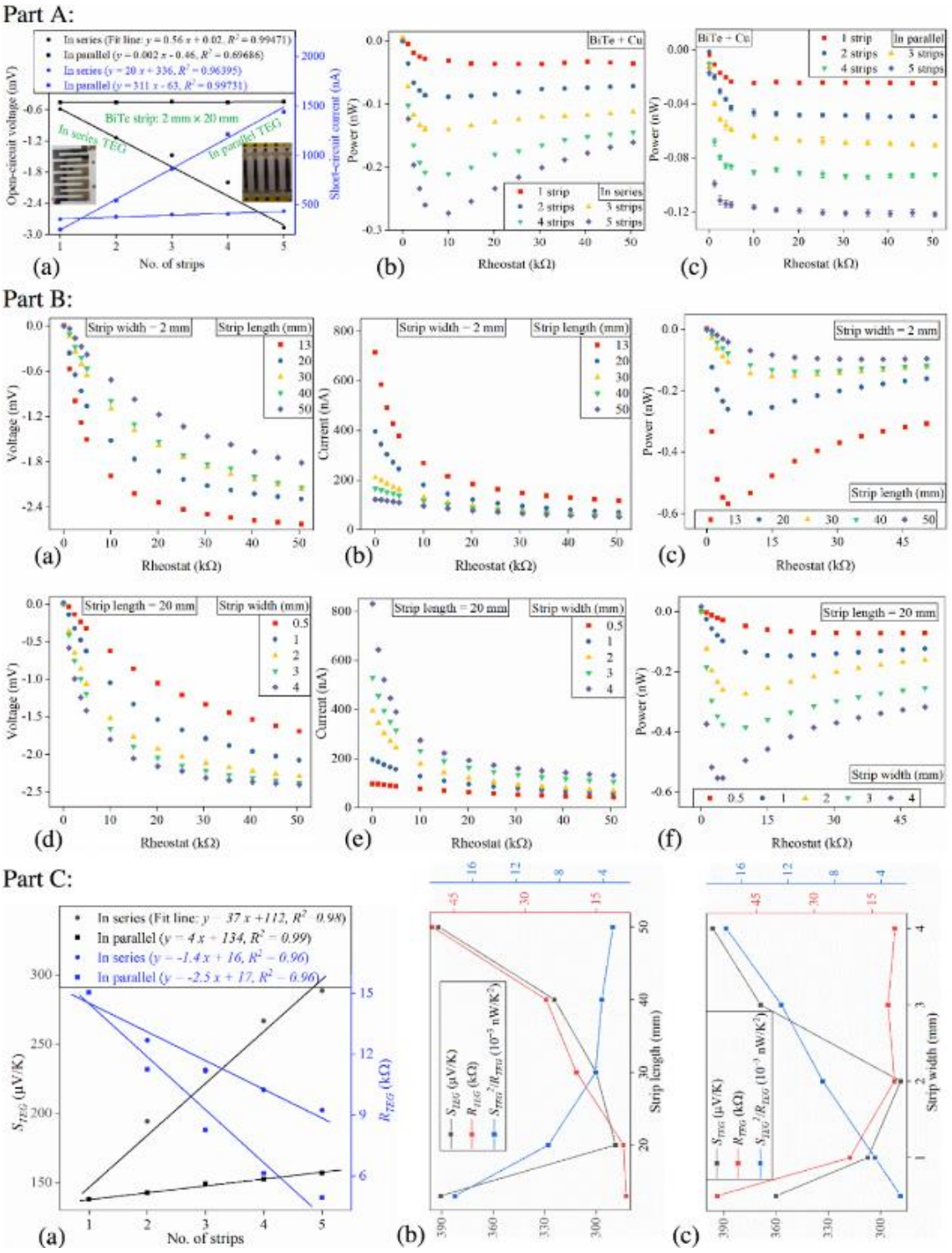


Figure 5.8. *Part A: (a) V_{OC} and I_{SC} of in-series and in-parallel connected Cu-TEGs as a function of the number of strips, with fit lines in parentheses* (*inset pictures: the fabricated in-series and in-parallel connected TEGs); (b & c) P output of in-series and in-parallel connected Cu-TEGs for 1 – 5 strips at a ΔT of 11.4 ± 0.2°C. Part B: (a-c) V, I and P*

output of in-series connected Cu-TEGs with 5 strips of fixed width (2 mm) but varying length (13 – 50 mm) under 11.4 ± 0.2°C; (d-f) V, I and P output of Cu-TEGs with 5 strips of fixed length (20 mm) but varying width (0.5 – 4 mm) under 11.4 ± 0.2°C. Part C: The calculated STEG and RTEG for (a) in-series and in-parallel modes; (b & c) strip dimension, using the data of P from Part A b c and Part B c f through Equation (5.1) (S_{TEG}^2/R_{TEG} is to describe the power output).

6.3.6 Large-scale manufacturability of in-line patterned flexible TEGs

Large-scale manufacture of sputtered TE films on a polymer web followed by inkjet printing of contact electrodes would be feasible for an industrial process. However, very wide strips of TE material are not desirable in a real application in flexible devices. Laser cutting can help make a wide strip segmented. The laser operates as a series of short pulses, so at low power, the TE layer is ablated as a series of dots (Figure 5.9 a). As the laser power was increased, the spots coalesce to form a cut line (Figure 5.9 c), however, a 9% laser power was found to damage the material (Figure 5.9 d). This progression can also be confirmed by the change in electrical resistance across the line as shown in Figure 5.9 e. A segmented specimen formed by laser cutting was found to show less change in the electrical property during buckling testing (Figure 5.9 f), and keeps a similar *I*, *V,* and *P* output (Figure 5.9 g-i), compared with a non-segmented sample. This makes the device more feasible with real applications (e.g. imbedding in wristband), as well as being compatible with large-scale manufacture, significantly boosting the commercialisation of flexible/wearable TEGs.

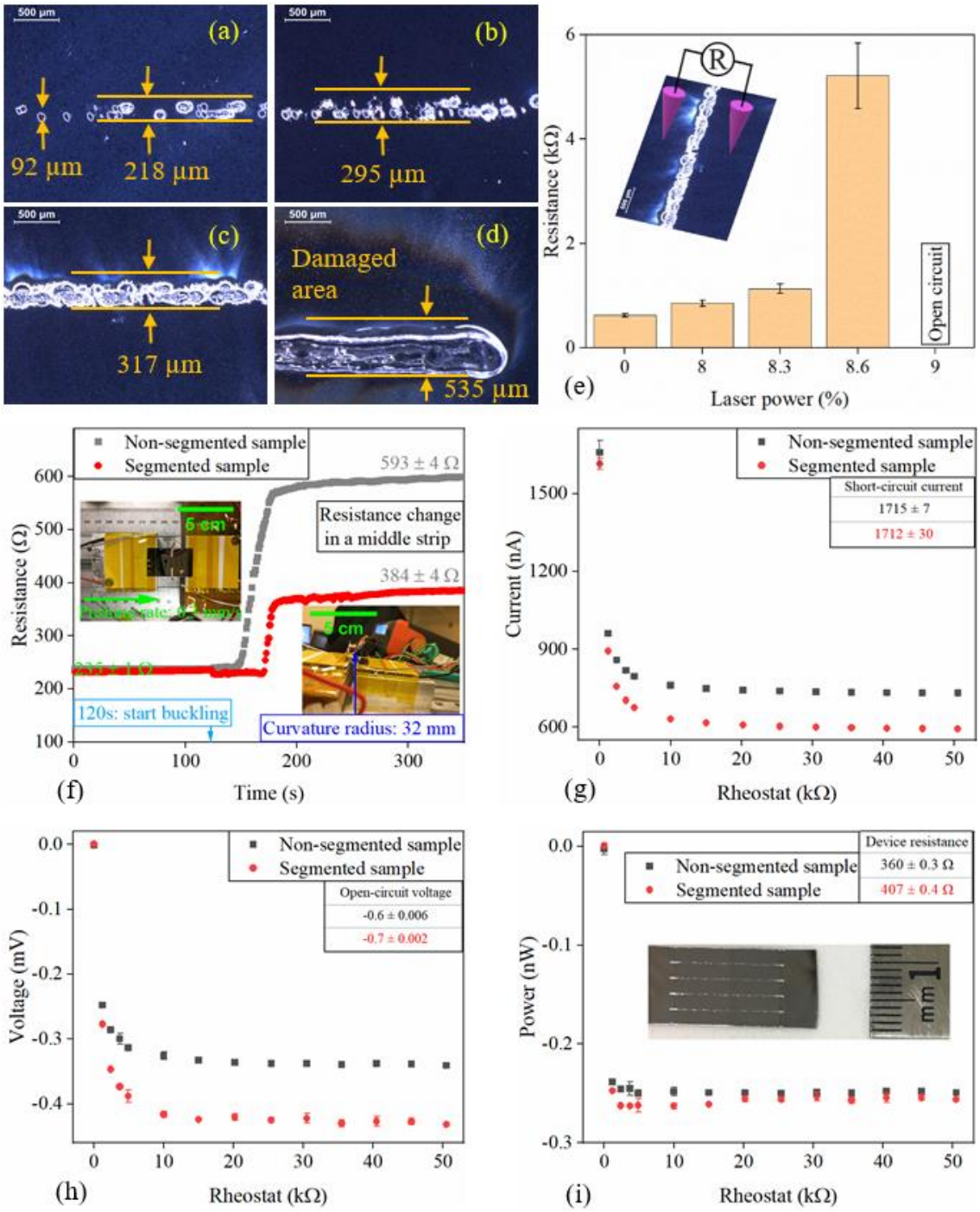


Figure 5.9. *(a-d) Optical microscopy images of laser-cut samples using different laser powers: 8%, 8.3%, 8.6%, and 9% of 40 W; (e) resistance crossing the laser-cut line of samples with different powers in laser cutting; (f) Change in resistance at a middle area of the pristine sample and segmented sample by laser cutting, in buckling testing; (g-i) Output I, V and P of pristine and segmented samples.*

6.4 Summary

An experimental study has been carried out to investigate electrode contacts (Ag, Al, Cu, and Au), in-line patterning connections (in-series and in-parallel), and dimension (strip length/width) of flexible Bi-Te based thermoelectric generators. Analysis of the semiconductor-metal interface (contact resistance, XPS, and EDX) revealed that: 1) Diffusion/reaction between Bi-Te and Ag created a prohibitively high resistance; 2) Al film was more oxidized than others leading to an oxidation layer at the Al/(Bi-Te) interface and a higher interface resistance. In terms of Seebeck performance, the power of a TEG was obtained from experiments while the Seebeck coefficient and internal resistance of the whole device was extracted from fits to the experimental data. Al-TEGs showed a lower power output because an oxidation layer in Al films significantly affected the current output; Cu-TEGs only showed a slightly poorer power output than Au-TEG (because Cu/(Bi-Te) has a slightly lower energy barrier for the carrier filtering effect and Cu-TEG has a higher device resistance). Cu was suggested in manufacture because the copper raw material is much cheaper than gold.

In-series connected TEGs showed a linear relationship of open-circuit voltage with the number of strips, and in-parallel connected TEGs showed a linear relationship of short-circuit current with the number of strips. This illustrates the options for portable devices requiring a voltage-dominant or a current-dominant power source. In addition, in-parallel connected TEGs had a much lower internal resistance than in-series connected ones, thus providing more options for application in portable devices, depending on their load resistance, because a maximum power output of TEGs can only be achieved if the internal resistance of TEG is equal to the load resistance of the portable device.

A shorter and wider TE strip achieved a greater power output. This study is the first to experimentally show a downward trend of output power as increasing the strip length.

Finally, I proposed an industrially feasible manufacturing approach to make flexible TEGs, through roll-to-roll sputtering of thermoelectric materials on a polymer web, inkjet printing of electrode contacts, and segmenting using a laser cuter. A segmented sample possessed an ability to relieve the strain while assembling TEG in a wristband, but also remain thermoelectric performance.

6.5 Reference

[1] Liu, W.; Bai, S. , Thermoelectric interface materials: A perspective to the challenge of thermoelectric power generation module, *Journal of Materiomics.* 2019*, 5*, 321-336, https://doi.org/10.1016/j.jmat.2019.04.004.

[2] Bartkowiak, M.; Mahan, G. D. , Chapter 8 Heat and electricity transport through interfaces, *Semiconductors and Semimetals.* 2001*, 70*, 245-271, https://doi.org/10.1016/S0080-8784(01)80142-3.

[3] Anonymous, Thermoelectric Module Design Theories, *Thermoelectrics Handbook.* 2006, 169-183, https://doi.org/10.1201/9781420038903-11.

[4] Liu, W.; Wang, H.; Wang, L.; Wang, X.; Joshi, G.; Chen, G.; Ren, Z. , Understanding of the contact of nanostructured thermoelectric n-type Bi2Te2.7Se0.3 legs for power generation applications, *Journal of Materials Chemistry A.* 2013*, 1*, 13093, https://doi.org/10.1039/c3ta13456c.

[5] Sokolova, V.; Dudkin, L.; Petrova, L. , Diffusion processes at GeTe/SnTe/Fe contacts, *Inorganic Materials.* 2000*, 36*, 16-21, https://doi.org/10.1007/BF02758372.

[6] Schelling, P. K.; Phillpot, S. R.; Keblinski, P. , Kapitza conductance and phonon scattering at grain boundaries by simulation, *Journal of Applied Physics.* 2004*, 95*, 6082-6091, https://doi.org/10.1063/1.1702100.

[7] Cahill, D. G.; Braun, P. V.; Chen, G.; Clarke, D. R.; Fan, S.; Goodson, K. E.; Keblinski, P.; King, W. P.; Mahan, G. D.; Majumdar, A.; Maris, H. J.; Phillpot, S. R.; Pop, E.; Shi, L. , Nanoscale thermal transport. II. 2003–2012, *Applied Physics Reviews.* 2014*, 1*, https://doi.org/10.1063/1.4832615.

[8] Du, Y.; Xu, J.; Paul, B.; Eklund, P. , Flexible thermoelectric materials and devices, *Applied Materials Today.* 2018*, 12*, 366-388, https://doi.org/10.1016/j.apmt.2018.07.004.

[9] Jie, Q.; Ren, Z. , Contacts for Skutterudites, *Advanced Thermoelectrics.* 2018*, 1*, 625-634, https://doi.org/10.1201/9781315153766-16.

[10] Ebling, D.; Bartholomé, K.; Bartel, M.; Jägle, M. , Module Geometry and Contact Resistance of Thermoelectric Generators Analyzed by Multiphysics Simulation, *Journal*

of Electronic Materials. 2010*, 39*, 1376-1380, https://doi.org/10.1007/s11664-010-1331-0.

[11] Fan, X. C.; Gu, M.; Shi, X.; Chen, L. D.; Bai, S. Q.; Nunna, R. , Fabrication and reliability evaluation of Yb0.3Co4Sb12/Mo–Ti/Mo–Cu/Ni thermoelectric joints, *Ceramics International.* 2015*, 41*, 7590-7595, https://doi.org/10.1016/j.ceramint.2015.02.083.

[12] Taylor, P. J.; Maddux, J. R.; Meissner, G.; Venkatasubramanian, R.; Bulman, G.; Pierce, J.; Gupta, R.; Bierschenk, J.; Caylor, C.; D'Angelo, J.; Ren, Z. , Controlled improvement in specific contact resistivity for thermoelectric materials by ion implantation, *Applied Physics Letters.* 2013*, 103*, 43902, https://doi.org/10.1063/1.4816054.

[13] Lin, W.; Wesolowski, D.; Lee, C. , Barrier/bonding layers on bismuth telluride (Bi2Te3) for high temperature thermoelectric modules, *Journal of Materials Science: Materials in Electronics.* 2011*, 22*, 1313-1320, https://doi.org/10.1007/s10854-011-0306-0.

[14] Laurence H Weitzman , Etching bismuth telluride, 1967, https://patents.google.com/patent/US3338765A/en.

[15] Zhang, J. F.; Yang, K.; Deng, C. M.; Deng, C. G.; Liu, M.; Dai, M. J.; Zhou, K. S. , Method for spray thick nickel coating on surface of semiconductor, 2014.

[16] Wang, Y. T.; Liu, W.; Fan, A. W.; Li, P. , Performance Comparison between Series-Connected and Parallel-Connected Thermoelectric Generator Systems, *Appl. Mech. Mater.* 2013*, 325-326*, 327-331, https://doi.org/10.4028/www.scientific.net/AMM.325-326.327.

[17] Li, W.; Paul, M. C.; Montecucco, A.; Siviter, J.; Knox, A. R.; Sweet, T.; Gao, M.; Baig, H.; Mallick, T. K.; Han, G.; Gregory, D. H.; Azough, F.; Freer, R. , Multiphysics simulations of thermoelectric generator modules with cold and hot blocks and effects of some factors, *Case Studies in Thermal Engineering.* 2017*, 10*, 63-72, http://dx.doi.org/10.1016/j.csite.2017.03.005.

[18] Mortazavinatanzi, S.; Rezaniakolaei, A.; Rosendahl, L. , Printing and Folding: A Solution for High-Throughput Processing of Organic Thin-Film Thermoelectric Devices, *Sensors (Basel, Switzerland).* 2018*, 18*, 989, https://doi.org/10.3390/s18040989.

[19] Meng, F.; Chen, L.; Sun, F. , Effects of thermocouples' physical size on the performance of the TEG–TEH system, *International Journal of Low-Carbon Technologies.* 2016*, 11*, 375-382, https://doi.org/10.1093/ijlct/ctt080.

[20] Kim, H. S.; Liu, W.; Ren, Z. , The bridge between the materials and devices of thermoelectric power generators, *Energy & Environmental Science.* 2017*, 10*, 69-85, https://doi.org/10.1039/C6EE02488B.

[21] Kishore, R.; Mahajan, R.; Priya, S. , Combinatory Finite Element and Artificial Neural Network Model for Predicting Performance of Thermoelectric Generator, *Energies.* 2018*, 11*, 2216, https://doi.org/10.3390/en11092216.

[22] Suarez, F.; Nozariasbmarz, A.; Vashaee, D.; Öztürk, M. C. , Designing thermoelectric generators for self-powered wearable electronics, 2016*, 9*, 299-2113, https://doi.org/10.1039/c6ee00456c.

[23] Kishore, R. A.; Sanghadasa, M.; Priya, S. , Optimization of segmented thermoelectric generator using Taguchi and ANOVA techniques, *Scientific Reports.* 2017*, 7*, 16746-15, https://doi.org/10.1038/s41598-017-16372-8.

[24] Hu, X.; Jood, P.; Ohta, M.; Kunii, M.; Nagase, K.; Nishiate, H.; Kanatzidis, M. G.; Yamamoto, A. , Power generation from nanostructured PbTe-based thermoelectrics: comprehensive development from materials to modules, *Energy & Environmental Science.* 2016*, 9*, 517-529, https://doi.org/10.1039/C5EE02979A.

[25] Stuart, B. W.; Tao, X.; Gregory, D.; Assender, H. E. , Roll-to-Roll Patterning of Al/Cu/Ag Electrodes on Flexible Polyethylene by Oil Masking: A comparison of Thermal Evaporation and Magnetron Sputtering, *Appl. Surf. Sci.* 2019*, 505*, 144294, https://doi.org/10.1016/j.apsusc.2019.144294.

[26] Eggenhuisen, T. M.; Galagan, Y.; Biezemans, A. F. K. V; Slaats, T. M. W. L; Voorthuijzen, W. P.; Kommeren, S.; Shanmugam, S.; Teunissen, J. P.; Hadipour, A.; Verhees, W. J. H.; Veenstra, S. C.; Coenen, M. J. J.; Gilot, J.; Andriessen, R.; Groen, W. A. , High efficiency, fully inkjet printed organic solar cells with freedom of design, *Journal of Materials Chemistry. A, Materials for Energy and Sustainability.* 2015*, 3*, 7255-7262, https://doi.org/10.1039/c5ta00540j.

[27] Abbel, R.; Teunissen, P.; Rubingh, E.; Lammeren, T. v.; Cauchois, R.; Everaars, M.; Valeton, J.; Geijn, S. v. d.; Groen, P. , Industrial-scale inkjet printed electronics manufacturing—production up-scaling from concept tools to a roll-to-roll pilot line, *Translational Materials Research.* 2014*, 1*, 15002, https://doi.org/10.1088/2053-1613/1/015002.

[28] Roshanghias, A.; Krivec, M.; Baumgart, M. , Sintering strategies for inkjet printed metallic traces in 3D printed electronics, *Flexible and Printed Electronics.* 2017*, 2*, 45002, https://doi.org/10.1088/2058-8585/aa8ed8.

[29] Lacy, F. , Developing a theoretical relationship between electrical resistivity, temperature, and film thickness for conductors, *Nanoscale Research Letters.* 2011*, 6*, 1-14, https://doi.org/10.1186/1556-276X-6-636.

[30] Camacho, J. M.; Oliva, A. I. , Morphology and electrical resistivity of metallic nanostructures, *Microelectronics Journal.* 2005*, 36*, 555-558, https://doi.org/10.1016/j.mejo.2005.02.068.

[31] Ding, G.; Clavero, C.; Schweigert, D.; Le, M. , Thickness and microstructure effects in the optical and electrical properties of silver thin films, *AIP Advances.* 2015*, 5*, 117234-11, https://doi.org/10.1063/1.4936637.

[32] Schmiedl, E.; Wissmann, P.; Finzel, H. , The Electrical Resistivity of Ultra-Thin Copper Films, *Zeitschrift Für Naturforschung. A, A Journal of Physical Sciences.* 2008*, 63*, 739-744, https://doi.org/10.1515/zna-2008-10-1118.

[33] Novelo, T. E.; Alonzo-Medina, G. M.; Amézaga-Madrid, P.; Maldonado, R. D. , Surface Morphology and Electrical Resistivity in Polycrystalline Au/Cu/Si(100) System, *Journal of Nanomaterials.* 2017*, 2017*, 1-8, https://doi.org/10.1155/2017/2079204.

[34] Knorr, K.; Stüßer, N.; Többens, D. M.; Mayer, H. M.; Lampert, G. , E9: The New High-Resolution Neutron Powder Diffractometer at the Berlin Neutron Scattering Center, *Materials Science Forum.* 2001*, 378-381*, 288-293, https://doi.org/10.4028/www.scientific.net/MSF.378-381.288.

[35] Wyckoff, R. W. G. , Crystal structures, 1963*, 1*, 7-83.

[36] Lejaeghere, K.; Van Speybroeck, V.; Van Oost, G.; Cottenier, S. , Error Estimates for Solid-State Density-Functional Theory Predictions: An Overview by Means of the Ground-State Elemental Crystals, *Critical Reviews in Solid State and Materials Sciences.* 2014*, 39*, 1-24, https://doi.org/10.1080/10408436.2013.772503.

[37] Akshay, V. R.; Suneesh, M. V.; Vasundhara, M. , Tailoring Thermoelectric Properties through Structure and Morphology in Chemically Synthesized n-Type Bismuth Telluride Nanostructures, *Inorganic Chemistry.* 2017*, 56*, 6264-6274, http://dx.doi.org/10.1021/acs.inorgchem.7b00336.

[38] Cowley, A. M.; Sze, S. M. , Surface States and Barrier Height of Metal-Semiconductor Systems, *Journal of Applied Physics.* 1965*, 36*, 3212-3220, https://doi.org/10.1063/1.1702952.

[39] Lüth, H. , Solid Surfaces, Interfaces and Thin Films, 2015, 380, https://doi.org/10.1007/978-3-319-10756-1.

[40] Nptel , Metal-semiconductor junctions, *NOC: Fundamentals of Electronic Materials and Devices.* , https://nptel.ac.in/content/storage2/courses/113106065/Week%204/Lesson9.pdf.

[41] Guo, L.; Wang, X. Q.; Zheng, X. T.; Yang, X. L.; Xu, F. J.; Tang, N.; Lu, L. W.; Ge, W. K.; Shen, B.; Dmowski, L. H.; Suski, T. , Revealing of the transition from n- to p-type conduction of InN:Mg by photoconductivity effect measurement, *Scientific Reports.* 2014*, 4*, 4371, https://doi.org/10.1038/srep04371.

[42] Yang, X. H.; Qin, X. Y.; Zhang, J.; Li, D.; Xin, H. X.; Liu, M. , Enhanced thermopower and energy filtering effect from synergetic scattering at heterojunction potentials in the thermoelectric composites with semiconducting nanoinclusions, *Journal of Alloys and Compounds.* 2013*, 558*, 203-211, https://dx.doi.org/10.1016/j.jallcom.2012.12.048.

[43] Zou, T. H.; Qin, X. Y.; Li, D.; Sun, G. L.; Dou, Y. C.; Wang, Q. Q.; Ren, B. J.; Zhang, J.; Xin, H. X.; Li, Y. Y. , Simultaneous enhancement in thermoelectric power

factor and phonon blocking in hierarchical nanostructured β-Zn4Sb3-Cu3SbSe4, *Applied Physics Letters.* 2014*, 104*, 13904, https://doi.org/10.1063/1.4861156.

[44] Babanly, M.; Shykhyev, Y.; Babanly, N.; Yusibov, Y. , Phase equilibria in the Ag-Bi-Te system, *Russian Journal of Inorganic Chemistry.* 2007*, 52*, 434-440, https://doi.org/10.1134/S0036023607030242.

[45] Zhang, M.; Park, H.; Kim, J.; Park, H.; Wu, T.; Kim, S.; Park, S.; Choa, Y.; Myung, N. V. , Thermoelectric Properties of Ultralong Silver Telluride Hollow Nanofibers, *Chemistry of Materials.* 1900*, 27*, 5189-5197, http://dx.doi.org/10.1021/acs.chemmater.5b00960.

[46] Meng-Pei Lu; Chien-Neng Liao; Jing-Yi Huang; Hung-Chang Hsu , Thermoelectric properties of Ag-doped Bi2(Se,Te)3 compounds: dual electronic nature of Ag-related lattice defects, *Inorganic Chemistry.* 2015*, 54*, 7438, https://doi.org/10.1021/acs.inorgchem.5b01031.

[47] Hodes, M. , Optimal Pellet Geometries for Thermoelectric Power Generation, *IEEE Transactions on Components and Packaging Technologies.* 2010*, 33*, 307-318, https://doi.org/10.1109/TCAPT.2009.2039934.

[48] Wang, W.; Cionca, V.; Wang, N.; Hayes, M.; O'Flynn, B.; O'Mathuna, C. , Thermoelectric Energy Harvesting for Building Energy Management Wireless Sensor Networks, *International Journal of Distributed Sensor Networks.* 2013*, 9*, 232438, https://doi.org/10.1155%2F2013%2F232438.

[49] Bahk, J.; Fang, H.; Yazawa, K.; Shakouri, A. , Flexible thermoelectric materials and device optimization for wearable energy harvesting, *J. Mater. Chem. C.* 2015*, 3*, 1362-1374, https://doi.org/10.1039/c5tc01644d.

[50] McEnaney, K. , Thermoelectrics and Aerogels for Solar Energy Conversion Systems, 2015, https://search.proquest.com/docview/1707152444.

[51] He, W.; Wang, S. , Performance Comparison of Different Exhaust Exchanger Types Considering Peak Net Power and Optimal Dimension in a Thermoelectric Generator System, *Advanced Theory and Simulations.* 2018*, 1*, 1800012-n/a, https://doi.org/10.1002/adts.201800012.

Chapter 7 A novel stacking design of flexible TEGs

A stacked TEG on flexible polymer sheet is investigated that can utilise a low-cost high throughput R2R process, employing a metal-insulator-semiconductor structure of <100-nm thick Cu and bismuth telluride films with a ~1-μm thick acrylate insulating coating. Thermoelectric strips connected in plane can be stacked and connected in the out-of-plane direction, which significantly decreases the size required in the substrate plane and also gives rise to the opportunity for greatly extended power output in a stacked device with potentially thousands of layers.

7.1 Introduction

CP-TEG (see Chapter 1 about CP-TEG *vs* IP-TEG) has already been commercialised in bulk TEGs and some μ-thick TEGs, however, to decrease the size of CP-TEGs to nano range is not practical since maintaining a large ΔT across a nano-thick TE leg is almost an impossible challenge [1, 2] leading to poor power output (e.g. [3-10]). Although the development of nano-size CP-TEG is restricted, nanomaterials still attract significant interest for scientists, and the research on IP-TEG is moving towards the use of nanomaterials (e.g. thin film [11], quantum well [12], and nanowire [13]), due to an extraordinary improvement in TE performance [14]. Chapter 3 observed an increase in PF for a thinner sputtered Bi-Te film, which experimentally confirmed the calculated prediction in [15]. Compared with CP-TEG, IP-TEG mainly has two drawbacks: (1) ΔT of wearable TEG will be perpendicular to a wearer's skin [16], while IP-TEG utilises ΔT in the plane which limits IP-TEG use on the human body [17]; (2) Because of a long-strip architecture in the plane, the R_{TEG} of IP-TEG is usually large leading to a relatively high voltage output but a tiny working current output thus the power output is limited [18-20].

Drawback (1) is a common question of how to apply IP-TEG in a real wearable application. To solve it, scientists have proposed a variety of feasible means/designs (e.g. planar [21], cylindrical [22], Y-type [23], corrugated-structure [24] or folded-mode [1], slope-type [25], coil-up coin-shape [26], and oxide-based transversal [27]). In terms of drawback (2), the high R_{TEG} and low power output can be adjustable according to the dimension of the TE strip. In the design of IP-TEG, the TE-strip dimension and fill factor (*FF*) are a major tradeoff [28, 29]. *FF* quantifies how efficiently a TEG occupies a substrate, i.e. the ratio between the surface area of TEG materials and the overall surface area of the device. A maximum power density requires a balance of *FF*, inter-strip spacing, dimension, and the number of TE strips. In this chapter, I will explore *FF* in the cross-plane direction of IP-TEG.

IP-TEG is typically fabricated with numbers of TE strips on a substrate that are electrically connected in series or parallel. Here, I investigate a stacking architecture for each TE strip, to improve TE performance. Funahashi *et al.* (2011, [30]) reported a bulk TEG based on multilayer ceramic capacitor technology in which a number of n-i-p junctions (where n, i, p are n-type, insulator, and p-type semiconductor, respectively) were stacked and co-fired. Funahashi's study stacked bulk layers along the in-plane direction, while I report here the stacking of nano-thickness coatings in the cross-plane direction.

The n-i-p structure is a traditional TEG design and more commonly used than m-i-s (where m, i, and s are metal, insulator, and semiconductor, respectively), because the m-i-s TEG has an inherent and parasitic drawback that a metal strip has good thermal conductivity and can conduct heat from the hot side to cold side (consequently a decrease in ΔT leads to less power output). However, many studies [1, 31] reported the m-i-s TEG and it has been confirmed that the difference of power outputs between these two

architectures (m-i-s *vs* n-i-p) is very small [1]. Most importantly, a stacked m-i-s structure in a thin-film configuration is easier to fabricate than a stacked n-i-p structure (e.g. the ease of synthesis/deposition, material stability, and reliability), causing fewer issues (e.g. a short or open circuit) for reliable TEG devices. Overall, a faster prototype/demonstration for commercialisation could be achieved with one type (n or p) coupled with a metal shunt [28], and I will utilise an m-i-s architecture in this study.

The manufacturing process of TEGs is based on the architecture of TEGs and also the TE material employed [32]. The TE, metal and insulator materials are Bi-Te, copper and acrylate coatings [33], respectively, and all are R2R manufacturable. Several m-i-s junctions are stacked in a single strip electrically connected in series or parallel, and then several single stacked strips are electrically in-plane connected in series or parallel. Connecting stacked layers in parallel is electrically equivalent to making a thicker TE layer, however stacking TE layers with a polymer interlayer in this way avoids the need to deposit a thick TE film, and a thinner TE film can show a better TE performance [34]. Secondly, inserting acrylate polymer layers in a stacked composite structure should improve the mechanical resilience of the device compared with a monolithic thick layer. The stacked arrangement also allows full flexibility of combining in-series and in-parallel connection of TE strips, thus allowing the preferred voltage and current characteristics of the device to be tailored for the application.

Therefore, in this study, I explore the feasibility of stacking TE materials in the cross-plane direction for IP-TEGs. All experimental designs are highly compatible with a real low-cost high throughput R2R process, all under the same vacuum condition, that I seek to emulate.

7.2 A novel stacking design

A stacked TEG was fabricated by depositing materials in sequence onto a polymer substrate, as shown in Figure 6.1. Specifically, Bi-Te, Cu, and acrylate coatings were patterned using polymer shadow masks (which could closely attach to the polymer substrate, thus avoiding shadowing issues, i.e. an unclear pattern, as can occur with a typical solid stainless-steel mask). ~125-µm PET sheets were designed (AutoCAD) and cut (TS 3040 40W Laser cutter). There were two types of stacking depending on the electrical connectivity of the stack: in-parallel and in-series (Figure 6.2). In the cross-plane direction of the PET substrate, a single strip was stacked up in an in-parallel or in-series structure of TEGs, and then these stacked single strips were connected by Cu contacts (under the same sputtering parameters as above) using polymer shadow masks, either in series or in parallel (see Figure 6.2) in the in-plane direction along the PET substrate.

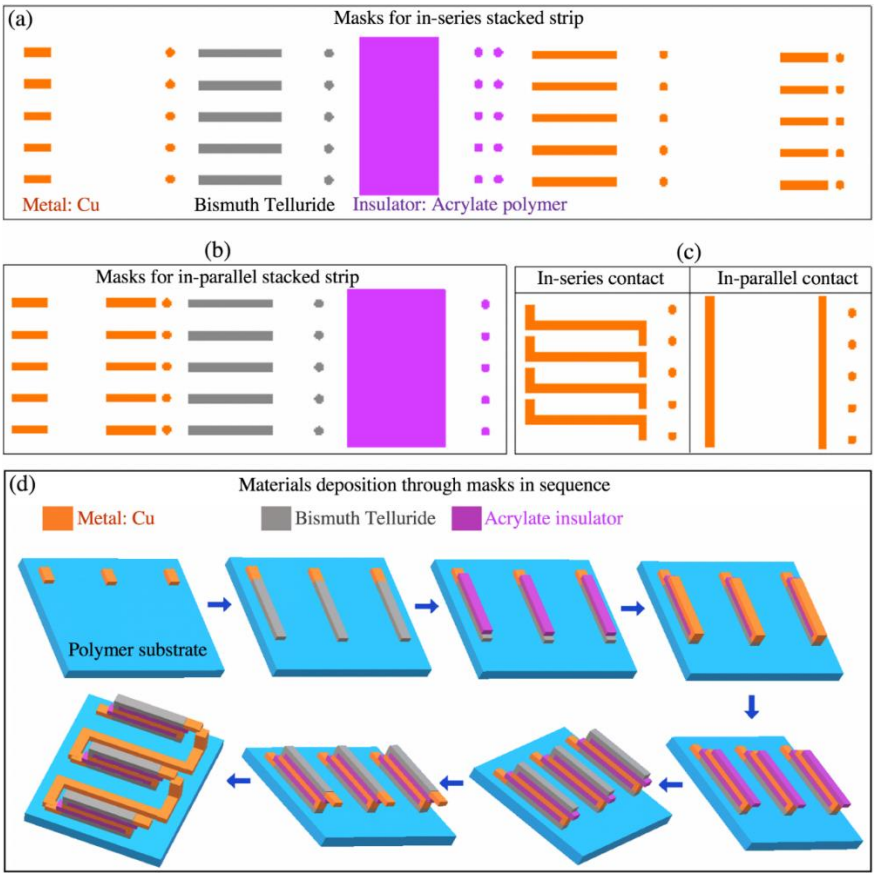


Figure 6.1. *Mask designs for making (a) in-series stacked strips, (b) in-parallel stacked strips, and (c) in-plane connects between individual stacks in series or parallel; (d) The fabrication process of in-series stacked strips, and then in-series connect these stacked strips in plane.*

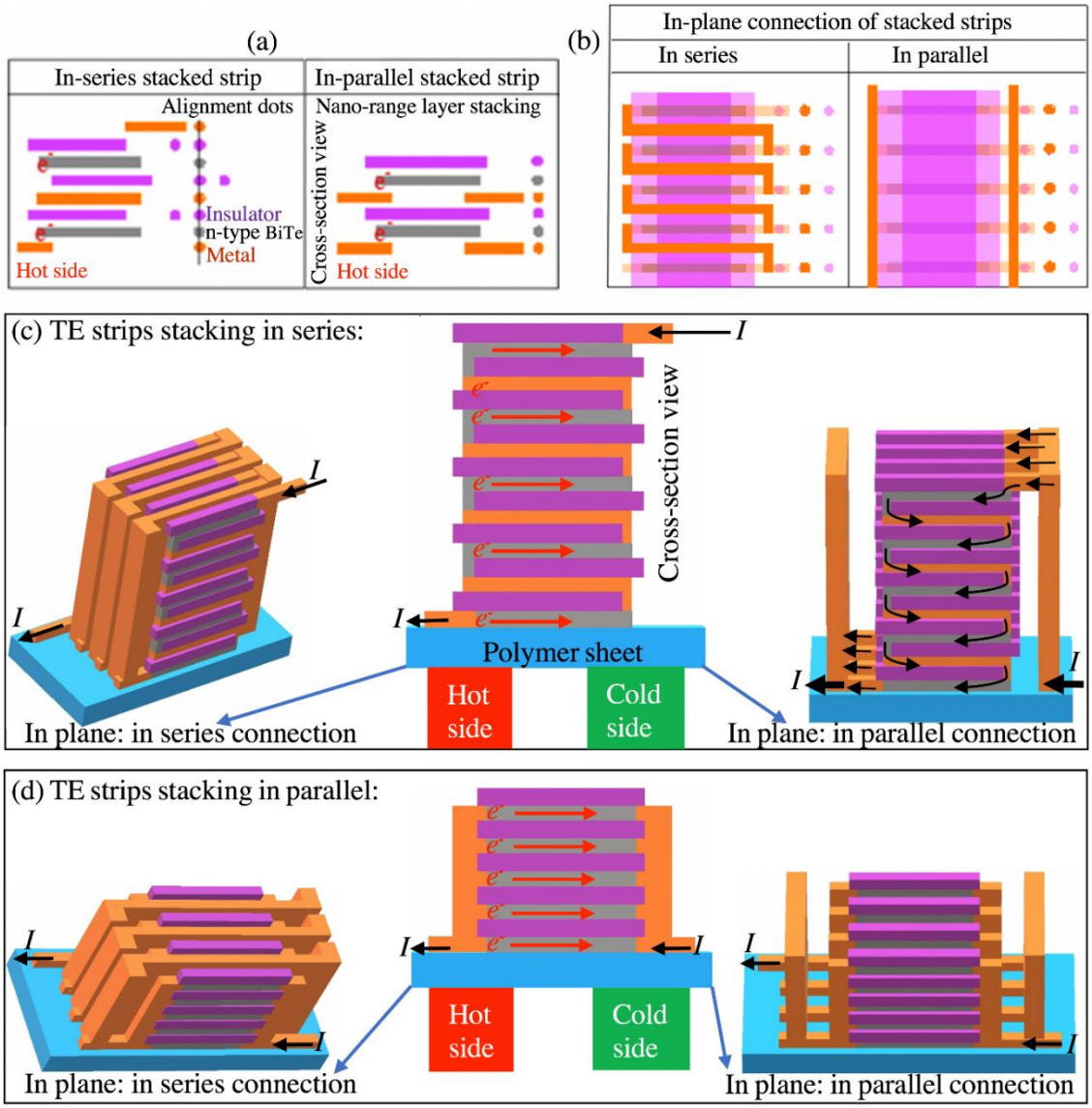


Figure 6.2. *(a) A cross-section view of an in-series and an in-parallel stacked strip (The orange colours indicate Cu strips, grey the Bi-Te sputtered TE layers, and purple the acrylate insulating layers. It demonstrates how the layers are stacked one by one from top to bottom ensuring that there is a contact region between Cu and Bi-Te layers. The acrylate layer insulates the region that it covers); (b) displays a top view of final devices*

with the lighter purple showing where offsetting of layers means there is less acrylate thickness; In-series/parallel connection in plane of (c) in-series stacked strips and (d) in-parallel stacked strips. The dimension of the Bi-Te strip was 2 mm × 20 mm. NB: the '7' shape of Bi-Te or Cu layers in the cross-section view of in-series stacked TEGs is not real. The thickness is approximately uniform for each layer thus there is a slope at the acrylate step.

7.3 COMSOL simulation

The TEG structure was designed in COMSOL Multiphysics software and simulated using the module of heat transfer in solids under a stationary study. The material property was from the materials library in COMSOL with a slight adjustment as shown in Table 6.I. A simulated temperature of 305 K considered the temperature of the human body and a slight heat loss from the body skin to TEGs. The ambient temperature was fixed at 293 K. Three parameters were used in the simulation of heat transfer: heat flux, surface-to-ambient radiation, and thermal contact. A minimum heat transfer coefficient (0.5 W m^{-2} K^{-1} under free convection in the air [35]) was used to simulate a low convection situation.

$$q = h \cdot (T_{sol.} - T_{amb.}) \tag{6.1}$$

where q is the convective heat flux, h is the heat transfer coefficient, $T_{sol.}$ is the temperature in the solid, and $T_{amb.}$ is the temperature in the ambient surrounding (293 K).

Table 6.I. *Material properties used in COMSOL simulation.*

Materials	Thermal conductivity [W/(m K)]	Surface emissivity	Thickness [nm]
PET	0.16 [36]	0.8 [37]	125000
Bi-Te	0.4 [38]	0.34 [39]	87
Cu	100 [40]	0.1 [41]	97
Acrylate	0.182 [42]	0.81 [43]	1195

In terms of the surface-to-ambient radiation, a variable surface emissivity was applied according to the values in Table 6.I:

$$-n \cdot q = \varepsilon \cdot \sigma \cdot (T_{amb.}^4 - T_{sol.}^4) \quad (6.2)$$

where ε is the surface emissivity, and σ is the Stefan-Boltzmann constant (a predefined physical constant: 5.67×10^{-8} W m^{-2} K^{-4}).

Thermal contact was a more complex simulation that studied the heat loss through the interface of two layers considering the thermal conductance of the contact surface, and gap and radiation. To make the simulation easier, only the surface roughness (~4 nm) and surface emissivity (0.1 – 0.8) were adjusted according to the value in this study, and others were maintained as default e.g. contact pressure (100 kPa), hardness (3 GPa), gas thermal conductivity (0.25 W m^{-1} K^{-1}), and gas particles diameter (0.37 nm).

7.4 Results and discussion

7.4.1 Surface topography and cross-section of stackings

The thicknesses of Bi-Te, Cu, and acrylate coatings were measured to be 87 (± 5), 97 (± 8), 1195 (± 155) nm, respectively. Figure 6.3 shows surface topographies of (a) the PET substrate, (b) Bi-Te, (c) Cu, and (d) acrylate on the PET substrate, as well as (e & f) stacked layers (the top layer is Cu). In Figure 6.3 e & f, the layer immediately beneath the top Cu layer is an acrylate insulating coating. The surface features on (e) and (f) are quite similar to that on (c), indicating that a Cu film can grow similarly on both PET and acrylate surfaces. Unlike the very fine crystals on the Cu film, bigger crystals are observed on Bi-Te films, causing a higher surface roughness. This has been confirmed in SEM images (Figure 6.4 A a & b) and TEM image (Figure 6.4 A d & B f), with consistent grain size for the Bi-Te of about 20 nm.

The acrylate coating displays a smooth surface as observed in Figure 6.3 d and Figure 6.4 A c. This smooth surface is a product of the deposition route: evaporation and condensation of a monomer liquid onto the substrate followed by a radiation curing. This process has previously been reported as a smoothing layer for gas barrier films [44], a reflector/interferometer in optical application [45], a dielectric layer in capacitors [46] and an insulator layer in organic transistors [47]. A thin, smooth, insulating layer in between the metal contact and the TE layer is important in a stacked structure, as any protrusion can cause a short circuit (locally thin areas can lead to carrier tunnelling) and it will affect the surface feature of the next metal or TE layer as well as their electrical properties. Most importantly, it is observed that as more layers are stacked, the surface roughness remains close to that of the immediately underlying smooth acrylate layer. A sufficiently thick acrylate coating presents a constant surface roughness due to its manufacturing process in which acrylate monomer is coated as a low viscosity liquid, filling in undulations in the layer beneath. As the surface roughness remains constant as the number of layers increases, it suggests that the roughness will not limit the number of layers that can be stacked to increase the device power output.

A cross-sectional image of the stacked structure is shown in Figure 6.4 A e, with a line profile across the cross-section (Figure 6.4 A f). A clear stacked structure is confirmed by C, Bi, and Cu profiles, representing acrylate, Bi-Te, and Cu, respectively. Te element is less detected and the ratio of Bi: Te is not correct in this line profile, because Te peak overlaps peaks of other elements (e.g. O).

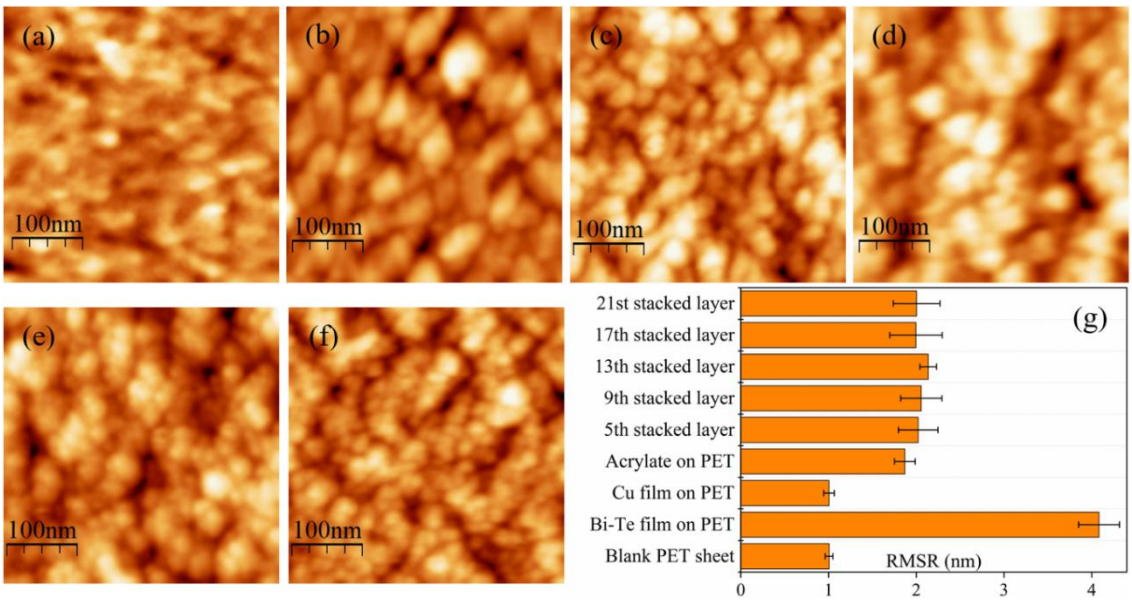


Figure 6.3. *(a-c) AFM images of (a) PET substrate, (b) Bi-Te, (c) Cu and (d) acrylate polymer coatings on PET sheets, (e) 9th stacked Cu film, (f) 13th stacked Cu film, (g) RMSR of PET, Bi-Te, Cu, acrylate coatings and roughness changes in stacked layers (the 5th, 9th, 13th, 17^{th,} and 21st layers are Cu and the beneath layer is acrylate). RMSR values are measured over an area of 400 nm by 400 nm in four different locations on each sample.*

7.4.2 Phase identification

XRD results of Bi-Te and Cu are shown in Figure 6.4 B a & b, though only one peak of Bi-Te (0 1 5) and one peak of Cu (1 1 1) are identified because the film is so thin. XPS results (Figure 6.4 B c & d) confirm that the elements Bi, Te, and Cu are present. The phase of Bi-Te has already been analysed in Chapter 3. In this chapter, both XRD and XPS results confirm the phase of Cu.

In terms of stacking layers (Figure 6.5), XRD peaks (0 1 5) of Bi-Te and (1 1 1) of Cu can be seen to increase in intensity as more layers are included in the stack. In addition, a new peak of Bi-Te (1 0 10) appears and grows. This is because more signals from the Bi-Te film can be detected in XRD as more layers are stacked (i.e. a thicker layer).

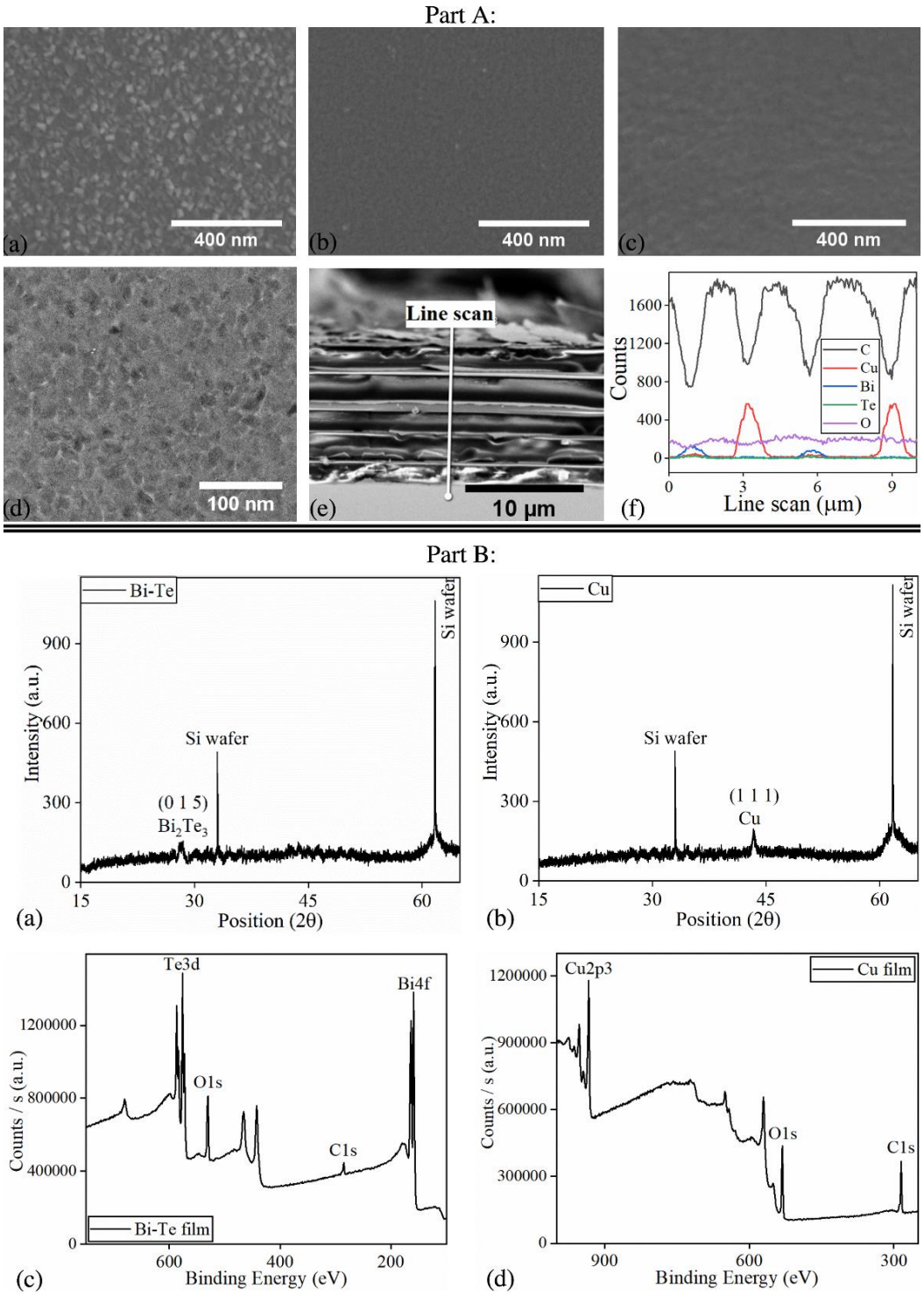


Figure 6.4. *Part A: (a-c) SEM surface image of Bi-Te, Cu, and acrylate coatings (3-nm Pt coating on acrylate polymer surface), (d) TEM image of Bi-Te film, (e-f) SEM cross-section view of stacked layers and elemental analysis in a line scan mode of EDX; Part B: (a-b) XRD patterns of Bi-Te and Cu films on Si wafers, (c-d) XPS analysis of Bi-Te and Cu films on polymer sheets.*

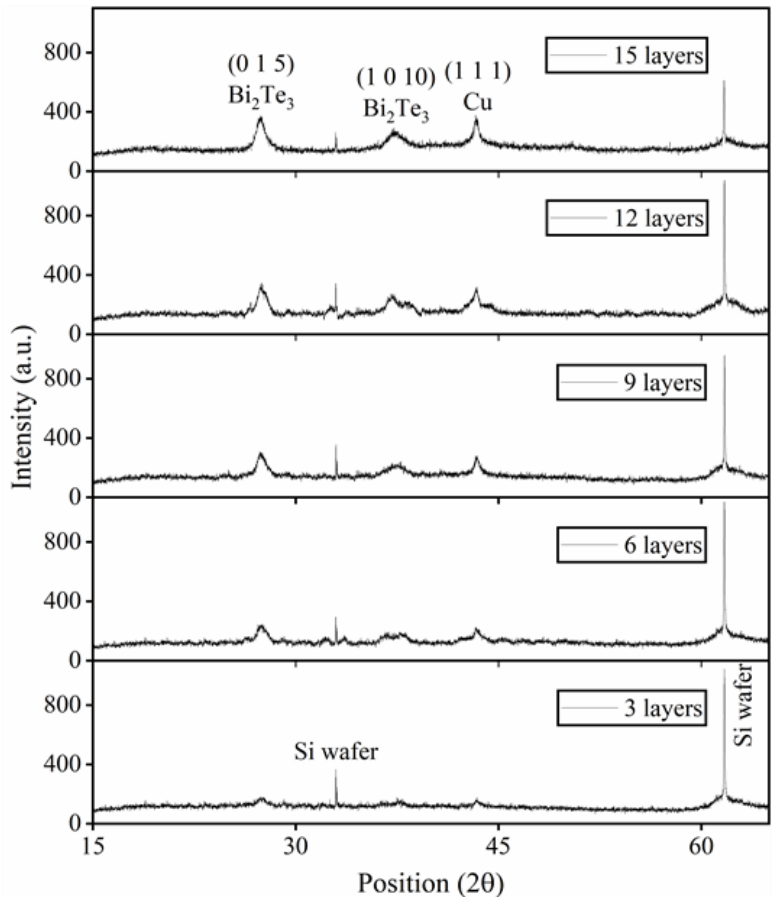


Figure 6.5. *XRD of in-parallel stacked coatings (15 layers: Si/m/n/i/m/n/i/m/n/i/m/n/i/m/n/i/m/n/i, where m is Cu film, n is n-type Bi-Te film, i is acrylate polymer coating).*

7.4.3 Thermoelectric performance

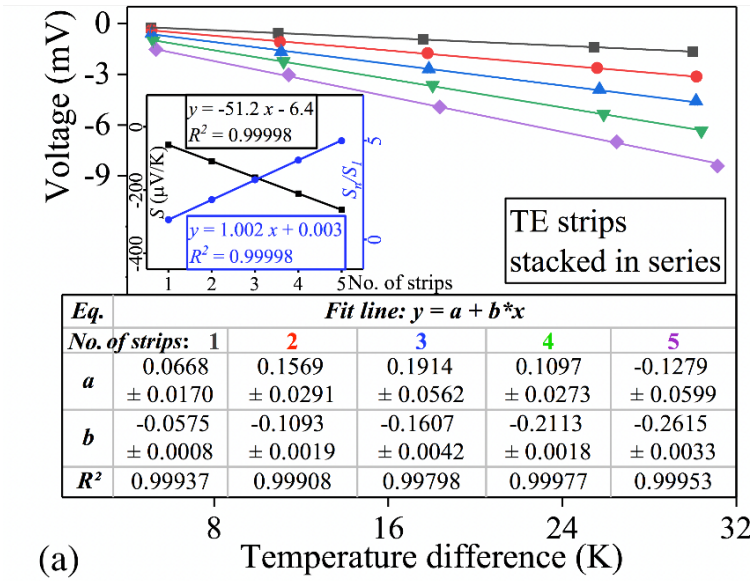
S of the Bi-Te film is found to be -57 (± 0.6) μV/K (n-type). *ρ* of Bi-Te and Cu films are 1.67 (± 0.21) and 0.032 (± 0.003) mΩ•cm, respectively. Thus, *PF* of Bi-Te film can be calculated as 2.0 (± 0.2) × 10^{-4} W/mK^2. The Seebeck behaviour of the Cu film (Ref. [55]: 1.6 μV/K, p-type) is unmeasurable in the Oxford Seebeck setup. Although there is a Seebeck effect for the Cu film, the fabricated TEG would contain both n-type (Bi-Te) and p-type (Cu), leading to an improvement on Seebeck performance.

7.4.3.1 Seebeck behaviour of stacked TEGs

The connection of TE strips in series and parallel should theoretically give rise to a voltage-dominant and current-dominant output, respectively. Figure 6.6 (a) and (b) plots the open-circuit voltage and short-circuit current as ΔT increases, corresponding to an in-series stacked structure and an in-parallel stacked structure, respectively. The slope of the fit line is defined as the Seebeck coefficient, S (see numbers '*b*' in table inset in Figure 6.6 a) to describe the induced voltage across a ΔT. Similarly, S' (see '*b*' in Figure 6.6 b table) can describe an induced TE current in response to ΔT across the two ends of TE strips stacked in parallel. Ideally, S or (S') should present a linear relationship with the number of strips. This is further analysed as shown in figures inset in Figure 6.6 (a) and (b). A plot of S_n (or S'_n) *vs* the number of strips shows an almost perfect linear relationship (R^2 approaches 1). For the S' values this plot passes through zero as expected, although for the case of S for the in series connected devices there is a small systematic error of 6.4 μV/K. Removing this systematic offset for the case of S, and then plotting the corrected S_n/S_1 (and S'_n/S'_1) shows in each case the expected linear trend with a slope very close to 1, as would be expected for the ideal device.

I considered the possible effect of a drop in temperature on the hot (non-ambient) side of the device due to the thickness increased with the number of stacked layers. Temperature measurement on a sample surface at the hot side of the device is shown in Figure 6.6 (c). As seen in an inset figure/table in Figure 6.6 (c), a total of 18 coating layers, which corresponds to 5-TE strips stacked in series, shows a slow rate of increasing temperature at an initial stage (i.e. the slopes of the fit line for 0 layer, and 18 layers (including 9 thermally insulating acrylic layers), are 0.263 °C/s and 0.249 °C/s, respectively). A lower equilibrium temperature is also observed (the equilibrium temperature for 0 layer and 18 layers are 35.31 ± 0.02°C and 34.81 ± 0.03°C, respectively). As the current and voltage

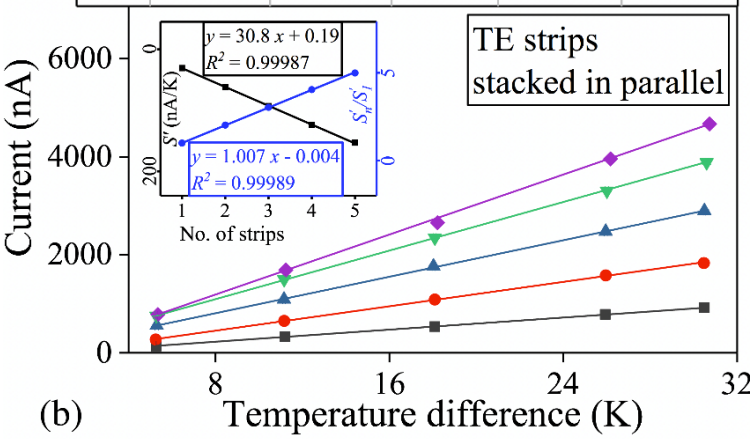
measurements are taken once the sample temperature has equilibrated, the effect of this temperature difference can be estimated. As an example, for the in-series case, using S = 57 μV/K this suggests that the 1st Bi-Te strip (see Figure 7.7 A a) would generate a potential difference of 873 μV, given a hot-side temperature of 35.31°C, i.e. ΔT = 15.31 K. The 5th Bi-Te strip (see Figure 7.7 A a), which has ΔT = 14.81 K due to the thermal insulation effect of the stack would generate 844 μV, i.e. less than 3% difference over 5 layers.



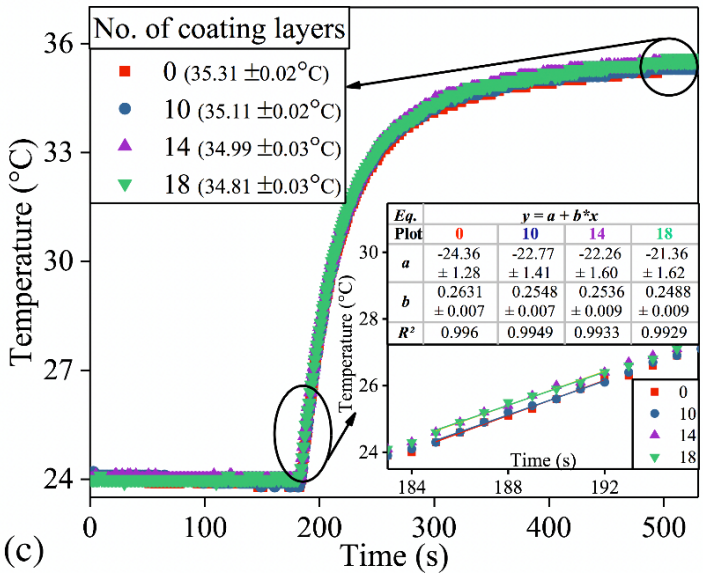
Eq.	*Fit line: y = a + b*x*				
No. of strips: 1	2	3	4	5	
a	0.0668 ± 0.0170	0.1569 ± 0.0291	0.1914 ± 0.0562	0.1097 ± 0.0273	-0.1279 ± 0.0599
b	-0.0575 ± 0.0008	-0.1093 ± 0.0019	-0.1607 ± 0.0042	-0.2113 ± 0.0018	-0.2615 ± 0.0033
R^2	0.99937	0.99908	0.99798	0.99977	0.99953

(a)

Eq.	*Fit line: y = a + b*x*				
No. of strips: 1	2	3	4	5	
a	-19.2106 ± 4.305	-44.9426 ± 14.66	64.4070 ± 6.376	104.7031 ± 10.46	-33.7944 ± 14.18
b	30.8094 ± 0.2711	62.1979 ± 0.6968	93.0188 ± 0.386	123.861 ± 0.9408	152.9567 ± 0.728
R^2	0.99977	0.99962	0.99995	0.99983	0.99993



(b)



(c)

Figure 6.6. *(a) A plot of open-circuit voltage vs ΔT as an increasing number of stacked strips in series (the slop of fit line is Seebeck coefficient; inset figure is plots of S (& the corrected S_n/S_1) vs No. of TE strips); (b) Plot of short-circuit current vs ΔT as the increasing number of stacked strips in parallel (the slop of fit line is defined S' in this study which describes the short-circuit current increased with an increased ΔT. Similarly, the corrected S_n'/S_1 is plotted/presented inset); (c) Plot of temperature on the sample surface vs time for samples with different stacked layers by applying a hot temperature at the bottom side of the sample (numbers in bracket describe the highest temperature under an equilibrium condition during Seebeck measurement; inset: a zoomed-in figure at the initial stage of increasing temperature, the slope of a fit line describes an increasing rate of temperature. NB: the offset in temperature with the number of stacks reflects variation in the exact time at which the heater is switched on).*

In addition to the simple thermocouple measurement, the possibility of a temperature gradient in a stacked TEG from bottom to top layers is considered using COMSOL simulation. The single surface emissivity parameter, ε, is used in the simulation and the various materials in the stack have different values of ε. The PET and acrylate layers are significantly the thickest and the top layer is acrylate, so these materials should have a predominant effect on the surface emissivity. Thus, the result of $\varepsilon = 0.8$ is likely closest to the real situation. However, to check the effect of the values chosen, simulations using three different values, $\varepsilon = 0.1$, 0.3, and 0.8, were trialled.

Figure 6.7 A and B simulate a temperature profile of the structure at the 'hot side' of a stacked TEG (with an *a*-*b* dimension of 2 mm × 2 mm) under a heater of 305 K applied at the bottom side of PET, and the heat transfer along a TE strip with a temperature of 305 K applied at the side face, respectively. In this case, I did not fix the temperature on the cold side (which simulates a real wearable condition). Simulated results of heat

transfer in a stacked structure are demonstrated in Figure 6.7 A. A decrease in temperature of successive TE layers is observed as more layers are stacked, and the decreasing trend is greater (i.e. a bigger slope of linear fit in Figure 6.7 A b) with a bigger ε since more heat radiates to the ambient. To illustrate this difference, Figure 6.7 A c shows the temperature difference between the 1st TE layer and the 5th TE layer at the hot side of the device for different ε. The maximum difference is 0.11 K, 0.022 K/strip ($\varepsilon = 0.8$), smaller than the measured result of 0.106 K/strip (section 3.3.1), using the idealized parameters in the COMSOL simulation e.g. free convection of air. As the loss in temperature of the upper layers is smaller in the simulation, the predicted change in voltage and current output would be smaller, suggesting that the experimental results are not underestimating the scale of the effect.

Therefore, to reduce the heat loss within the stack, decreasing the main contributor to the device thickness (i.e. the acrylate insulating layer) would be favourable provided that its reliable electrical insulating property is maintained. As there is a significant temperature drop across the substrate, it is also favourable to decrease this thickness and to improve its thermal conduction properties on the hot side.

The reduction in ΔT on the upper layer could be an issue if many layers are stacked (e.g. imagine a stack of 1000 layers). However, it is notable that this is only the case when the heat is applied to the polymer substrate (i.e. the bottom of the device substrate), which is common in laboratory measurements. This, however, may not be the case in architectures deployed in wearable applications. If it can be compared with the coil-up coin-shape [26] as an example, the heat source is designed on the cross-sectional side of IP-TEGs, thus all TE materials would obtain the same ΔT.

The COMSOL simulation also allows us to consider the effect of heat transfer along the length of a TE strip. The temperature difference that is required for power generation can

only be maintained if the heat from the hot side does not warm the material on the cold side. Figure 6.7 B b shows a simulated profile of temperature along the strip length at the top surface of the device. It is clear that if the length of the strip is greater than ~6 mm, the temperature of the cold side is not affected by heat from the hot side, as the cold side surface reaches the ambient temperature (293 K). This 6-mm length seems to be a limitation for the application of the IP-TEGs to prevent a loss of ΔT, i.e. less TE performance. In this study, the length of the TE strip is 20 mm, hence, no matter how many layers are stacked, the temperature at the cold side will remain 293 K. This is consistent with the experimental measurement of temperature at the cold side of TEGs i.e. the temperature was found to be the same as ambient.

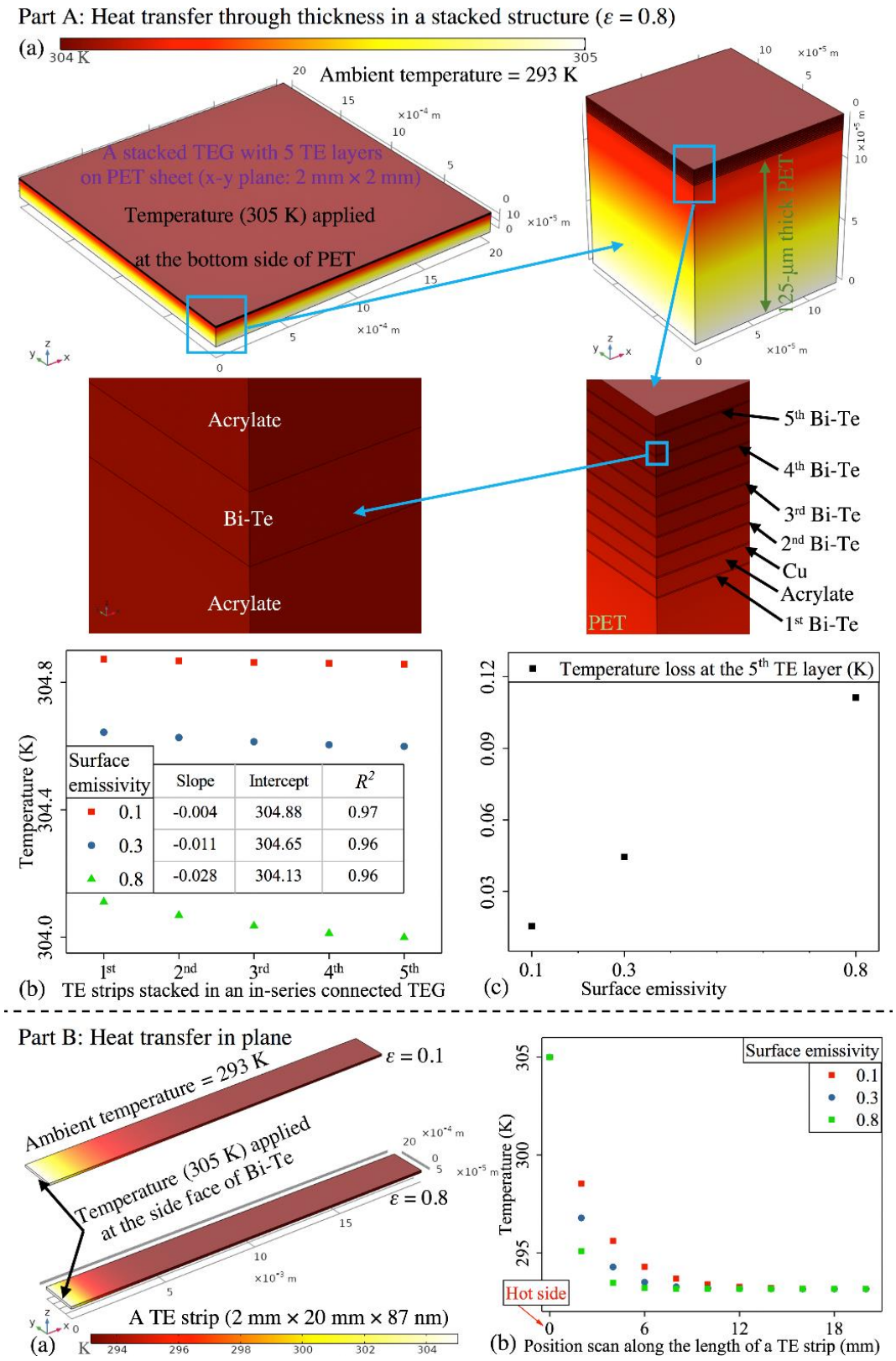


Figure 6.7. *COMSOL simulation of heat transfer in TEGs under an ambient condition of 293 K and a heat of 305 K to simulate a real wearable application (ΔT = ~11.4 K, as same as the experimental study). Part A: (a) An in-series stacked structure with five TE*

strips and Cu and acrylate coatings grown on PET (2 mm × 2 mm ×125 μm) with a heat applied at the bottom face of the PET (ε = 0.8), with increasingly zoomed images following the arrows. The cross-section side of the top region where the coatings are look darker than the top side in the first two images: this is because the frame of each layer is indicated with a black line which is not resolved in large-area images. It is not an indication of a sudden drop in temperature in the top section of the sample, as is clearly demonstrated in the close-up images. (b) The simulated temperature at the side face of each TE layer in the stacked TEG in (a) (at the hot side of the strip), with the surface emissivity of 0.1, 0.3, and 0.8 (insert table is the data of linear fits. The temperature of 1st TE layer could represent the temperature on the top of PET sheet. The bottom side of PET is 305 K), (c) Heat loss at the 5th TE layer compared to that at the 1st TE layer from results in (b); Part B: (a) A TE strip under a heater applied at the side face, (b) Temperature scan at the upper surface from the hot side along the length of a TE strip in (a).

7.4.3.2 Thermoelectric strips connected in plane *vs* in stacking

Fabricating TE strips in this novel stacked formation is compared here with making connections between strips in the plane of the substrate, as shown in Figure 6.8. Compared with the in-parallel TEG, the in-series configuration is found to have a much higher power output. The measured maximum power output (P_{max}) reaches -0.26 nW (the stacked in-series case) and -0.27 nW (the in-plane in-series case) under a rheostat of ~10 kΩ. As shown in [48] the P_{max} is reached when a load resistance is equal to the internal resistance of a TEG.

In-series and in-parallel structures can provide a maximum voltage and a maximum current, respectively, and according to the requirements of a particular application, a power source that is either current dominant or voltage dominant will be preferred. A

linear relationship between voltage or current with the number of strips was predicted in [49] from MATLAB simulation. Performances of in-plane and stacked structures can be directly compared in plots of Figure 6.8 B. In this case, the voltage for in-series connected devices, and the current for in-parallel connected devices are plotted as a function of the number of strips at each of i) the maximum rheostat setting in this experiment, 50 kΩ, where there is little change with load resistance, and ii) at the rheostat setting (load resistance) that gives the P_{max} of the device, the point at which the device, ideally, would be used. Note that the load resistance of the P_{max} changes with the number of strips. The load resistance of the P_{max} is determined by a fit of the power data to equation (6.3) [50]:

$$P = I^2 \cdot R_L = \left(\frac{S_{TEG} \cdot \Delta T}{R_{TEG} + R_L}\right)^2 \cdot R_L \qquad (6.3)$$

In each case, the plots of *V*, *I,* or *P* increase linearly with the number of strips, and there is close agreement between the performance of the in-plane and stacked structures. A slight decrease in the slope of linear fit for the stacked case demonstrates a loss in TE performance as more layers are stacked, which could be attributed to the temperature loss at the top layer as discussed above.

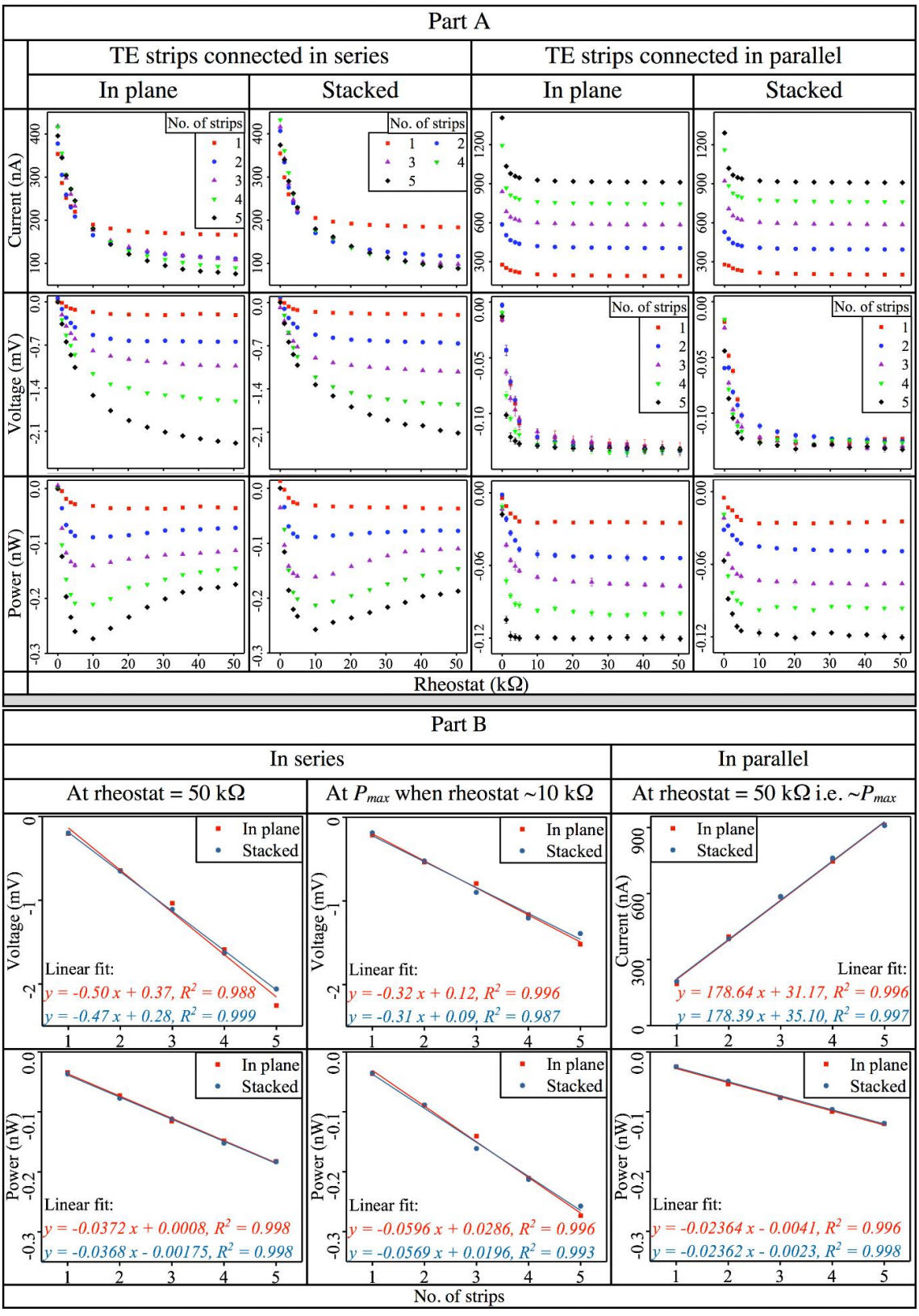


Figure 6.8. *Part A: comparisons of the measured current, voltage, and calculated power output between TEGs structured in plane and in stacking. The data for the stacked TEG just contain one stack. Both in-series stacked TEG and in-parallel stacked TEG with*

various TE strips (1 – 5) are presented; Part B: plots of V, I, and P as the number of strips in the device, comparing in the in-plane devices with the stacked devices.

Most notably, Figure 6.8 reveals that whether TE strips are connected in series or parallel, the stacked architecture can provide a very similar TE output to the in-plane TEG. This electrical response is accompanied by a greater *FF* for the architecture in the stacked case. For example, in the case of TE strip (2 mm × 20 mm), an in-plane TEG with 5 strips connected in series occupies an *a-b* dimension of (5 × 2 + 5 × 2 + 10 × 1) mm × (20 + 2) mm = 660 mm^2 (corresponding to the width of 5 metal strips + 5 TE strips + 10 inter-strip spacings; the length of metal or TE strip + the margin at two ends), while a stacked TEG (which can generate same power to an in-plane TEG, see Figure 7.8) only requires an *a-b* dimension of 2 mm × 25 mm = 50 mm^2 and *c-axis* of ~11.8 μm (~435-nm thick Bi-Te of 5 layers, ~582-nm thick Cu of 6 layers and ~10.8-μm thick acrylate of 9 layers, for a 5 TE-strip stacked TEG).

It is clear that the stacked architecture improves *FF* immensely. Extrapolating these data to more layers, if it is assumed that the linearity (seen in Figure 6.8) was continued I would envisage that, for example, a 1000 TE-strip stacked TEG could generate a power of approximately (0.26/5) × 1000 = 52 nW while only occupying an *a-b* dimension of 50 mm^2 with about (11.8/5) × 1000 = 2360 μm thickness in stacking. To make this even thinner, decreasing thickness of insulator layers to nano range is of interest for further studies. A challenge will be to make an acrylate layer as thin (and smooth) as possible (which is dependent on the manufacturing process) while avoiding any charge leakage (short/tunnelling). Various thinner electrically insulating but thermally conductive materials could be investigated although any such material would also need to avoid doping problems with the TE material, as the acrylate trialled here appears to.

The negligible change in surface roughness (see Figure 6.3 g) with more stacked layers suggests that stacking thousands of layers is feasible to achieve significant power output provided (that side contacts can be printed that can accommodate this thickness). Most importantly, afterward, these stacked TEGs (i.e. a single stacked strip in the plane view) can additionally be connected in plane, and thus further increasing TE output linearly.

7.4.3.3 In-plane connection of stacked TEGs

Both in-series stacked strips (Figure 6.9 A) and in-parallel stacked strips (Figure 6.9 B) involving 2 or 5 TE strips were connected in plane (in series and parallel). A P_{max} of ~1.4 nW (with V of ~5.5 mV at the maximum power point) is obtained when 4 stacks of strips are connected in series in the plane of the substrate, with each stacked strip containing 5 TE strips connected in series, and I of ~4.2 μA is obtained with 4 stacks of strips connected in parallel in the plane with each stacked strip containing 5 TE strips connected in parallel at the P_{max} of ~0.7 nW. Hence, an in-series mode for both in-stacking and in-plane connections benefits voltage (and power) output, while an in-parallel mode for both in-stacking and in-plane connections is favourable to current output.

In this study, the maximum power density is 0.003 nW mm^{-2}, corresponding to the prototype of P_{max} ~1.4 nW. This device only stacks five TE strips. It is noted that the power density will linearly increase with the number of stacks and these stacked layers could be in a range of nm thick, envisaging a stack with thousands of layers thus a significant power density.

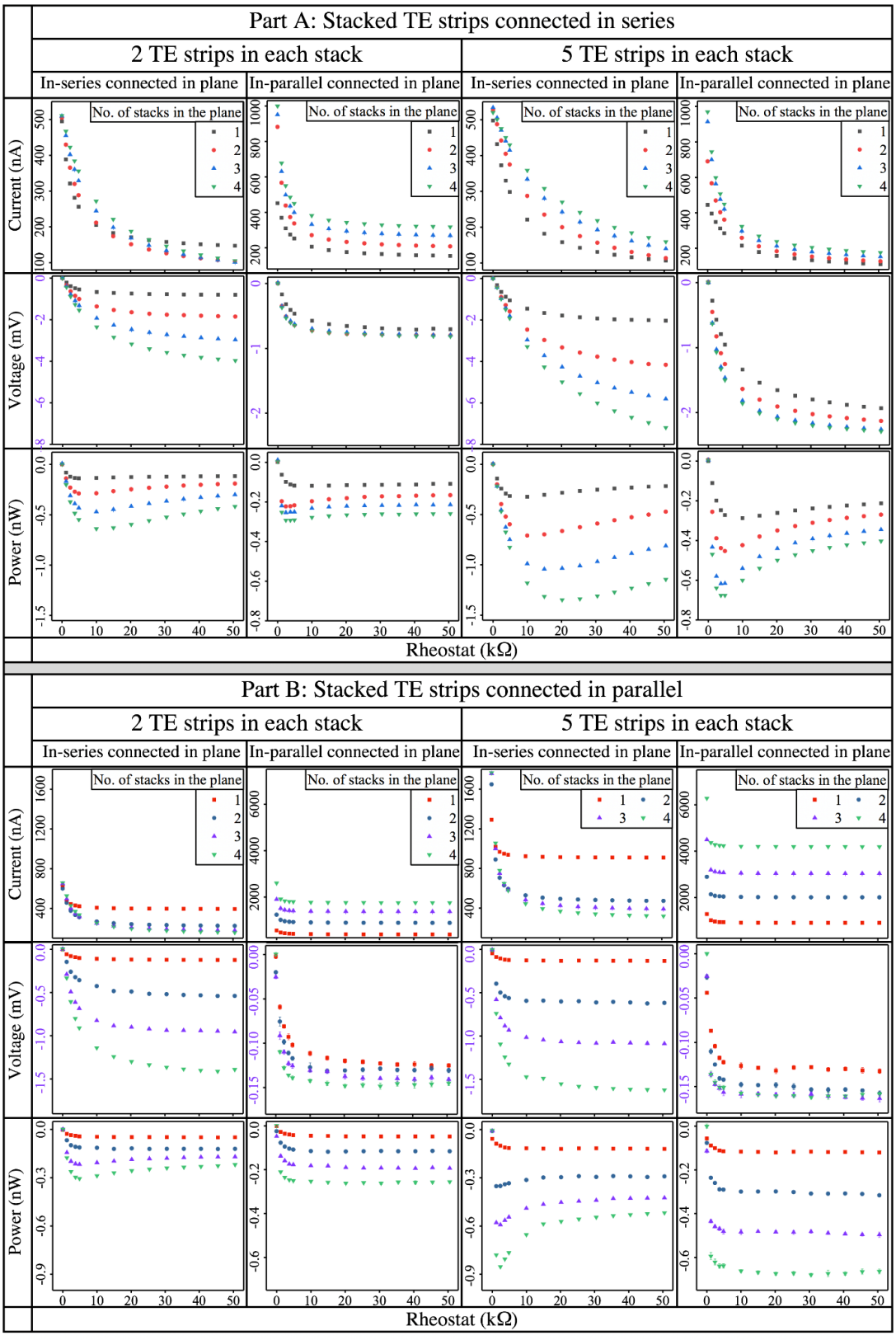
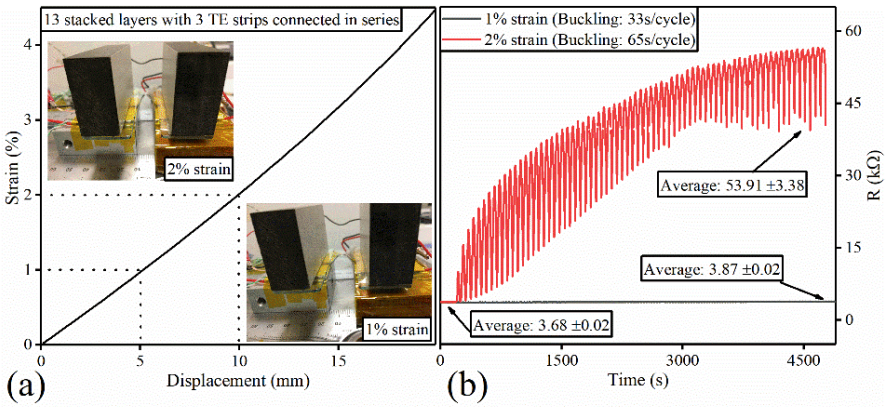


Figure 6.9. *Part A: in-plane connection (in series & in parallel) of in-series stacked (2 & 5) TE strips; Part B: in-plane connection (in series & in parallel) of in-parallel stacked (2 & 5) TE strips.*

7.4.3.4 Mechanical test

With a vision towards flexible/wearable electronics, the effect of mechanical deformation on these devices, both during manufacture and in the application, should be considered. A 1% strain is of interest in both situations, corresponding to a typical 85 N tensioning load between rollers in the Oxford R2R web coater, and stretchability requirements in use as reported in [51]. Cyclical bending fatigue of a stacked strip, such as might be encountered in use as a flexible device, is explored. A relation of strain and displacement during buckling is calculated as shown in Figure 6.10 a, with respect to a ~21-mm long specimen. There is found to be a negligible change (~5%) in the internal resistance of a stacked strip cycled under a 1% strain over 150 cycles (a 5000 s test), see Figure 6.10 b, while the resistance significantly increases under a 2% strain cycle and there is an upward trend in resistance over the 75 cycles of the test. The 1% strain cycling is further analysed with regards to TE performance, as shown in Figure 6.10 c. The change in power output over the first 100 cycles is negligible, and afterward, a slight decrease (~30%) is observed. By comparison, the TE coating directly deposited on PET sheets under the same condition of 1% strain buckling, the internal resistance was measured to increase by ~15%, and the TE performance is completely destroyed (a decrease of ~99%) after 12 cycles (see Figure 6.11). Hence, using the stacked architecture, both TE and metal strips are protected between the acrylate polymer layers, and thus maintaining TE performance.


13 stacked layers with 3 TE strips connected in series
2% strain
1% strain
Strain (%)
Displacement (mm)
(a)
1% strain (Buckling: 33s/cycle)
2% strain (Buckling: 65s/cycle)
Average: 53.91 ±3.38
Average: 3.87 ±0.02
Average: 3.68 ±0.02
R (kΩ)
Time (s)
(b)

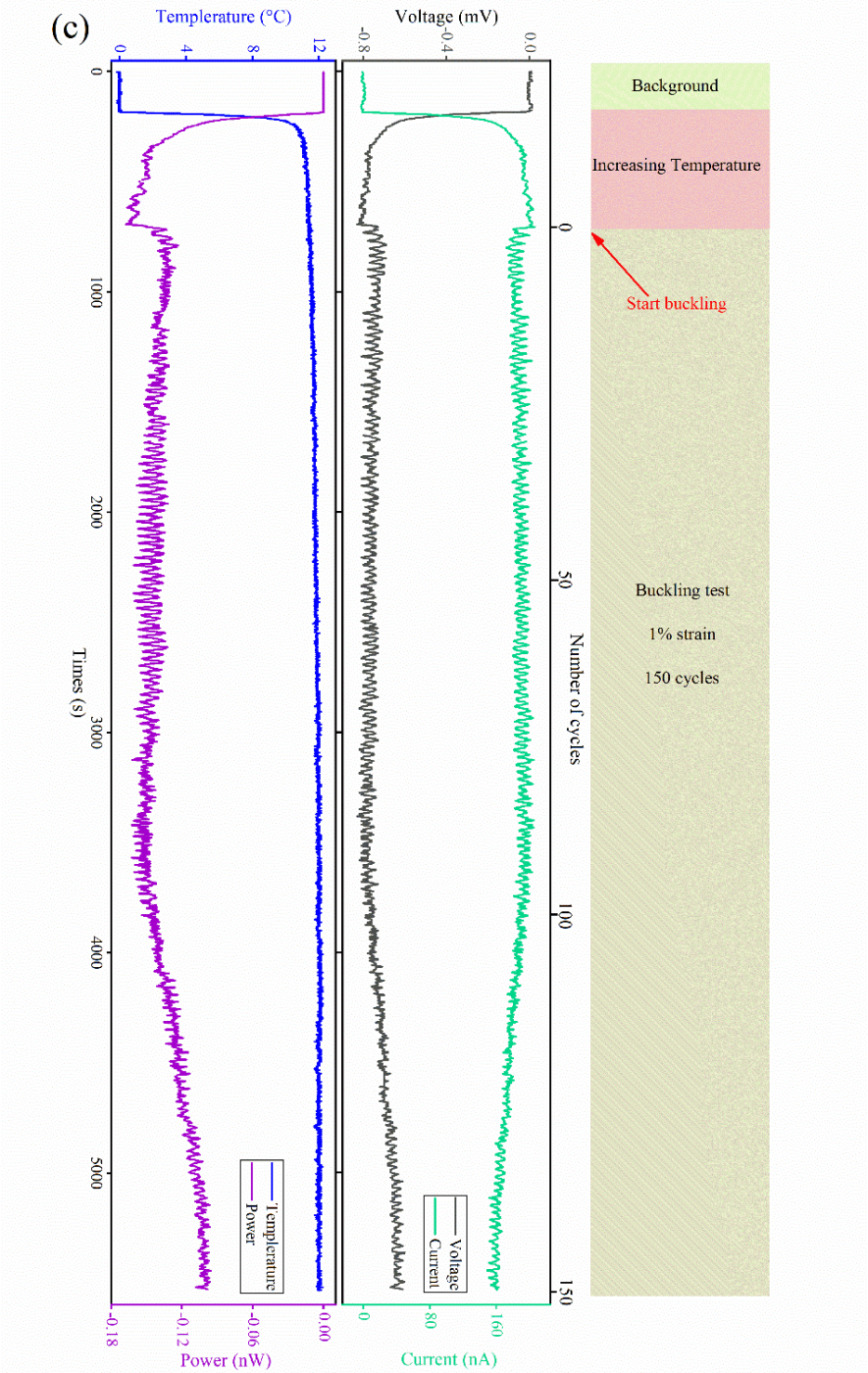

(c)
Templerature (°C)
Voltage (mV)
Background
Increasing Temperature
Start buckling
Buckling test
1% strain
150 cycles
Times (s)
Number of cycles
Templerature
Power
Voltage
Current
Power (nW)
Current (nA)

Figure 6.10. *Cyclical strain testing under buckling of a series-connected stack of 3 TE strips. (a) The calculated relation between the strain and displacement during buckling tests; (b) Change in the internal resistance of the stacked TEG during buckling test; (c) Current, voltage, and power output of a stacked strip (with 3 TE strips) during buckling test (Seebeck setup uses a load resistor of ~4 kΩ which is close to the internal resistance of the stacked TEG to obtain a maximum power output. Temperature increases from 180 s and gets equilibrium at 690 s).*

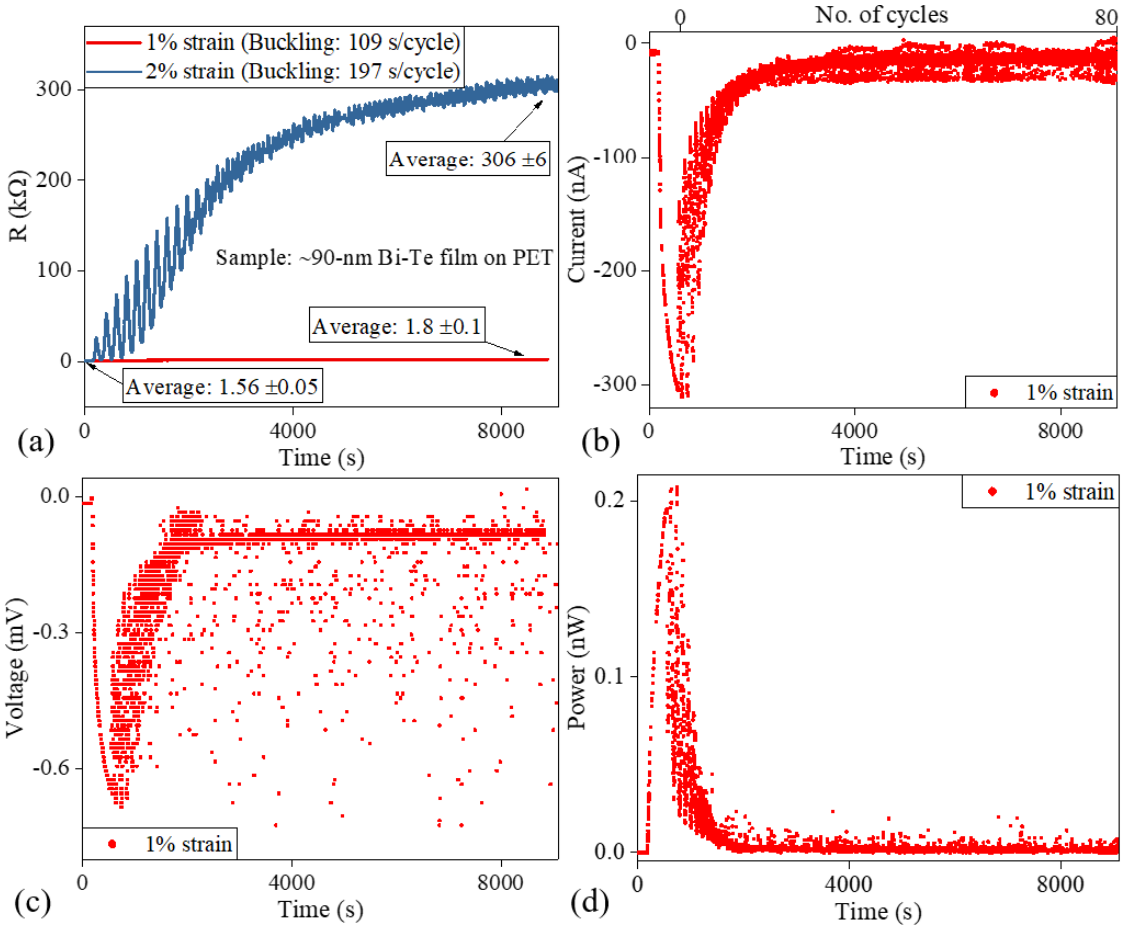


Figure 6.11. *Cyclical strain testing under buckling of a Bi-Te film directly grown on a PET sheet, as a contrast to the stacked structure in Figure 6.10. NB: the cyclical speed (s/cycle) is much different because the displacement (i.e. the buckling strain) is dependent on the sample thickness as the calculation method used in this study.*

7.5 Summary

A process based on low-cost high throughput roll-to-roll manufacture was used to explore the feasibility of forming a stacked TEG in the cross-plane direction, which has the potential to locally provide sufficient power to wearable electronics e.g. personal sensors and wireless earphones. Bi-Te and Cu films, each less than 100-nm thick, were fabricated as thermoelectric and contact materials, and ~1-μm thick acrylate coating behaved as an insulating layer in between Bi-Te and Cu layers. Conclusions are as follows:

(1) AFM, SEM, and TEM images confirmed the smooth surface of these coatings. Most importantly, surface roughness remained steady as more layers were stacked due to the nature of the acrylate layer deposition process. An SEM cross-sectional view of stacked layers presented a uniform stacking/alternating architecture.

(2) XRD, XPS, and HRTEM identified the phases of Bi-Te and Cu films, indicating that room-temperature sputtering could also produce films with significant crystallinity.

(3) A temperature gradient arose in stacked TEGs from bottom to top layers because a thick acrylate layer also behaved as a thermal insulator, thus the top thermoelectric layer would produce slightly less power than the bottom one due to a smaller temperature difference. A comparison of in-plane and stacked devices showed only a very small difference in output, as predicted from the observed temperature change over 5 layers. As more layers were stacked of course the effect would increase. This would not be a significant problem in an application that the architecture applies heat to the cross-section of the device.

(4) The stacked architecture only occupied a one-strip dimension in the *a*-*b* plane which significantly improved the spatial fill factor of the device.

(5) In-series connection in plane of in-series stacked strips could generate a maximum voltage (and power) output, while in-parallel connected in-parallel stacked strips in

plane could generate maximum current output. Combinations of the two could be used to design a power output suitable for applications of wearable devices required current or voltage power source.

(6) An acrylate polymer matrix could protect the Bi-Te and Cu films, which maintained the performance of stacked TEGs within a 100-cycle buckling fatigue test under 1% strain.

7.6 Reference

[1] B. W. Stuart, X. Tao, D. Gregory, and H. E. Assender, "Roll-to-Roll Patterning of Al/Cu/Ag Electrodes on Flexible Polyethylene by Oil Masking: A comparison of Thermal Evaporation and Magnetron Sputtering," *Applied Surface Science*, pp. 144294, 2019. https://doi.org/10.1016/j.apsusc.2019.144294.

[2] M. Powalla, S. Paetel, D. Hariskos, R. Wuerz, F. Kessler, P. Lechner, W. Wischmann, and T. M. Friedlmeier, "Advances in Cost-Efficient Thin-Film Photovoltaics Based on Cu(In,Ga)Se2," *Engineering*, vol. 3, no. 4, pp. 445-451, 2017. http://dx.doi.org/10.1016/J.ENG.2017.04.015.

[3] W. Qu, M. Plötner, and W. Fischer, "Microfabrication of thermoelectric generators on flexible foil substrates as a power source for autonomous microsystems," *Journal of Micromechanics and Microengineering*, vol. 11, no. 2, pp. 146-152, 2001. https://doi.org/10.1088/0960-1317/11/2/310.

[4] K. Tappura, "A numerical study on the design trade-offs of a thin-film thermoelectric generator for large-area applications," *Renewable Energy*, vol. 120, pp. 78-87, 2018. http://dx.doi.org/10.1016/j.renene.2017.12.063.

[5] N. Park, T. Park, J. Ahn, S. Kang, W. Lee, Y. Yoon, S. Yoon, and S. Lee, "Thermoelectric characterization and fabrication of nanostructured p-type Bi0.5Sb1.5Te3 and n-type Bi2Te3 thin film thermoelectric energy generator with an in-plane planar structure," *AIP Advances*, vol. 6, no. 6, pp. 65123-10, 2016. http://dx.doi.org/10.1063/1.4955000.

[6] T. Ming, W. Yang, X. Huang, Y. Wu, X. Li, and J. Liu, "Analytical and numerical investigation on a new compact thermoelectric generator," *Energy Conversion and Management*, vol. 132, pp. 261-271, 2017. http://dx.doi.org/10.1016/j.enconman.2016.11.043.

[7] T. Nguyen Huu, T. Nguyen Van, and O. Takahito, "Flexible thermoelectric power generator with Y-type structure using electrochemical deposition process," *Applied Energy*, vol. 210, pp. 467-476, 2018. http://dx.doi.org/10.1016/j.apenergy.2017.05.005.

[8] T. Sun, J. L. Peavey, M. David Shelby, S. Ferguson, and B. T. O'Connor, "Heat shrink formation of a corrugated thin film thermoelectric generator," *Energy Conversion and Management*, vol. 103, pp. 674-680, 2015. http://dx.doi.org/10.1016/j.enconman.2015.07.016.

[9] H. Yamamuro and M. Takashiri, "Power Generation in Slope-Type Thin-Film Thermoelectric Generators by the Simple Contact of a Heat Source," *Coatings*, vol. 9, no. 2, pp. 63, 2019. https://doi.org/10.3390/coatings9020063.

[10] J. Weber, K. Potje-Kamloth, F. Haase, P. Detemple, F. Völklein, and T. Doll, "Coin-size coiled-up polymer foil thermoelectric power generator for wearable electronics," *Sensors & Actuators: A. Physical*, vol. 132, no. 1, pp. 325-330, 2006. https://doi.org/10.1016/j.sna.2006.04.054.

[11] S. Teichert, A. Bochmann, T. Reimann, T. Schulz, C. Dreßler, and J. Töpfer, "An oxide-based thermoelectric generator: Transversal thermoelectric strip-device," *AIP Advances*, vol. 5, no. 7, pp. 77105-6, 2015. http://dx.doi.org/10.1063/1.4926384.

[12] P. M. Mayer and R. J. Ram, "Optimization of Heat Sink-Limited Thermoelectric Generators," *Nanoscale and Microscale Thermophysical Engineering*, vol. 10, no. 2, pp. 143-155, 2006. https://doi.org/10.1080/10893950600643063.

[13] J. P. Carmo, L. M. Goncalves, and J. H. Correia, "Thermoelectric Microconverter for Energy Harvesting Systems," *IEEE Transactions on Industrial Electronics*, vol. 57, no. 3, pp. 861-867, 2010. https://doi.org/10.1109/TIE.2009.2034686.

[14] K. Suemori, S. Hoshino, and T. Kamata, "Flexible and lightweight thermoelectric generators composed of carbon nanotube–polystyrene composites printed on film substrate," *Applied Physics Letters*, vol. 103, no. 15, pp. 153902, 2013. https://doi.org/10.1063/1.4824648.

[15] C. S. Kim, G. S. Lee, H. Choi, Y. J. Kim, H. M. Yang, S. H. Lim, S. Lee, and B. J. Cho, "Structural design of a flexible thermoelectric power generator for wearable applications," *Applied Energy*, vol. 214, pp. 131-138, 2018. http://dx.doi.org/10.1016/j.apenergy.2018.01.074.

[16] M. Strasser, R. Aigner, C. Lauterbach, T. F. Sturm, M. Franosch, and G. Wachutka, "Micromachined CMOS thermoelectric generators as on-chip power supply," *Sensors & Actuators: A. Physical*, vol. 114, no. 2, pp. 362-370, 2004. http://dx.doi.org/10.1016/j.sna.2003.11.039.

[17] Jin Xie, Chengkuo Lee, and Hanhua Feng, "Design, Fabrication, and Characterization of CMOS MEMS-Based Thermoelectric Power Generators," *Journal of Microelectromechanical Systems*, vol. 19, no. 2, pp. 317-324, 2010. https://doi.org/10.1109/JMEMS.2010.2041035.

[18] Z. Wang, V. Leonov, P. Fiorini, and C. Van Hoof, "Realization of a wearable miniaturized thermoelectric generator for human body applications," *Sensors & Actuators: A. Physical*, vol. 156, no. 1, pp. 95-102, 2009. http://dx.doi.org/10.1016/j.sna.2009.02.028.

[19] J. Su, V. Leonov, M. Goedbloed, Y. van Andel, M. C. de Nooijer, R. Elfrink, Z. Wang, and R. J. M. Vullers, "A batch process micromachined thermoelectric energy harvester: fabrication and characterization," *Journal of Micromechanics and Microengineering*, vol. 20, no. 10, pp. 104005, 2010. https://doi.org/10.1088/0960-1317/20/10/104005.

[20] M. Kim and T. Oh, "Thermoelectric Thin Film Device of Cross-Plane Configuration Processed by Electrodeposition and Flip-Chip Bonding," *Materials Transactions*, vol. 53, no. 12, pp. 2160-2165, 2012. https://doi.org/10.2320/matertrans.M2012265.

[21] T. Colpitts, R. Venkatasubramanian, E. Siivola, and B. O'Quinn, "Thin-film thermoelectric devices with high room-temperature figures of merit," *Nature*, vol. 413, no. 6856, pp. 597-602, 2001. http://dx.doi.org/10.1038/35098012.

[22] T. C. Harman, P. J. Taylor, M. P. Walsh, and B. E. LaForge, "Quantum Dot Superlattice Thermoelectric Materials and Devices," *Science*, vol. 297, no. 5590, pp. 2229-2232, 2002. https://doi.org/10.1126/science.1072886.

[23] X. Sun, Y. M. Lin, S. B. Cronin, M. S. Dresselhaus, J. Y. Ying, and G. Chen, "Theoretical modeling of thermoelectricity in Bi nanowires," *Eighteenth International Conference on Thermoelectrics. Proceedings, ICT'99 (Cat. No.99TH8407)*, pp. 394-397, 1999. https://doi.org/10.1109/ICT.1999.843413.

[24] L. Zhao, B. Zhang, J. Li, M. Zhou, W. Liu, and J. Liu, "Thermoelectric and mechanical properties of nano-SiC-dispersed Bi2Te3 fabricated by mechanical alloying and spark plasma sintering," *Journal of Alloys and Compounds*, vol. 455, no. 1-2, pp. 259-264, 2008. https://doi.org/10.1016/j.jallcom.2007.01.015.

[25] X. Tao, K. Wan, J. Deru, E. Bilotti, and H. E. Assender, "Thermoelectric behaviour of Bi-Te films on polymer substrates DC-sputtered at room-temperature in moving web deposition," *Surface & Coatings Technology*, vol. 385, pp. 125393, 2020. http://dx.doi.org/10.1016/j.surfcoat.2020.125393.

[26] N. Mingo, "Thermoelectric figure of merit of II-VI semiconductor nanowires," *Applied Physics Letters*, vol. 85, no. 24, pp. 5986-5988, 2004. http://dx.doi.org/10.1063/1.1829391.

[27] S. Qu, Y. Chen, W. Shi, M. Wang, Q. Yao, and L. Chen, "Cotton-based wearable poly(3-hexylthiophene) electronic device for thermoelectric application with cross-plane temperature gradient," *Thin Solid Films*, vol. 667, pp. 59-63, 2018. http://dx.doi.org/10.1016/j.tsf.2018.09.046.

[28] X. Zhao, W. Han, C. Zhao, S. Wang, F. Kong, X. Ji, Z. Li, and X. Shen, "Fabrication of Transparent Paper-Based Flexible Thermoelectric Generator for Wearable Energy Harvester using Modified Distributor Printing Technology," *ACS applied materials & interfaces*, vol. 11, no. 10, pp. 10301-10309, 2019. https://doi.org/10.1021/acsami.8b21716.

[29] Yaoguang Shi, Yancheng Wang, Deqing Mei, Bo Feng, and Zichen Chen, "Design and Fabrication of Wearable Thermoelectric Generator Device for Heat Harvesting,"

IEEE Robotics and Automation Letters, vol. 3, no. 1, pp. 373-378, 2018. https://doi.org/10.1109/LRA.2017.2734241.

[30] J. Bahk, H. Fang, K. Yazawa, and A. Shakouri, "Flexible thermoelectric materials and device optimization for wearable energy harvesting," *J. Mater. Chem. C*, vol. 3, no. 4, pp. 1362-1374, 2015. https://doi.org/10.1039/c5tc01644d.

[31] G. Meijer, M. Pertijs, and K. Makinwa, "9.3 Thermoelectric Energy Harvesting, in Smart sensor systems : emerging technologies and applications," , 2014. http://eu.wiley.com/WileyCDA/WileyTitle/productCd-0470686006.html.

[32] S. LeBlanc, "Thermoelectric generators: Linking material properties and systems engineering for waste heat recovery applications," *Sustainable Materials and Technologies*, vol. 1-2, no. C, pp. 26-35, 2014. http://dx.doi.org/10.1016/j.susmat.2014.11.002.

[33] D. W. Newbrook, R. Huang, S. P. Richards, S. Sharma, G. Reid, A. L. Hector, and (Kees) de Groot, C H, "Mathematical model and optimization of a thin-film thermoelectric generator," *Journal of Physics: Energy*, vol. 2, no. 1, pp. 14001, 2019. https://doi.org/10.1088/2515-7655/ab4242.

[34] S. Funahashi, T. Nakamura, K. Kageyama, and H. Ieki, "Monolithic oxide-metal composite thermoelectric generators for energy harvesting," *Journal of Applied Physics*, vol. 109, no. 12, pp. 124509-4, 2011. http://dx.doi.org/10.1063/1.3599890.

[35] Y. Ding, Y. Qiu, K. Cai, Q. Yao, S. Chen, L. Chen, and J. He, "High performance n-type Ag2Se film on nylon membrane for flexible thermoelectric power generator," *Nature Communications*, vol. 10, no. 1, pp. 1-7, 2019. https://doi.org/10.1038/s41467-019-08835-5.

[36] Kumar, Babu, Subramanian, Bandla, Thakor, Ramakrishna, and Wei, "The Design of a Thermoelectric Generator and Its Medical Applications," *Designs*, vol. 3, no. 2, pp. 22, 2019. https://doi.org/10.3390/designs3020022.

[37] Z. Ding, G. A. W. Abbas, H. E. Assender, J. J. Morrison, S. G. Yeates, E. R. Patchett, and D. M. Taylor, "Vacuum production of OTFTs by vapour jet deposition of dinaphtho[2,3-b:2′,3′-f]thieno[3,2-b]thiophene (DNTT) on a lauryl acrylate functionalised dielectric surface," *Organic Electronics*, vol. 31, pp. 90-97, 2016. https://doi.org/10.1016/j.orgel.2016.01.024.

[38] C. F. Struller, P. J. Kelly, N. J. Copeland, V. Tobin, H. E. Assender, C. W. Holliday, and S. J. Read, "Aluminium oxide barrier films on polymeric web and their conversion for packaging applications," *Thin solid films*, vol. 553, pp. 153-156, 2014. http://dx.doi.org/10.1016/j.tsf.2013.10.091.

[39] J. Affinito, P. Martin, M. Gross, C. Coronado, and E. Greenwell, "Vacuum deposited polymer/metal multilayer films for optical application," *Thin solid films*, vol. 270, no. 1, pp. 43-48, 1995. https://doi.org/10.1016/0040-6090(95)06853-8.

[40] A. Yializis, G. L. Powers, and D. G. Shaw, "A new high temperature multilayer capacitor with acrylate dielectrics," *IEEE transactions on components, hybrids, and manufacturing technology*, vol. 13, no. 4, pp. 611-616, 1990. https://doi.org/10.1109/33.62516.

[41] K. Zhang, C. Chen, S. Anastasova, B. Gil, B. Lo, and H. Assender, "Roll-to-roll processable OTFT-based amplifier and application for pH sensing," , 2019. https://doi.org/10.1109/BSN.2019.8771092.

[42] M. Hodes, "Optimal Pellet Geometries for Thermoelectric Power Generation," *IEEE Transactions on Components and Packaging Technologies*, vol. 33, no. 2, pp. 307-318, 2010. https://doi.org/10.1109/TCAPT.2009.2039934.

[43] Y. T. Wang, W. Liu, A. W. Fan, and P. Li, "Performance Comparison between Series-Connected and Parallel-Connected Thermoelectric Generator Systems," *Applied Mechanics and Materials*, vol. 325-326, pp. 327-331, 2013. https://doi.org/10.4028/www.scientific.net/AMM.325-326.327.

[44] D. Enescu, "Thermoelectric Energy Harvesting: Basic Principles and Applications," *Green Energy Advances*, 2019. https://doi.org/10.5772/intechopen.83495.

[45] D. Kim and J. A. Rogers, "Stretchable Electronics: Materials Strategies and Devices," *Advanced Materials*, vol. 20, no. 24, pp. 4887-4892, 2008. https://doi.org/10.1002/adma.200801788.

[46] Engineering ToolBox, "Convective Heat Transfer," , 2003. https://www.engineeringtoolbox.com/convective-heat-transfer-d_430.html.

[47] Q. Wei, C. Uehara, M. Mukaida, K. Kirihara, and T. Ishida, "Measurement of in-plane thermal conductivity in polymer films," *AIP advances*, vol. 6, no. 4, pp. 45315-6, 2016. https://doi.org/10.1063/1.4948447.

[48] E. Caravaca, D. Bird, H. Grau, V. Panchal, and N. M. Ravindra, "Effects of Emissivity on Combustion Behavior of Energetic Materials," *TMS 2019 148th Annual Meeting & Exhibition Supplemental Proceedings*, pp. 1629-1641, 2019. https://doi.org/10.1007/978-3-030-05861-6_152.

[49] K. Kato, K. Kato, Y. Hatasako, Y. Hatasako, M. Kashiwagi, M. Kashiwagi, H. Hagino, H. Hagino, C. Adachi, C. Adachi, K. Miyazaki, and K. Miyazaki, "Fabrication of a Flexible Bismuth Telluride Power Generation Module Using Microporous Polyimide Films as Substrates," *Journal of electronic materials*, vol. 43, no. 6, pp. 1733-1739, 2014. https://doi.org/10.1007/s11664-013-2852-0.

[50] K. W. Mauser, S. Kim, S. Mitrovic, D. Fleischman, R. Pala, K. C. Schwab, and H. A. Atwater, "Resonant thermoelectric nanophotonics," *Nature nanotechnology*, vol. 12, no. 8, pp. 770-775, 2017. https://doi.org/10.1038/nnano.2017.87.

[51] S. Ryu, W. Jhung, and Y. Kim, "A study on the thermal conductivity measurements of Cu thin films utilizing temperature distribution," *Metals and materials international*, vol. 15, no. 5, pp. 713-718, 2009. https://doi.org/10.1007/s12540-009-0713-9.

[52] Peng Wang, Zhi Xie, Hongji Meng, and Zhenwei Hu, "Effects of the temperature and roughness on the metal emissivity," *The 27th Chinese Control and Decision Conference (2015 CCDC)*, pp. 6197-6200, 2015. https://doi.org/10.1109/CCDC.2015.7161926.

[53] A. P. Drin', V. V. Efanova, and N. I. Shut, "Thermal conductivity and kinetics of polymerization of an acrylate polymer coating," *Journal of engineering physics and thermophysics*, vol. 66, no. 2, pp. 164-171, 1994. https://doi.org/10.1007/BF00862717.

[54] R. G. Belliveau, S. A. DeJong, N. D. Boltin, Z. Lu, B. M. Cassidy, S. L. Morgan, and M. Myrick, "Mid-infrared emissivity of nylon, cotton, acrylic, and polyester fabrics as a function of moisture content," *Textile research journal*, vol. 90, no. 13-14, pp. 004051751988882-1445, 2019. https://doi.org/10.1177/0040517519888825.

[55] A. Slachter, F. L. Bakker, J-P. Adam and B. J. van Wees, Thermally driven spin injection from a ferromagnet into a non-magnetic metal, *Nature Phys*., 6, 879–882, 2010. https://doi.org/10.1038/nphys1767

Chapter 8 Conclusions and future work

8.1 Conclusions

Flexible electronics technology is playing an important role in the upcoming era of the Internet of Things and Artificial Intelligence. With an increasing demand for commercial flexible electronics, seeking a scale-up/cost-effective means for commercialisation is vital to transfer the laboratory outcome to industry. This project investigated flexible/wearable thermoelectric generators as an example flexible electronics system: they can provide a local/constant low-power source for a variety of wearable technologies. Bismuth telluride can be sputtered onto a fast-moving polymer web using large area roll-to-roll processing. Five key challenges were proposed and explored herein.

Sputtering of a thick film under a fast roll-to-roll process is challenging because of the low deposition rate of the sputtering technique. This project found that a thinner Bi-Te film could also possess a better thermoelectric performance.

A hot deposition is desirable for high performance of functional materials, but heating the polymer web during roll-to-roll is inapplicable. Herein, two feasible post-deposition treatments (infrared and electron beam) were trialled in roll-to-roll processing. The annealed film showed an improvement in thermoelectric performance.

Strain-induced failure of flexible electronics is a non-negligible factor either during roll-to-roll fabrication or for wearable use. Two types of substrate-to-coating interlayers (acrylate and PDMS) showed the ability to improve the mechanical resilience of functional coatings on flexible polymer substrate.

Patterning of flexible electronics is a key challenge in roll-to-roll processing because the current printing technique cannot fabricate nano-thick functional materials. In this study, a selective metallisation technique was explored for patterning. The fabricated device

could work, however the performance was poor because the oil used in this technique degraded the functional coating severely. This needs further study.

The dimension of the thermoelectric strip and the contact materials in a thermoelectric generator has been predicted, through many modelling/calculation studies, to influence the performance. This project found that a wider/shorter strip could generate more power, and copper was suggested as the best material for the contacts considering the cost and performance. Besides, this work also invented a stacked architecture for thermoelectric generators, suitable for roll-to-roll deposition, bringing the possibility to greatly extend the power output.

Overall, this project achieves significant steps towards to the commercialisation of flexible thermoelectric generators. Once the issue of patterning technique is further studied and well addressed, this roll-to-roll manufacture technique would be applied to the fabrication of other flexible thin-film electronics, playing an important role in advanced manufacture for the upcoming era of the Internet of Things.

8.2 Suggestions for future work

There are still some further studies to do in the future:

Chapter 3: to further balance the fast roll-to-roll process and low vacuum-deposition rate, a much thinner film could be investigated by varying the speed of the coating drum and other sputtering parameters. This needs a tradeoff between the number of passing the target source (ideally <5 times) and the film performance.

Chapter 4: the dynamic e-beam and IR annealing are effective to improve the performance of ~1-μm thick Bi-Te film. Next, further studies could apply a stronger e-beam/IR to a thinner film, or between successively deposited layers in a roll-to-roll process.

Besides, putting a buffer layer beneath the functional coating as well as a protective layer on top of the functional coating is expected to significantly improve the mechanical resilience of the functional coating.

Chapter 5: In terms of the selective metallisation technique with sputtering, further investigations of the oil type, precise control of oil pattern, and other post-deposition (or in situ) treatments should be considered in the future.

Chapter 6 & 7: More novel designs of flexible thin-film TEGs should be considered. How to integrate the TEG in a wearable device is of interest.